

NO-A177 376

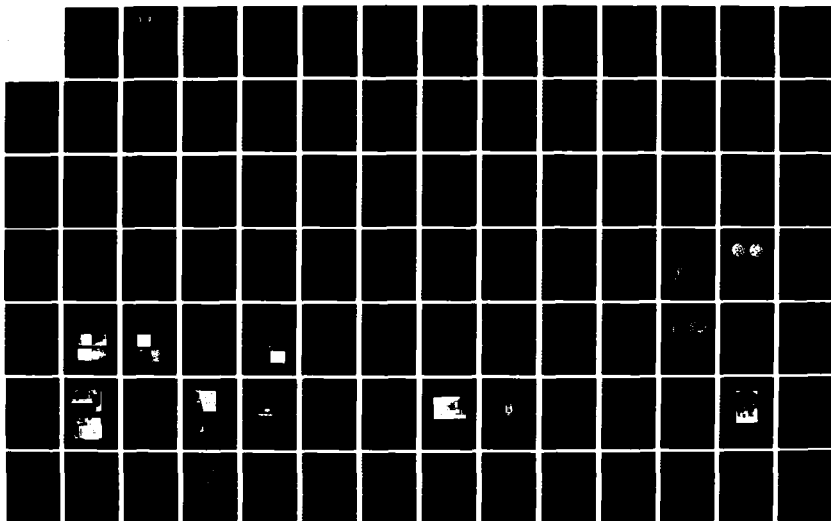
ORDERED CARBON - METAL ALLOYS FOR EXTRATERRESTRIAL  
POWER SYSTEMS(U) AUBURN UNIV AL DEPT OF MECHANICAL  
ENGINEERING B A CHIN ET AL 88 DEC 86 8628C2ETPS  
AFOSR-TR-87-0101 AFOSR-83-0168

1/3

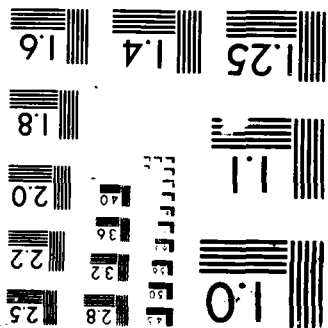
UNCLASSIFIED

F/G 11/6

NL

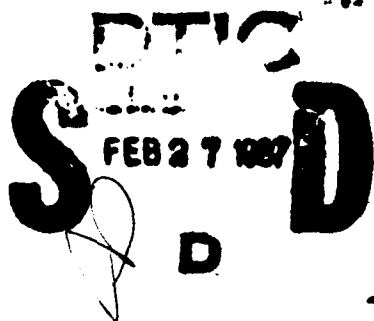


MICROCOPY RESOLUTION TEST CHART  
 NATIONAL BUREAU OF STANDARDS-1963-A



AD-A177 376

AFOSR-TR. 87-0101



Report No.: 862BC2ETPS

Approved for public release;  
distribution unlimited.

ORDERED CARBON - METAL ALLOYS FOR  
EXTRATERRESTRIAL POWER SYSTEMS

Final Progress Report

AFOSR Grant: 83-0168

B. A. Chin  
N. H. Madsen  
K. C. Yeh  
P. F. Gills  
Jie Chen

Materials Engineering  
Auburn University, AL 36849  
Phone: (205) 826-4820

AIR FORCE OFFICE OF SCIENTIFIC RESEARCH (AFSC)  
NOTICE OF DISSEMINATION  
This technical report has been reviewed and is  
approved for public release and its  
distribution is unlimited.  
DATE 14W APR 190-12.  
CHIEF, Technical Information Division

DTIC FILE COPY

87 2 20 201

## REPORT DOCUMENTATION PAGE

1a. REPORT SECURITY CLASSIFICATION Unclassified			1b. RESTRICTIVE MARKINGS None		
2a. SECURITY CLASSIFICATION AUTHORITY			3. DISTRIBUTION/AVAILABILITY OF REPORT Not Restricted <b>Approved for public release; distribution unlimited.</b>		
2b. DECLASSIFICATION/DOWNGRADING SCHEDULE N/A			4. MONITORING ORGANIZATION REPORT NUMBER(S) <b>AFOSR-TR- 87-0101</b>		
4. PERFORMING ORGANIZATION REPORT NUMBER(S) 862BC2ETPS			5. NAME OF MONITORING ORGANIZATION AFOSR- <del>PKD</del>		
6a. NAME OF PERFORMING ORGANIZATION Auburn University		6b. OFFICE SYMBOL (If applicable) N/A		7a. NAME OF MONITORING ORGANIZATION AFOSR- <del>PKD</del>	
6c. ADDRESS (City, State and ZIP Code) Department of Mechanical Engineering Auburn, AL 36849		7b. ADDRESS (City, State and ZIP Code) Building 410 Bolling AFB, D.C. 20332-6448		8. PROCUREMENT INSTRUMENT IDENTIFICATION NUMBER Grant # AFOSR-83-0168	
8a. NAME OF FUNDING/SPONSORING ORGANIZATION AFOSR/NE		8b. OFFICE SYMBOL (If applicable) NE		9. SOURCE OF FUNDING NOS.	
8c. ADDRESS (City, State and ZIP Code) Building 410 Bolling AFB, D.C. 20332-6448		PROGRAM ELEMENT NO. 61102E		PROJECT NO. 2306	TASK NO. A2
11. TITLE (Include Security Classification) Ordered Carbon - Metal Alloys for Extraterrestrial Power Systems		10. WORK UNIT NO.			
12. PERSONAL AUTHOR(S) Bryan A. Chin, N. H. Madsen, K. C. Yeh, P. F. Gills, Jie Chen					
13a. TYPE OF REPORT Final Report		13b. TIME COVERED FROM 6/84 TO 12/86		14. DATE OF REPORT (Yr., Mo., Day) 86/12/8	
15. PAGE COUNT 268		16. SUPPLEMENTARY NOTATION N/A			
17. COSATI CODES		18. SUBJECT TERMS (Continue on reverse if necessary and identify by block number)			
FIELD	GROUP	SUB. GR.			
Material	Alloys	Mech. Proper.			
19. ABSTRACT (Continue on reverse if necessary and identify by block number)		High Temperature, Alloys, Mechanical Properties			
The objective of this research is to investigate a new class of material composed of 30-60 atomic percent (C-Ti) for ultrahigh temperature applications in space power systems. The alloy system under investigation exhibits melting temperatures in excess of 2500 degrees C and form long range ordered structures which are expected to yield materials with exceptional high temperature strength and resistance to environmental degradation.					
20. DISTRIBUTION/AVAILABILITY OF ABSTRACT UNCLASSIFIED/UNLIMITED <input checked="" type="checkbox"/> SAME AS RPT. <input type="checkbox"/> DTIC USERS <input type="checkbox"/>			21. ABSTRACT SECURITY CLASSIFICATION UNCL		
22a. NAME OF RESPONSIBLE INDIVIDUAL Major Joseph Hager		22b. TELEPHONE NUMBER (Include Area Code) (202) 767-4933		22c. OFFICE SYMBOL AFOSR/NE	

Report No.:862BC2ETPS

**ORDERED CARBON - METAL ALLOYS FOR  
EXTRATERRESTRIAL POWER SYSTEMS**

Final Progress Report

AFOSR Grant: 83-0168

B. A. Chin  
N. H. Madsen  
K. C. Yeh  
P. F. Gills  
Jie Chen

Materials Engineering  
Auburn University, AL 36849  
Phone: (205) 826-4820



Accession For	
NTIS CRA&I	<input checked="checked" type="checkbox"/>
DTIC TAB	<input type="checkbox"/>
Unannounced	<input type="checkbox"/>
Justification	
By	
Distribution/	
Availability Codes	
Dist	Avail and/or Special
A-1	

## TABLE OF CONTENTS

LIST OF TABLES . . . . .	ix
LIST OF FIGURES . . . . .	x
I. INTRODUCTION . . . . .	1
II. THEORY OF ORDERED ALLOYS . . . . .	5
Critical Ordering Temperature	
Bragg-Williams, Kirkwood, Quasichemical methods	
Cluster-Variation, Concentration Waves and Band	
Theory	
Ordering Energy	
III. EXPERIMENTAL RESULTS OF PREVIOUS INVESTIGATORS . . .	39
Phase Diagram and Structure of C-Ti Alloys	
Structure and Properties of Low Carbon Weight	
Percentage C-Ti alloys (C < 0.5 w/o)	
Mechanical Properties of Titanium Carbide	
IV. EXPERIMENTAL PROCEDURES . . . . .	57
Specimen Preparation	
Equipment	
Experimental Procedure	
Failure Analysis	
V. EXPERIMENTAL RESULTS . . . . .	72
Optical Metallography	
Hardness Measurements	
Compression Test Results	
Scanning Electron Microscopy	
VI. DISCUSSION . . . . .	114
VII. CONCLUSION . . . . .	121
REFERENCES . . . . .	122

APPENDICES . . . . . 128

- A. Dimensional Measurements of Compression Specimens
- B. Gamma Phase Particle Distribution for All Compression Specimens
- C. Room Temperature Compressive Properties
- D. Elevated Temperature Compressive Properties
- E. True Stress vs True Strain Curves for All Compression Tests At Room Temperature
- F. True Stress vs True Strain Curves for All Compression Tests At Elevated Temperature

## LIST OF TABLES

1. Heat of Formation of Standard States from Monatomic Gases . . . . .	38
2. Tensile Properties of Ti-C Alloys . . . . .	44
3. Comprssive Properties of C-Ti Alloys at Room Temperature . . . . .	87
4. Compressive Properties of C-Ti Alloys at Elevated Temperature . . . . .	95



## LIST OF FIGURES

1. Determination of S at T from Equation 21 . . . . .	13
2. Lattice Collection in Bethe's Approximations . . . . .	18
3. Configuration Cv for a Simple Cubic AB Alloy . . . . .	23
4. Configuration Energy as a Function of T . . . . .	24
5. Long-Range Order S as a Function of T . . . . .	24
6. Comparson of Tc, Theory and Experiment . . . . .	25
7. Comparson of Configurational Cv, Theory and Experiment . . . . .	26
8. Block Diagram Showing Basic Steps to Self Consistent Electronic Theory of the Alloys Ordering Energy and in Determining Alloy Thermodynamics . . . . .	34
9. Phase Diagram for the C-Ti Alloy System . . . . .	40
10. 0.2 w/o C, 6 hrs. at 920°C, Water Quenched. $\alpha$ , Transformed $\beta$ and $\gamma$ . x200 . . . . .	41
11. 0.2w/o C, as Cast. $\gamma$ Stringers Plus Serrated $\alpha$ . x400 . . . . .	41
12. 11.2w/o C, 1 min. at 1800°C, Quenched. Liquid Plus $\gamma$ . x200 . . . . .	41
13. 0.4w/o C, 36 hrs. at 800°C, Water Quenched. Equiaxed $\alpha$ Plus $\gamma$ . x150 . . . . .	41
14. 4.0w/o C, 48 hrs. at 1200°C, Water Quenched. Transformed $\beta$ Plus $\gamma$ . Structure in $\gamma$ is $\beta$ . . . . .	42
15. 11.2w/o C, 200 hrs. at 700°C, Water Quenched. $\gamma$ Plus $\alpha$ . Structuer in $\gamma$ is $\alpha$ . x500 . . . . .	42
16. 17.5w/o C, 120 hrs. at 900°C, Water Quenched. Single Phase $\gamma$ . x200 . . . . .	42

17. Properties of a Ti-0.16w/o C Alloy . . . . .	45
18. Microstructures of a Ti-0.16w/o C Alloy. x250 . . . .	45
19. Properties of a Ti-0.27w/o C Alloy . . . . .	46
20. Microstructures of a Ti-0.27w/o C Alloy. x250 . . . .	46
21. Properties of a Ti-0.47w/o C Alloy . . . . .	48
22. Microstructures of a Ti-0.47w/o C Alloy. x250 . . . .	48
23. Mechanical Properties of Ti-C Alloys . . . . .	49
24. Optical Micrographs of Polished and Etched Substoichiometric TiC Samples . . . . .	51
25. Variation of Knoop Hardness with C/Ti Atom Ratio . .	52
26. Stress-Strain Curve for Annealed Polycrystalline TiC (1700°C , 4 hrs.) Deformed in Compression at Temperature Indicated (°C) ( $\dot{\epsilon} = 1.7 \times 10^{-4} \text{ S}^{-1}$ ) . . . . .	52
27. Yield Stress as a Function of Temperature in Polycrystalline TiC Deformed in Compression . . . . .	53
28. Yield Stress vs (Grain Size) $^{-1/2}$ for Polycrystalline TiC Deformed in Compression at Temperature Indicated . .	53
29. SEM Fractograph of TiC Specimens Hot Pressed from Unsieved Starck Powder. Bending Tests Performed at (a) Room Temperature, (b) 1100°C . . . . .	55
30. Log of Yield Stress vs Reciprocal of Absolute Temperature for Polycrystalline TiC Deformed in Compression . . . . .	55
31. Induction Generator and Melting Furnace used to Produce C-Ti Alloys . . . . .	59
32. Close Up of Induction Melting Coil, Crucible and Quartz Tube . . . . .	59
33. The Diamond Impregnated Soft Core Tube was to Prepare Cylindrical Compression Specimens . . . . .	61
34. The Diamond Slitting Saw used to Cut Compression Specimens . . . . .	61

35. Compression Test Sample Before Test . . . . .	62
36. Data Acquisition Unit for Recording Load and Stroke Information from Compression Test . . . . .	65
37. Heating Element for Elevated Temperature Compression Tests . . . . .	66
38. Flow Chart of MTS Data Acquisition System . . . . .	68
39. Picture of an Elevated Temperature Compression Test in Progress . . . . .	70
40. Transverse Photomicrograph of Ti-2w/o C Alloy. Globular Phase is Gamma Phase. Volume Fraction of Gamma Phase is 30%. . . . .	73
41. Transverse Photomicrograph of Ti-4w/o C Alloy. Volume Fraction of Gamma Phase is 31% . . . . .	73
42. Transverse Photomicrograph of Ti-5w/o C Alloy. Volume Fraction of Gamma Phase is 46% . . . . .	74
43. Transverse Photomicrograph of Ti-6w/o C Alloy. Volume Fraction of Gamma Phase is 50% . . . . .	74
44. Transverse Photomicrograph of Ti-7w/o C Alloy. Volume Fraction of Gamma Phase is 52% . . . . .	75
45. Transverse Photomicrograph of Ti-10w/o C Alloy. Volume Fraction of Gamma Phase is 82% . . . . .	75
46. Gamma Phase Size Distribution : Ti-2w/o C. Microstructure of Alloy shown in Figure 40 . . . . .	76
47. Gamma Phase Size Distribution : Ti-4w/o C. Microstructure of Alloy shown in Figure 41 . . . . .	77
48. Gamma Phase Size Distribution : Ti-5w/o C. Microstructure of Alloy shown in Figure 42 . . . . .	78
49. Gamma Phase Size Distribution : Ti-6w/o C. Microstructure of Alloy shown in Figure 43 . . . . .	79
50. Gamma Phase Size Distribution : Ti-7w/o C. Microstructure of Alloy shown in Figure 44 . . . . .	80
51. Gamma Phase Size Distribution : Ti-10w/o C. Microstructure of Alloy shown in Figure 45 . . . . .	81

52. Microhardness Tests of Alpha-Ti . . . . .	83
53. Microhardness Tests of Gamma Phase . . . . .	84
54. Compression Test Sample after Test . . . . .	86
55. Characteristic True Stress vs True Strain Curve for C-Ti Alloys with Different Volume Fraction of Gamma Phase . . . . .	88
56. Yield Stress as a Function of Gamma Phase . . . . .	89
57. True Failure Strain as a Function of Gamma Phase . . . . .	91
58. Characteristic True Stress vs True Strain Curve at Elevated Temperatures for 57% Gamma Phase . . . . .	93
59. Characteristic True Stress vs True Strain Curve at Elevated Temperature for 10% Gamma Phase . . . . .	94
60. True Maximum Flow Stress as a Function of Volume Fraction of Gamma Phase at Elevated Temperature . . . . .	96
61. Yield Stress as a Function of Volume Fraction of Gamma Phase at Elevated Temperature . . . . .	97
62. True Failure Strain as a Function of Volume Fraction of Gamma Phase at Elevated Temperature . . . . .	99
63. True Maximum Flow Stress as a Function of Temperature . . . . .	100
64. Yield Stress as a Function of Temperature . . . . .	101
65. True Failure Strain as a Function of Temperature . . . . .	102
66. Transition Temperature as a Function of Volume Fraction of Gamma Phase . . . . .	103
67. Fracture Features of C-Ti Alloys Containing 57% Gamma Phase at T= 25°C . . . . .	105
68. Fracture Features of C-Ti Alloys Containing 57% Gamma Phase at T= 350° C . . . . .	106
69. Fracture Features of C-Ti Alloys Containing 57% Gamma Phase at T= 450° C . . . . .	107

70. Fracture Features of C-Ti Alloys Containing 57% Gamma Phase at T= 550° C . . . . .	108
71. Fracture Features of C-Ti Alloys Containing 10% Gamma Phase at T= 25° C . . . . .	110
72. Fracture Features of C-Ti Alloys Containing 10% Gamma Phase at T= 350° C . . . . .	111
73. Fracture Features of C-Ti Alloys Containing 10% Gamma Phase at T= 450° C . . . . .	112
74. Fracture Features of C-Ti Alloys Containing 10% Gamma Phase at T= 550° C . . . . .	113
75. Y.S./d <sup>-1/2</sup> as a Function of Volume Fraction of Gamma Phase . . . . .	118
76. Y.S./d <sup>-1/2</sup> as a Function of %Gamma Phase and Test Temperature . . . . .	120

## I. INTRODUCTION

Application requiring combustion, power generation or heat transfer on land, on the air and in space by methods other than direct conversion (photovoltaic) will require new concepts materials to obtain optimum performance under desired high operating temperatures. Traditional materials such as zircaloy, stainless steel, precipitation and dispersion strengthened steels and on some exotic applications, Nb and V steels, do not have the necessary combined ultrahigh temperature strength, irradiation resistance and strength to weight ratios that are desired. Operating temperatures in excess of 1500 degrees C, where most of the above traditional materials melt, are desired.

Carbon based materials (C materials) are a superb candidate for development. C fiber-C matrix materials have been highly successful on the space shuttle where they have been used for components ranging from cargo bay doors to high temperature motor casings. Such materials, however, are not suited for sustained high temperature application or to cases which require exposure to nuclear radiation or long term exposure to fluid or gas pressure. Testing in high temperature gas cooled reactors has identified two problems with C materials.

The first is the permeability of the C material to radioactive fission gases [1,2]. Despite the development of ultrahigh density C materials, special C coatings, and differential pressurization of components, leakage of C clad fuel occurs after very short neutron exposures ( $\phi t < 1 \times 10^{21} \text{ n/cm}^2$ ). Heat pipe components, fabricated from pure C or C composite materials, would therefore be unable to maintain proper partial pressure for operation. The second problem results from volumetric change (desification) that occur in C materials upon neutron irradiation [1]. These changes are highly orientation dependent. The C fibers, which contain material with the basal planes aligned perpendicular to the stress axes, undergo a substantially different volumetric change than the matrix material, leading to the generation of high internal stress, cracking and ultimate failure.

A class of materials which promise to overcome the above described problems is ordered C-metal alloys. Ordered alloys offer many potential advantages over conventional alloys at elevated temperatures [2-5]. The atomic ordering produces a pronounced increase in work hardening, [5-9] improves the fatigue resistance, [10] and retards, because of stronger binding and closer packing of atoms, thermally activated processes such as creep and grain growth [11]. In addition, the strength of ordered alloys is less sensitive to temperature than conventional disordered alloys. In fact some alloys show an increase rather

than a decrease in strength with increasing temperature up to the critical ordering point [12]. The critical ordering point is the temperature at which the material reverts from a defined periodic arrangement of alloying elements to the random arrangement found in conventional materials. Electron, ion bombardment and recent neutron irradiation results show the long range ordered (LRO) alloys to be highly swelling resistant [13-15].

Despite the above advantages, the LRO alloys have seen only limited application because of a lack of ductility associated with the ordered state [16-18]. Recently Liu and his coworkers at ORNL have succeeded in producing  $(\text{Fe,Ni})_3\text{V}$  long range ordered alloys which show tensile elongations greater than 30% [19-21]. This has been achieved by controlling the ordered lattice structure through use of the e/a ratio or average electron density per atom outside the inert gas shell. In other words by creating off stoichiometric compounds.

Ordered C-metal alloys represent a new approach which combines the desirable qualities of C (high temperature resistance, low weight, low vapor pressure) with the radiation and permeability resistance of ordered materials. These alloys, containing 38-60 atomic percent carbon, all exhibit melting temperature in excess of 2500 degrees C [22,23]. By careful control of the alloy composition, desirable ordered structures can be maintained at temperatures in excess of  $0.7 T_m$  (approx. 1800 degrees C). The alloys will be relatively lightweight, yet



resistant to irradiation damage. Control of the ordered structure by modification of the e/a ratio will produce compositions with good ductility, strength, creep and fatigue properties. In addition, the C-metal alloys will eliminate the permeability problem associated with pure C materials.

The C-Ti system based upon its ability to obtained an ordered structure over a range of compositions and its ultrahigh melting temperature (3080 degrees C). The objective of this study is to investigate the structure-property relationships of 0-40 weight percent(w/o) carbon of the C-Ti system. The experiments concentrate on an investigation of the effect of C content on the mechanical properties. These studies provide a theoretical and experimental basis for understanding the properties of C base alloys.

## II. THEORY OF ORDERED ALLOYS

There are a number of theoretical models available which allow the calculation of the critical ordering temperature, maximum degree of order and specific heat as a function of temperature for ordered alloy systems. It is the objective of this research to apply these theories to the C-Ti alloy system. The results of the above computations will provide a theoretical basis upon which the most promising alloy systems and ranges of compositions can be chosen for melting and experimentation. It is hoped that before alloying additions are made that we will be able to extend these theoretical calculations to ternary systems [24].

Unlike conventional alloys, which from a random mixture of atoms on lattice sites, long range ordered (LRO) alloys exhibit periodic arrays which form an ordered crystal structure. In general, unlike atoms tend to be closer together and like atoms further apart. The tendency to order increases with decreasing temperature, therefore, the ordered arrangement of atoms must be more stable or energetically favorable at lower temperature than a random distribution. For this to be true, the attraction between unlike atoms stronger than the attraction between like atoms. As the temperature of the alloy increases, the energy of

thermal vibration increases and when this exceeds the so called ordering energy, the atoms have sufficient energy to redistribute themselves into a disordered or random mixture. It is at this point that the disordered structure becomes the stable configuration. Thus, we expect a transition temperature at which the ordered phase becomes unstable. This transition temperature, the critical temperature,  $T_c$ , is analogous to the Curie temperature in ferromagnetism.

#### Critical Ordering Temperature

To predict the critical ordering temperature for C-Ti alloys, a review of various theoretical models of ordering was undertaken. This review is summarized in what follows. Above the critical temperature the alloy is completely disordered. Once the critical temperature is reached, atomic ordering begins and at each temperature below the critical temperature (after suitable time) an equilibrium degree of order will be reached. Thus, at the stoichiometric composition of the alloy, the equilibrium degree of order at high temperatures will be zero and at 0 degree kelvin the alloy will be completely ordered. alloys which are not stoichiometric will not reach perfect order, but will have a characteristic maximum degree of order depending on the composition.

the first suggestion that some alloys can exhibit an ordered structure, or supper-lattice was put forth in 1919 by Tammann

[25] after his observations in the Cu-Au system. Since that time a number of efforts have been made to theoretically describe and predict the cooperative phenomena of ordering [26].

The first successful theory of the stability of superlattices, as a function of temperature, was developed by Bragg and Williams [27]. Later, Bethe [28] developed a more refined method, which was extended by several authors. Neither one of these methods were very clear about the assumptions which were made; Kirkwood [29] remedied this by developing a theory based entirely on the standard concepts of statistical mechanics. The quasichemical method was developed also at this time by Guggenheim [30] and was later shown to be equivalent to Bethe's method [31].

The more theories, including: the Cluster-variation method developed by Takagi [32], Kikuchi [33], Yang, Li [34] and Hill [35], the method of concentration waves [11], and a band theory model [37]. In addition to these, numerical methods based on the random walk or Monte Carlo Method [38] have been developed.

Except for band theory, all of the above models require the interaction or ordering energies of the alloy,

$$V^i = V_{AA}^i + V_{BB}^i - V_{AB}^i \quad \text{-----}(1)$$

where the superscript  $i=1$  denotes nearest neighbors,  $i=2$  denotes next nearest neighbors, etc., and the subscripts denote which pair of atoms the energy  $V_{\alpha\beta}$  represents. Unfortunately, this energy parameter is hard to come by, This will be discussed later.

## Bragg-Williams, Kirkwood, Quasichemical Methods

To specify the degree of order of the arrangement, Bragg and Williams introduced the long range order parameter  $s$  in their original paper [27]. When perfect order is achieved in a binary alloy of components A and B, the lattice sites occupied by A atoms are called  $\alpha$  sites and those occupied by B atoms are called  $\beta$  sites. Let  $N$  be the total Number of atoms (A and B) and thus the total number of lattice sites, (i.e. no vacancies); and  $F_A$  and  $F_B$  (where  $F_B = 1 - F_A$ ) be the fraction of A and B atoms in the alloy respectively. Also let the fraction of  $\alpha$  sites occupied by A atoms be denoted by  $r_\alpha$  (right atoms), the fraction of  $\alpha$  sites occupied by B atoms be  $w_\alpha$ , where  $w_\alpha = 1 - r_\alpha$  and similarly define  $r_\beta$  and  $w_\beta = 1 - r_\beta$  represent the rightly and wrongly occupied  $\beta$  sites. The long range order parameter  $s$  may be defined as

$$s = \frac{r_\alpha - F_A}{1 - F_A} = \frac{r_\beta - F_B}{1 - F_B} \quad \text{-----}(2)$$

Thus,  $s$  is defined as unity for perfect order and vanishes in the completely disordered state.

Now, let  $Q$  be the total number of all types of nearest neighbor pairs in the lattice and each atoms be surrounded by  $z$  nearest neighbors, thus

$$Q = (Z/2) N \quad \text{-----}(3)$$

Also let the number of pairs, which are AA, BB and AB be denoted by  $Q_{AA}$ ,  $Q_{BB}$ ,  $Q_{AB}$  respectively. Consider an alloy with  $F_A N$   $\alpha$  sites and  $F_B N$   $\beta$  sites. Then according to equation (2) the

average number of A and B atom on  $\alpha$  and  $\beta$  sites are as follows [26]:

$$\text{A atoms on } \alpha \text{ sites: } r_{\alpha} F_A N = (F_A + F_B s) F_A N,$$

$$\text{A atoms on } \beta \text{ sites: } w_{\beta} F_B N = (1 - s) F_A F_B N,$$

$$\text{B atoms on } \alpha \text{ sites: } w_{\alpha} F_A N = (1 - s) F_B F_A N,$$

$$\text{B atoms on } \beta \text{ sites: } r_{\beta} F_B N = (F_B + F_A s) F_B N,$$

The number  $g(s)$  of distinguishable arrangements or configurations for a given state  $s$  is then

$$g(s) = \frac{[F_A N]}{[F_A + F_B s] F_A N! [(1-s) F_A F_B N]!} \frac{[F_B N]}{[(1-s) F_A F_B N]! [(F_B + F_A s) F_B N]!} \quad (5)$$

Assuming, that the lattice vibrations are independent of the configuration of the atoms in the lattice, the partition function in the canonical ensemble may be written as

$$z(T, s) = \sum_r e^{-W_r / K T} \quad (6)$$

where  $T$  is the absolute temperature,  $s$  is the long range order,  $K$  is the Boltzmann constant and  $W_r$  is the configurational energy of the state  $r$ . The summation extends over all the state  $r$  of a given order  $s$ .

Our knowledge of  $W_r$  is scant at best at this time and is approximated here as consisting mainly of the interaction energies of pairs of nearest neighbors. These energies as identified in eq.(1) are  $V_{AA}$ ,  $V_{BB}$ ,  $V_{AB}$ , corresponding to nearest neighbor pairs  $Q_{AA}$ ,  $Q_{BB}$ ,  $Q_{AB}$  respectively. Therefore the configurational energy is roughly given by

$$W_r = - (Q_{AA}V_{AA} + Q_{BB}V_{BB} + Q_{AB}V_{AB}), \quad \text{-----}(7)$$

for any specified configuration  $r$ . The configurational free energy  $F(s)$  is given by

$$F(s) = -KT \ln(Z(T, s)) \quad , \quad \text{-----}(8)$$

and once this is minimized the equilibrium value of  $s$  will be determined. The corresponding energy of the alloy is

$$E(s) = W(s) = \frac{\sum_r W_r e^{-u_r \beta}}{\sum_r e^{-u_r \beta}} \quad \text{-----}(9)$$

where  $\beta$  is  $1/KT$ .

Now, using the conventional procedures of statistical mechanics, we define  $U(s)$  by relation

$$\sum_r e^{-u_r \beta} = g(s) e^{-U(s) \beta} \quad \text{-----}(10)$$

Here  $g(s)$  is the same as in eq. (5). Now, eq. (8) can be written as

$$F(s) = U(s) - KT \ln(g(s)) \quad , \quad \text{-----}(11)$$

and the energy of the alloy can be written as

$$E(s) = \frac{\partial}{\partial(1/T)} \frac{U(s)}{T} \quad \text{-----}(12)$$

The above equations for the free energy and internal energy define the thermodynamics of the system [26]. All that is left to do is to calculate the partition function. This however has proved illusive and various approximations have been made, the first of which was the Bragg-Williams approximation [27]. Their approximation consists of replacing the true value of  $W_r$  for each

configuration of  $s$  by the simple average  $\langle W_r \rangle$  of all staets belonging to a given  $s$ ,

$$\langle W_r \rangle = - (\langle Q_{AA} \rangle V_{AA} + \langle Q_{BB} \rangle V_{BB} + \langle Q_{AB} \rangle V_{AB}) \quad , \quad --(13)$$

where  $\langle Q_{AA} \rangle$ ,  $\langle Q_{BB} \rangle$  and  $\langle Q_{AB} \rangle$  are the sample averages of the number of pairs of each kind in each state  $r$  of  $s$ . Consider  $\langle Q_{AA} \rangle$ , AA pairs may result from two arrangements: (1) one A atom on an  $\alpha$  site and other one on a  $\beta$  site, and (2) both atoms on  $\beta$  sites. On the average there are  $F_A N (F_A + F_B s)$   $\alpha$  sites occupied by A atoms. There are then  $z N F_A^2 (1-s) (F_A + F_B s)$  AA pairs of type (1). The number of AA pairs with both atoms on  $\beta$  sites is  $1/2 z N F_A^2 (F_B - F_A) (1-s)^2$  [26]. Therefore,

$$\begin{aligned} \langle Q_{AA} \rangle &= z N F_A^2 (1-s) (F_A + F_B s) + 1/2 z N F_A^2 (F_B - F_A) (1-s)^2 \\ &= 1/2 z N (F_A^2 - F_A^2 s^2) \quad \text{-----} (14) \end{aligned}$$

and similarly,

$$\begin{aligned} \langle Q_{BB} \rangle &= 1/2 z N (F_B^2 - F_A^2 s^2) \\ \langle Q_{AB} \rangle &= 1/2 z N (2 F_A F_B + 2 F_A s^2). \end{aligned}$$

Substituting equations (14) into (13) leads to

$$\begin{aligned} \langle W_r \rangle &= (Nz/2) (F_A^2 V_{AA} + 2 F_A F_B V_{AB} + F_B^2 V_{BB}) \\ &\quad - (Nz/2) F_A^2 (2 V_{AB} - V_{AA} - V_{BB}) s^2 \quad \text{-----} (15) \end{aligned}$$

Since  $\langle W_r \rangle$  is independent of temperature in this approximation, by equations (10) and (12)

$$\langle W_r \rangle = E(s) = U(s) \quad \text{-----} (16)$$



Thus, the configurational free energy becomes

$$\begin{aligned}
 F(s) - F(0) = & NKT[F_A(F_A + F_B s) \ln(F_A(F_A + F_B s)) + \\
 & F_B(F_B + F_A s) \ln(F_B(F_B + F_A s)) \\
 & + 2F_A F_B (1-s) \ln(F_A F_B (1-s)) - 2F_A \ln F_A - 2F_B \ln F_B] \\
 & - NzVF_A^2 s^2 \quad \text{-----} (17)
 \end{aligned}$$

after using the expression for  $g(s)$  in eq. (5) and eq. (15) for the energy in eq. (11), where  $V$  is  $V'$  as defined in equation 1, in the nearest neighbor approximation. For the alloy of composition  $F_A = F_B = 1/2$ , this expression reduces to

$$\begin{aligned}
 F(s) - F(1) = & (NKT/2)((1+s) \ln(1+s) + (1-s) \ln(1-s) - 2 \ln 2) \\
 & + 1/4 NzV(1-s^2) \quad \text{-----} (18)
 \end{aligned}$$

The equilibrium state of the configuration in the alloy is found by minimizing the free energy. Thus, the condition

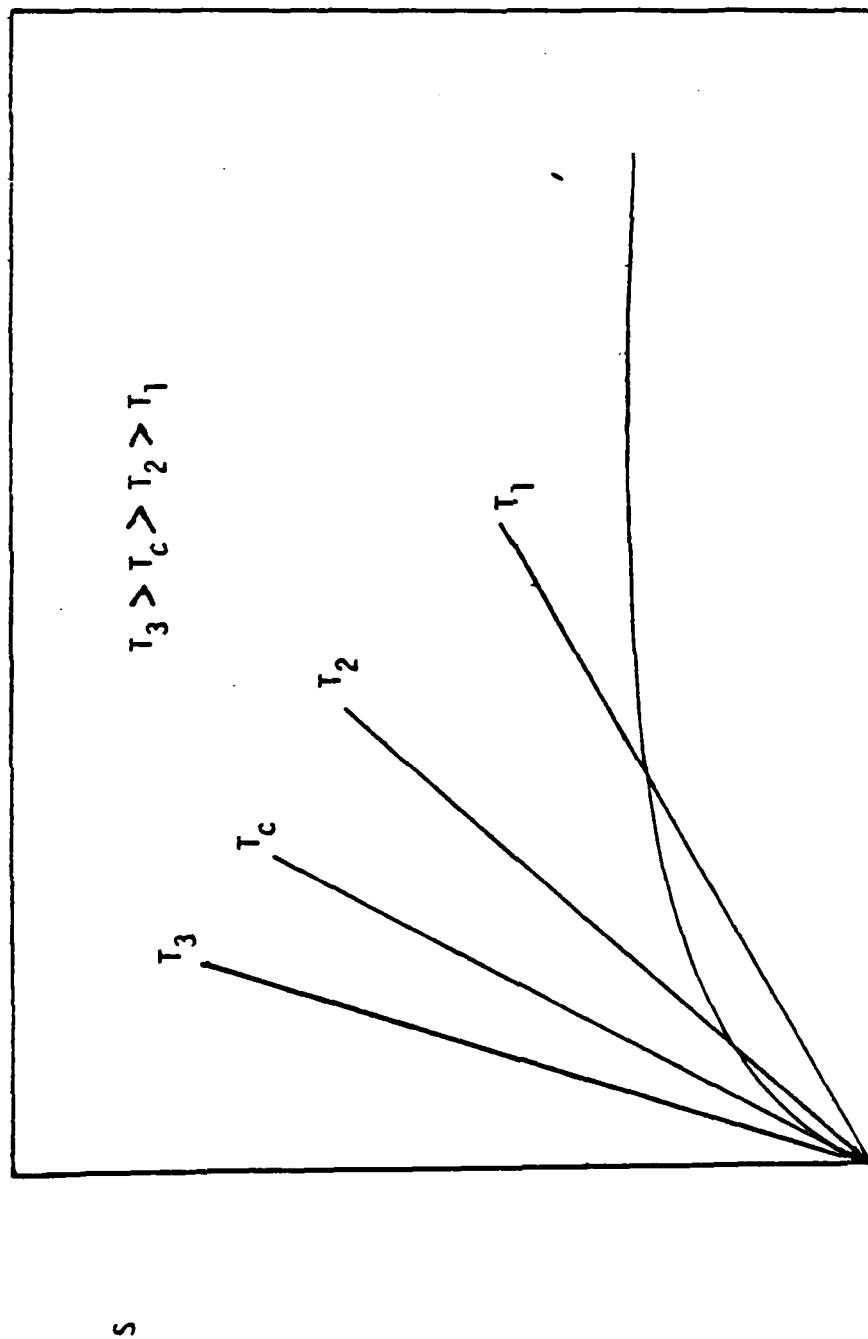
$$\frac{\partial F}{\partial s} = 0 \quad \text{-----} (19)$$

gives  $s = \tanh(zV/2KT)s \quad \text{-----} (20)$

This equation determines the equilibrium value of  $s$  as a function of  $T$ . The above equation can be decomposed into

$$s = \tanh X \text{ and } s = 2KT/zNX \quad \text{-----} (21)$$

When these two equation are plotted as a function of  $X$  the intersection of the curves give the equilibrium value of  $s$  at  $T$  (see Figure 1). There are two solution of (21), one at  $s=0$  and one at  $s>0$  for all  $T$  less than some  $T$ . The solution  $s=0$  corresponds to the maximum free energy or the unstable state of order, whereas the solution of  $s>0$  corresponds to the minium free



X

Figure 1. Determination of  $S$  at  $T$  from equation 21.

energy of equilibrium value of order. The solution of  $s > 0$  indicates the existence of the ordered state at temperature below a critical value. The value of  $s$  decreases very slowly at first, then as the temperature continue to increase drop off abruptly at  $T_c$ , and vanishes at all temperature greater than  $T_c$ . The critical temperature is found by the conditions

$$\frac{\partial F}{\partial s} = \frac{\partial^2 F}{\partial s^2} = s = 0 \quad \text{-----}(22)$$

These conditions lead to

$$KT_c = zV/2 \quad \text{-----}(23)$$

for the critical temperature of an alloy with composition  $F_A = F_B = 1/2$ .

A higher approximation, developed by Kirkwood [29], is one which takes into account, on the average, the energy spread of  $W_r$  for a given  $s$  around its average value  $\langle W_r \rangle$ . Although it is not possible to know the actual distribution of  $W_r$ , we can find the moments of deviations from  $\langle W_r \rangle$ . We write equation (10) as

$$U(s)/KT = \ln[g(s)] - \ln[\sum_r e^{-W_r/KT}] \quad \text{-----}(24)$$

and expanding the exponentials,

$$\frac{U(s)}{KT} = -\ln 1 - \frac{\langle W_r \rangle}{KT} + \frac{1}{2!} \frac{\langle W_r^2 \rangle}{(KT)^2} - \frac{1}{3!} \frac{\langle W_r^3 \rangle}{(KT)^3} + \dots \quad (25)$$

where  $\langle W_r^n \rangle = \frac{g(s)}{\sum_r} (W_r^n / g(s))$ .

Upon further expansion of the logarithm above,  $U(s)$  can be written as

$$U(s) = \langle W_r \rangle - \frac{1}{2!} \frac{1}{KT} (\langle W_r^2 \rangle - \langle W_r \rangle^2) + \frac{1}{3!} \frac{1}{(KT)^2} (\langle W_r^3 \rangle - 3\langle W_r \rangle \langle W_r^2 \rangle + 2\langle W_r \rangle^3) \quad \text{-----} (26)$$

where  $\langle W_r^2 \rangle - \langle W_r \rangle^2 = \langle (W_r - \langle W_r \rangle)^2 \rangle$  is the second moment and  $\langle W_r^3 \rangle - 3\langle W_r \rangle \langle W_r^2 \rangle + 2\langle W_r \rangle^3 = \langle (W_r - \langle W_r \rangle)^3 \rangle$  is the third.

Substituting  $\langle W_r \rangle$  for the alloy  $F_A = F_B = 1/2$  into the above equation gives  $U(s)$ ,

$$U(s) = - \frac{Nz}{2} V_{AB} + \frac{1}{2} NzV \left( \frac{1}{2} (1-s^2) - \frac{V}{KT} \frac{1}{8} (1-s^2)^2 - \frac{V^2}{KT} \frac{1}{12} s^2 (1-s^2)^2 + \dots \right) \quad \text{-----} (27)$$

The free energy is found by substituting the above equation and equation (5) for  $g(s)$ , into equation (11),

$$F(s) - F(1) = - \frac{N}{2} KT ((1+s)\ln(1+s) + (1-s)\ln(1-s) - 2\ln 2) + \frac{N}{KT} zV \left( \frac{1}{4} (1-s^2) - \frac{V}{KT} \frac{1}{8} (1-s^2)^2 - \frac{V}{KT} \frac{1}{12} s^2 (1-s^2) + \dots \right) \quad \text{-----} (28)$$

The Bragg-Williams solution corresponds to keeping only the first and second terms of the above equation and ignoring all higher order terms. Again the equilibrium value of  $s$  at  $T$  is found by minimizing  $F(s)$ ,

$$\ln \frac{1+s}{1-s} = \frac{zV}{KT} s \left( 1 - \frac{V}{KT} \frac{1}{2} (1-s^2) + \frac{V^2}{KT} \frac{1}{6} (1-s^2)(1-3s^2) + \dots \right) \quad \text{-----} (29)$$

This function drops off much more rapidly at  $T_c$  compared to the Bragg-Williams approximation and is almost identical to Bethe's and Guggenheims quasichemical model [26]. However, difference in

the specific heats do arise. The critical temperature is again found by the condition of  $\partial F/\partial s = \partial^2 F/\partial s^2 = s = 0$ , and is

$$2 \frac{KT_c}{zV} = 1 - \frac{1}{2} \frac{V}{KT_c} + \frac{1}{6} \left( \frac{V}{KT_c} \right)^2 + \dots \quad --(30)$$

Kirkwood solution has the advantage over Bragg and Williams in that it is easily adapted to different types of lattices and to nonstoichiometry. Also, in principle, it is possible to obtain any degree of accuracy; however, equation (30) tends to converge very slowly at temperatures below  $T_c$  and higher order terms are necessary for reliable results.

Bethe's solution [28] has been shown to be Guggenheim's quasichemical method of solution. His original model, as will be presented here, is basically a construction of the grand partition function for a small group of lattice sites in which the variables of temperature, volume and absolute activities play important roles. However, the original model was not constructed as a canonical ensemble, instead Bethe based his development on nearest neighbor interactions and the short range order parameter. The short range order parameter, as defined by Bethe, is not based on  $\alpha$  and  $\beta$  sites in the lattice but on the configuration of nearest neighbors. This parameter measures the way in which, on the average, each atom is surrounded by its neighbors, or the extent of local order. The short range order is defined as

$$\sigma = \frac{(q - q_r)}{(q_m - q_r)} \quad \text{-----}(31)$$

where  $q = Q_{AB}/Q$ ,  $q_m$  is the maximum value of  $q$  and  $q_r$  is the value of  $q$  in the disordered state. Here, the limits of zero and one are obtained for complete disorder and order respectively, as for the long range order.

Now, we select an arbitrary group of sites for consideration on the basis of nearest neighbor interactions, consider for example Figure 2. The group consists of an interior and a boundary, all remaining sites of lattice are exterior. The influence of the exterior atoms are taken into account only on the average. For simplicity the method is developed for an AB alloy.

For the first approximation we selected an  $\alpha$  site as the interior. Thus the boundary will consist of  $z$  nearest neighbor  $\beta$  sites. For the second approximation the group may be selected as in Figure (2b); the larger the group chosen, the greater the accuracy. However the mathematics become correspondingly more complicated [28]. Considering the first approximations, we assume that a state of long range order exists in the exterior. This ordering will affect the boundary of our group by encouraging A atoms to  $\alpha$  sites and B atoms to  $\beta$  sites. This tendency to order on the boundary, due to the exterior, is denoted by an ordering energy  $u$ . The energy  $u$  is equal to the difference in energy of a wrong atom on an  $\alpha$  or  $\beta$  site and a right atom on an  $\alpha$  or  $\beta$  site.

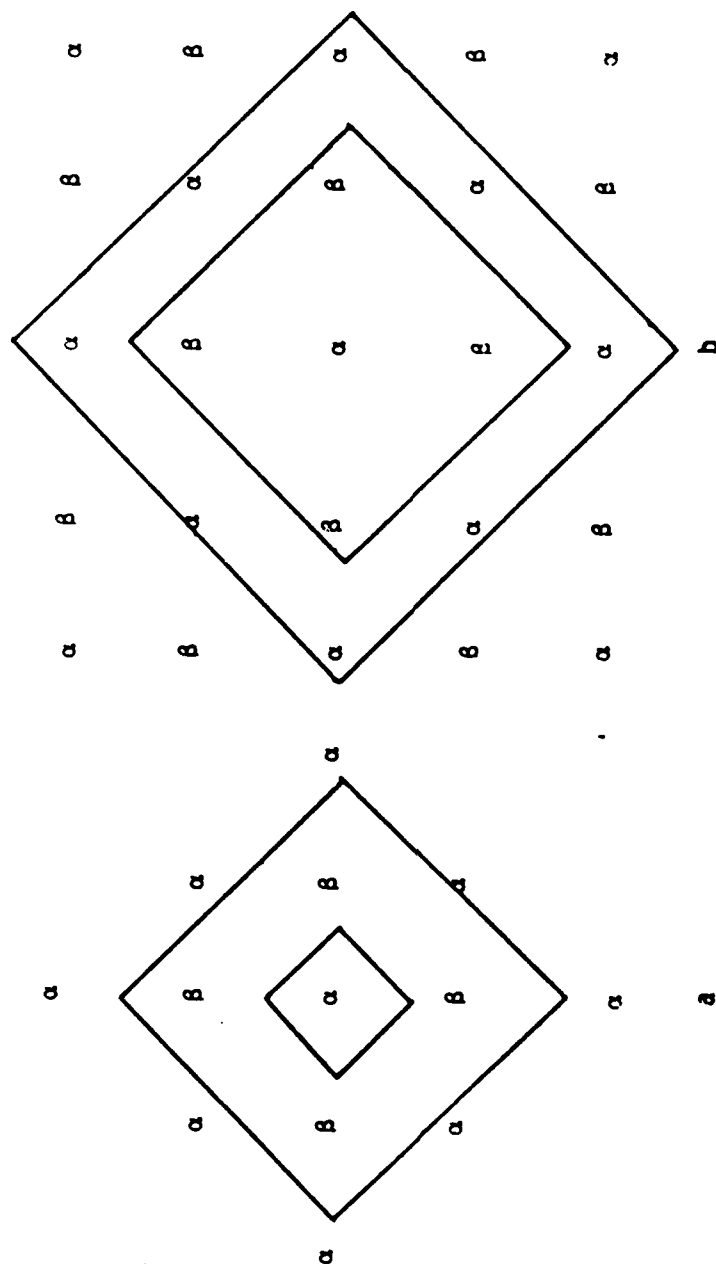


Figure 2. Lattice Collection in Bethe's Approximations.

Consider now, the energy of the alloy which is determined by the number of pairs  $Q_{AA}$ ,  $Q_{BB}$  and  $Q_{AB}$  for a definite arrangement of atoms on the lattice sites. The energy of a crystal of pure A with  $F_A N$  atoms will be  $-V_{AA}$  (# of pairs) or  $-z/2 F_A N V_{AA} = -F_A Q V_{AA}$  and similarly for a crystal of B atoms only, the energy is  $-F_B V_{BB} Q$ . Thus the energy of the alloy, with respect to the pure crystals of its components is

$$E = -V_{AA} Q_{AA} - V_{AB} Q_{AB} - V_{BB} Q_{BB} + (V_{AA} F_A Q + V_{BB} F_B Q). \quad \text{----(32)}$$

This reduces to

$$E = ((1/2)(V_{AA} + V_{BB}) - V_{AB}) Q_{AB} = -V Q_{AB} \quad \text{----(33)}$$

since

$$\begin{aligned} Q_{AA} &= F_A Q - Q_{AB}/2 \\ Q_{BB} &= F_B Q - Q_{AB}/2 \end{aligned} \quad \text{-----(34)}$$

So that the superlattice will be stable at lower temperature  $V$  must be taken less than zero. The Boltzmann factor is then

$$e^{-V/KT} = \epsilon \quad \text{-----(35)}$$

For the boundary, the relative probability of finding an A atom instead of a B atom due to the exterior is

$$e^{-U/KT} = x \quad \text{-----(36)}$$

From the two Boltzmann factors above various probabilities in the interior and in the boundary may now be found.

If the central atom is A, a right atom, the relative probability of finding  $n$  wrong A atoms in the boundary,  $Pr(n)$ , is

$$Pr(n) = \binom{z}{n} \epsilon^n x^n \quad \text{-----(37)}$$

If the center atom is a B atom the probability of finding  $n$  wrong



atoms on the boundary is

$$Pw(n) = \binom{z}{n} x^n \epsilon^{z-n} \quad \text{-----(38)}$$

since each of the  $z-n$  right atoms in the boundary has an interaction energy  $V$  with the wrong interior B atom. The binomial coefficient  $\binom{z}{n}$  is the number of ways of arranging  $n$  wrong A atoms in the  $z$  boundary sites. The total relative probability for the interior atoms being correct is

$$r_i = \sum_{n=0}^z Pr(n) = (1 + \epsilon x)^2, \quad \text{-----(39)}$$

and for being wrong is

$$w_i = \sum_{n=0}^z Pw(n) = (\epsilon + x)^2. \quad \text{-----(40)}$$

The normalized probabilities are then

$$r_\alpha = \frac{r_i}{r_i + w_i}, \text{ and } w_\alpha = \frac{w_i}{r_i + w_i}. \quad \text{-----(41)}$$

It is also necessary to calculate the relative probability of sites in the boundary being wrongly occupied. This is the average number of wrong atoms in the boundary divided by  $z$ . The relative probability of finding  $n$  wrong atoms in the boundary is  $Pr(n) + Pw(n)$ . The average number of wrong atoms in the boundary is calculated as follows:

$$\langle n \rangle = zw_\beta = \frac{\sum_{n=0}^z n(Pr(n) + Pw(n))}{\sum_{n=0}^z (Pr(n) + Pw(n))}. \quad \text{---(42)}$$

Here,  $w_\beta$  is the normalized probability of having a wrong atom in the boundary  $\beta$  sites, therefore

$$w = \frac{\frac{\epsilon x}{1 + \epsilon x} r_i + \frac{x}{\epsilon + x}}{r_i + w_i} \quad \text{-----} (43)$$

Now in order to determine the unknown energy  $u$  in  $x$ , Bethe introduced a symmetry or consistency condition. Since there are an equivalent number of  $\alpha$  and  $\beta$  sites and A and B atoms for an AB alloy at stoichiometry, the probability must be symmetric, i.e. the same probabilities hold whether an  $\alpha$  or  $\beta$  site is chosen as the origin of our group. Thus,

$$w_\alpha = w_\beta \quad \text{-----} (44)$$

This is called the consistency equation. Putting equations (41) and (43) into the above equation the value of  $u$  at  $T$  can be found as a function of  $V$  and  $T$ ,

$$\left[ \frac{x + \epsilon}{1 + \epsilon x} \right]^{z-1} = x \quad \text{-----} (45)$$

The short range order  $\sigma$  and the configurational energy of the alloy can now be found. The number of AB pairs is  $z-n$  for a right center atom, and  $n$  for a wrong center atom, therefore on the average the fraction of AB atoms in the alloy is

$$q = \frac{Q_{AB}}{Q} = \frac{\sum_{n=0}^z (z-n)Pr(n) + \sum_{n=0}^z nPw(n)}{z(r_i + w_i)} \quad \text{--} (46)$$

For the AB alloy  $q_m = 1$  and  $q_r = 0.5$ , thus, from eq. (31),  $\sigma = 2q - 1$ , or from equation (46),

$$\sigma = 1 - \frac{4\epsilon x}{1 + \epsilon x} \frac{1}{1 + x^{z/2-1}} \quad \text{-----} (47)$$

The configurational energy is then

$$E = VQ_{AB} = -VQ_q = - (VQ/2)(\sigma + 1) \quad \text{-----} (48)$$

Measured from the completely ordered alloy this energy becomes

$$E - E(0) = - (VQ/2)(1 - \sigma). \quad \text{-----(49)}$$

The long range order can be found by use of equations (2), (39), (40), and (41) and is

$$s = 2r_\alpha - 1 = \frac{(1+\epsilon x)^2 - (\epsilon+x)^2}{(1+\epsilon x)^2 + (\epsilon+x)^2}. \quad \text{----(50)}$$

Recalling that at complete disorder

$$r_\alpha = r_\beta = w_\alpha = w_\beta = 1/2$$

and using equation (45), the critical temperatures for an AB alloy is given by

$$\frac{V}{KT_c} = \ln \frac{z}{z-2} \quad [26]. \quad \text{-----(51)}$$

In this form, extension to other lattices besides simple cubic AB alloys is quite laborious. However, this is equivalent to the quasichemical method of Fowler and Guggenheim [31]; and Takagi's combinatorial analysis [32] allows a simpler extension to different compositions and structure.

A comparison of the three early models can be seen in Figures 3, 4 and 5. All three of these models have neglected important physical considerations, as do the more recent models, these include: (1) interaction of atoms which are not nearest neighbors, (2) changes in cell size, lattice symmetry and thermal expansion, (3) lattice vibrations, (4) limit of the validity of the ordering energy and finally, (5) effect of size differential in the ordering phenomena. A comparison of theory and experiment, Figures 6 and 7 shows poor quantitative agreement.

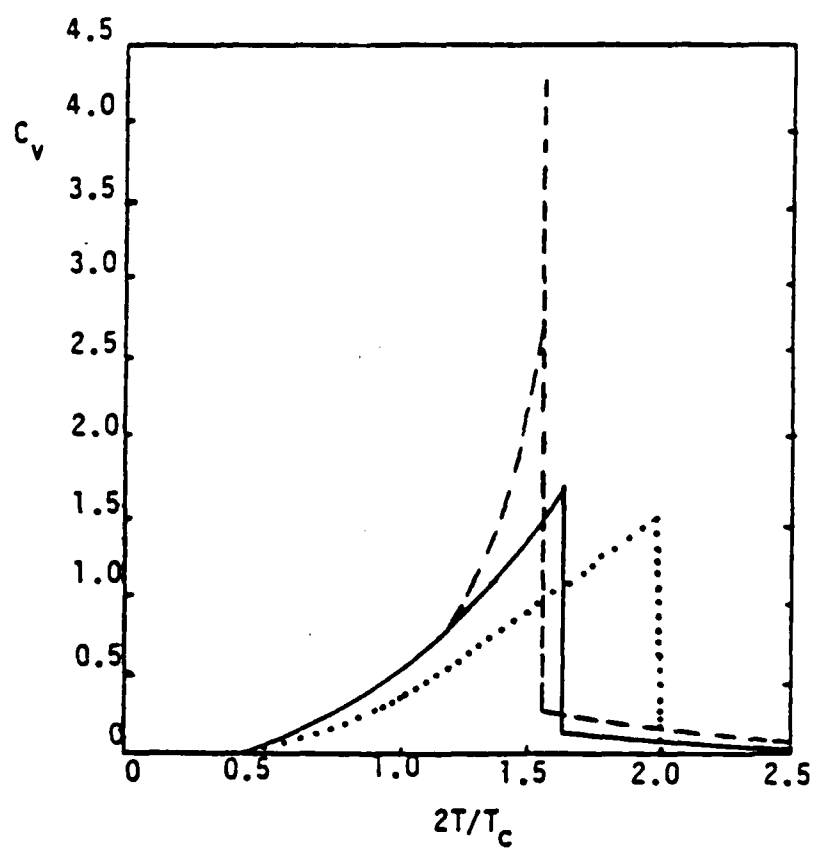


Figure 3. Configurational  $C_v$  for a simple cubic AB alloy. [26]

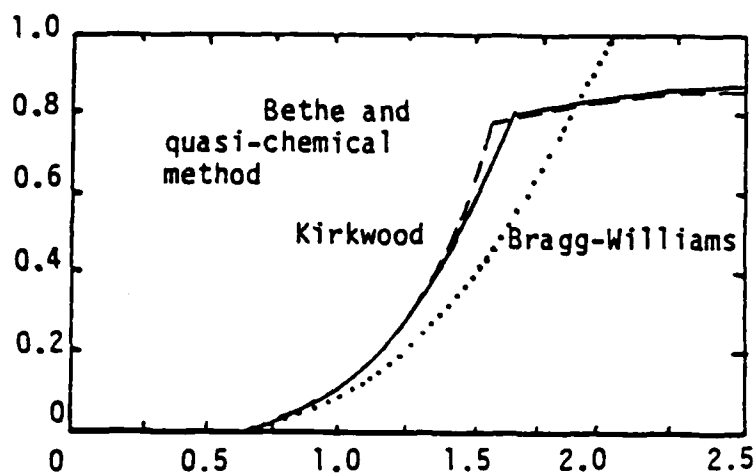


Figure 4. Configurational Energy as a function of  $T$ . [26]

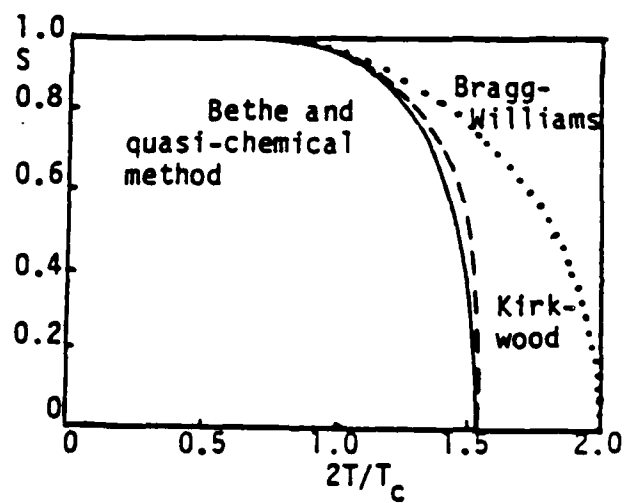


Figure 5. Long-range order  $S$  as a function of  $T$ . [26]

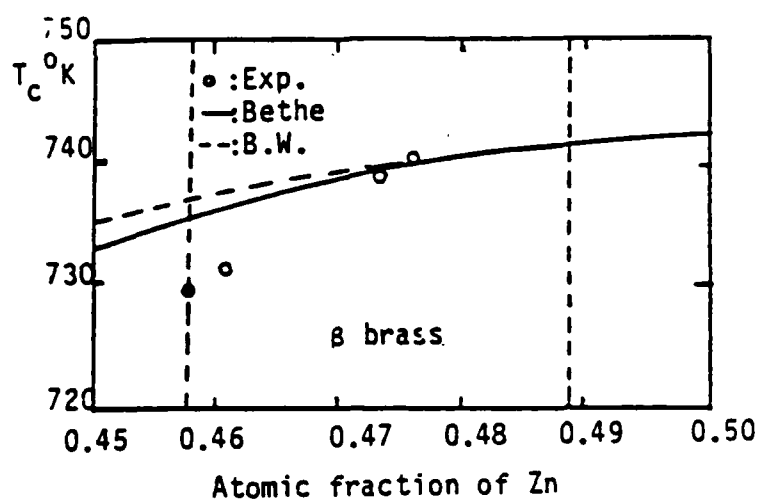


Figure 6. Comparison of  $T_c$ , Theory and Experiment. [26]

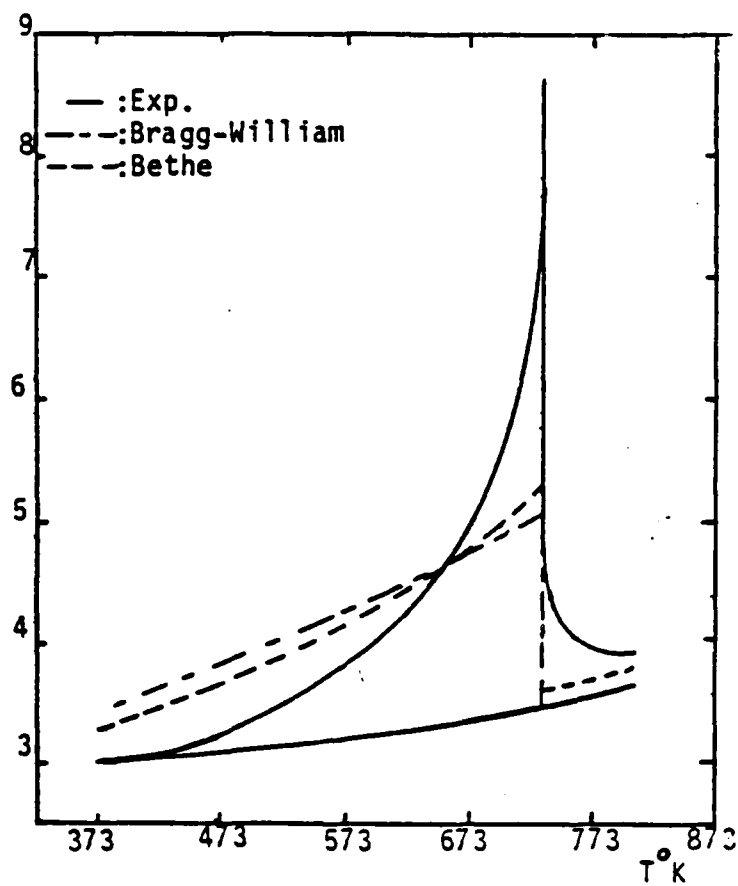


Figure 7: Comparison of Configurational  $C_v$ , Theory and experiment. [26]

qualitatively the models are essentially correct [26]. The more recent models are somewhat more quantitatively correct and will be briefly explained.

#### Cluster-Variation, Concentration Waves and Band Theory

The cluster-variation [39] method is an extension of the quasichemical model. This model uses the same type of energy terms as the earlier theories. However, it introduces a way of arriving at a better approximation to the entropy. The free energy is written in terms of the different configurations a cluster can have and is then minimized with respect to the configurations. For example, for the FCC structure a tetragonal group of atoms is chosen as the basic cluster; distribution variables are assigned to each configuration of the group and the free energy is written in terms of these variables. Minimizing the free energy with respect to these variables produces a set of simultaneous algebraic equations, usually of higher order. The values of the distribution variables which satisfy these equations represent the equilibrium configurations of the system [40]. The early formulation of the method did not allow one to choose very large clusters (which increases the accuracy) due to the large number and nature of the simultaneous equations. Kikuchi, however, has developed an iteration scheme, Natural Iteration [39], which is particularly suited to the method and guarantees convergence.



A number of authors, [41, 42, 43], have used this method and results agree fairly well with experiment. This is perhaps one of the more promising methods of describing cooperative phenomena.

The idea of concentration waves was introduced by Landau [44] and Lifshitz [45] in (1937, 1941) in the development of the phenomenological theory of phase transitions of the second kind. This method, applied to the order-disorder transition in alloys [46] has proved to be fruitful. This theory enables one to understand the symmetry aspects of the order-disorder transition, to take into consideration long range interactions in the alloy and to predict the structure of the ordered phases, which the other theories do not allow, based on concrete interatomic potentials.

All of the preceding theories reduce to the comparison of the free energy of the ordered and disordered phases calculated from nearest or at best next nearest interactions. The question of whether or not the structure of the ordered phase is stable [at the relevant choice of interatomic energies i.e. what value of  $i$  is chosen in equation (1)] and what the structure of the ordered phase is are not considered. The early theories as well as the cluster-variation improvement become especially unsatisfactory in light of recent developments in the pseudo-potential theory of metal alloys and covalent compounds (a large part of the C-Ti bonds are covalent) as well as the theory of stress induced interactions in a solid solution. Studies show

that interatomic interactions which are responsible for ordering cannot be short range. Thus for substantial improvement of the above theories, the real long range interactions must be taken into account.

These difficulties are overcome by using the method of static concentration waves. Atomic distribution in a binary alloy can be described by means of the function  $n(\mathbf{r})$ . This one function adequate because the occupational probabilities  $n_A(\mathbf{r})$  and  $n_B(\mathbf{r})$  for A and B atoms respectively are not independent. They must satisfy the identity

$$n_A(\mathbf{r}) + n_B(\mathbf{r}) = 1, \quad \text{-----}(52)$$

here  $\mathbf{r}$  is a crystal lattice vector. This function can be used for interstitial as well as substitutional alloys. In the disordered state the probabilities  $n(\mathbf{r})$  are the same for all sites which can be occupied. They are equal to the atomic fraction  $c$  of the relevant component in a substitutional alloy and in an interstitial solution they equal the fraction of interstitial sites which are occupied. In the ordered phases  $n(\mathbf{r})$  becomes dependent on the site coordinate  $\mathbf{r}$ . For instance, if  $n(\mathbf{r})$  describes  $t$  values  $n_1, n_2, \dots, n_t$  on a set of crystal sites  $(\mathbf{r})$ , then describes the sublattices into which the disordered lattice has been subdivided as a result of ordering. The  $n_i$  are occupational probabilities of the sites of the 1st, 2nd --  $t$ -th sublattice. The function  $n(\mathbf{r})$  can be expanded in the form of a Fourier series, i.e. it can be represented as a

superposition of static concentration waves:

$$n(\mathbf{r}) = c + 1/2 \sum [Q(\mathbf{k}_j) \exp(i\mathbf{k}_j \mathbf{r}) + Q^*(\mathbf{k}_j) \exp(-i\mathbf{k}_j \mathbf{r})], \quad (53)$$

where  $\exp(i\mathbf{k}\mathbf{r})$  is a static concentration wave,  $\mathbf{k}_j$  is a non-zero wave vector defined in the first Brillouin zone of the disordered alloy,  $\mathbf{r}$  is a site vector of the lattice ( $\mathbf{r}$ ) describing a position which can be occupied by an atom, the index  $j$  denotes the wave vector in the Brillouin zone and  $Q(\mathbf{k}_j)$  is a static concentration wave amplitude. Alternatively this can be written by combining those terms whose wave vector  $\mathbf{k}_j$ 's enter into the stars (the star is a set of wave vector  $\mathbf{k}_j$ , which may be obtained from one wave vector by applying to it all operations of the symmetry group of the disordered phase):

$$n(\mathbf{r}) = c + \sum_s n_s E_s(\mathbf{r}), \quad \text{-----} (54)$$

$$\text{where } E_s(\mathbf{r}) = 1/2 \sum (\mathbf{r}(\mathbf{j}_s) \exp(i\mathbf{k}_{j_s} \mathbf{r}) + \mathbf{r}^*(\mathbf{j}_s) \exp(-i\mathbf{k}_{j_s} \mathbf{r})) \quad (55)$$

and

$$Q(\mathbf{k}_{j_s}) = n_s \mathbf{r}_s(\mathbf{j}_s). \quad \text{-----} (56)$$

The summation is carried out over all wave vectors in the star,  $n$ 's are the long range order parameters and  $\mathbf{r}_s(\mathbf{j}_s)$  are coefficients which determine the symmetry of the occupation probabilities  $n(\mathbf{r})$  with respect to rotation and reflection symmetry conditions. The requirements that in the completely ordered state, when all  $n(\mathbf{r})$  are either zero or unity, that all  $n(\mathbf{r})$  are equal to unity completely defines the constants  $\mathbf{r}_s(\mathbf{j}_s)$ . It turns out that the concentration waves are related to the amplitude of coherent scattering in X-Ray diffraction by the

equation

$$Y(q) = 1/2 (f_B - f_A) \sum_j [Q(k_j) \sum_r \exp(-i(q-k_j)r) + Q^*(k_j) \sum_r \exp-(q+k_j)r] \quad (57)$$

where  $f_A$  and  $f_B$  are the form factors of the A and B atoms respectively.

Now, the configuration part of the Hamiltonian of the alloy is

$$H = 1/2 \sum V(r, r') c(r) c(r'), \quad (58)$$

where the summation is over all of the lattice sites and

$c(r) = 1$  if there is a solute atom at  $r$ ,

$c(r) = 0$  if not.

The interchange energy  $V(r, r')$  is defined by the equation

$$V(r, r') = V_{AA}(r, r') + V_{BB}(r, r') - 2V_{AB}(r, r'). \quad (59)$$

This is analogous to energy defined in equation (1), however it takes into account all interactions in the lattice.

The problem of knowing the ordered phase structure reduces to determining the function  $n(r)$ . Notice that  $n(r)$  follows a sort of Pauli exclusion principle: each lattice site is either occupied by one or zero atoms of some definite type. Thus we can reason that it follows the Fermi-Dirac distribution:

$$n(r) = \frac{1}{\exp \frac{-\mu + \phi(r)}{KT} + 1} \quad (60)$$

where the chemical potential  $\mu$  is determined by the condition of conservation of mass

$$\sum_r n(r) = \sum_r \left[ \frac{1}{\exp \frac{-\mu + \phi(r)}{KT} + 1} \right] = N_1 \quad (61)$$

where  $N_1$  is the number of solute atoms. In the self-consistent field approximation,  $\phi(r)$  is

$$\phi(r) = \sum V(r, r') n(r'). \quad \text{-----} (62)$$

This approximation neglects correlation effects. Substituting this potential into (60)

$$n(r) = \frac{1}{\exp \frac{-\mu}{KT} + \frac{1}{KT} \sum V(r, r') n(r') + 1} \quad (63)$$

which corresponds to the free energy

$$\Omega = U - TS - \mu \sum n(r) \quad \text{-----} (64)$$

where  $U = 1/2 \sum_r \sum_{r'} V(r, r') n(r) n(r')$

is the internal energy and

$$S = -K \sum_r [n(r) \ln(n(r)) + (1-n(r)) \ln(1-n(r))] \quad (65)$$

is the entropy. The Helmholtz free energy of the system is

$$F = U - TS. \quad \text{-----} (66)$$

By using the expression for  $n(r)$  in equation (54), and equation (63) the equilibrium values of  $n_s$  at  $T$  can be found:

$$c + \sum n_s E_s(r) = \exp \frac{-\mu + V(0)c + \sum_{s=1}^t V(k_s) n_s E_s(r)}{KT} + 1. \quad (67)$$

Here  $V(k) = \sum V(r) \exp(ikr)$  is the Fourier transform of the interatomic potential, and can be found by measuring the diffuse scattering from a single crystal of the disordered alloy, [46]

$$I_{\text{diff}}(k) = (f_A - f_B)^2 \frac{c(1-c)}{1 + \frac{c(1-c)}{KT} V(k)}. \quad (68)$$

This method can be used to predict the critical temperature,

ordered structure and stability apparently with much greater ease and accuracy than the former theories [46]. The critical temperature calculated for the  $\text{CuAu}_3$  alloy by this method is only 19 degrees lower than the actual experimental value. This accuracy is exceptional as compared to the previous models. It also has the advantage that the interaction energies are in no way ambiguous and are measurable through X-Ray diffraction.

One of the band theory models of the ordering phenomena [37] uses a tight binding Hartree Hamiltonian to determine the ordering energy incorporated with the cluster-variation method for the entropy of the system. Here the bulk density of states is derived from a configurational average over the local densities of states at the central site of a cluster. The free energy of the alloy is determined by minimizing a model free-energy function over the space of possible electron-ion configurations. These configurations may be classified by the values of certain order parameters ( $\alpha$ ) which measure multisite correlations, e.g., long-range order, short range order, three-body correlation, etc. Thus at a temperature  $T$ ,

$$\begin{aligned} F(T,c) &= \min_{\alpha} F(T,c;\alpha) \\ &= E(T,c;\alpha) - TS(c,\alpha) \end{aligned} \quad \text{-----(69)}$$

where  $c$  is the composition. A schematic of the free energy calculation is shown in Figure 8. In Figure 8,  $N_{i\sigma}(w)$  is the local density of states and  $\langle n_{i\sigma} \rangle$  is the thermal averaged occupation of sites.

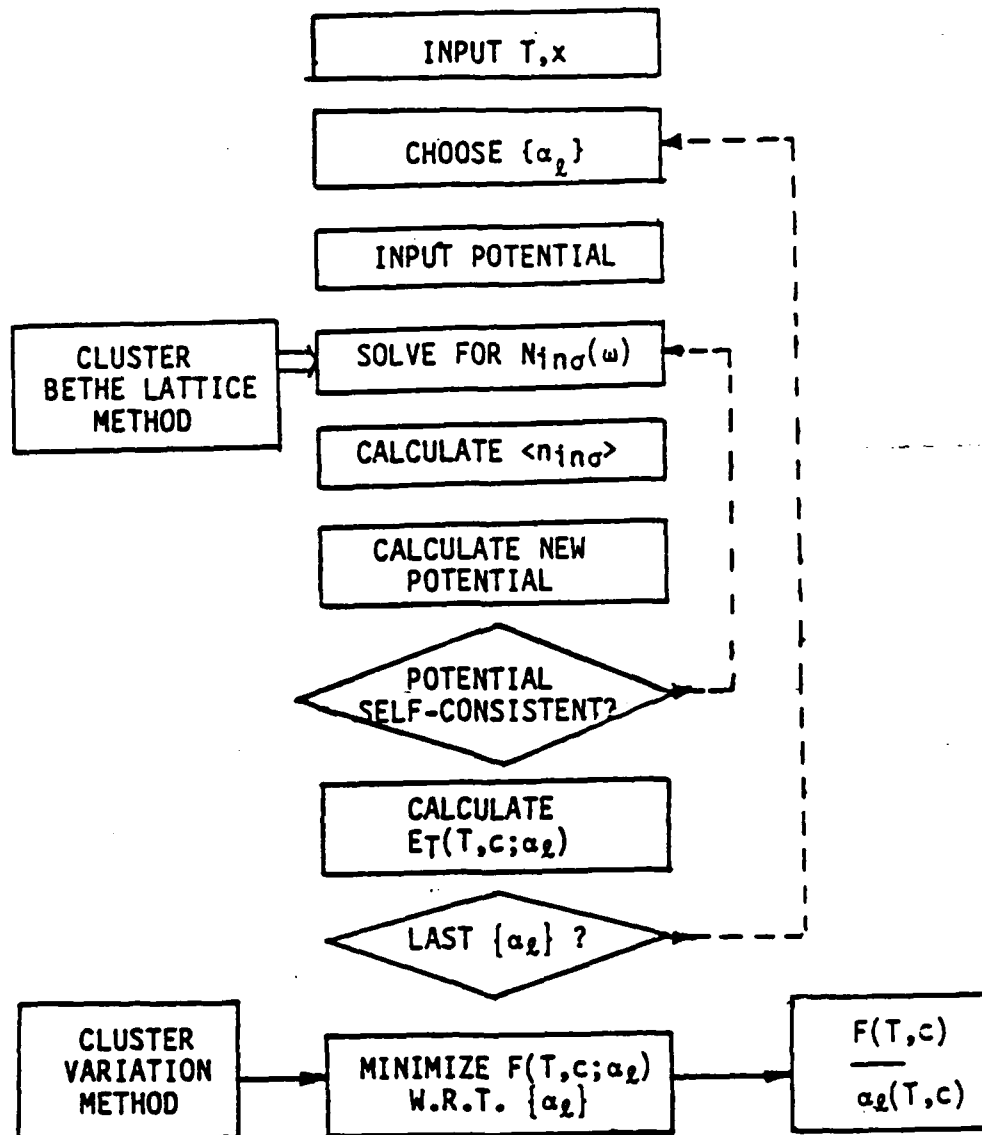


Figure 8. Block Diagram Showing Basic Steps to Self Consistent Electronic Theory of the Alloys Ordering Energy and in Determining Alloy Thermodynamics.

This model predicts a critical temperature of the CuAu system which is in error by 19% which is more accurate than the early set of models but can not compare with the accuracy obtained in the method of concentration waves. One notable point of this theory however is that it actually calculates the atomic interaction energies as a function of short-range order. These energies are constant only near  $\sigma = 0$  and can vary in magnitude as much as 60%. This makes the early Ising models and the cluster-variation model even more unsatisfactory since they are based on a prior knowledge of this energy, which is assumed constant at all values of order.

Since Fosdick [38] first applied the Monte Carlo method to order-disorder transformations in solids a number of attempts have been made to improve and extend this procedure [47]. Unfortunately the stability of any given configuration in this model is again based on the nearest neighbor interaction energies. Since the method can require a lot of computation time and exhibits the same energetic restrictions as early Ising theories, this method of approaching the problem of ordering does not seem to be worth the effort in this research.

#### Ordering Energy

It seems that the most productive model available to predict the ordering phenomena is the method of static concentration waves. This is the theory that is being pursued to predict the



ordering properties of the C-Ti system. The absence of ambiguity as far as energy terms are concerned makes this theory more desirable than the Ising model. The band model is orders of magnitude more involved, as well as less accurate. However, it will be desirable to compare predictions made by the Ising models and to this end an understanding of the ordering energy in equation (1) is necessary.

Some justification of choosing nearest neighbor interaction energies instead of long-range effects in ordering seems to be found in the quantum theory which holds that forces between atoms decrease rapidly as the distance separating them increases. As stated earlier, the pair interaction energies  $V_{AA}$ ,  $V_{BB}$  are the interaction energies between pairs of atoms in the pure elemental crystals and  $V_{AB}$  the interaction in the alloy. However, this definition is very ambiguous. What do we measure to find these energies, or how do we calculate them? The energy  $V^1$  in equation (1) is the first term in the expansion of the Fourier Transform of the long-range interaction energy used in the static concentration wave model, where for a FCC lattice, [46]

$$V(k_0) = V(2\pi a^*3) = -4w_1 + 6w_2 - 8w_3 \quad \text{-----}(70)$$

where  $w$  are the energies corresponding to each coordination shell.

The simple nearest neighbor approximation has been shown to be extremely crude [49,50], for instance, it cannot explain why most order-disorder transformations are first order, why the maximum value of  $T_c$  often occurs away from stoichiometry or why

an FCC alloy should order at all. Freidel [50] and others [51] have been able to show that because conduction electrons in a metal are limited to energies below the Fermi surface a complete screening of the ionic metal cores are not possible, thus long range effects are present. The pseudo-potential theory [52] also points to many body interactions. However, neither one of these methods of calculating interaction energies can be used for the alloy system under investigation with any faith due to the presence of covalent bonding. These bonds have a strong angular nature and many body interactions [23].

A theory recently developed to find the ordering energies of transition metal alloys [53] is available, however it has not been used extensively and requires a number of parameters which might be as difficult as ordering energies themselves to obtain.

After looking in several references [54,55,56] we found values that were experimentally verified (see table 1) and used these in calculating the critical temperature for the Cu-Au alloy system. The critical temperature calculated from these values using the Bragg-Williams approximation was five orders of magnitude higher than the measured value. Clearly the heats of formation are not the interaction energies which we are looking for, although they must be connected in some way. It now appears that the only way to arrive at an acceptable number for these energies is through X-Ray diffraction.

Table 1

Heats of Formation of Standard States from  
Monatomic Gases

Bond	Energy
Au-Au	$88.0 \pm 0.5$ Kcal/mole
Cu-Cu	80.7 Kcal/mole
Au-Cu	$55.4 \pm 2.2$ Kcal/mole

### III. EXPERIMENTAL RESULTS OF PREVIOUS INVESTIGATORS

#### Phase Diagram and Structure of C-Ti Alloys

Results are available from a limited number of investigations on alloys from the C-Ti system. The phase diagram for the C-Ti system is shown in Figure 9. Note that most of the lines in the C-Ti system are dotted. This indicates the lack of adequate data to firmly establish the position of these phase fields. In many cases these dotted phase lines are based upon calculation.

Figures 10 through 16 [57] show the microstructure of the C-Ti alloys with different carbon contents (0.4 w/o to 17.5 w/o). As shown in Figure 13 to 16, the amount of  $\gamma$  in the two-phase region,  $\alpha$  plus  $\gamma$  (room temperature), and  $\beta$  plus  $\gamma$  (temperature over 920 degrees C), increase with increasing carbon content until the  $\gamma$  field is reached. The phase within the  $\gamma$  in Figures 14 and 15 is either  $\alpha$  or transformed  $\beta$  which has precipitated as a result of decreasing solubility in TiC with decreasing temperature. It is interesting to note that the surface energy of the  $\gamma$  in contact with the C-Ti liquid solution is significantly different from the surface energy of this phase in contact with the  $\beta$  phase of the same carbon content. In the first case the liquid serves as the matrix with  $\gamma$  as the included

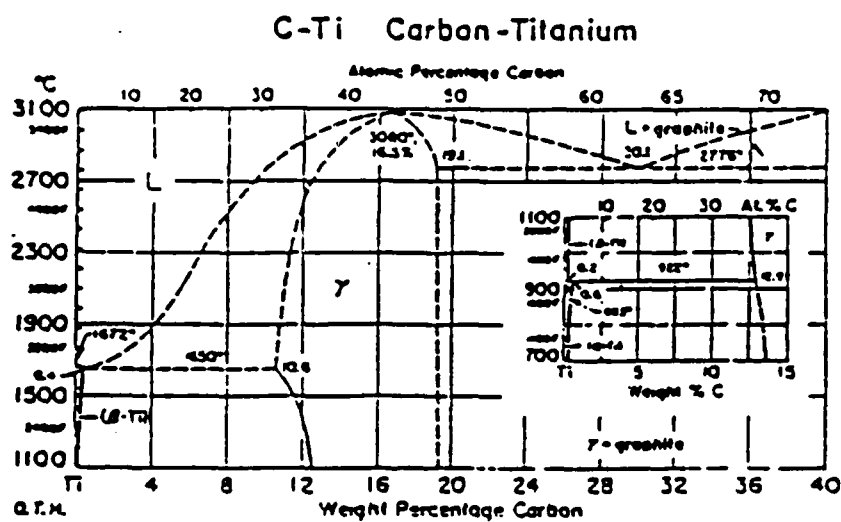


Figure 9. Phase Diagram for the C-Ti Alloy System.



Figure 10. 0.2 w/o C, 6 hrs.  
at 920°C, Water  
Quenched.  $\alpha$ ,  
Transformed  $\beta$   
and  $\gamma$ . x200



Figure 11. 0.2w/o C, as Cast.  
 $\gamma$  Stringers Plus  
Serrated  $\alpha$ . x400



Figure 12. 11.2w/o C, 1 min.  
at 1800°C, Quenched.  
Liquid Plus  $\gamma$ . x200

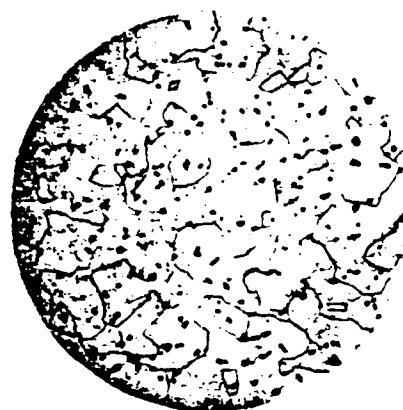


Figure 13. 0.4w/o C, 36 hrs.  
at 800°C, Water  
Quenched. Equiaxed  
 $\alpha$  Plus  $\gamma$ . x150



Figure 14. 4.0w/o C, 48 hrs.  
at 1200°C, Water  
Quenched.  
Transformed  $\beta$   
Plus  $\gamma$ . Structure  
in  $\gamma$  is  $\beta$

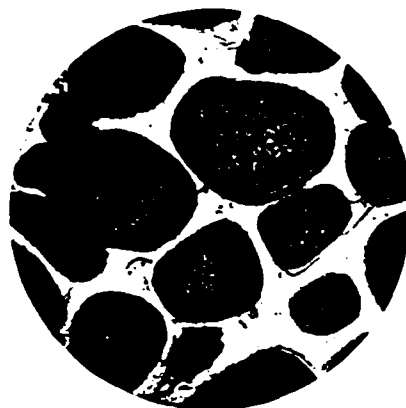


Figure 15. 11.2w/o C, 200  
hrs. at 700°C,  
Water Quenched.  
 $\gamma$  Plus  $\alpha$ .  
Structure in  $\gamma$   
is  $\alpha$ . x500



Figure 16. 17.5w/o C. 120  
hrs. at 900°C,  
Water Quenched.  
Single Phase  $\gamma$ .  
x200

phase; and in the second case the  $\gamma$  tends to serve as the matrix for the  $\beta$ , as is indicated by the  $\beta$  precipitates in the  $\gamma$  phase and by the sharp angles the  $\gamma$  constituents have developed at grain boundaries of  $\beta$ , Figure 14. Figure 15 gives the appearance of the liquid serving as matrix around the phase for a different composition alloy. The  $\gamma$  phase has a face-centered cubic X-ray diffraction pattern and the compound was a NaCl type.

Structure and Properties of Low Carbon Weight  
Percentage C-Ti alloys (C<0.5w/o)

Previous investigations in the C-Ti system have concentrated on determining and understanding the properties of low weight percentage C-Ti alloys (C<0.5w/o) [58-59], single crystal TiC [60-63] and polycrystalline TiC [64-68]. The properties of the three binary C-Ti alloys, given in Table 2 [59], illustrate the solid-solution strengthening effect of carbon. Figure 17 shows the effect of heat-treating temperature on the properties of a Ti-0.16w/o C alloys. Microstructures for corresponding conditions are given in Figure 18. When this alloy is annealed and quenched from the  $\beta$ -carbide field, there is a marked decrease in strength and toughness caused by the formation of TiC, and consequent lowering of the carbon in solid solution. Data for the Ti-0.27w/o C, the strength, particularly the yield strength, is increased by dissolving the TiC particles through the use of high temperature  $\alpha$  anneal. The high tensile ductilities are found when the Ti-0.27w/o C alloy is quenched from the  $\alpha$ - $\beta$



Table 2

## Tensile Properties of Ti-C Alloys

Specimen No.	Carbon Content, Pct	Annealing Treatment Temperature, °C	Time, Hr	Microstructure			Average VHN, 0.05 Kg Load	Elongation, Pct in 1/2 in.	Reduction in Area, Pct	Ultimate Tensile Strength, Pci	0.01 Pct Offset Yield Strength, Pci	0.1 Pct Offset Yield Strength, Pci	0.2 Pct Offset Yield Strength, Pci
				Phases Present	Grain Size, $\mu$	Grain Size, $\mu$							
TM-33-30	0.16	800	16	$\alpha$	0.02	160	160	50	65	59,600	48,600	—	53,800†
TM-33-9	0.16	700	4	$\alpha$	0.06	164	164	45	70	59,300	48,400	—	54,100†
TM-33-21	0.16	850	2	$\alpha + \beta^*$	0.10	164	164	45	66	59,300	48,400	—	54,100†
TM-33-23	0.16	900	2	$\alpha + \beta^*$	0.06	165	165	50	71	59,400	48,500	48,100	49,900†
TM-33-7	0.16	910	1	$\alpha + \beta^*$	—	165	165	62	71	59,400	48,500	48,100	49,900†
TM-33-14	0.16	850	1	$\beta^* + \text{TIC}$	—	161	161	36	65	52,100	43,800	38,000	41,200
TM-34-20	0.37	800	16	$\alpha + \text{TIC}$	0.02	171	171	39	64	62,100	44,800	38,000	53,200
TM-34-9	0.37	700	4	$\alpha$	0.06	183	183	43	64	59,600	48,100	—	54,900†
TM-34-21	0.37	850	2	$\alpha$	0.15	180	180	46	66	62,100	48,700	—	60,300†
TM-34-23	0.37	900	2	$\alpha + \beta^*$	—	184	184	58	64	60,500	48,600	—	65,500†
TM-34-7	0.37	910	1	$\alpha + \beta^*$	—	184	184	61	72	60,500	48,600	44,800	48,100
TM-34-14	0.37	850	1	$\beta^* + \text{TIC}$	0.02	178	178	42	61	59,600	48,400	38,700	56,500†
TM-30-20	0.47	800	16	$\alpha + \text{TIC}$	0.02	185	185	37	56	65,400	58,400	—	69,900†
TM-30-9	0.47	700	4	$\alpha + \text{TIC}$	0.03	185	185	53	61	71,600	67,000	—	76,800†
TM-30-31	0.47	850	2	$\alpha + \text{TIC} + \beta^*$	—	225	225	51	61	80,000	71,800	—	78,300†
TM-30-23	0.47	900	2	$\alpha + \beta^*$	—	226	226	50	64	83,000	71,000	—	78,000†
TM-30-7	0.47	910	1	$\alpha + \beta^*$	—	183	183	50	69	73,500	67,800	59,800	62,000
TM-30-14	0.47,	950	1	$\beta^* + \text{TIC}$	—	164	164	43	66	63,900	58,600	47,500	49,000

\*  $\beta$  transformed to  $\alpha$  on quenching.

† Yield point.

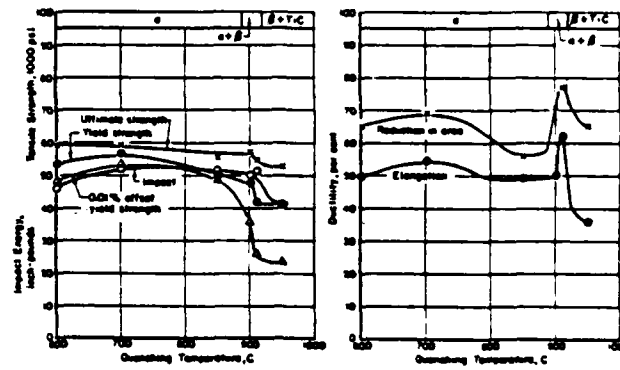
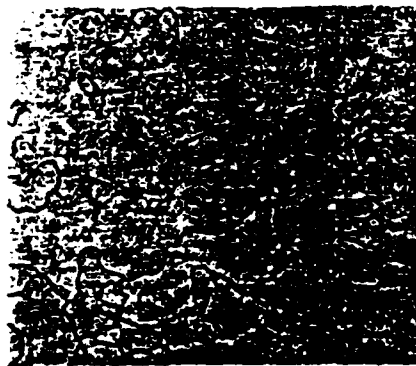


Figure 17. Properties of a Ti-0.16w/o C Alloy. ]



a—Annealed 16 hr at 600°C and water-quenched.



c—Annealed 2 hr at 850°C and water-quenched.



b—Annealed 2 hr at 900°C and water-quenched.



d—Annealed 1 hr at 950°C and water-quenched.

Figure 18. Microstructures of a Ti-0.16w/o C Alloy.  
x250 [59]

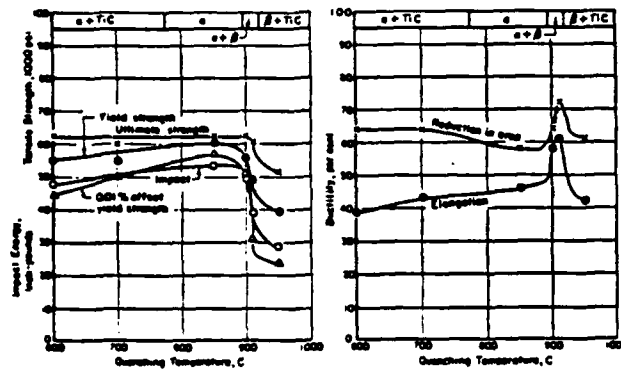


Figure 19. Properties of a Ti-0.27w/o C Alloy. [59]

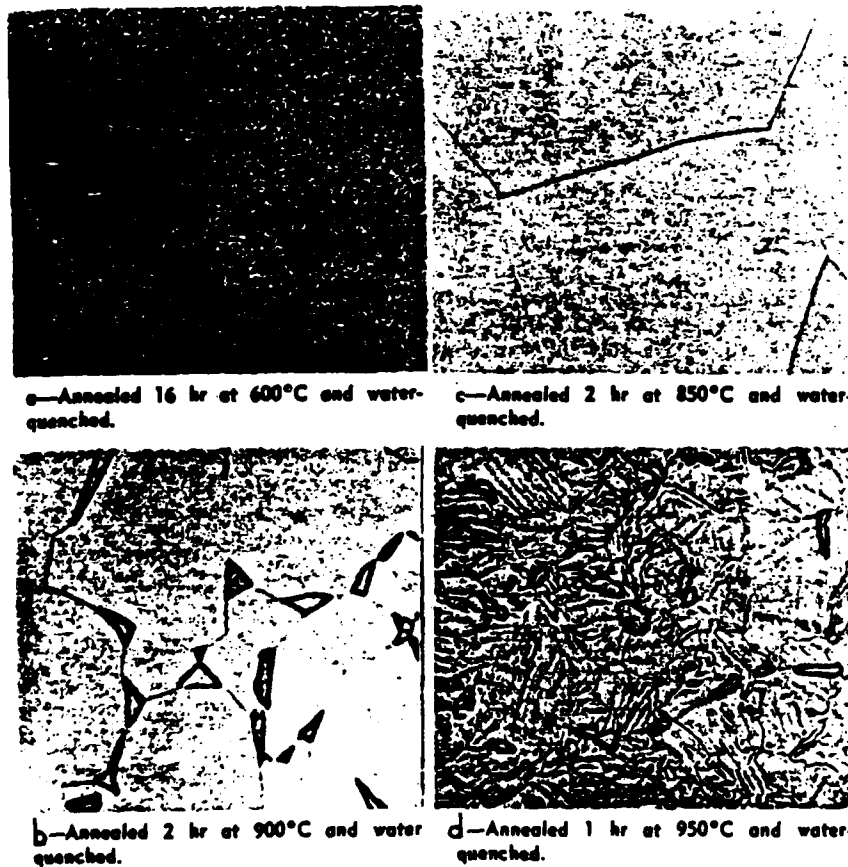


Figure 20. Microstructures of a Ti-0.27w/o C Alloy. x250 [59]

field. At a level of 0.47w/o C the strength properties are greatly increased when the carbon is put in solid solution through the use of increasingly higher annealing temperatures, and they are decreased sharply when the alloy is quenched from the  $\beta$ -carbide field. Figure 21 shows the properties of a Ti-0.47w/o C alloy. Microstructures of this alloy are given in Figure 22.

A further illustration of how heat treatment can affect the properties of Ti-C alloys is given in Figure 23, where properties are plotted vs carbon content for three different heat treatments. Tensile ductilities and toughness decrease with increasing carbon content, whether in solution or not. Carbon in solid solution appears to decrease tensile ductility and increase toughness slightly.

#### Mechanical Properties of Titanium Carbide

Polycrystalline TiC have been produced by hot press sintering of near stoichiometric TiC powders. The results show that TiC is brittle at room temperature and becomes ductile above 800 degrees C. Katz and Lipsitt [64] have shown these stoichiometric compositions of TiC to be highly sensitive to grain boundary impurities. Above 1000 degrees C a grain boundary segregant containing Si, Fe, Cu becomes near molten and results in greatly reduced strength. A large amount of porosity has been identified in scanning electron micrographs of the fractured

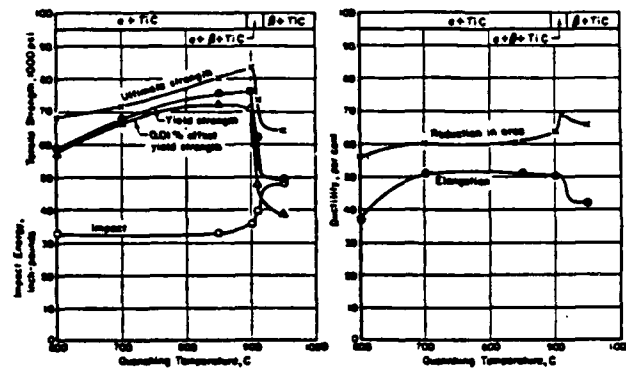


Figure 21. Properties of a Ti-0.47w/o C Alloy, [59]

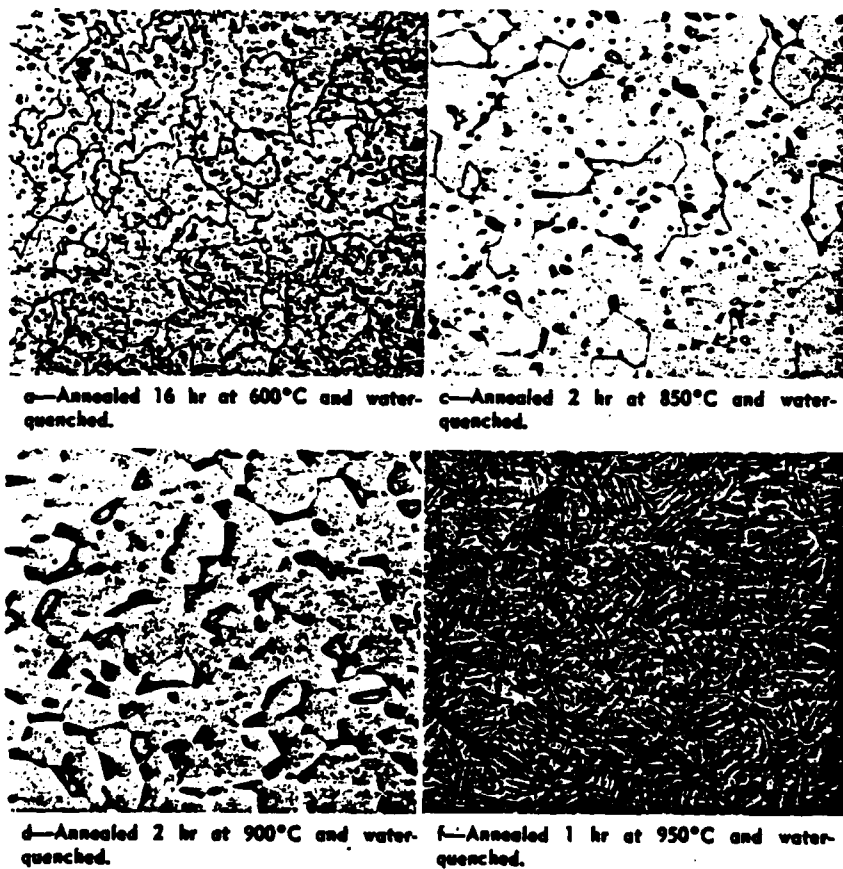


Figure 22. Microstructures of a Ti-0.47w/o C Alloy. x250 [59]

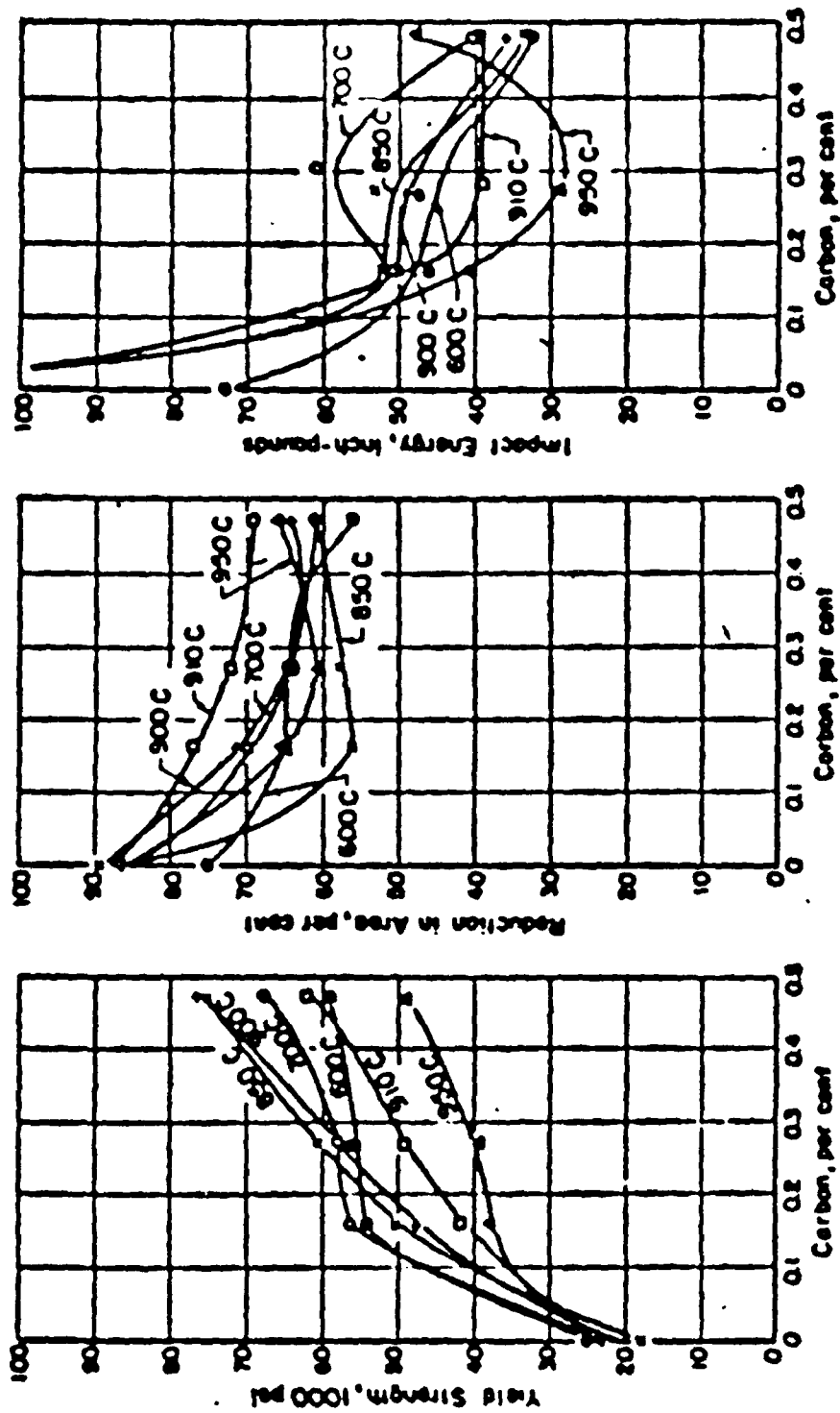


Figure 23. Mechanical Properties of Ti-C Alloys. [59]

specimens and is attributed to the heat treatment and fabrication process. This porosity is expected to adversely affect the material ductility and strength.

The optical micrographs of polycrystalline substoichiometric TiC with different compositions are shown in Figure 24 [67]. Grain sizes ranged from 14 to 22  $\mu\text{m}$  and increased monotonically with decreasing stoichiometry. Pores were evenly distributed, and also grew with decreasing stoichiometry. Hardness was shown to drop steadily as expected with decreasing C/Ti atom ratios (Figure 25).

#### Compression Test Results

Typical nominal stress-nominal strain curves ( $\sigma$ - $\epsilon$ ) [68] for 1700 degrees C annealed polycrystalline TiC, having an average grain size of 8.2  $\mu\text{m}$ , deformed in compression at 900 degrees C to 1700 degrees C are shown in Figure 26. Yield-point behavior is observed for specimen deformed at 1000 degrees C. The yield stress in polycrystalline TiC is strongly dependent on the temperature of deformation, as shown in Figure 27. Similar observations were reported for both single-crystal [60] and polycrystalline TiC [64,67]. The dependence of the yield stress on grain size, as shown in Figure 28, follows a Hall-Petch type [68] relation

$$\sigma_y = \sigma_0 + Kd^{-1/2} \quad \text{-----}(71)$$

where  $\sigma_y$  is the yield stress,  $\sigma_0$  a friction stress, K a constant

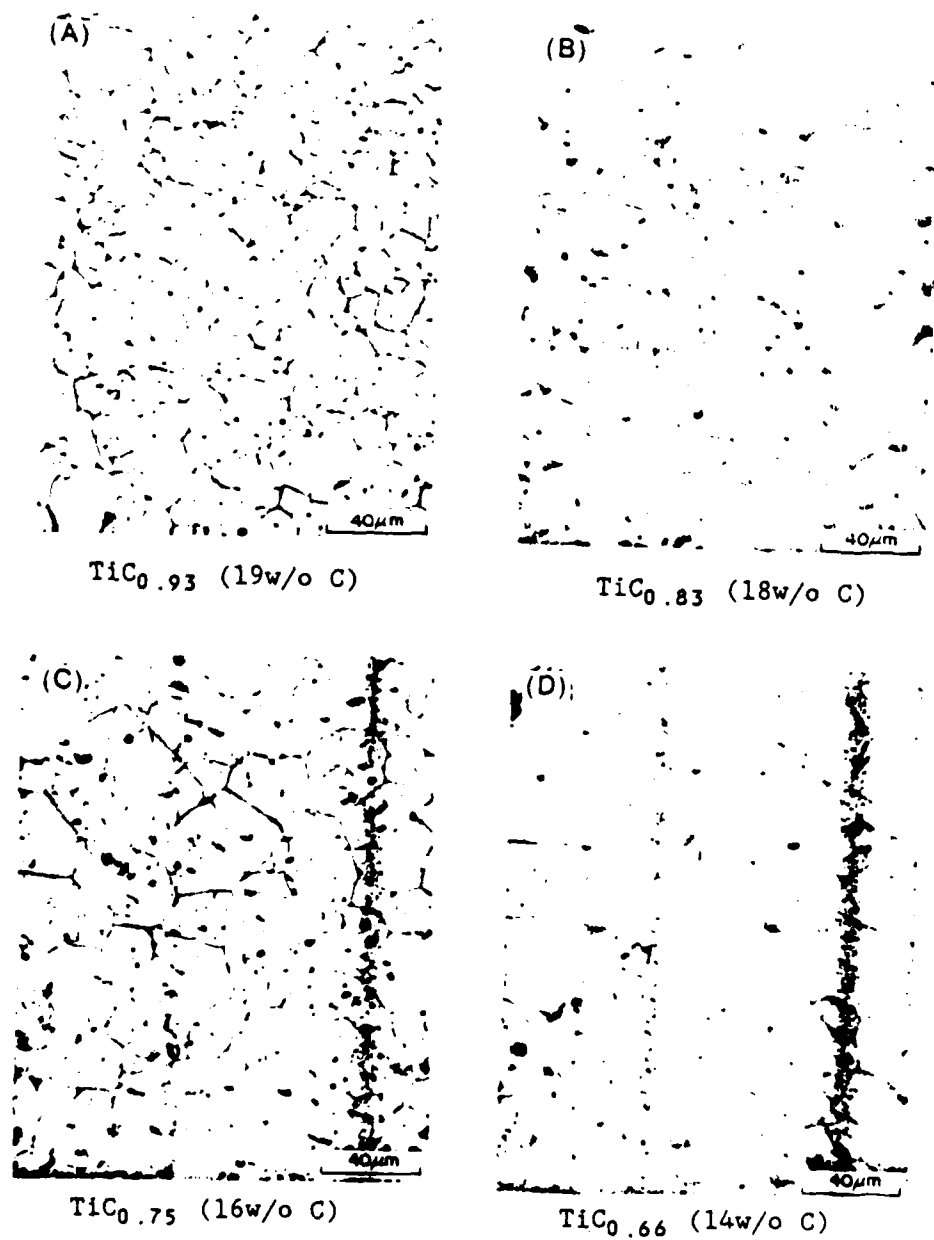


Figure 24. Optical Micrographs of Polished and Etched Substoichiometric TiC Samples. (A)  $\text{TiC}_{0.93}$  (B)  $\text{TiC}_{0.83}$  (C)  $\text{TiC}_{0.75}$  and (D)  $\text{TiC}_{0.66}$ . [67]



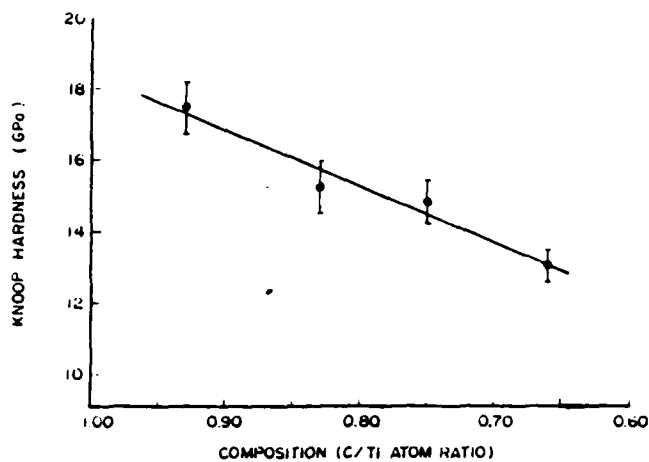


Figure 25. Variation of Knoop Hardness with C/Ti Atom Ratio.[66]

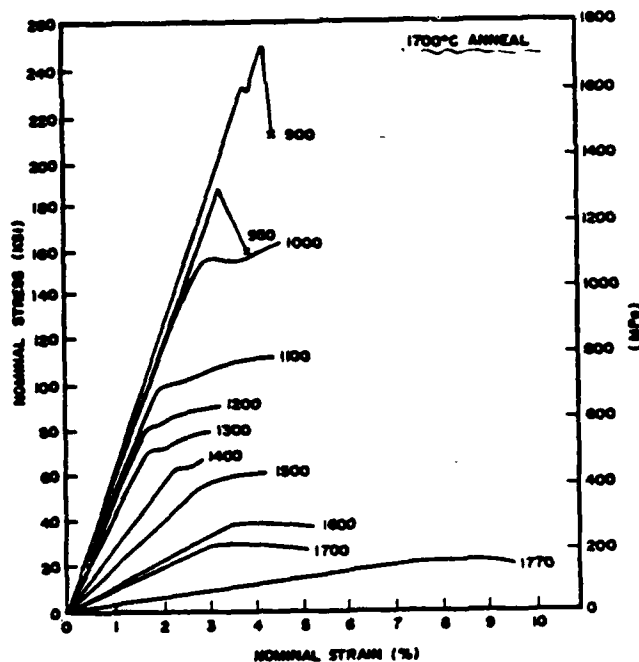


Figure 26. Stress-Strain Curve for Annealed Polycrystalline TiC (1700°C, 4 hrs.) Deformed in Compression at Temperature Indicated(°C) ( $\dot{\epsilon} = 1.7 \times 10^{-4} \text{ s}^{-1}$ ). [66]

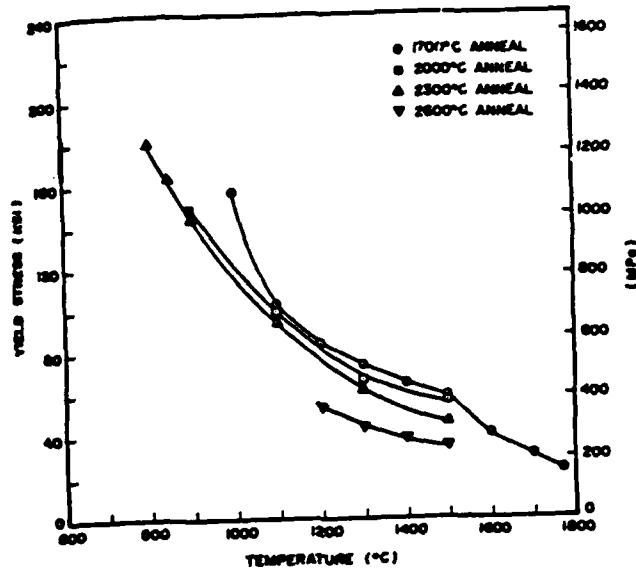


Figure 27. Yield Stress as a Function of Temperature in Polycrystalline TiC Deformed in Compression.[68]

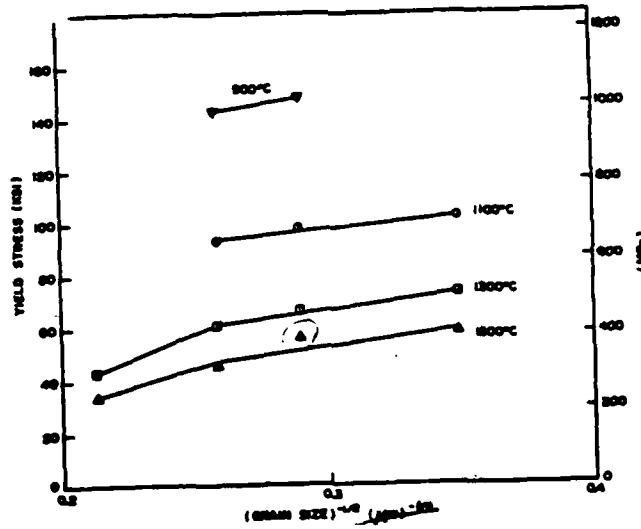


Figure 28. Yield Stress vs (Grain Size)<sup>-1/2</sup> for Polycrystalline TiC Deformed in Compression at Temperature Indicated.[68]

associated with the propagation of deformation across the grain boundaries, and  $d$  the grain diameter.

Figure 29a [66] is an SEM micrograph of the fracture surface of a specimen tested at room temperature. The fracture is predominantly transgranular cleavage. Figure 29b is the corresponding fractograph for a specimen tested at 1100 degrees C. Here the fracture is much more intergranular, and the extent of intergranular fracture continues to increase as the test temperature is raised. Similar observation was reported for polycrystalline TiC [68].

#### Deformation Mechanisms

In TiC, three thermally activated dislocation mechanisms [68] have been proposed to operate during deformation at different test temperatures: (1) Peierls stress [69] ( $<1200^{\circ}\text{C}$ ); (2) diffusion of carbon [64] ( $1200^{\circ}\text{C}$  to  $1400^{\circ}\text{C}$ ); and (3) diffusion of titanium [65] ( $>1500^{\circ}\text{C}$ ). A phenomenological relation commonly used to establish a law governing the deformation behavior is the dependence of the yield stress ( $\sigma_y$ ) on temperature, which can be expressed as

$$\sigma_y = \sigma_0 \exp(B/KT) \quad \text{-----(72)}$$

where  $\sigma_0$  is a constant,  $K$  the Boltzmann constant,  $B$  an activation energy, and  $T$  the absolute temperature. Figure 30 is a plot of  $\log \sigma_y$  as a function of  $1/T$  for polycrystalline TiC having different grain sizes tested in compression. A change in slope

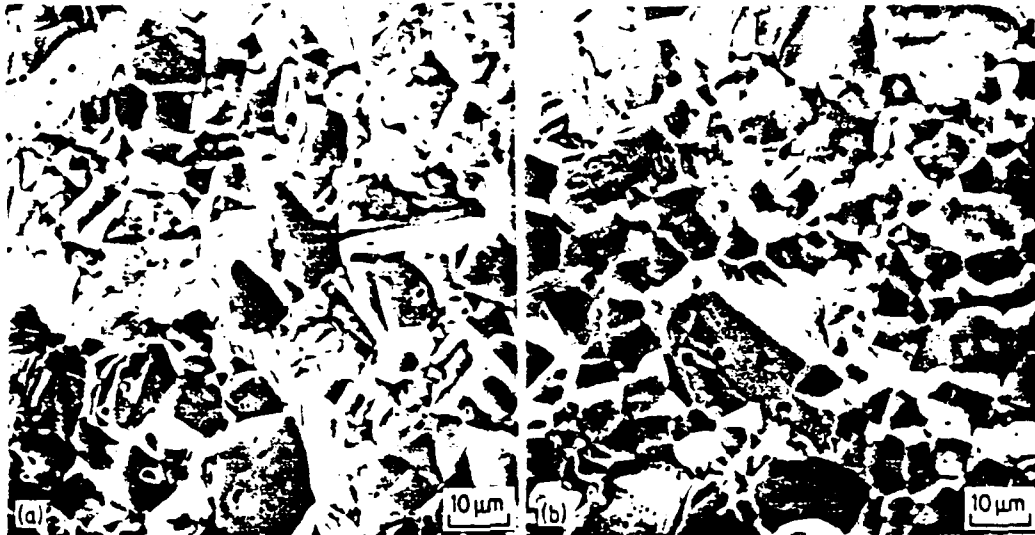


Figure 29. SEM Fractograph of TiC Specimens Hot Pressed from Unsieved Starck Powder. Bending Tests Performed at (a) Room Temperature, (b) 1100°C. [68]

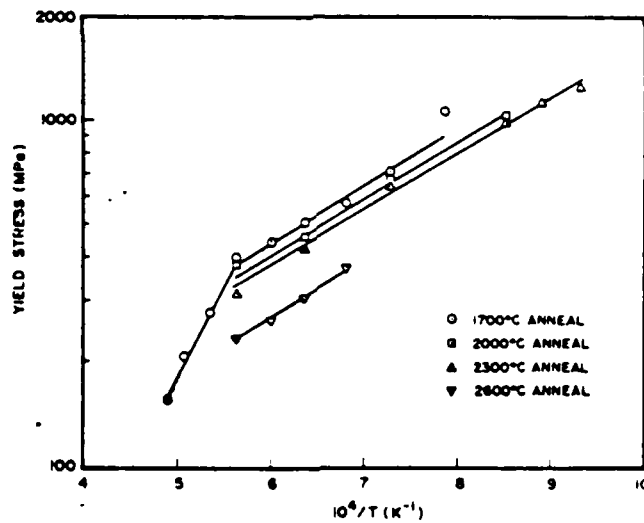


Figure 30. Log of Yield Stress vs Reciprocal of Absolute Temperature for Polycrystalline TiC Deformed in Compression. [68]

was observed at 1500 degrees C. Below 1500 degrees C the magnitude of the slope is nearly the same for specimens having four grain sizes; above 1500 degrees C the slope is larger by more than a factor of 3. Other investigations [60,70] in both single-crystal and polycrystalline TiC have indicated the existence of one such change in slope. However, the temperature at which this change occurred was determined to be different by various investigators. It has also been found to depend on the degree of substoichiometry of TiC [60].

#### IV. EXPERIMENTAL PROCEDURES

##### Specimen preparation

A series of C-Ti alloys was melted to investigate the properties of the system. Alloys containing between 0 and 7 weight percent carbon were prepared by induction melting. Because of the high melting point associated with these alloys and the limited power of the available induction generator, alloys with greater than 7 w/o carbon could not be produced by induction melting. In the process, titanium (99.7% purity) and graphite powder were placed into a graphite crucible which is 0.51 inches in diameter and 1.34 inches high. This crucible was placed inside a quartz tube with inside diameter of 0.63 inches that contains a tantalum sheet encircling the inside diameter. The crucible was supported by a ceramic rod. The induction coil encircles the outside of the quartz tube. The tantalum sheet serves as a radiation reflector but additionally serves as a gathering material to protect the melt from oxidation. The graphite crucible is the susceptor and quartz tube serves as the containment of the inert gas atmosphere. Both the graphite crucible and graphite powder were spectrographic grade material. The bottom ceramic rod was used to limit heat transfer by conduction out of crucible. An infrared sensor was used to

monitor the temperature of the melt. This sensor is suspended from the top support of the heating system. Figures 31 and 32 show the system in operation. An argon atmosphere was maintained in the quartz tube during heating and cooling of the melts. A graphite bar was used to stir the fluid alloy mixture to increase the diffusion of carbon into titanium, enhancing the formation of a homogeneous material composition and reducing porosity of the melts. The alloys in the 0 to 7 w/o carbon region were produced using an induction generator set to provide a direct current of 40 amps at 230 volts. The melts were limited in size to 0.35 inches in diameter and 0.5 inches high.

Alloys with compositions greater than 7 w/o carbon were produced by arc melting under an inert gas atmosphere. A gas cooled electrode which is composed of Tungsten-2% Thoria was used to produce the melts. Initially, problems were encountered when the cooling gas blew the graphite powder out of the crucible. A method was developed in which the graphite powder was sealed into holes that were drilled in the pure Ti rod. This enabled high carbon weight percent alloys to be prepared. Quality of alloys produced by the arc melting process was less desirable than alloys produced by induction melting. Arc melted alloys tended to be less homogenous and contained amount of porosity.

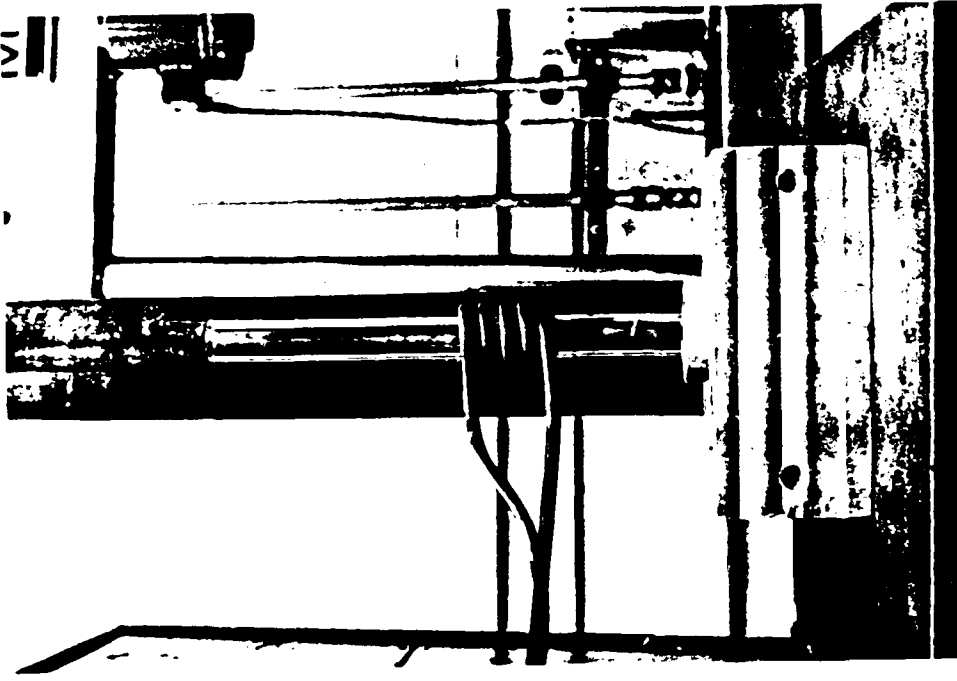


Figure 32. Close Up of Induction Melting  
Coil, Crucible and Quartz Tube

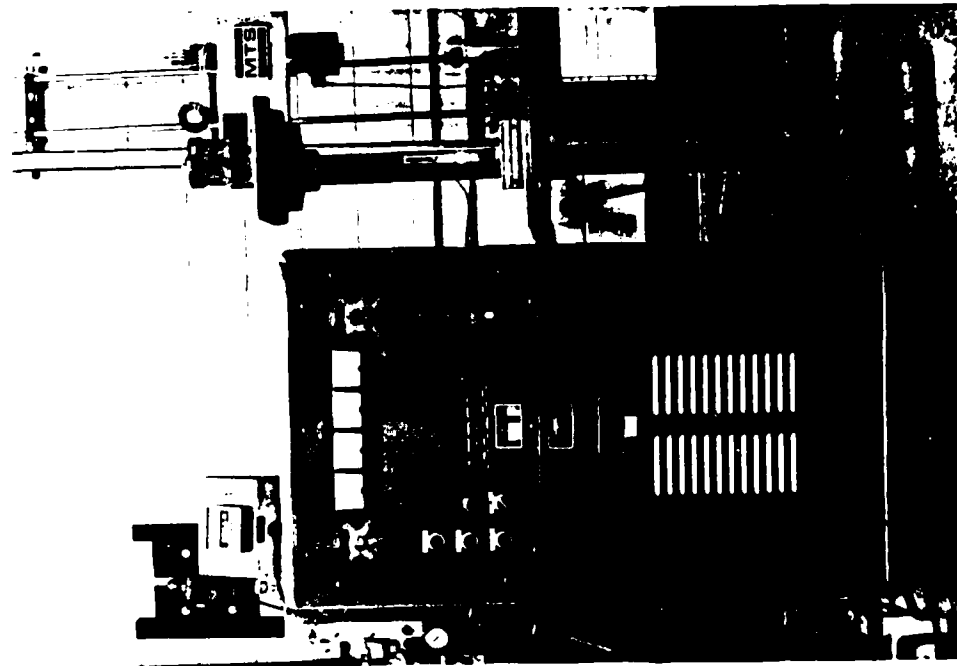


Figure 31. Induction Generator and Melting  
Furnace used to Produce C-Ti  
Alloys



## Fabrication

Techniques have been developed for the fabrication of subsize compression specimens [71] from C-Ti alloys. Because of the small size and properties of the available material, a diamond impregnated soft core tube (Figure 33) which has an outside diameter of 6.4 mm and inside diameter of 4.4 mm was used to prepare cylindrical compression specimens. The drill utilizes water as a lubricant and coolant to protect the samples from overheating. After a cylinder is cut from the melt, a diamond slitting saw was used to cut both ends of the cylinder to length and obtain parallel ends. Low carbon content alloys were gummy in nature, thus requiring sharpening of the diamond blade with a carbon block to remove cut particles stuck in the blade. Figure 34 shows the diamond slitting saw. Although the alloys were not excessively hard, large amounts of time were required to prepare the cylindrical compression sample, which measured 4.40 mm in diameter by 6.86 mm high. A diameter to length ratio of 1.50 to 1.75 was used for all tested specimens. These specifications meet ASM Metal Handbook requirements for subsize compression samples [71]. Prior to compression testing, specimens were ultrasonically cleaned in acetone. Figure 35 shows a typical compression specimen.

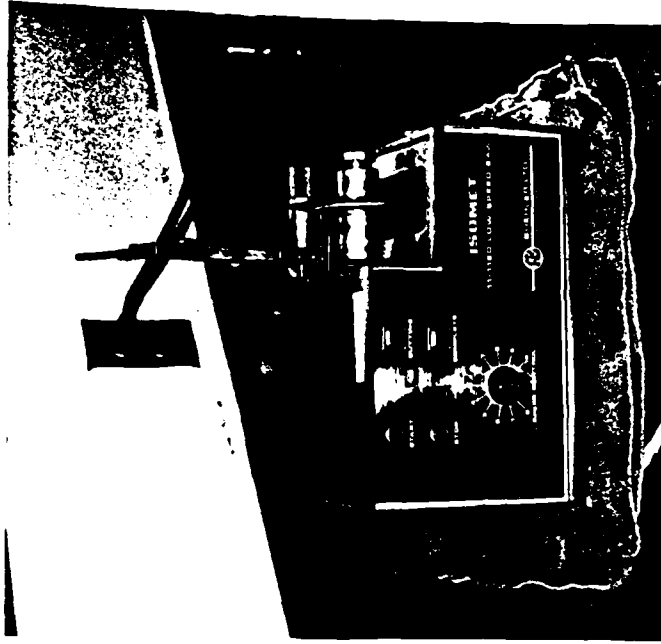


Figure 34. The Diamond Slitting Saw used to Cut Compression Specimens

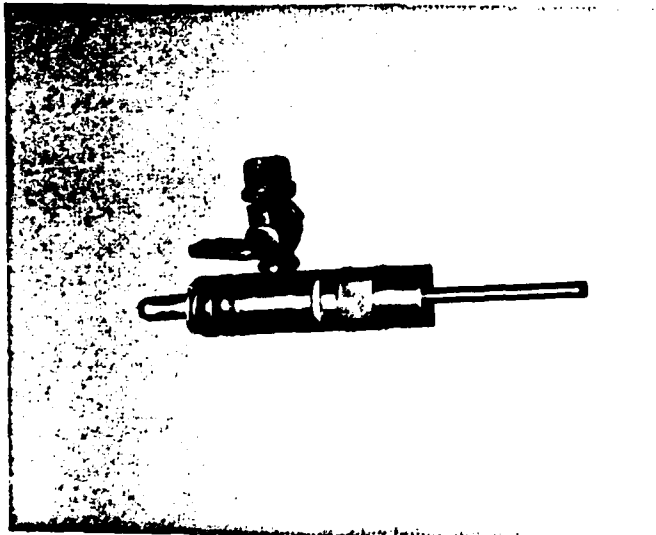


Figure 33. The Diamond Impregnated Soft Core Tube was to Prepare Cylindrical Compression Specimens

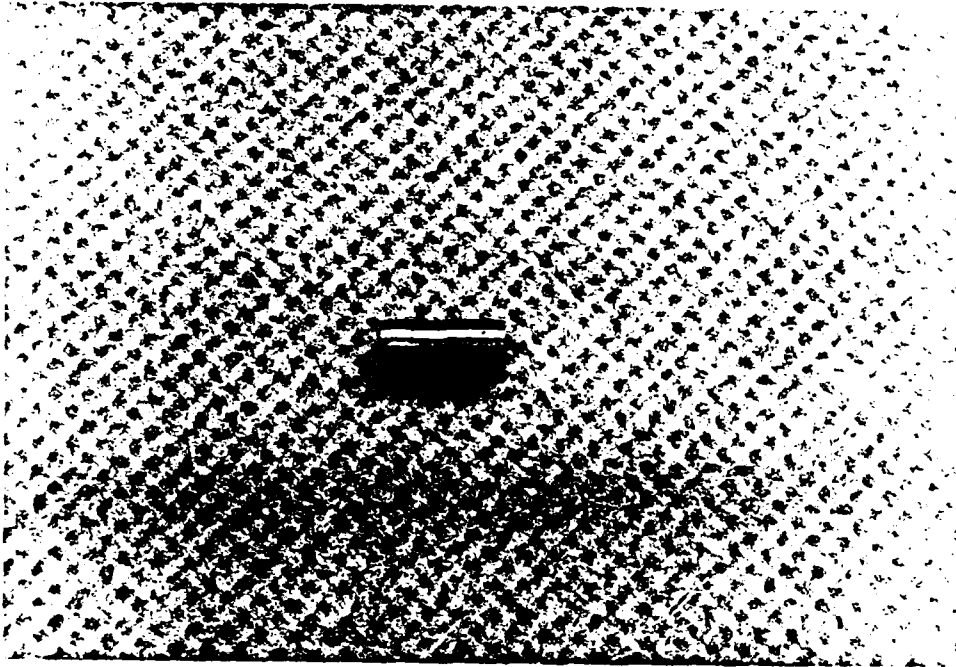


Figure 35. Compression Test Sample Before Test

### Fabrication

Techniques have been developed for the fabrication of subsize compression specimens [71] from C-Ti alloys. Because of the small size and properties of the available material, a diamond impregnated soft core tube (Figure 33) which has an outside diameter of 6.4 mm and inside diameter of 4.4 mm was used to prepare cylindrical compression specimens. The drill utilizes water as a lubricant and coolant to protect the samples from overheating. After a cylinder is cut from the melt, a diamond slitting saw was used to cut both ends of the cylinder to length and obtain parallel ends. Low carbon content alloys were gummy in nature, thus requiring sharpening of the diamond blade with a carbon block to remove cut particles stuck in the blade. Figure 34 shows the diamond slitting saw. Although the alloys were not excessively hard, large amounts of time were required to prepare the cylindrical compression sample, which measured 4.40 mm in diameter by 6.86 mm high. A diameter to length ratio of 1.50 to 1.75 was used for all tested specimens. These specifications meet ASM Metal Handbook requirements for subsize compression samples [71]. Prior to compression testing, specimens were ultrasonically cleaned in acetone. Figure 35 shows a typical compression specimen.

and the maximum output voltage of both load and stroke cells is 10 volts. Calibrated subscales of 10%, 20%, and 50% are available for both stroke and load.

#### Data Acquisition Unit

The data acquisition system (Figure 36) is composed of three parts : an HP-7046B X-Y recorder, a Nicolet-3091 digital oscilloscope with bubble memory, and an HP-3497A data acquisition unit combined with an HP-9836 minicomputer. These data acquisition systems monitor the compressive data coming from the load and stroke sensors, and transmit the data to the computer which analyzes, plots, and prints the incoming data.

#### Heating Elements

Compression tests were conducted at elevated temperatures (159 degrees C - 850 degrees C) using a specially fabricated furnace. The furnace consisted of a quartz tube for electrical insulation surrounded by 30 turns of nichrome wire 1.0 mm in diameter. The wire was, in turn, covered by a layer of fiberglass which served as a thermal insulator (Figure 37). The dimensions of the quartz tube were 30\*32\*160 mm. Power to the heating element was supplied by a variac transformer, with the temperature controlled by adjusting the output voltage of the transformer.

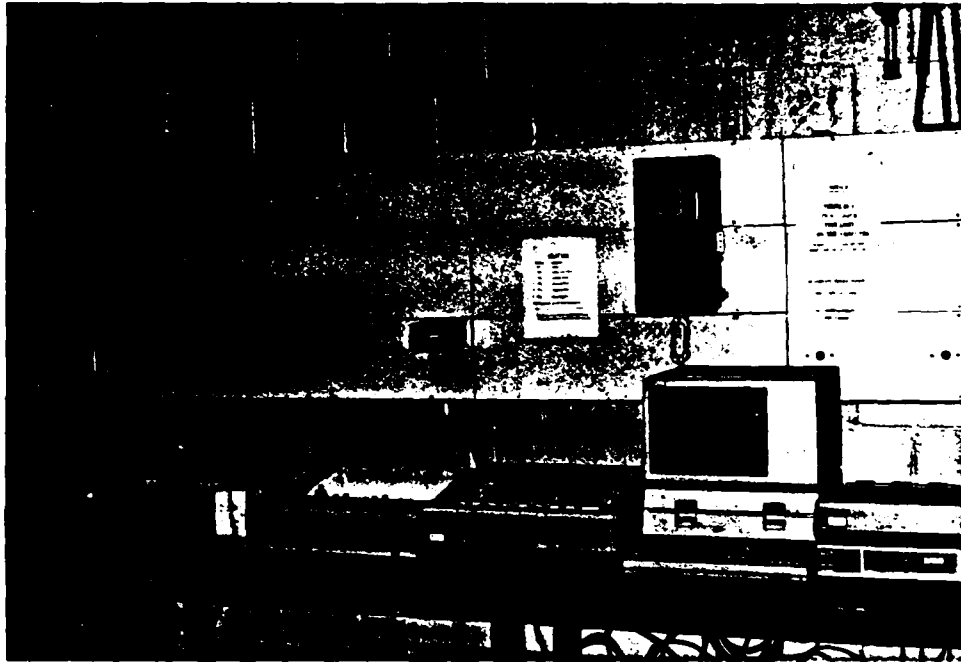


Figure 36. Data Acquisition Unit for Recording Load and Stroke Information from Compression Test

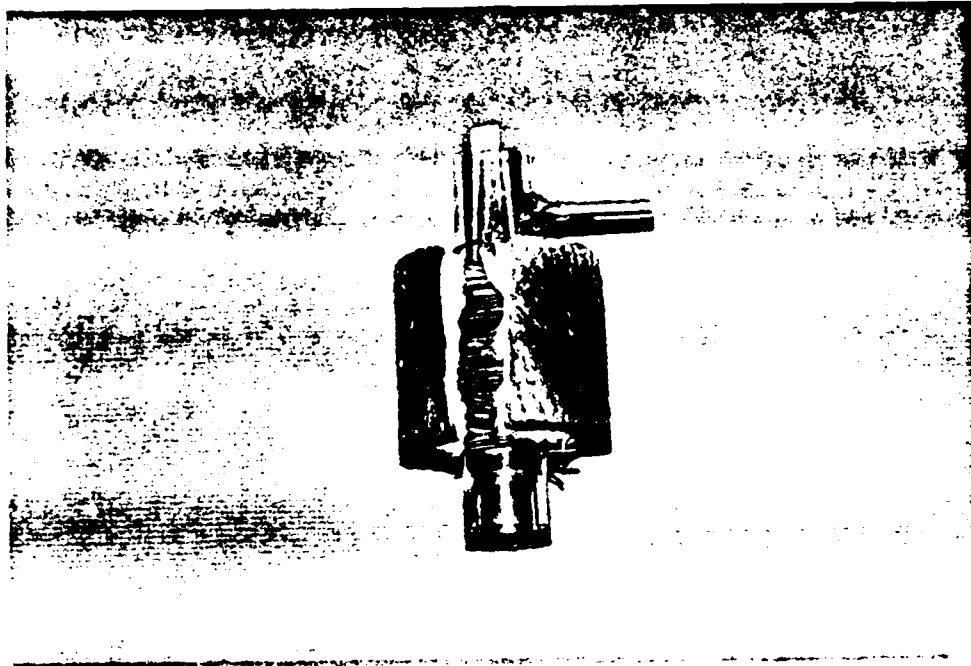


Figure 37. Heating Element for Elevated Temperature  
Compression Tests

### Experimental Procedure

Figure 38 shows the flow chart of the MTS data acquisition system. Chosen strain rate was obtained by setting the maximum stroke length and adjusting the time to reach the total stroke length. The relationship is shown below :

$$\text{strain rate} = \frac{\text{Maximum Ls}}{(\text{Lg}) * (\text{Time To Reach Maximum Ls})}$$

### Room Temperature Compression Tests

The strain rate was fixed at  $10^{-4} \text{ sec}^{-1}$  for room temperature compression tests. The X-Y recorder and HP-3497A data acquisition unit were used separately to continuously digitize and store the data from the load and stroke sensors of the MRS machine. For these tests, the range of load, coarse stroke, and fine stroke were set at 100 KN, 10 mm, and 100% respectively. Material type, specimen number, gage length, cross-sectional area and specifics of each test specimen were entered into the computer before performing the test. The specimen was placed on the compression test platens, which were attached to the ram of the MTS machine. Upon finishing the tests, the computer plotted, printed and stored the data automatically. The X-Y recorder was used to plot the stress-strain diagram while the test was in progress.



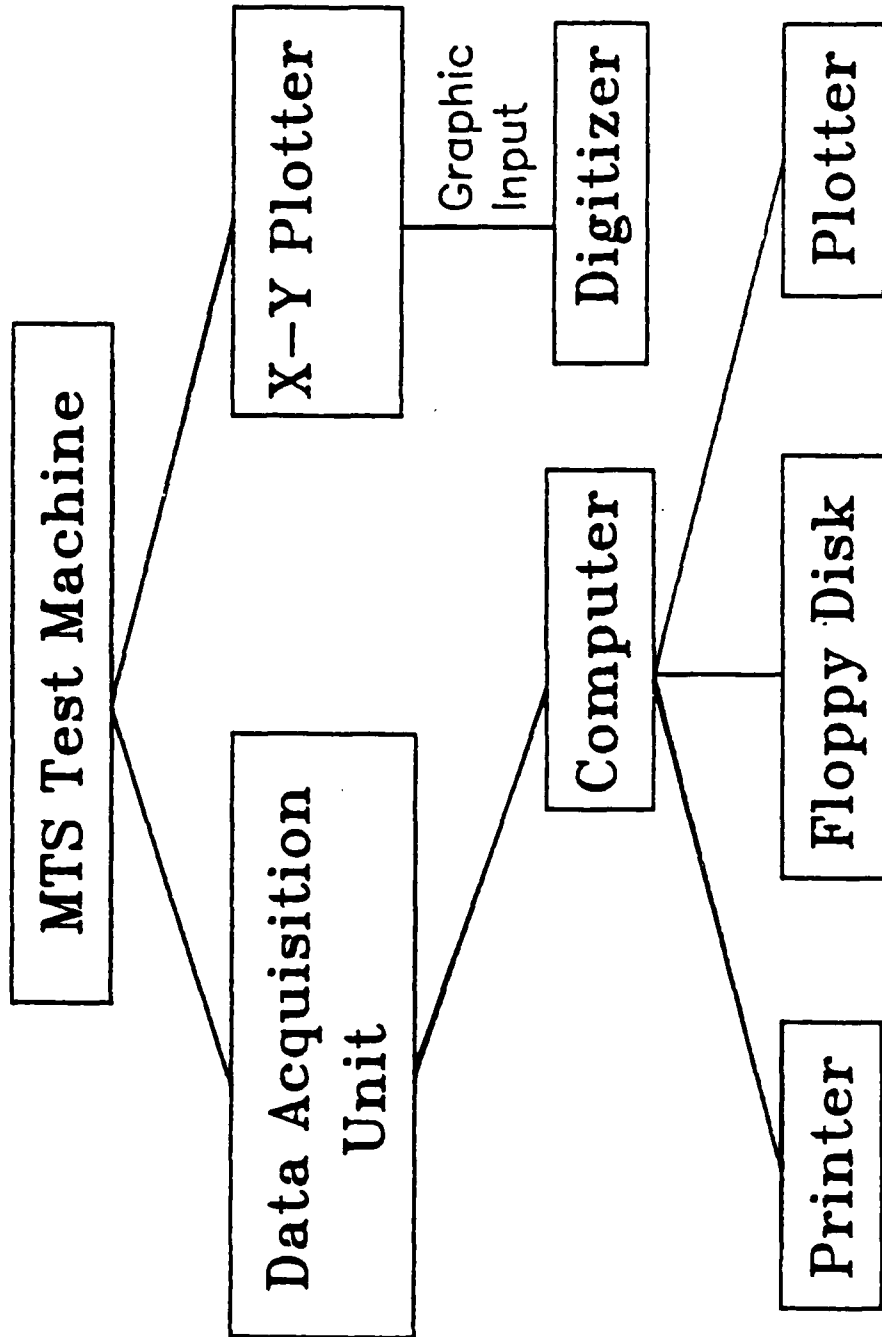


Figure 38. Flow Chart of MTS Data Acquisition System.

### Elevated Temperature Compression Tests

The specimen was placed between cylindrical linkages made of Inconel 706, and the quartz tube wound heating element placed over the linkages. This assembly was then attached to the load frame. The furnace, supported by a three-prong clamp (Figure 39), was flushed continuously with argon during testing to prevent oxidation of the specimen. Before testing, the specimens were heated for 20 minutes to allow thermal equilibrium to be reached. The chosen temperatures ( $150^{\circ}\text{C}$ ,  $350^{\circ}\text{C}$ ,  $450^{\circ}\text{C}$ ,  $550^{\circ}\text{C}$ , and  $850^{\circ}\text{C}$ ) were controlled and maintained by varying the output voltage of a variac transformer. Temperature was measured using K-type thermocouples mechanically attached to the central gage section of the specimen.

### Failure Analysis

To investigate the deformation and fracture mechanisms, selected specimens were examined in detail with an JSM-840 scanning electron microscope operated at 20KV. The scope is equipped with Energy Dispersive Spectrometers (EDS) capable of compositional analysis. The SEM examination involved the study of both macroscopic and microscopic surface features. Macroscopic features were studied from 20X to 50X. The center and edge of the fracture surface were examined for features. All microscopic features were studied from 200X to 600X. Additionally, the microstructure of the C-Ti alloys was examined

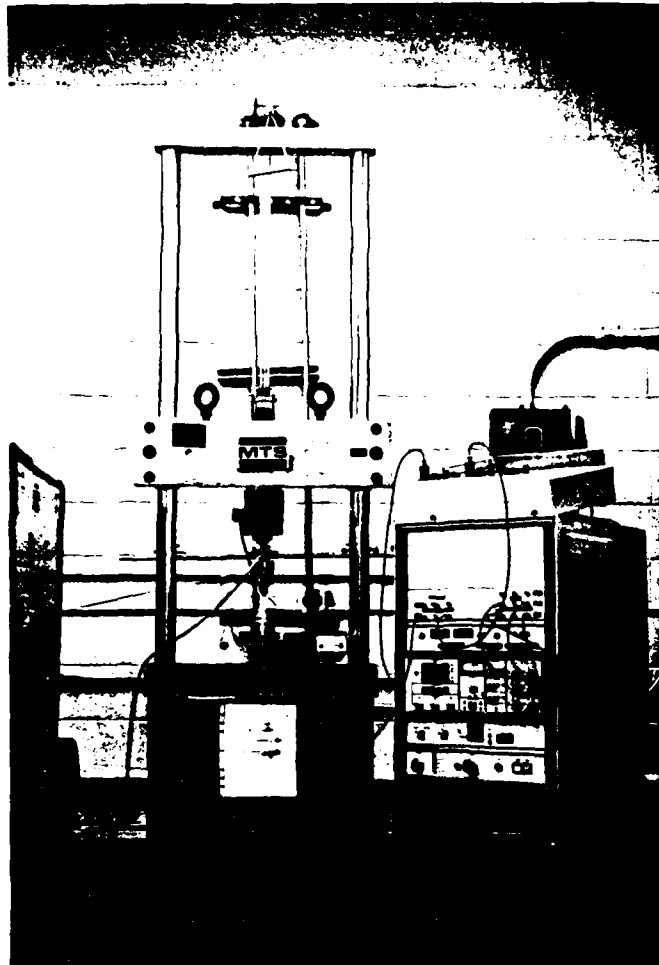


Figure 39. Picture of an Elevated  
Temperature Compression Test  
in Progress

using a Zeiss photomicroscope. Specimens for optical microscopy were polished and etched with a mixture of water, Nitric Acid, and Hydrofluoric Acid in proportions of 5:5:2 for 1 second.

## V. EXPERIMENTAL RESULTS

### Optical Metallography

Metallographic samples were prepared from the bottom surface of the compression sample. Figures 40 through 45 display representative microstructures of the C-Ti alloys. Samples were produced by the previously mentioned induction melting procedure or arc melting procedure. Figure 40 is the photomicrograph of a 2 weight percent (w/o) C-Ti alloy. Figures 41 through 45 are microstructures of alloys with increasing carbon contents (4w/o to 10w/o). The microstructures consist principally of a mixture of Alpha-Ti and Gamma phases at room temperature. A third carbon rich phase was found in some of the higher carbon percentage alloys and is thought to be the result of localized incomplete diffusion of carbon into the melt. A comparison of the results with the published phase diagram for the C-Ti system (Figure 9) show agreement with the anticipated phases and the microstructure for the alloys of 2 to 10 w/o carbon with the above noted exception of the high carbon content phase.

Figures 46 through 51 show the Gamma-phase particle size distribution and the volume fraction of Gamma phase (2-10 w/o C). The Gamma-phase particle size distribution was calculated by using the intercept method. Five microphotographs of the same



Figure 41. Transverse Photomicrograph of  
Ti-4w/o C Alloy. Volume  
Fraction of Gamma Phase is 31%



Figure 40. Transverse Photomicrograph of  
Ti-2w/o C Alloy. Globular Phase  
is Gamma Phase. Volume Fraction  
of Gamma Phase is 30%.



Figure 43. Transverse Photomicrograph of  
Ti-6w/o C Alloy. Volume Fraction of  
Gamma Phase is 50%



Figure 42. Transverse Photomicrograph of  
Ti-5w/o C Alloy. Volume Fraction of  
Gamma Phase is 46%



Figure 44. Transverse Photomicrograph of  
Ti-7w/o C Alloy. Volume Fraction of  
Gamma Phase is 52%

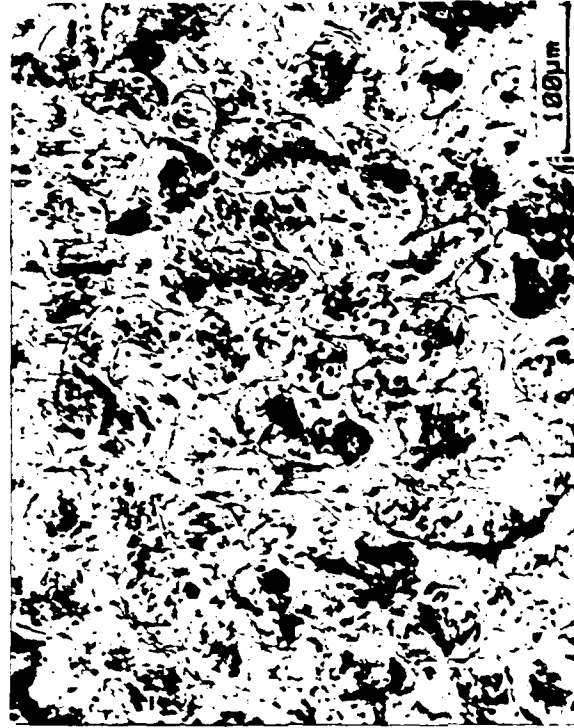


Figure 45. Transverse Photomicrograph of  
Ti-10w/o C Alloy. Volume Fraction of  
Gamma Phase is 82%



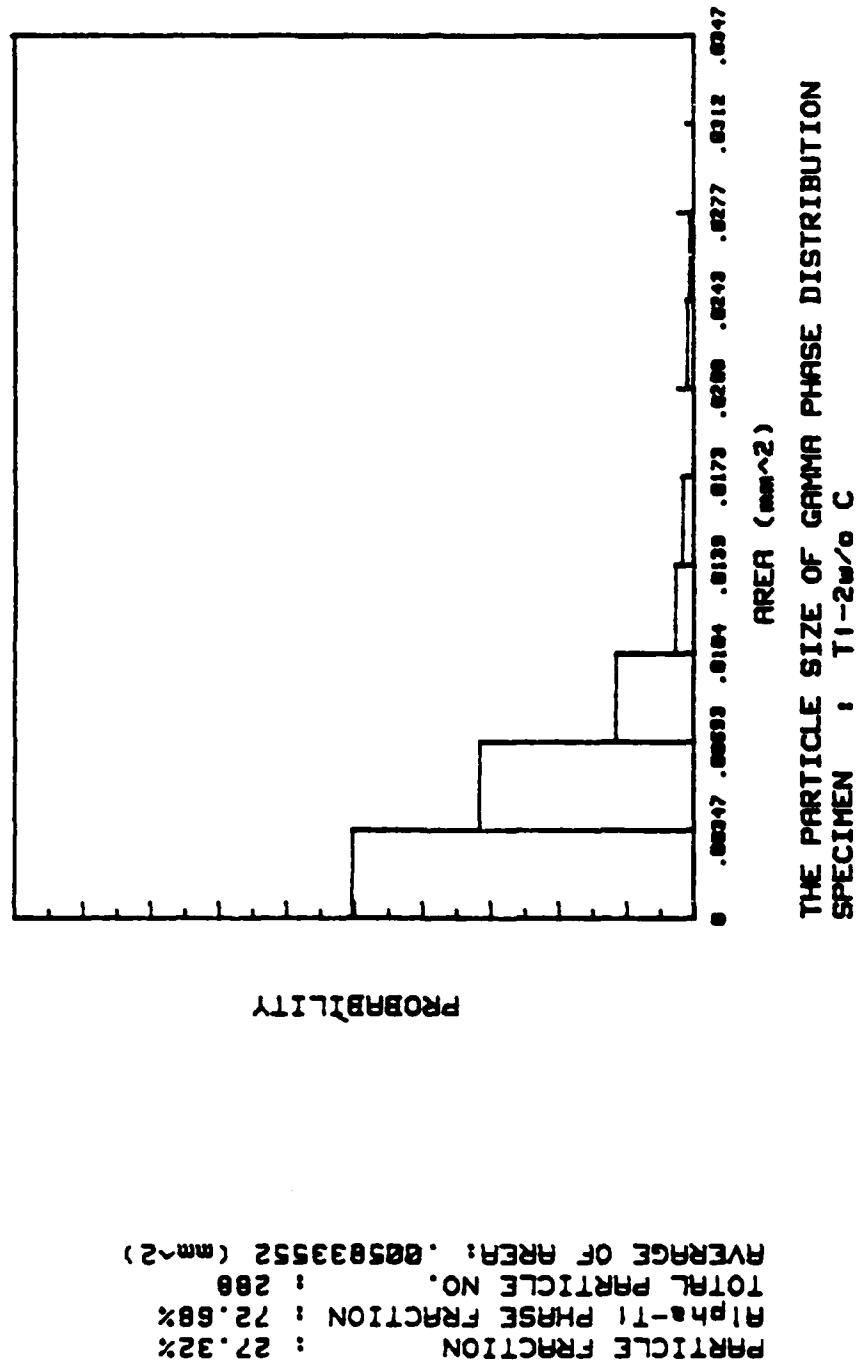


Figure 46. Gamma Phase Size Distribution : Ti-2w/o C. Microstructure of Alloy shown in Figure 40.

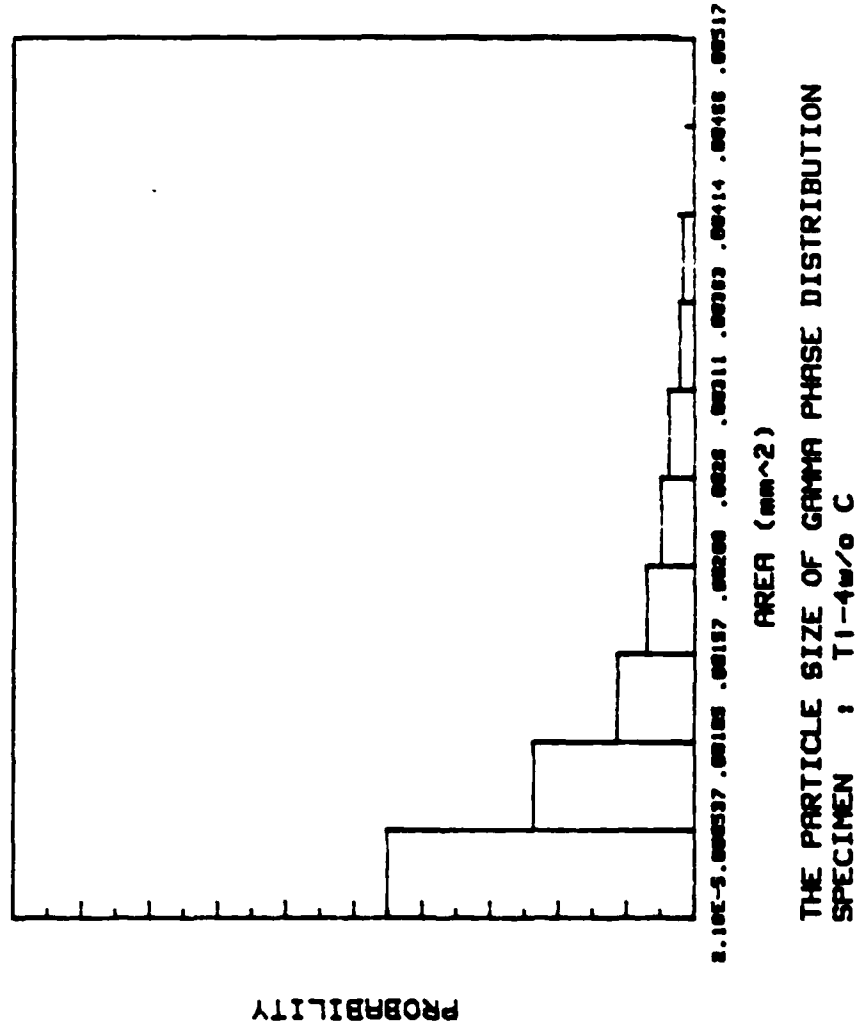


Figure 47. Gamma Phase Size Distribution : Ti-4w/o C. Microstructure of Alloy shown in Figure 41.

PARTICLE FRACTION : 30.12 %  
ALPHA-TI PHASE FRACTION : 69.88 %  
TOTAL PARTICLE NO. : 186  
AVERAGE OF AREA : 0.001143929 (mm<sup>2</sup>)

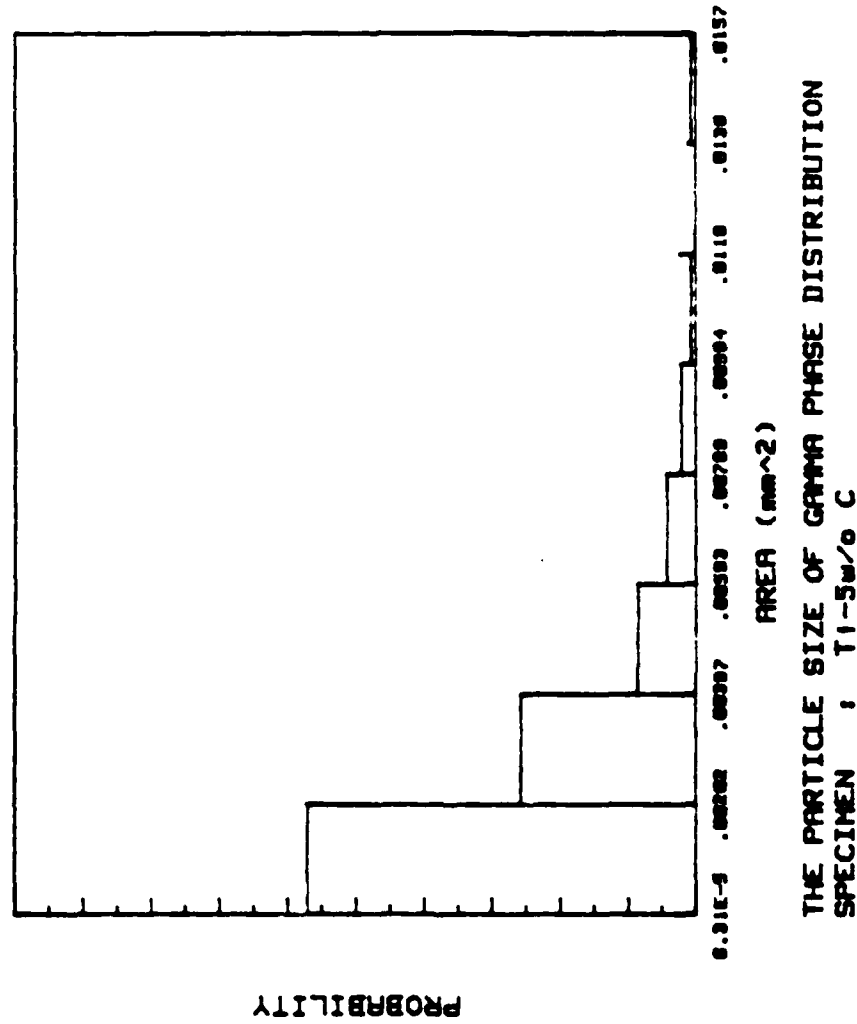


Figure 48. Gamma Phase Size Distribution : T1-5w/o C. Microstructure of Alloy shown in Figure 42.

PARTICLE FRACTION : 45.88 %  
Alpha-T1 PHASE FRACTION : 54.12 %  
TOTAL PARTICLE NO. : 148  
AVERAGE OF AREA: .002367031 (mm<sup>2</sup>)

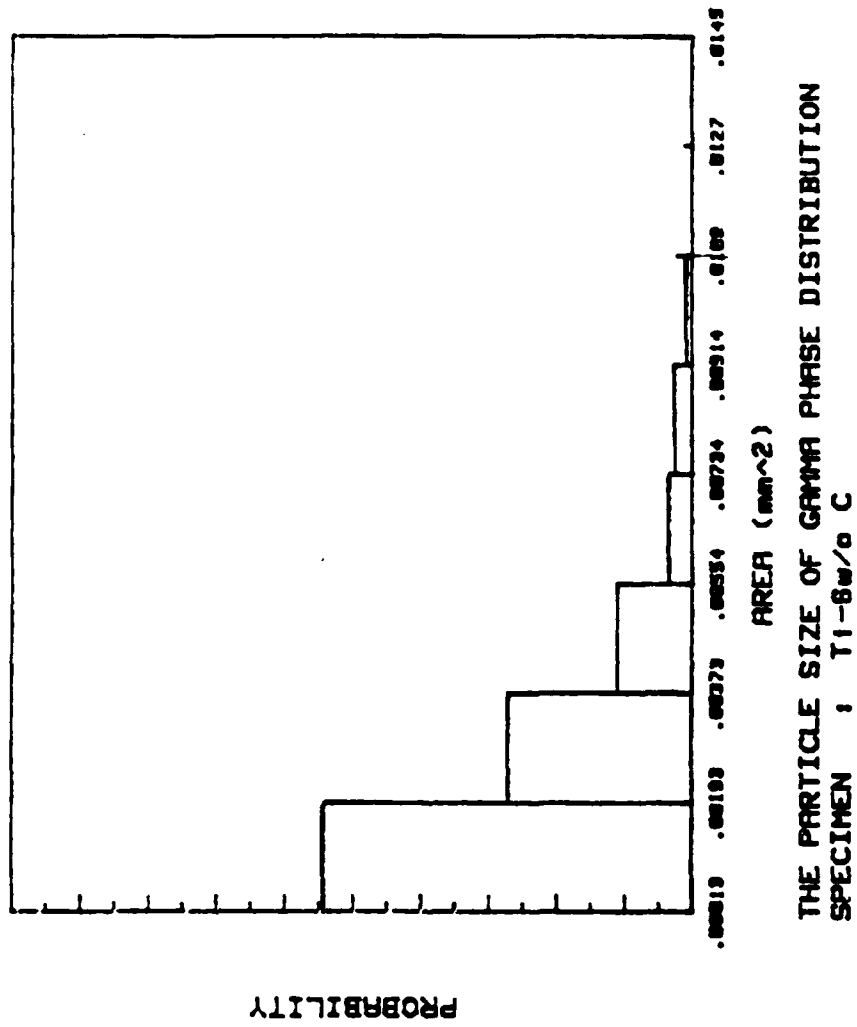


Figure 49. Gamma Phase Size Distribution : T1-6w/o C. Microstructure of Alloy shown in Figure 43.

PARTICLE FRACTION : 49.94 %  
Alpha-Ti PHASE FRACTION : 50.06 %  
TOTAL PARTICLE NO. : 118  
AVERAGE OF AREA : .003005189 (mm<sup>2</sup>)

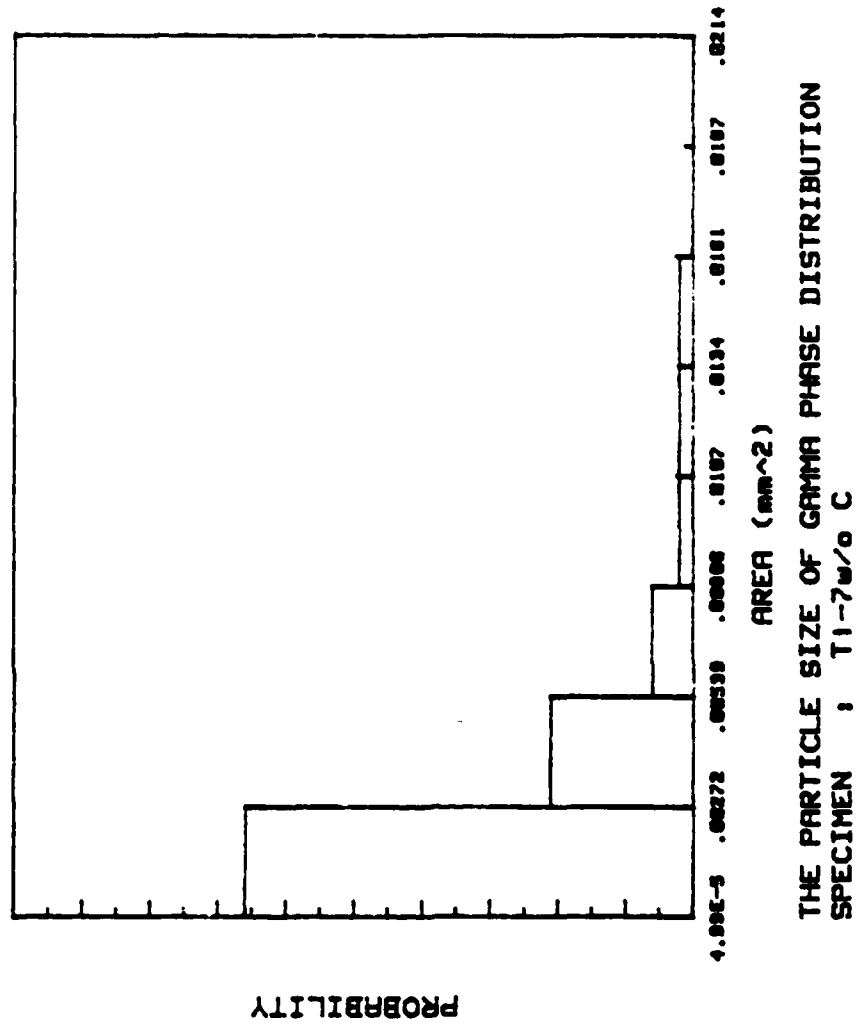
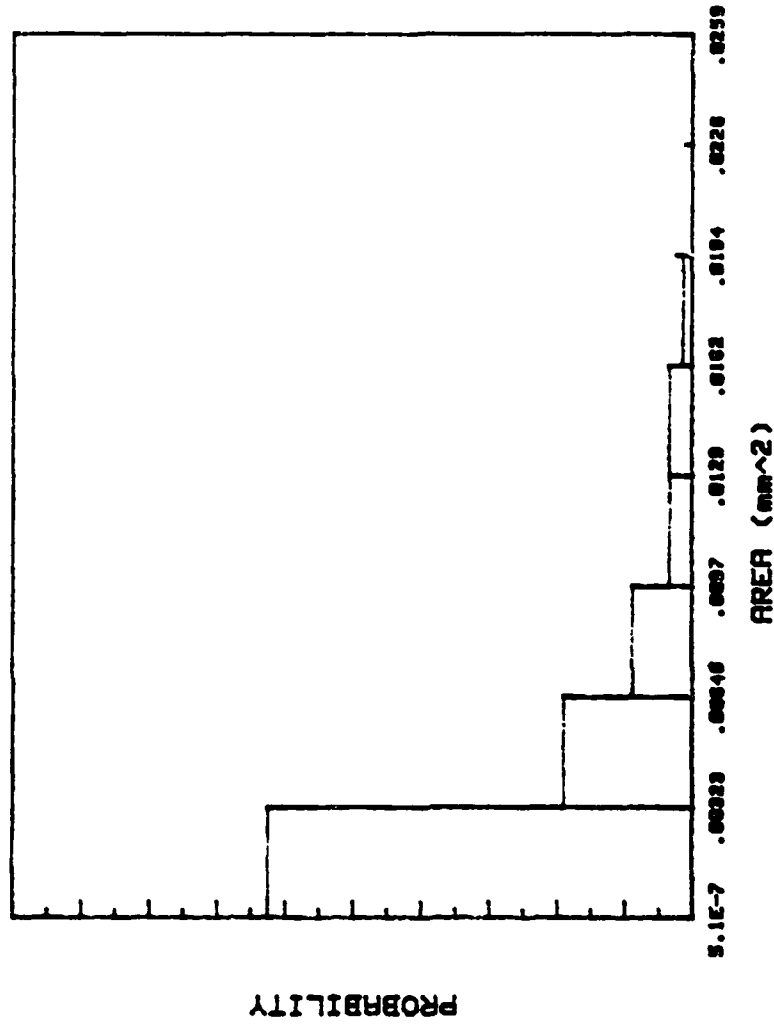


Figure 50. Gamma Phase Size Distribution : Ti-7w/o C. Microstructure of Alloy shown in Figure 44.

PARTICLE FRACTION : 51.75 %  
Alpha-Ti PHASE FRACTION : 48.25 %  
TOTAL PARTICLE NO. : 100  
AVERAGE OF AREA: .003689578 (mm<sup>2</sup>)



THE PARTICLE SIZE OF GAMMA PHASE DISTRIBUTION  
SPECIMEN : Ti-10w/o C

Figure 51. Gamma Phase Size Distribution : Ti-10w/o C. Microstructure of Alloy shown in Figure 45.

PARTICLE FRACTION : 81.39 %  
Alpha-Ti PHASE FRACTION : 18.61 %  
TOTAL PARTICLE NO. : 147  
AVERAGE OF AREA : .00480768 (mm<sup>2</sup>)

specimen were taken prior to the compression test to calculate the volume fraction of Gamma-phase of the alloys. The phase distribution was measured using a HP-9111A graphics tablet in conjunction with an HP-9836 microcomputer. The mean value of five measurements from each specimen was included in this study. The results show that the volume fraction of Gamma phase increases as the carbon content is increased. Because of this, the strength of C-Ti alloys increases.

#### Hardness Measurements

Hardness measurements were made on the alloys to aid characterization of their mechanical properties. The macroscopic hardness measurements were found to vary with carbon content. The rockwell C hardness varied from a value of 22 for a 2 w/o carbon alloy to 40 for the 10 w/o carbon alloy. In addition to macrohardness measurement, microhardness measurements (using a Vicker hardness unit) were made on the Alpha-Ti and Gamma phase structures seen in the photomicrographs of figures 40 through 45. The diamond indentations on the Alpha-Ti phase were clear and large, but due to the increased hardness of Gamma phase indentations appear much smaller. Figure 52 and figure 53 compare the microhardness of Alpha-Ti and Gamma phase for the 2 w/o C and 10 w/o C alloys. From this data it is concluded that the microhardness of the Gamma phase increases as the carbon content is increased. The Vicker hardness value of Alpha-Ti is

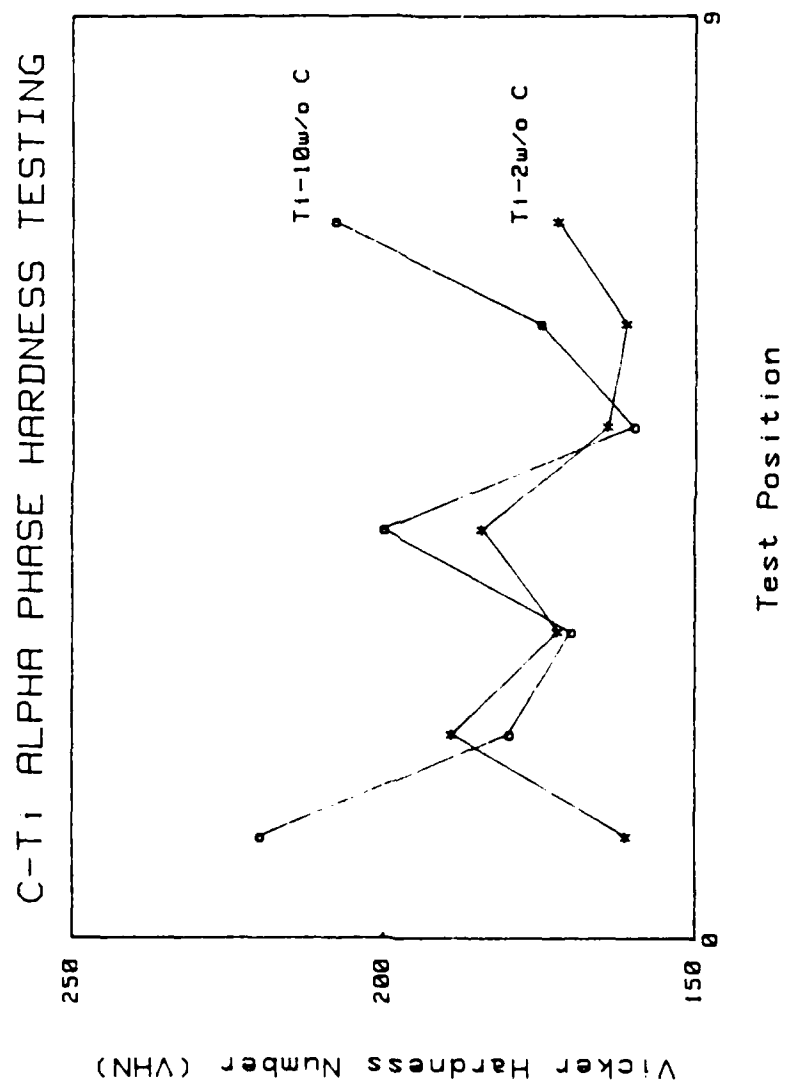


Figure 52. Microhardness Tests of Alpha-Ti.



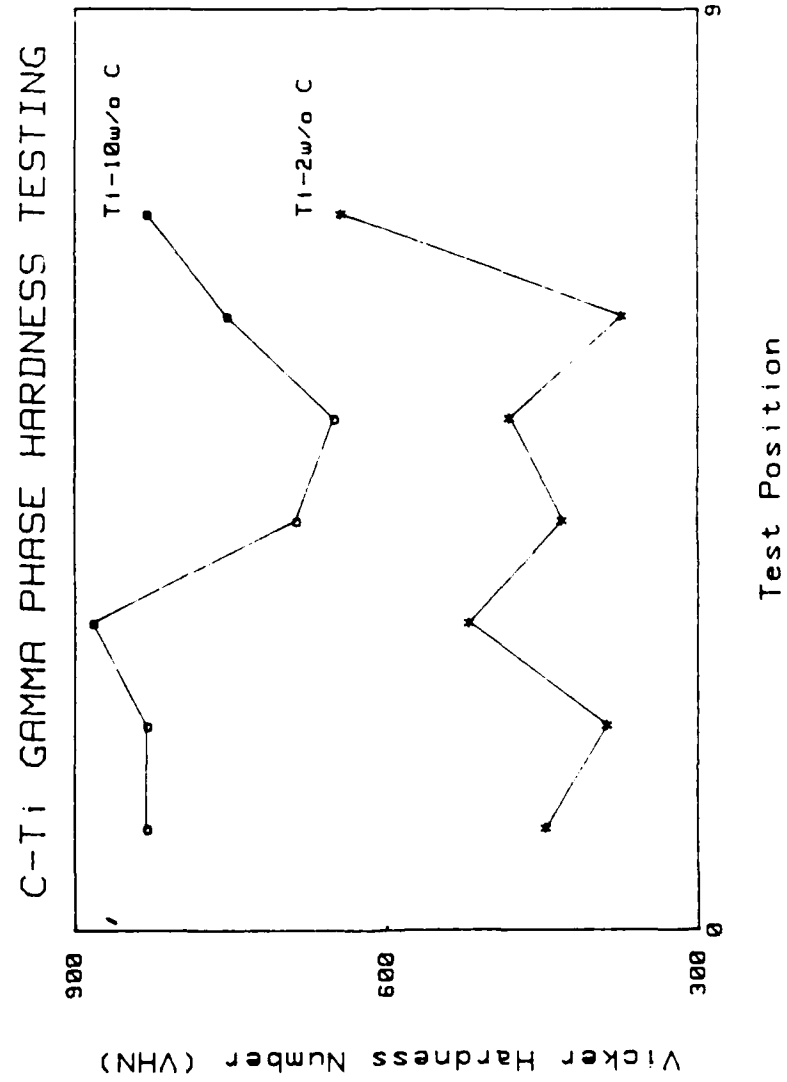


Figure 53. Microhardness Tests of Gamma Phase.

insensitive to carbon content. The hardness of C-Ti is therefore dictated by the volume fraction and distribution of Gamma phase.

### Compression Test Results

#### Room Temperature Compression Tests

Compression tests at a fixed strain rate ( $10^{-4}$  sec $^{-1}$ ) were performed on the C-Ti alloys at differing temperatures, with a total of 34 specimens tested. Tabulated results of all room temperature compression tests are given in APPENDIX C. Figure 54 shows a typical compression specimen after testing. Macroscopic failure occurred along a 45 degree plane. The compression test results will be discussed in the following section, Yield Stress and True Failure Strain.

#### Yield Stress (Y.S.)

A summary of the mechanical properties of some of the tested C-Ti alloys at room temperature is given in Table 3. Figure 55 shows the characteristic stress vs strain curve for C-Ti alloys with different volume fraction of Gamma phase. This curve indicates that the elastic modulus of C-Ti alloys increases as the volume fraction of Gamma phase increases. The plot of yield stress as a function of Gamma phase fraction is shown in Figure 56. The data points for 100% Gamma phase are taken from references [67] and [72]. Yield stress is obtained by using the 0.2% offset yield stress method.

AD-A177 376

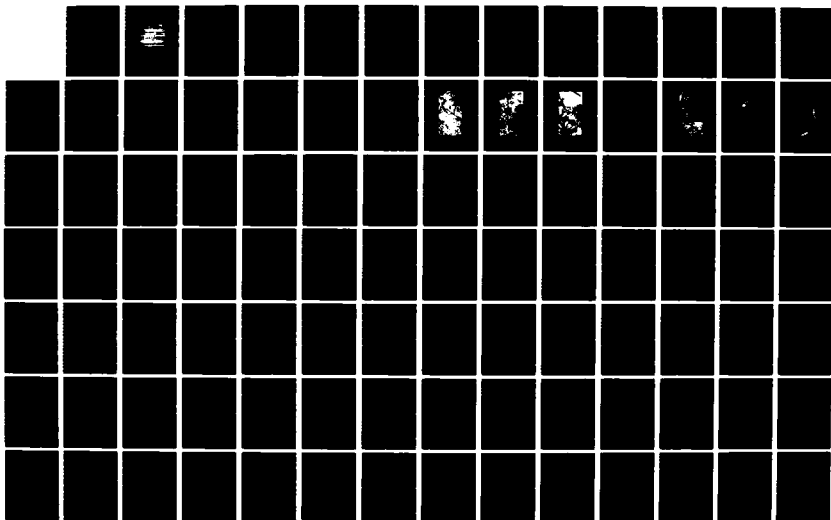
ORDERED CARBON - METAL ALLOYS FOR EXTRATERRESTRIAL  
POWER SYSTEMS(U) AUBURN UNIV AL DEPT OF MECHANICAL  
ENGINEERING B A CHIN ET AL 08 DEC 86 8628C2ETPS  
AFOSR-TR-87-0101 AFOSR-83-0168

2/3

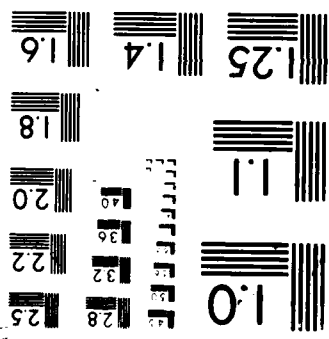
UNCLASSIFIED

F/G 11/6

NL



MICROCOPY RESOLUTION TEST CHART  
1010-10A



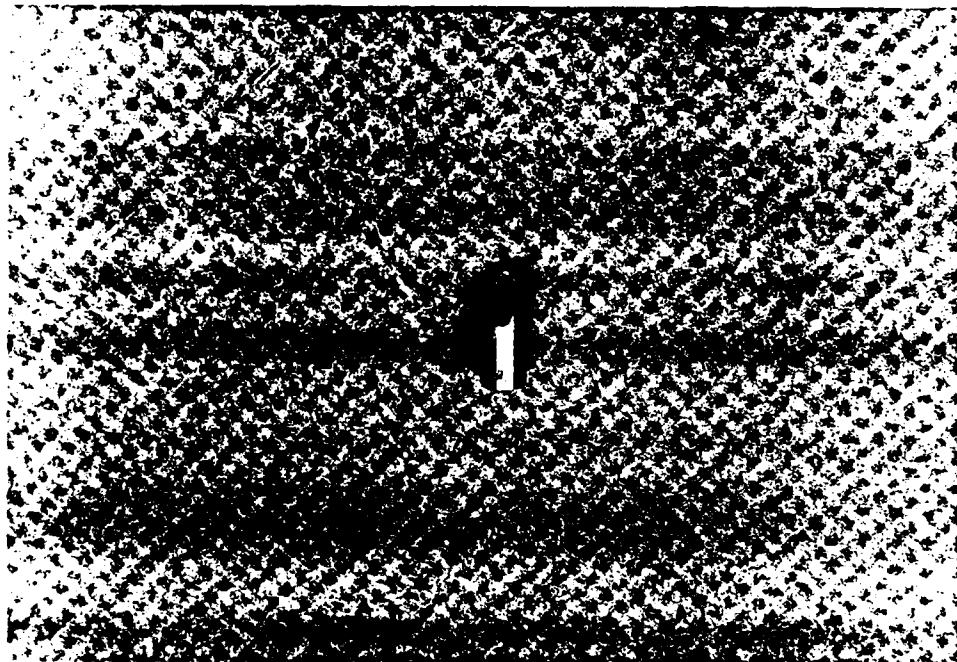
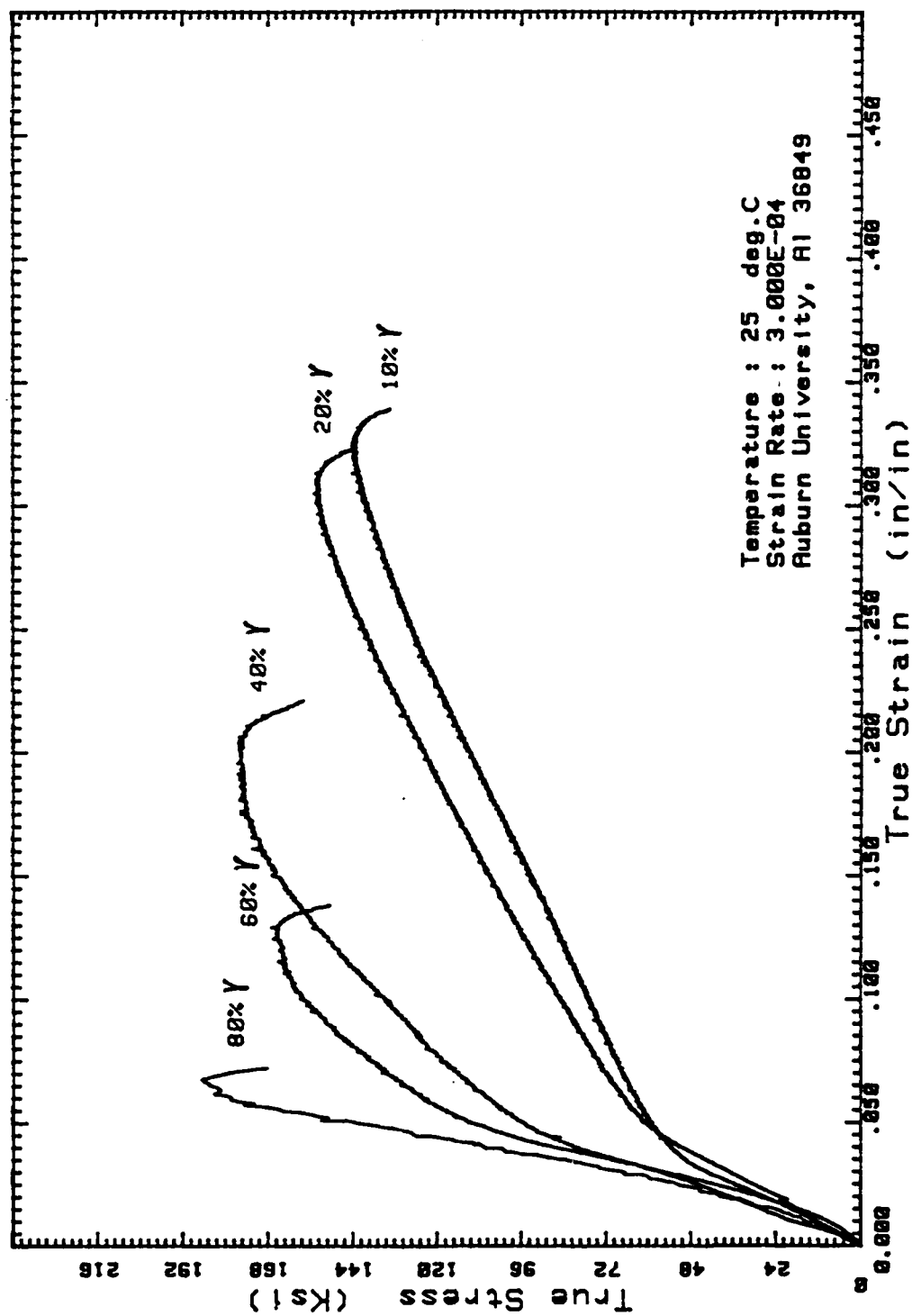


Figure 54. Compression Test Sample after Test

Table 3  
Summary of Average Mechanical Properties  
for C-Ti Alloys at Room Temperatuer

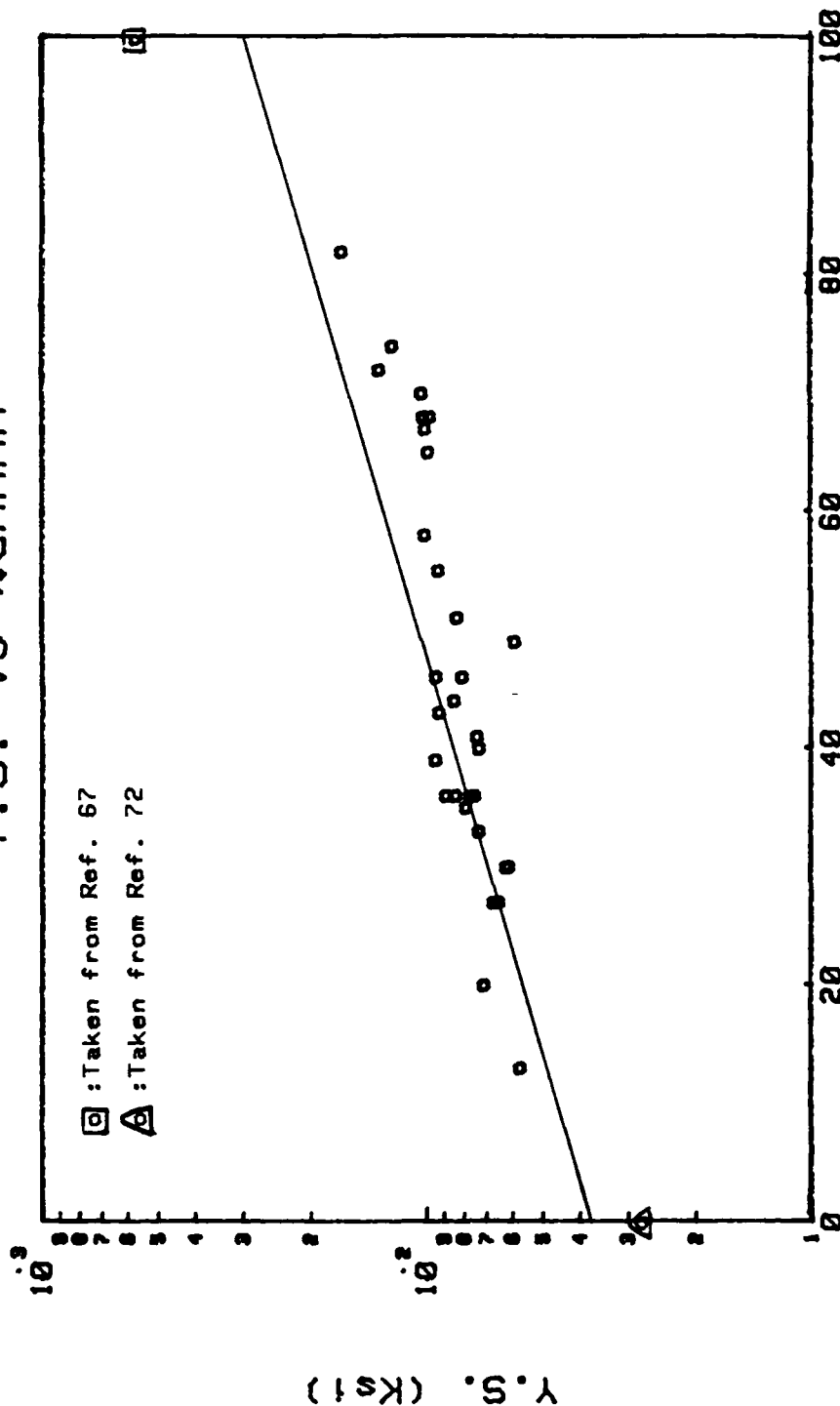
Specimen No.	Y.S. (Ksi)	True M.F.S. (Ksi)	True Failure Strain (%)	%Gamma Phase
W1	166	189	1.8	80%
I18	103	166	7.8	60%
I7	90	176	14.7	40%
I28	60	154	22.3	20%
I27	50	143	26.0	10%
Ti*	20	34	54.0	0%

\* --- Data is taken from Ref. [72].



55. Characteristic True Stress vs True Strain Curve for C-T1 Alloys with Different Volume Fraction of Gamma Phase.

# Y.S. vs %GAMMA



%GAMMA

Figure 56. Yield Stress as a Function of Gamma Phase.



points indicate a dramatic rise exponentially in yield stress as the volume fraction of Gamma phase increases. The values ranged from 168 Ksi for 82% Gamma phase to 58 Ksi for 10% Gamma phase.

#### True Failure Strain ( $\epsilon_f$ )

True failure strain was measured by the following method. The true failure plastic strain on the true stress-true strain curve was calculated by drawing a line, with slope equal to the elastic modulus, from the failure point on the curve to the intersection with the strain axis. This intersection denotes true failure plastic strain of the specimen. A plot of true failure plastic strain as a function of the volume fraction of Gamma phase is shown in Figure 57. There is a dramatic decrease in the ductility as the volume fraction of Gamma phase rises. The results are very promising in that alloys containing 82% and 95% Gamma phase still show 2-5% ductility. This indicates that there must be a significant fraction of the Gamma phase which is deforming.

#### Elevated Temperature Compression Tests

Appendix D lists the mechanical properties of the C-Ti alloys which were tested in compression at temperatures from 150 to 850 degrees C. A total of thirty-four specimens were tested in the manner described in Section IV. The results are presented

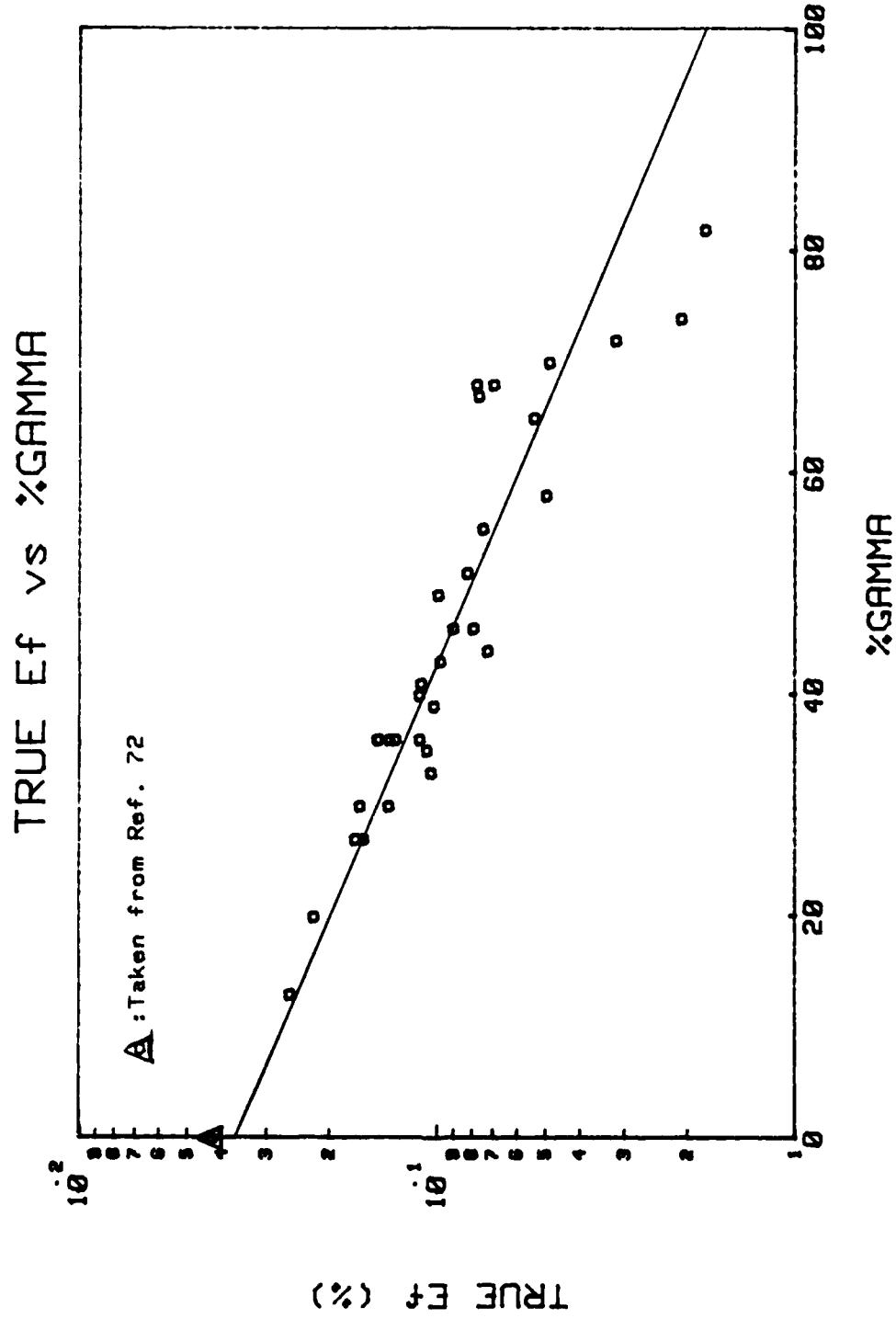


Figure 57. True Failure Strain as a Function of Gamma Phase.

in the following sections, True Maximum Flow Stress, Yield Stress, and True Failure Strain.

#### True Maximum Flow Stress (M.F.S.)

The true maximum flow stress is directly obtained from a true stress-true strain curve. Figures 58 and 59 show the characteristic true stress vs true strain curve for C-Ti alloys in different temperatures ranging from 150 to 850 degrees C. These curves indicate that the maximum flow stress decreases as the test temperature increases for a constant volume fraction of Gamma phase. A summary of the mechanical properties of chosen tested alloys for 57% & 10% Gamma phase at elevated temperatures is given in Table 4. A plot of true maximum flow stress as a function of Gamma phase is shown in Figure 60. The true maximum flow stress increases exponentially as the volume fraction of Gamma phase increases for a constant test temperature.

#### True Failure Strain and Yield Stress

The method of measuring yield stress and true failure strain has been described previously. Figure 61 shows the plot of yield stress as a function of Gamma phase. The yield stress increases as the test temperature decreases and drops exponentially with decreasing volume fraction of Gamma phase for a constant temperature. The dependence of yield stress as a function of

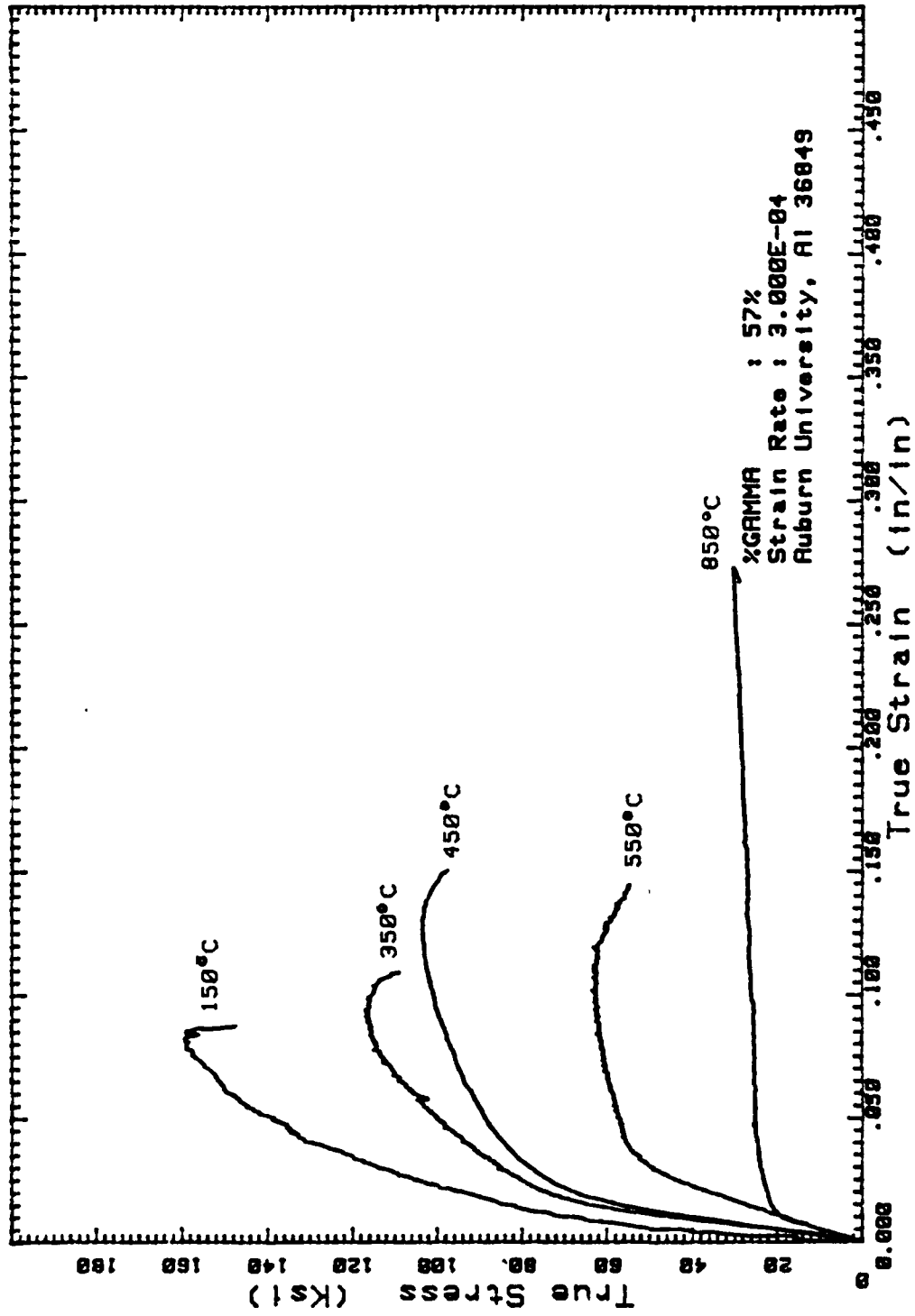


Figure 58. Characteristic True Stress vs True Strain Curve at Elevated Temperatures for 57% Gamma Phase.

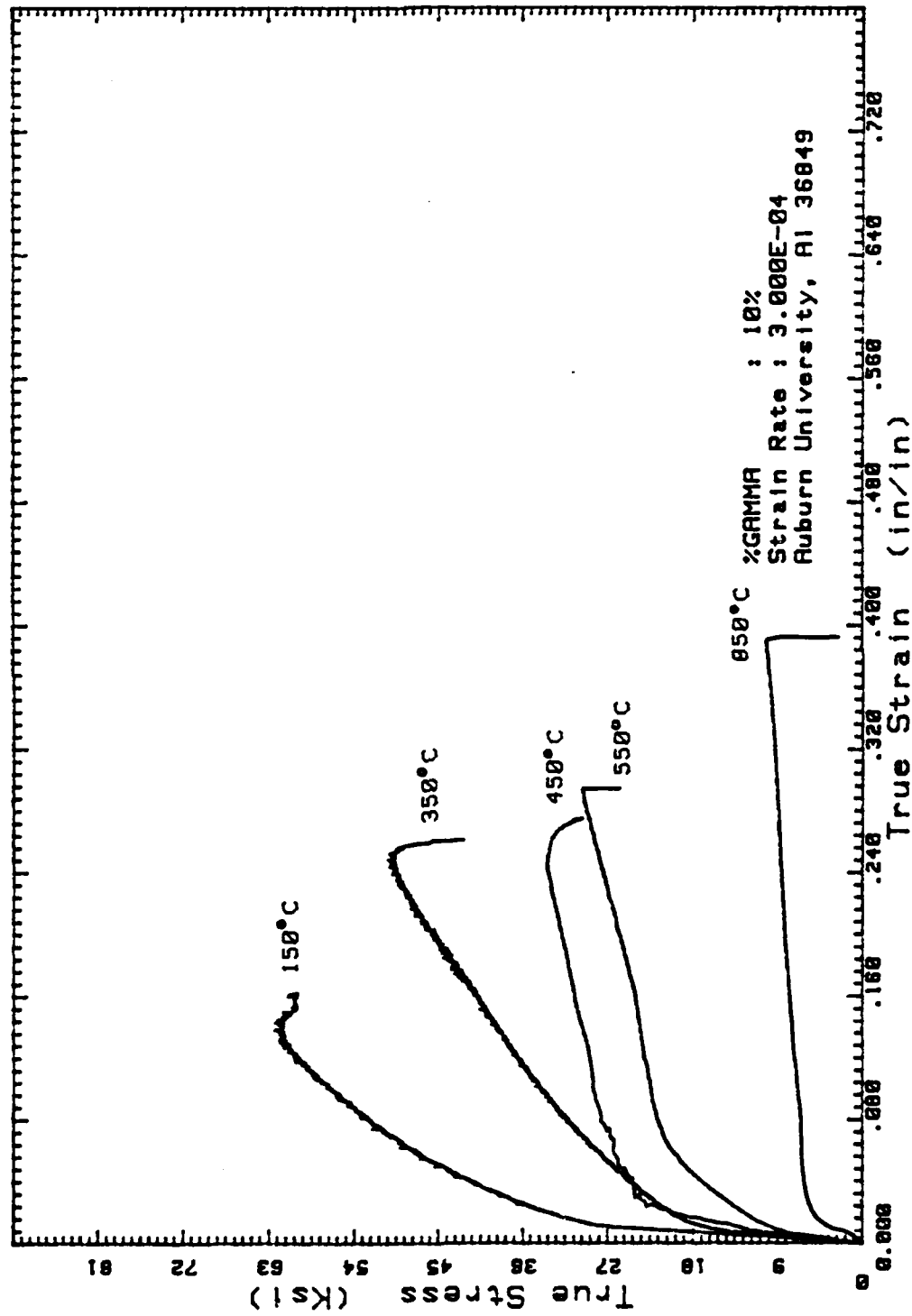


Figure 59. Characteristic True Stress vs True Strain Curve at Elevated Temperature for 10% Gamma Phase.

Table 4

Summary of Average Mechanical Properties for C-Ti Alloys  
at Elevated Temperature

-----  
-----  
Volume Fraction of Gamma Phase - 57%  
-----

Specimen No.	Test Temp. ( $^{\circ}$ C)	Y.S. (Ksi)	True M.F.S. (Ksi)	True Failure Strain (%)
HE4	850	21	30	26.2%
HD5	550	50	63	11.3%
HC6	450	64	103	13.1%
HB6	350	66	116	9.1%
HA4	150	65	160	6.8%

-----  
-----  
Volume Fraction of Gamma Phase - 10%  
-----

Specimen No.	Test Temp. ( $^{\circ}$ C)	Y.S. (Ksi)	True M.F.S. (Ksi)	True Failure Strain (%)
HE1	850	5	10	37.4%
HD1	550	10	30	27.8%
HC1	450	18	34	24.7%
HB1	350	18	50	23.9%
HA1	150	29	62	18.2%

-----

# M.F.S. vs %GAMMA

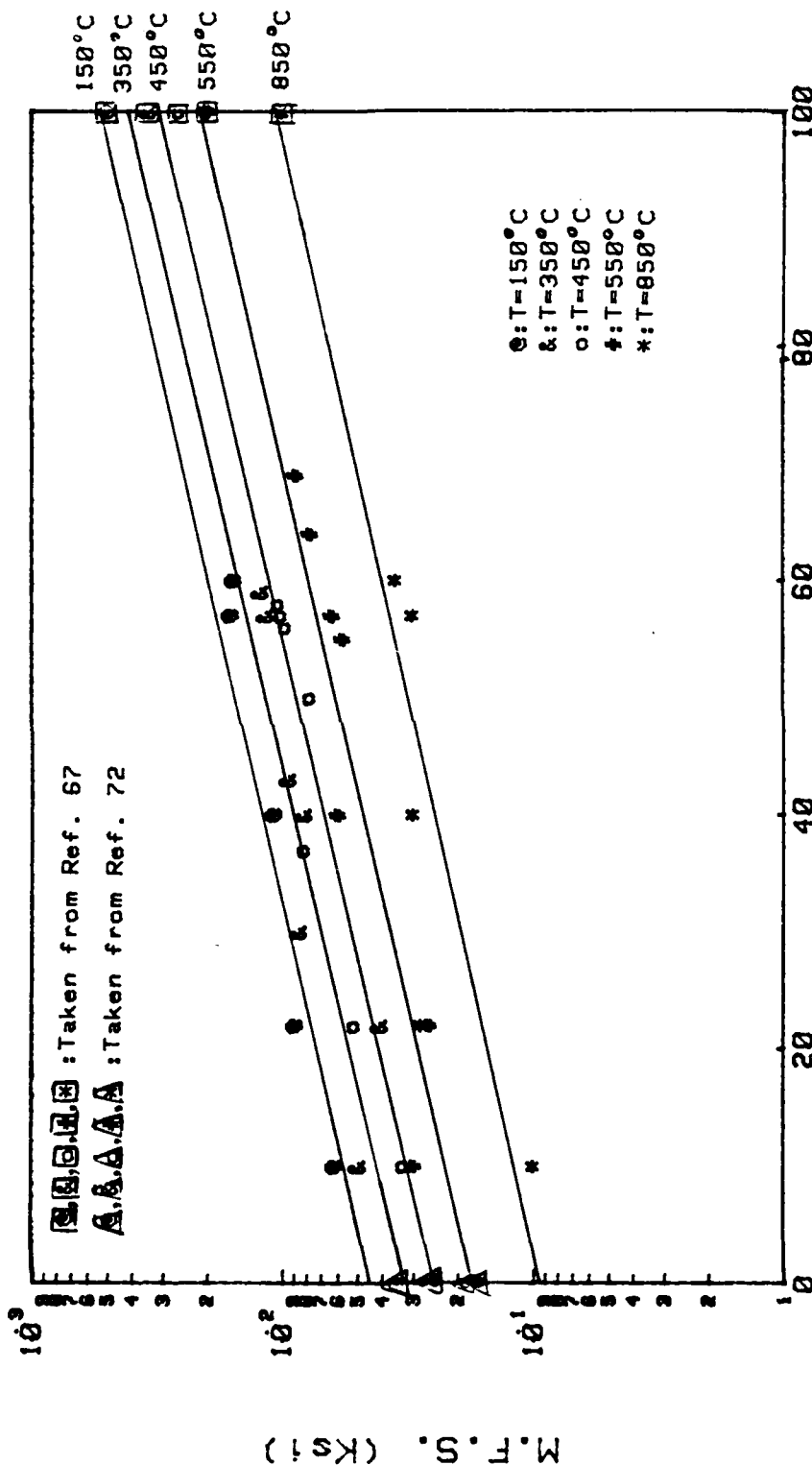


Figure 60. True Maximum Flow Stress as a Function of Volume Fraction of Gamma Phase at Elevated Temperature.

## Y.S. vs %GAMMA

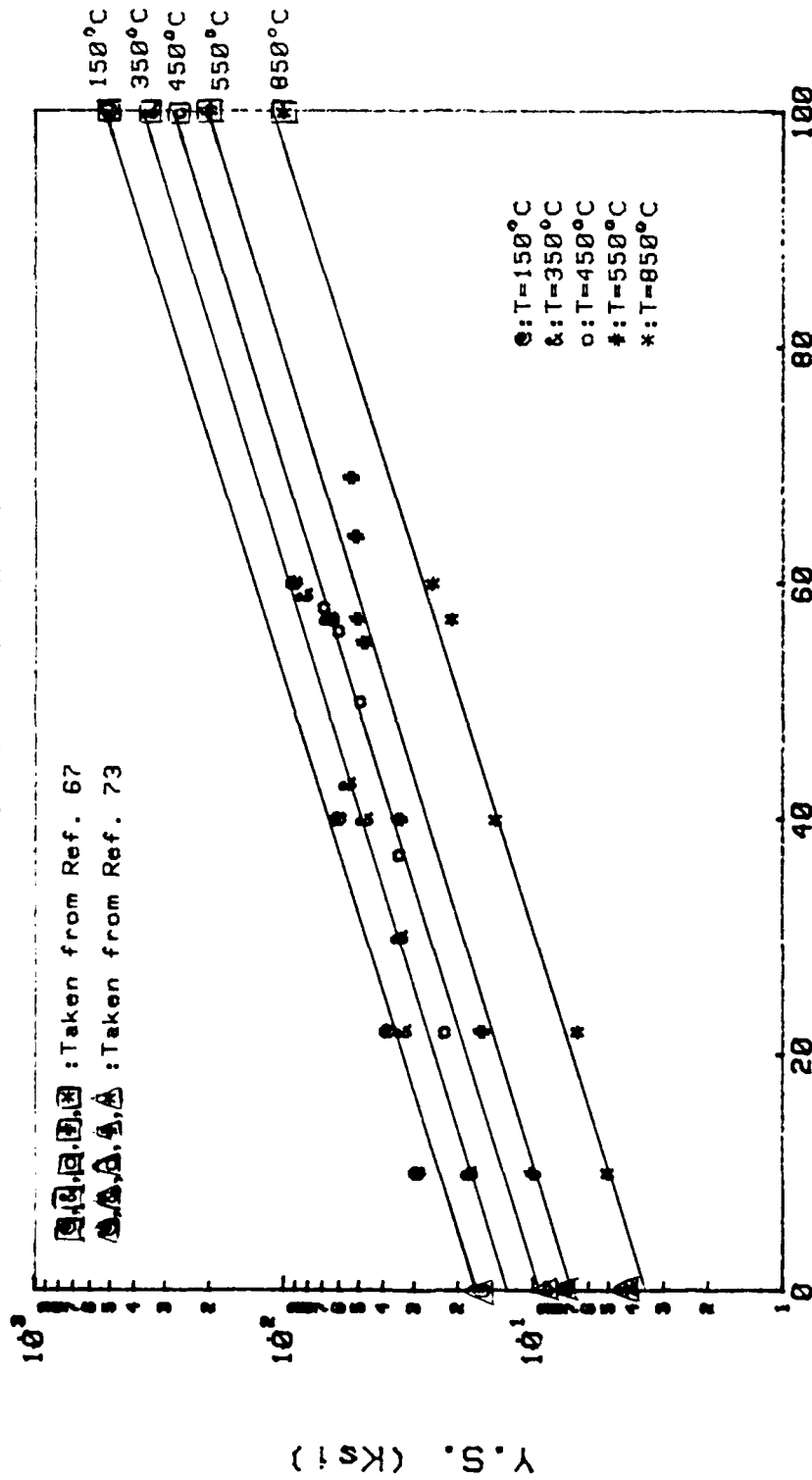


Figure 61. Yield Stress as a Function of Volume Fraction of Gamma Phase at Elevated Temperature.



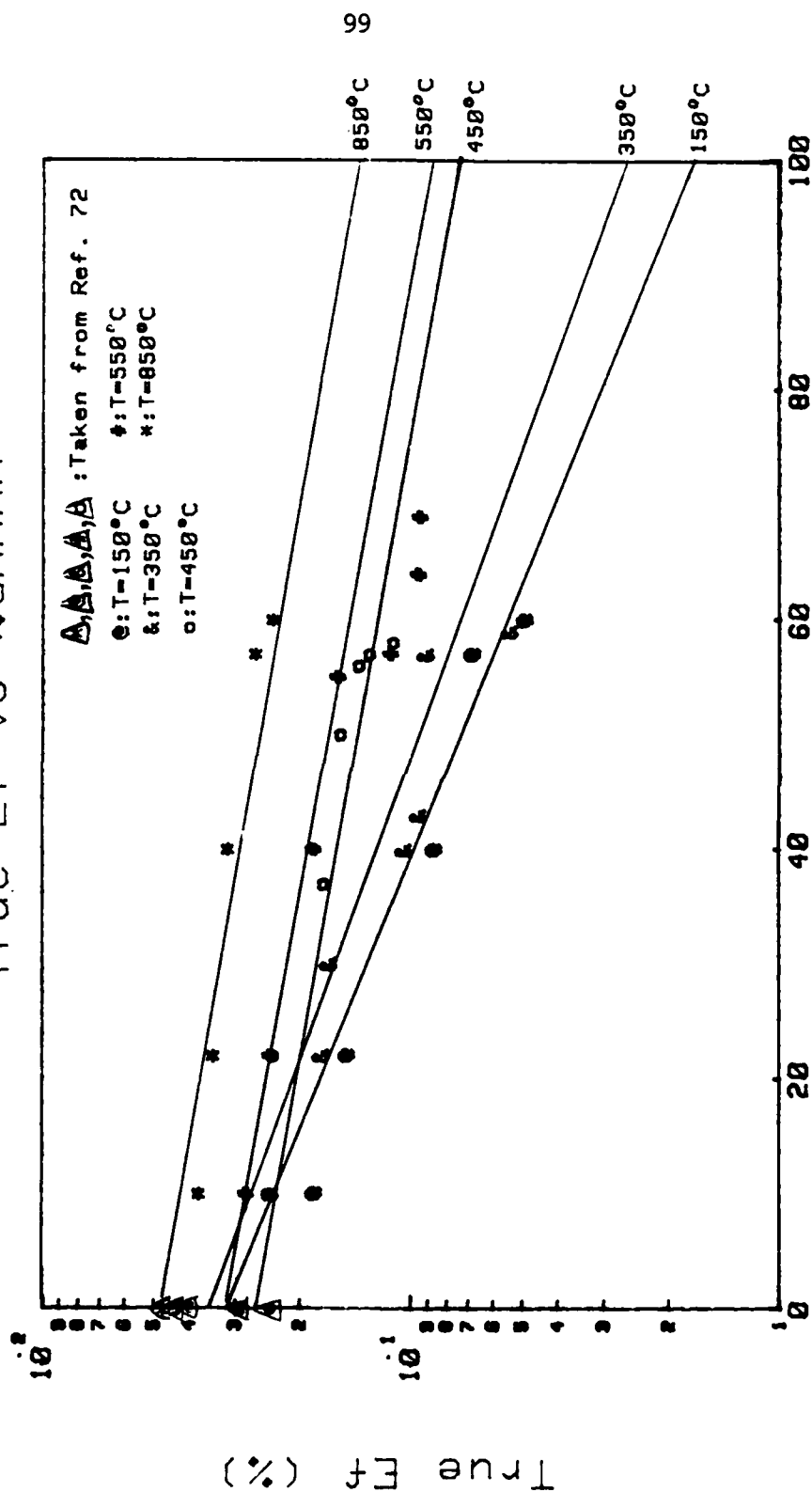
fraction of Gamma phase nearly are identical at different test temperatures.

The plot of true failure strain as a function of fraction of Gamma phase is shown in Figure 62. The true failure plastic strain decreases exponentially with increasing volume fraction of Gamma phase for constant temperature. The data points indicate that the slope becomes larger as the test temperature falls below 350 degrees C.

#### Related The Results At Room Temperature and Elevated Temperatures

Figures 63 through 65 display the true maximum flow stress, yield stress, and true failure strain as a function of reciprocal test temperature with different volume fraction of Gamma phase. The data points for the 100% Gamma phase and Ti are taken from references [67], [68], [72], and [73]. A change in the controlling deformation mechanism is seen to occur as indicated by the change in slope of the plot. The changes in slope occur at different transition temperatures exist for C-Ti alloys containing different volume fraction of Gamma phase. This indicates that the changes in controlling mechanism is a function of both temperature and composition. The range of transition temperature is from 470 degrees C for 10% Gamma phase to 500 degrees C for 60% Gamma phase. Figure 66 plots the transition temperature as a function of volume fraction of Gamma phase. The transition temperature increases linearly with increasing volume

# True Ef vs %GAMMA



%GAMMA

Figure 62. True Failure Strain as a Function of Volume Fraction of Gamma Phase at Elevated Temperature.

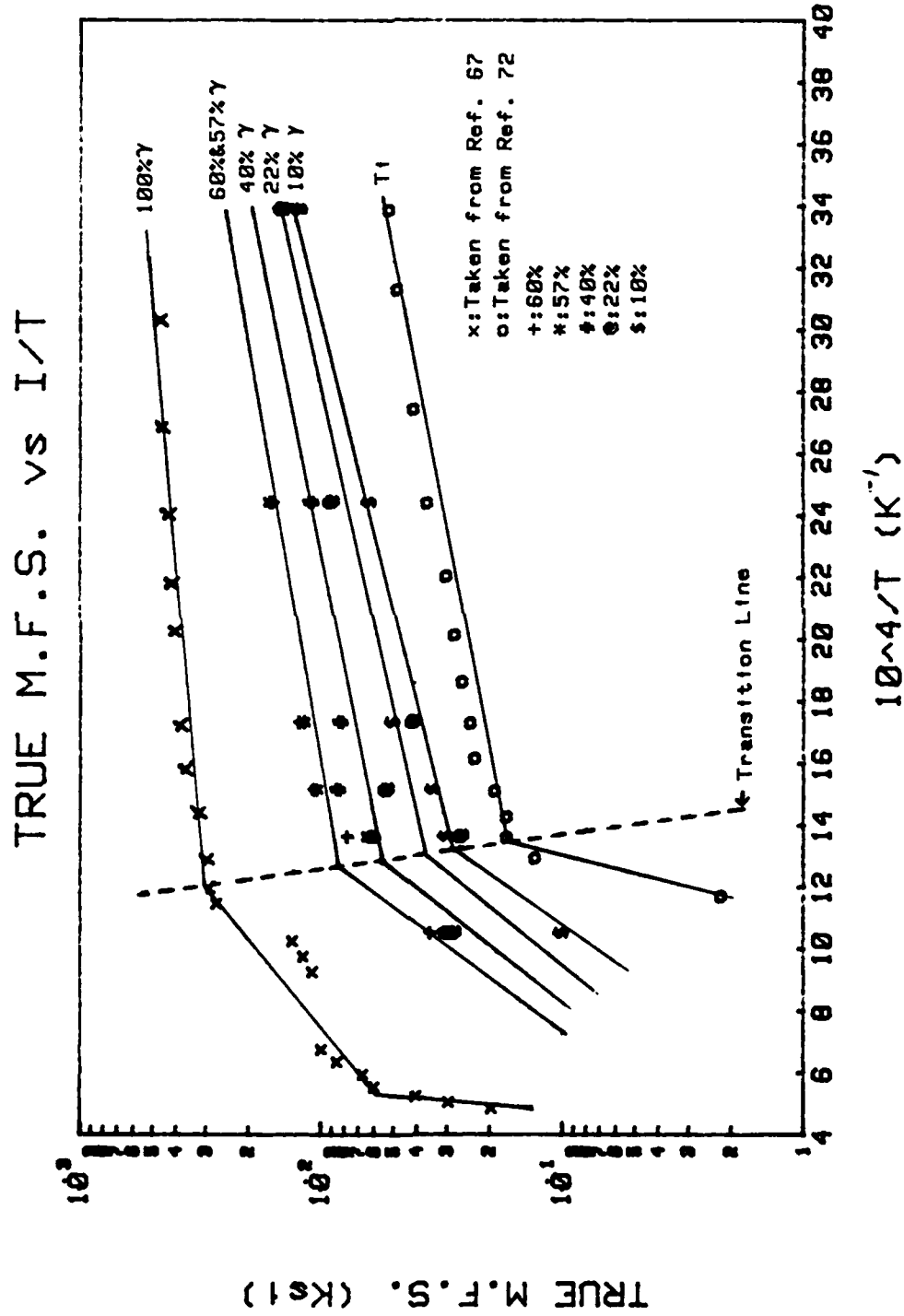


Figure 63. True Maximum Flow Stress as a Function of Temperature.

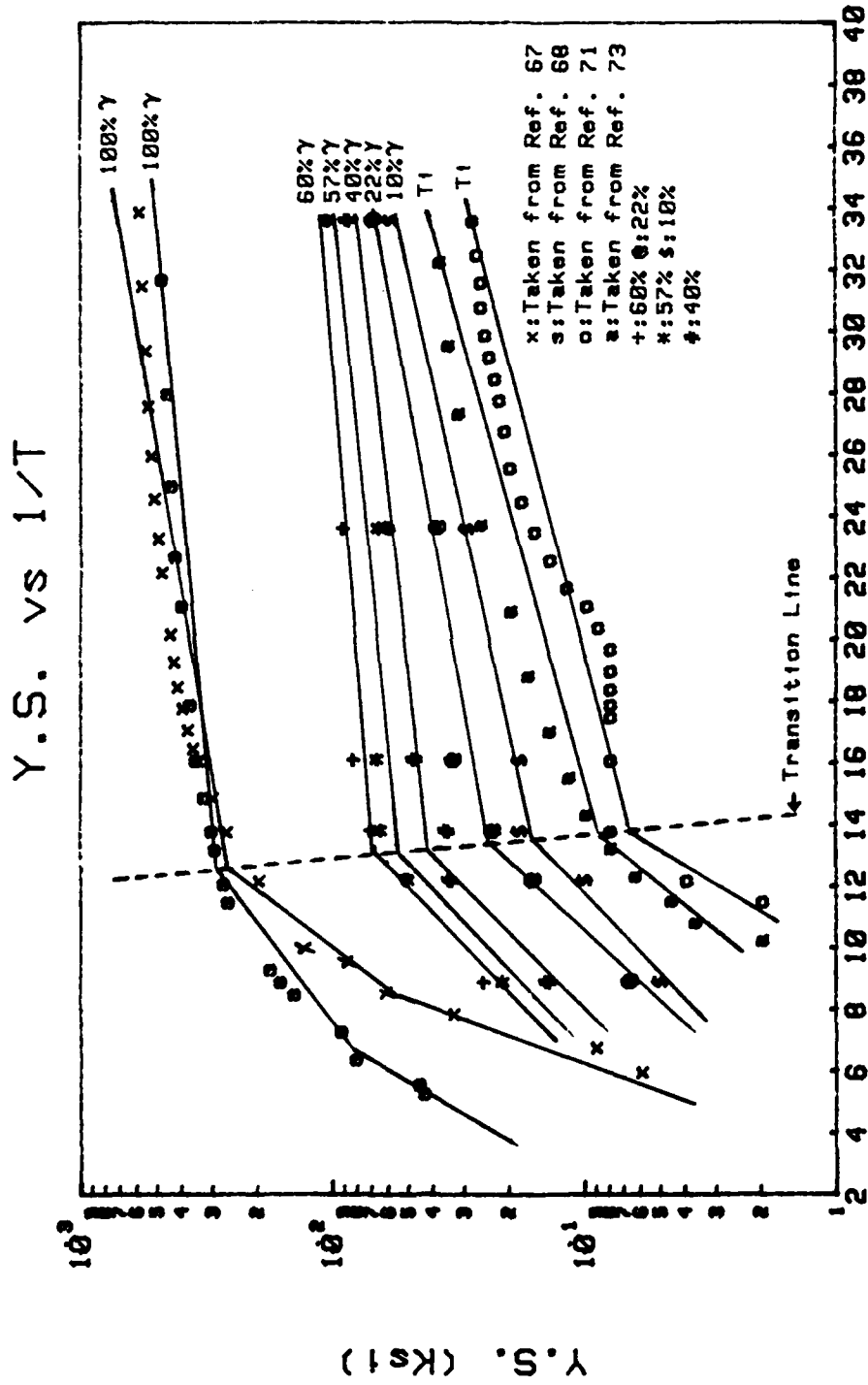


Figure 64. Yield Stress as a Function of Temperature.

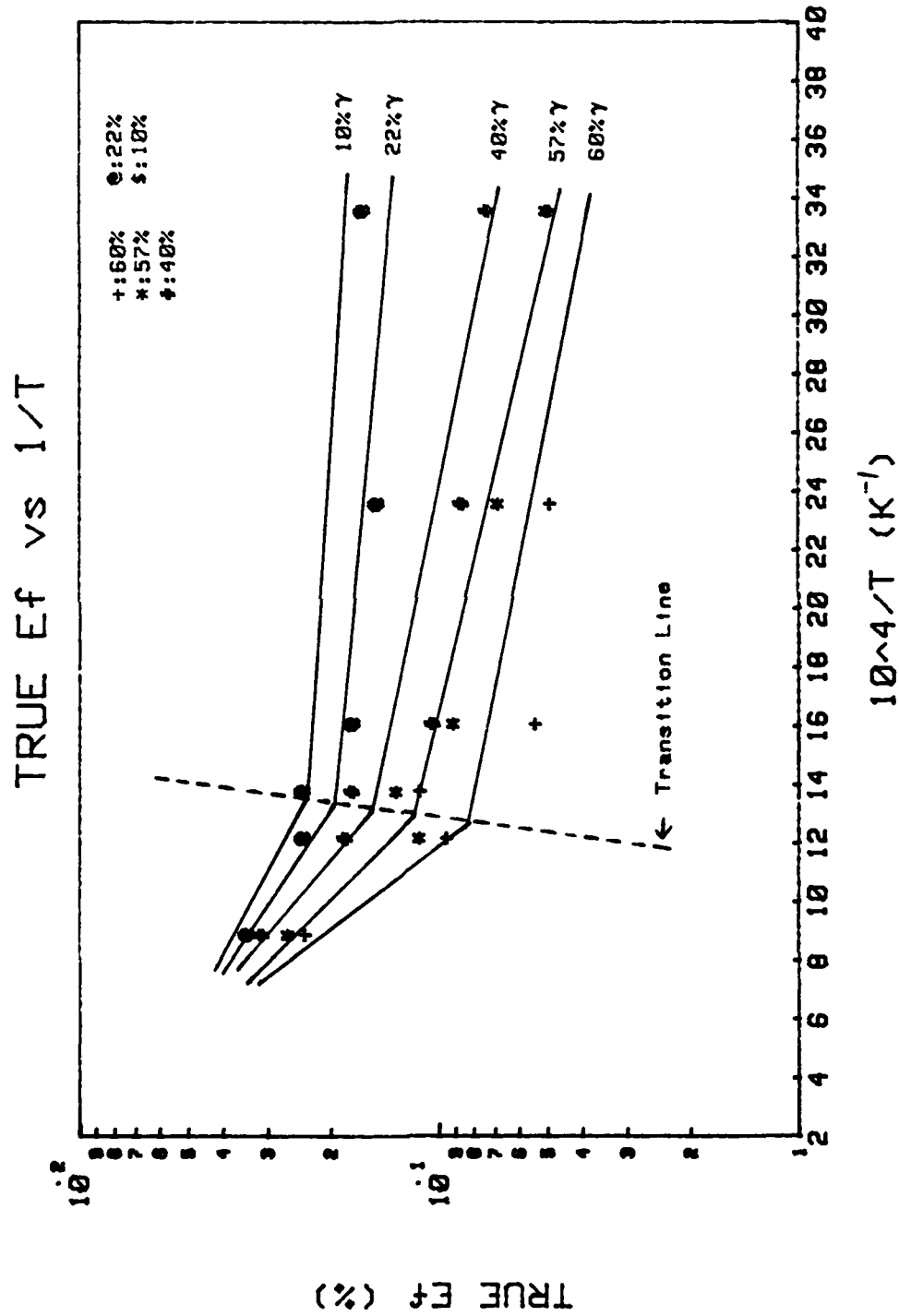


Figure 65. True Failure Strain as a Function of Temperature.

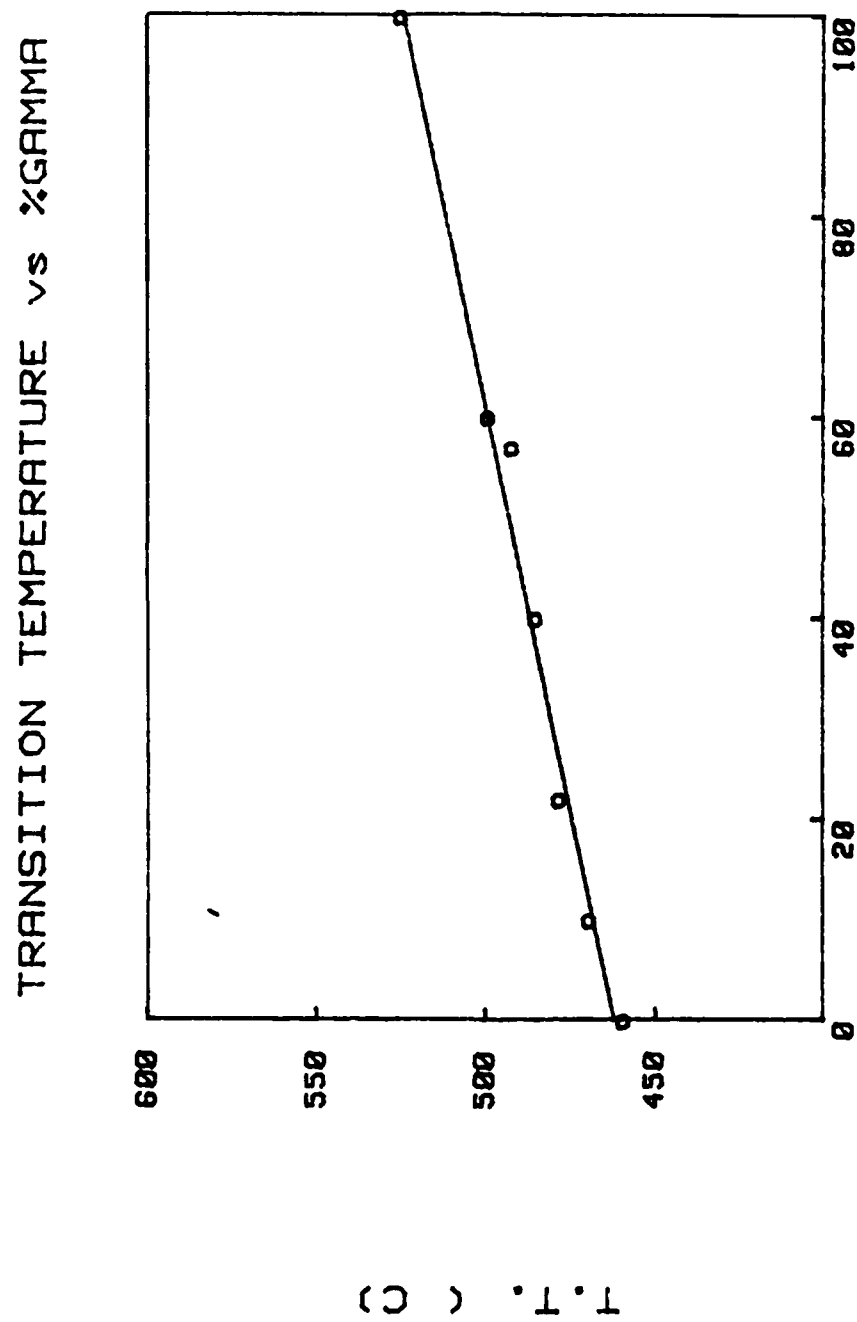


Figure 66. Transition Temperature as a Function of Volume Fraction of Gamma Phase.

transition temperature increases linearly with increasing volume fraction of Gamma phase.

#### Scanning Electron Microscopy

To investigate the macroscopic and microscopic fracture surface, two sets of specimens tested at room temperature and elevated temperatures were selected for SEM study. Each set contained four specimens having the same volume fraction of Gamma phase, 57% and 10%. All specimens were cleaned in an Acetone solution to remove the oxide layer on the fracture surface. The examination procedure is described in detail in Section IV.

#### Fracture Surface Observation

##### C-Ti alloys containing 57% Gamma phase

Figures 67 through 70 show the fracture surface of C-Ti alloys containing 57% Gamma phase tested at different temperatures ranging from 25 degrees C to 550 degrees C. The arrow shown on each photograph indicates the slip direction during the compression test. Examination of the fractographs indicate that the amount of cleavage failure decreases with the increasing temperature. There is a significant amount of smooth slip surface in specimens which were tested at temperature above 450 degrees C. There is an abundance of secondary cracks which indicates that significant energy was expended in the initiation and propagation of these cracks prior to final failure. This phenomenon existed in specimens with test temperature below 350

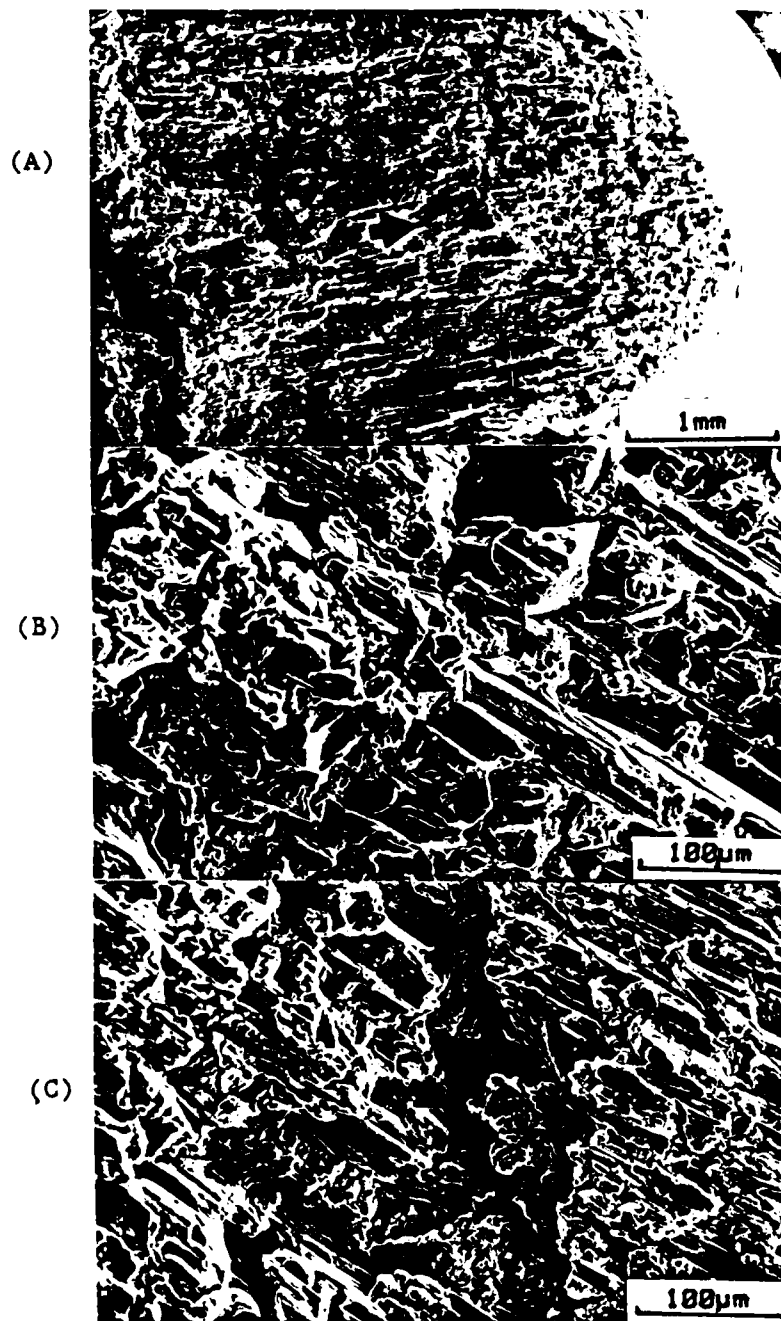


Figure 67. Fracture Features of C-Ti Alloys  
Containing 57% Gamma Phase  
at T= 25°C (A) Complete Cross Section,  
(B) (C) Higher Magnification



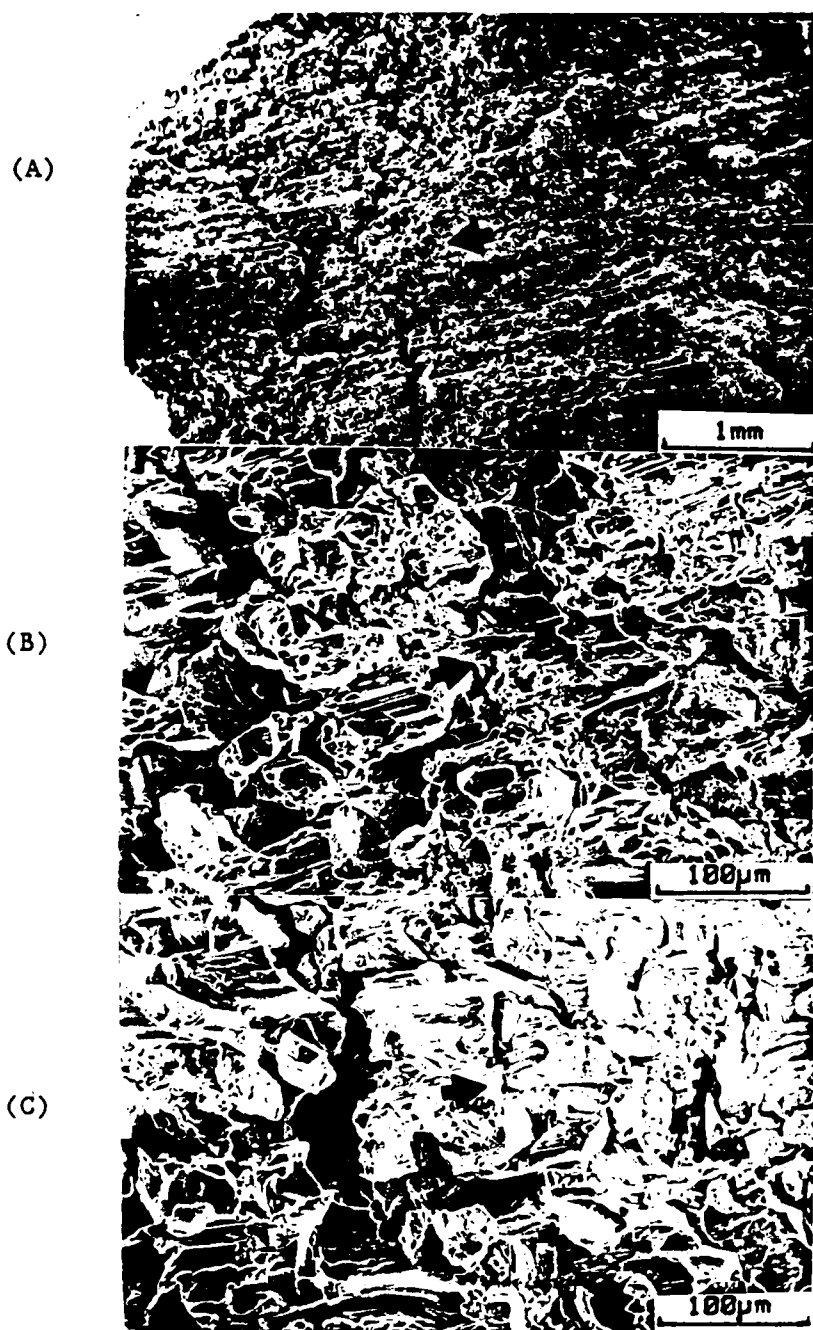


Figure 68. Fracture Features of C-Ti Alloys  
Containing 57% Gamma Phase  
at  $T = 350^{\circ}\text{C}$  (A) Complete Cross Section,  
(B) (C) Higher Magnification

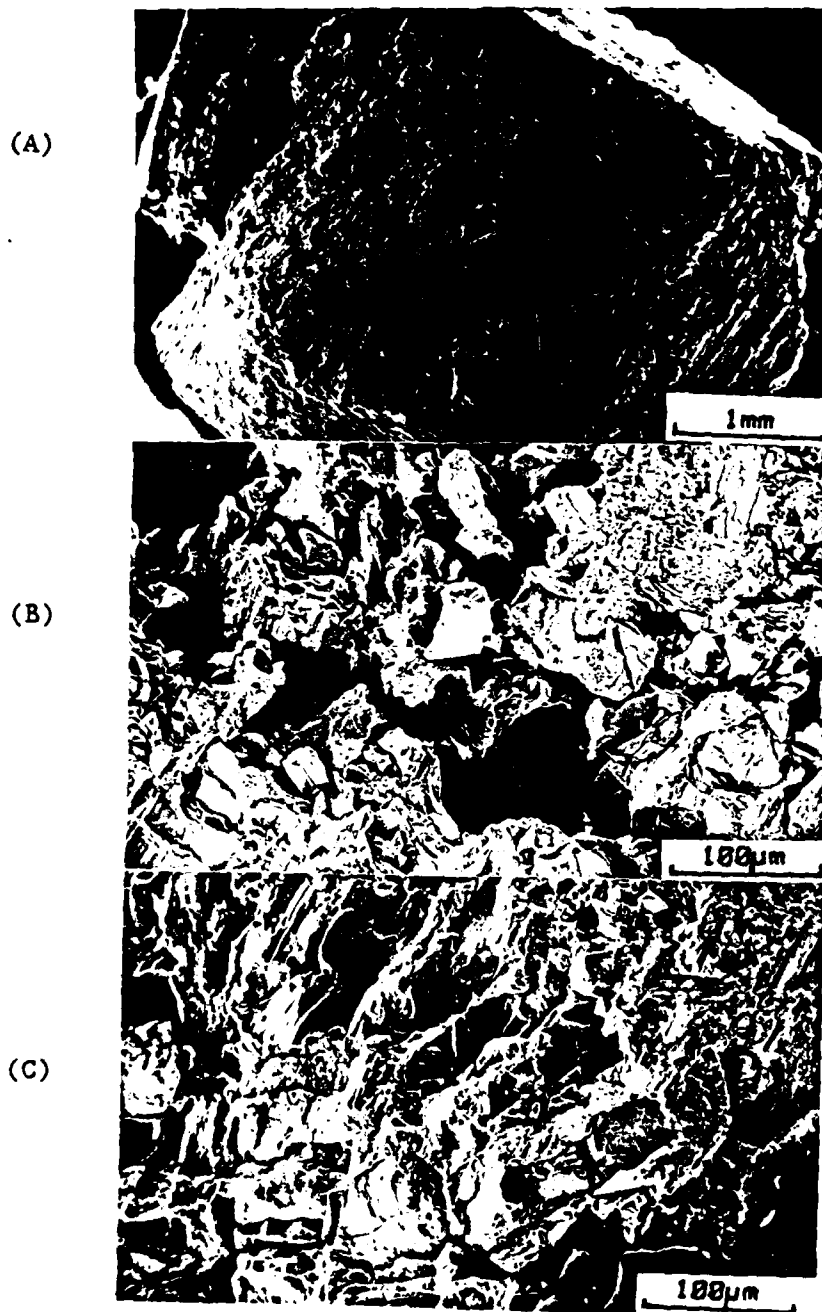


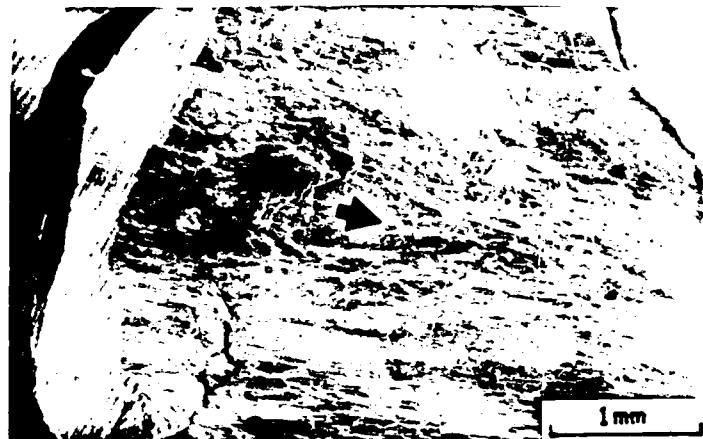
Figure 69. Fracture Features of C-Ti Alloys  
Containing 57% Gamma Phase  
at  $T = 450^{\circ}\text{C}$  (A) Complete Cross Section,  
(B) (C) Higher Magnification

degrees C. All specimens exhibited mixed mode fracture (intergranular and transgranular); but the dominant fracture mode was intergranular. These features indicate that failure occurred along the boundary between Alpha-Ti and Gamma phase.

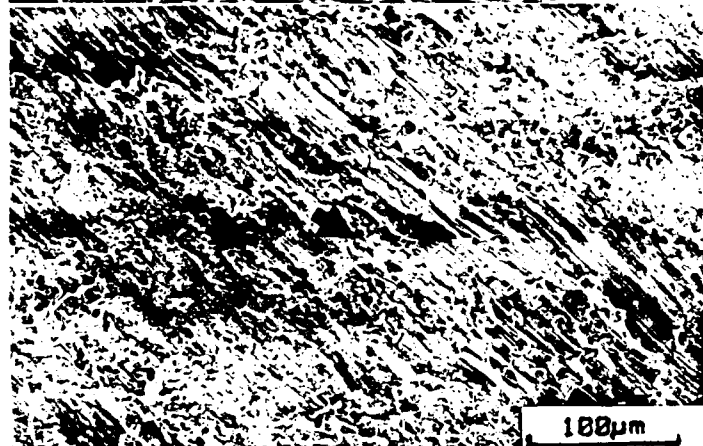
C-Ti alloys containing 10%  
Gamma phase

The fracture features of C-Ti alloys containing 10% Gamma phase are shown in Figures 71 through 74. Only a small amount of cleavage failure and secondary cracking are observed in these specimens. A large amount of smooth slop surface exists in all specimens. The difference between specimens below and above 350 degrees C is that there are several large cracks existing in specimens with temperatures below 350 degrees C.

(A)



(B)



(C)

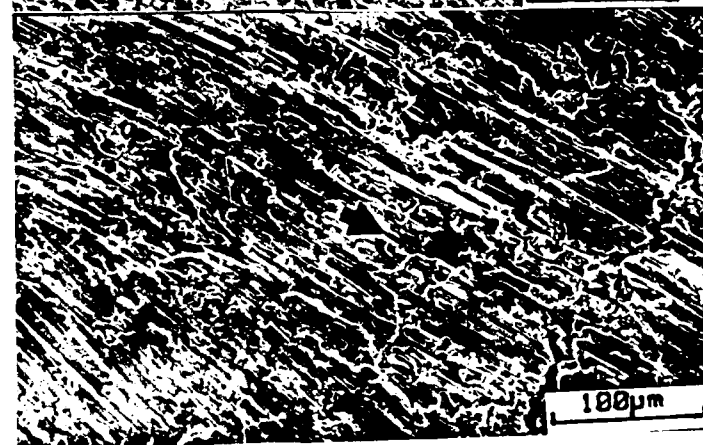


Figure 71. Fracture Features of C-Ti Alloys  
Containing 10% Gamma Phase  
at  $T = 25^{\circ} \text{C}$  (A) Complete Cross Section,  
(B) (C) Higher Magnification

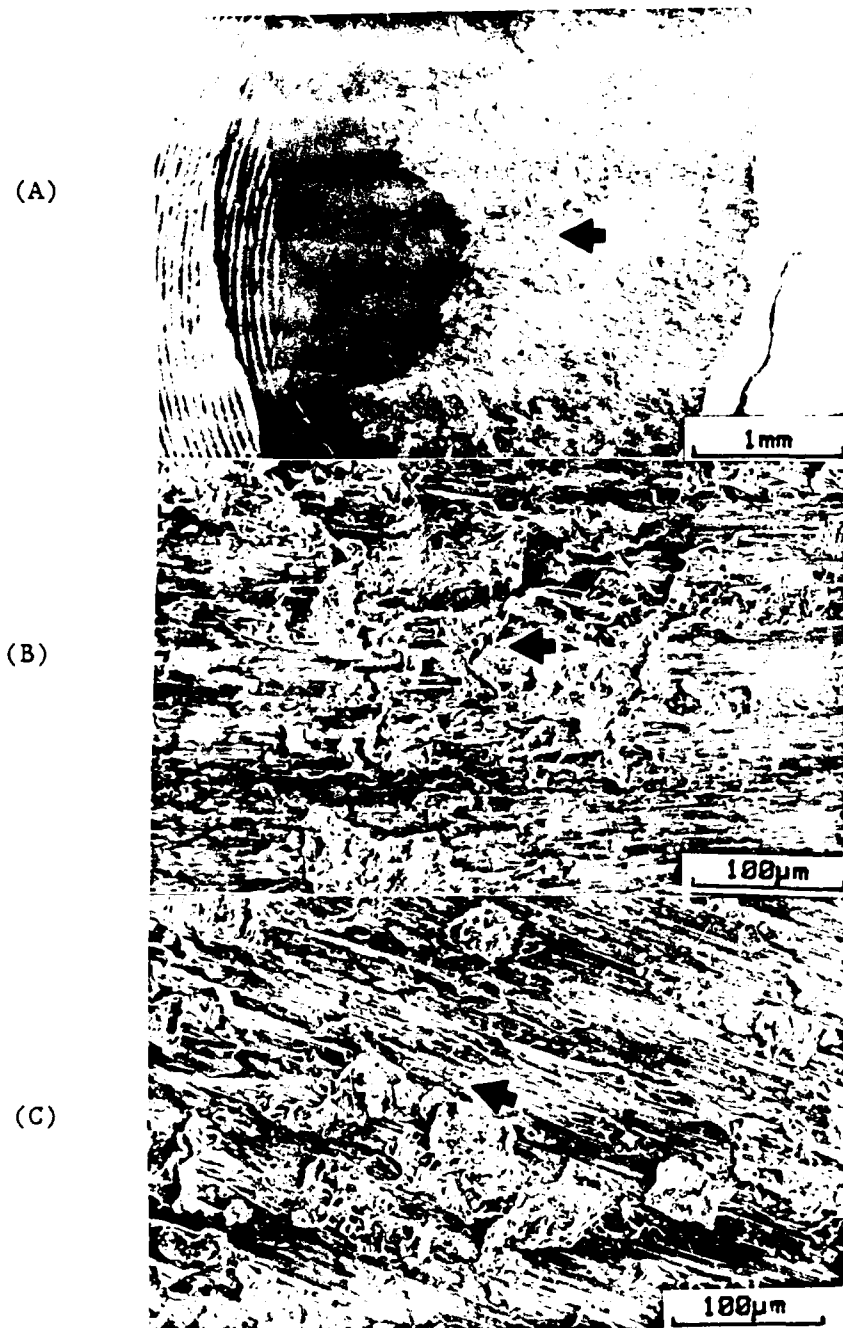


Figure 72. Fracture Features of C-Ti Alloys  
Containing 10% Gamma Phase  
at  $T = 350^{\circ}\text{C}$  (A) Complete Cross Section,  
(B) (C) Higher Magnification

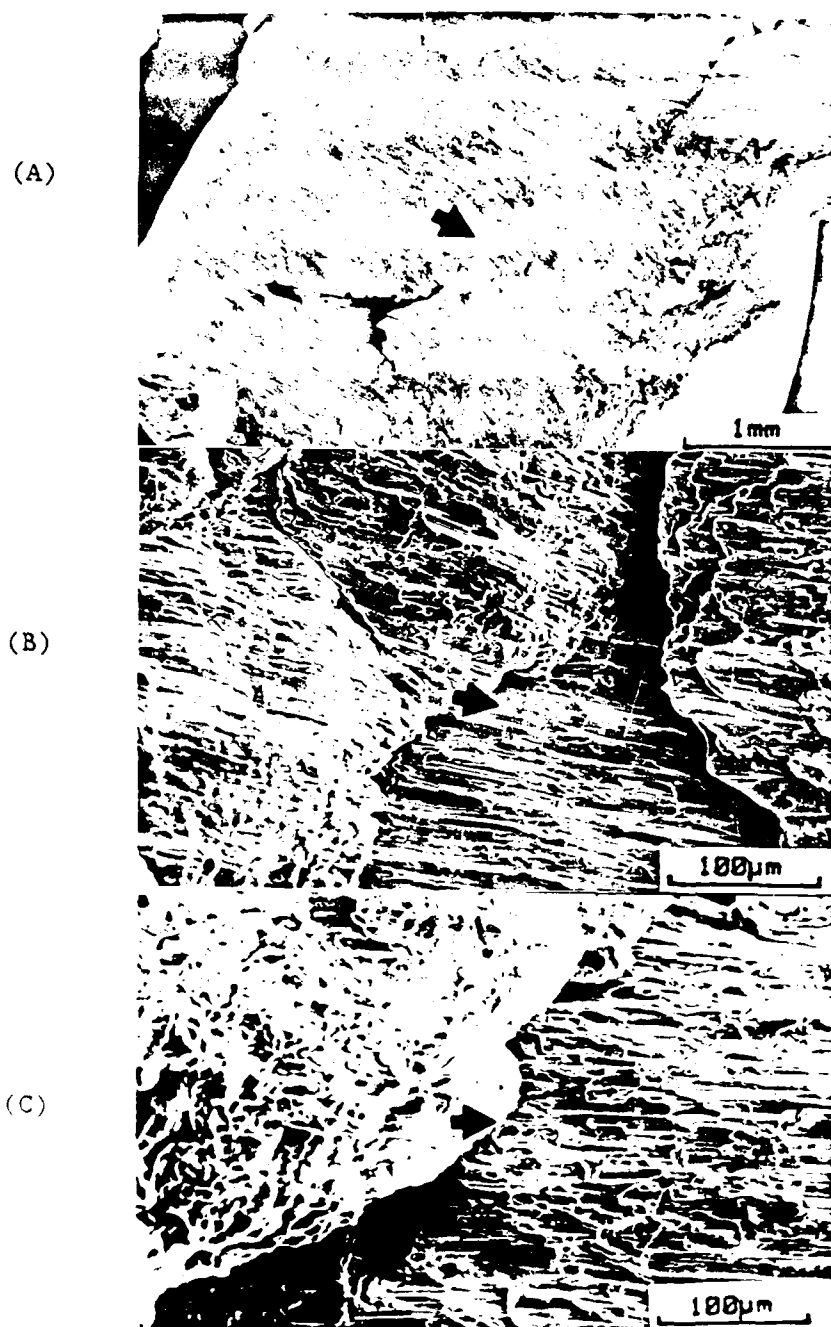


Figure 73. Fracture Features of C-Ti Alloys  
Containing 10% Gamma Phase  
at  $T = 450^{\circ}\text{C}$  (A) Complete Cross Section,  
(B) (C) Higher Magnification

#### IV. DISCUSSION

The microhardness measurements indicate that the strength of C-Ti alloys is dictated by the volume fraction and distribution of Gamma phase. This is consistent with compression test data (Figure 56) that show the yield stress decreases with decreasing volume fraction of Gamma phase at room temperature. This characteristic is similar to the hypothetical model of Lipsitt [67]. The hypothetical model describes that the predominant contribution to the bonding of Gamma phase is from covalent metal-metal bonds and the strength of these bonds. As the carbon contents decreases, the number of these strengthened Ti-Ti bonds decreases and the overall lattice resistance to dislocation movement decreases. From our experimental results, the volume fraction of Gamma phase increases as the carbon contents increases. The true failure strain increases with decreasing volume fraction of Gamma phase. This phenomenon can be explained by the Lipsitt model. The overall lattice resistance to dislocation movement declines with decreasing volume fraction of Gamma phase. Therefore, the mobility of plastic deformation decreases and the ductility decreases as the volume fraction of Gamma phase increases.

The above observations occurred at elevated temperature as well as at room temperature. Figure 60 and 61 display that the yield stress and true maximum flow stress increases with volume fraction of Gamma phase at constant test temperature. Figure 62 exhibits that the true failure strain drops much more sharply at temperatures below 350 degrees C than at temperatures above 350 degrees C. The fractographs display that smooth slip surface exist in C-Ti alloys containing low volume fraction of Gamma phase; the amount of cleavage failure largely increases in C-Ti alloys containing high volume fraction of Gamma phase (test temperature below 350 degrees C). The mobility of dislocation decreases rapidly as test temperature decreases. This information indicates that ductility of C-Ti alloys with high volume fraction of Gamma phase decreases abruptly at test temperature below 350 degrees C.

Compression test results display that the true maximum flow stress decreases with increasing test temperature at constant volume fraction of Gamma phase. This decrease is apparently due to the annealing and recovery of the dislocation structure at elevated temperature resulting in a decreased strain hardening ability of the material. A thermally excited lattice structure assists deformation and reduces strength at elevated temperature. The fractographs show that the amount of secondary cracks increases as test temperature decreases. The amount of secondary cracks that exist is indicative of the amount of energy



expended in the initiation and propagation of these cracks prior to failure. Thus, the yield stress increases as test temperature decreases at constant volume fraction of Gamma phase. The amount of smooth slip surface increases with increasing test temperature. This information indicates that the mobility of dislocations increases as test temperature increases. This phenomenon causes the true failure strain to decrease with decreasing test temperature.

Figure 64 (Y.S. vs  $1/T$ ) denotes a dependence of the yield stress ( $\sigma_y$ ) on temperature. A phenomenological relation commonly used to establish a law governing the deformation behavior is the dependence of the yield stress on temperature, which can be expressed as

$$\sigma_y = A \exp(Q/RT) \quad . . . . . (73)$$

Where A is a constant, R the Universal gas constant, Q an activation energy, and T the absolute temperature. A similar observation was applied to polycrystalline TiC by Lipsitt [68]. Changes in slope were observed in plots of true maximum flow stress, yield stress, and true failure strain vs  $1/T$ . Re-examination of previous data [60,68,70] from both single-crystal and polycrystalline TiC hint the existence of such a change in slope. The observed changes in slope suggest that there is a change in the rate-controlling mechanism of deformation at and above the transition temperature (T.T.). T.T. was found to increase linearly with increasing volume fraction of

Gamma phase. An increase in the volume fraction of Gamma phase increases the number of carbon atoms that will become interstitial atoms in a C-Ti alloy. Ogden [58] indicates that the carbon interstitials in solid solution in titanium cause titanium to undergo a brittle-to-ductile transition. The higher the carbon interstitials content, the higher is the transition temperature. The mechanism which causes the transition temperature to occur in our study is still unclear. It is suggested that transmission electron microscopy be used to examine regions of deformation in the Gamma particles and the grain boundaries to help define the deformation mechanisms and improve the properties of C-Ti alloys. The results of this study suggest the mechanical properties of C-Ti alloys are controlled by two factors, the volume fraction of Gamma phase and test temperature.

To examine the effect of Gamma phase size on the observed properties, the Hall-Petch relation ( $\sigma_y = \sigma_0 + d^{-1/2}$ ) was used. A similar observation was reported by Lipsitt [68] that the dependence of the yield stress on grain size followed a Hall-Petch type relation. This relationship was described in Section III. A plot of  $\sigma_y/d^{-1/2}$  vs Gamma phase fraction is shown in Figure 75. By using a statistical program, the mathematic relation between yield stress, grain size, and volume fraction of Gamma phase was developed. This relation can be expressed as

$$\sigma_y = A(d^{-1/2}) * [\exp(B * X_r)] \quad \text{-----} (74)$$

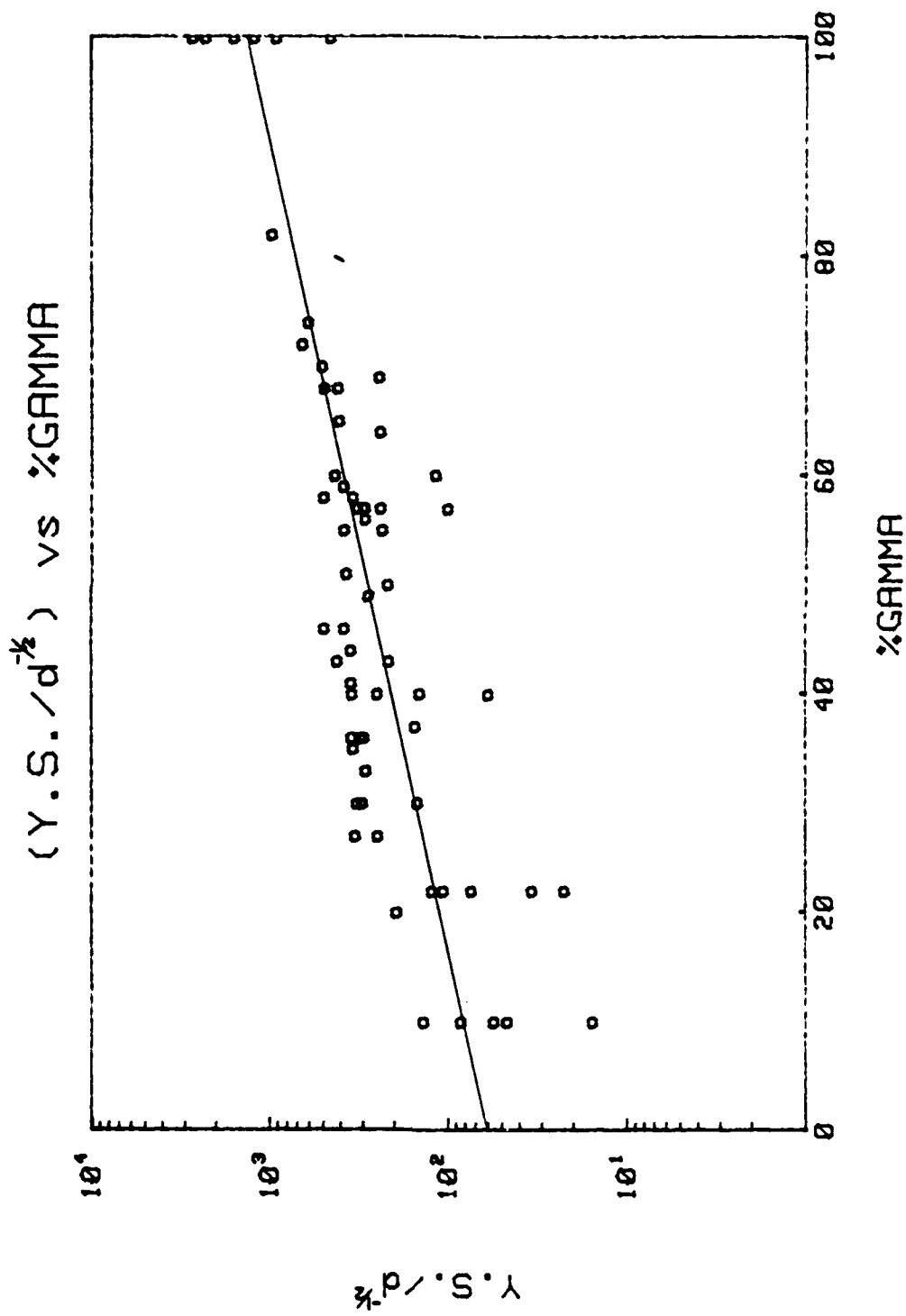


Figure 75. Y.S./d<sup>1/2</sup> as a Function of Volume Fraction of Gamma Phase.

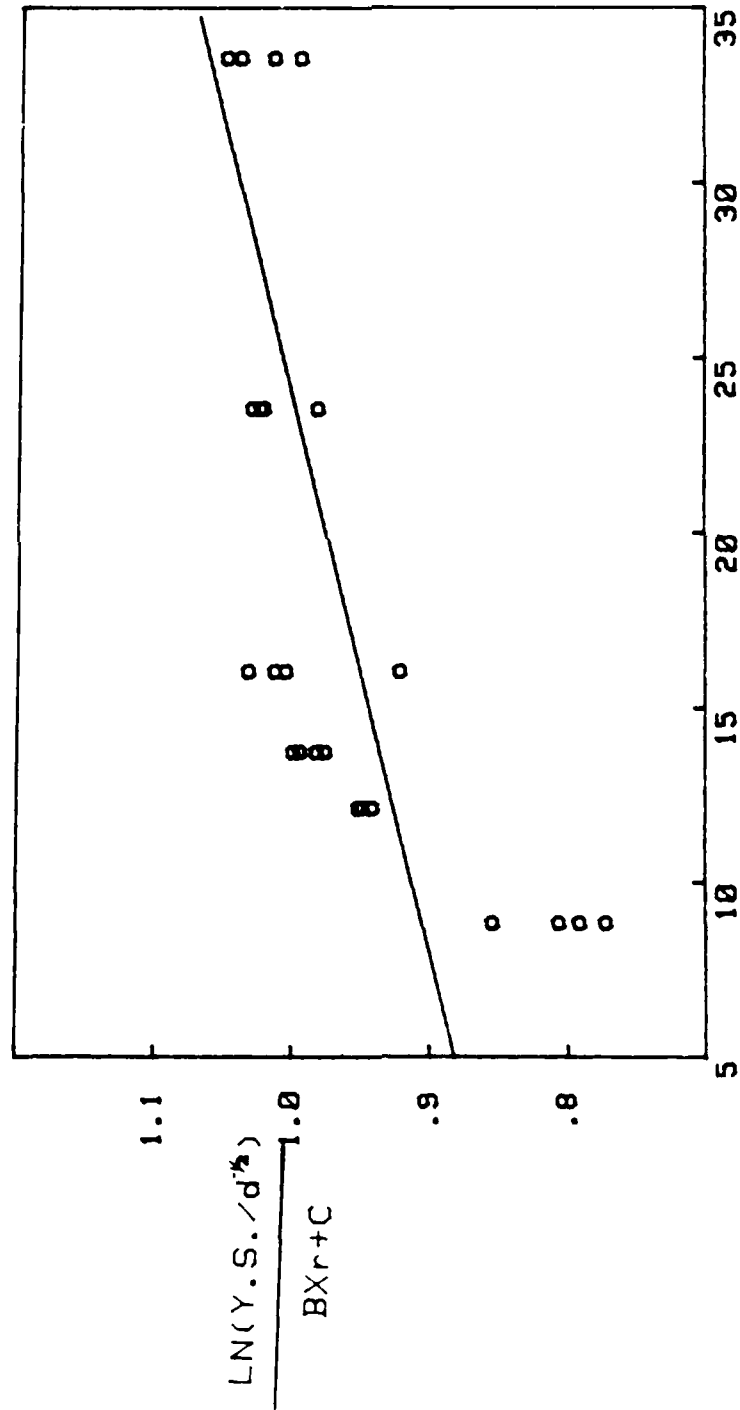
where A and B are constants,  $X_r$  the volume fraction of Gamma phase. Figure 76 is the plot of  $\sigma_y/d^{-1/2}$  as a function of volume fraction of Gamma phase and test temperature.

A unified equation for the dependence of the yield stress on grain size, Gamma phase fraction, and test temperature was developed from equations (73) and (74). The relation can be expressed as

$$\sigma_y = A (d^{-1/2}) * [\exp(B * X_r)] * [\exp(Q/RT)]. \quad \text{---(75)}$$

Equation (75) indicates that we can obtain the yield stress of C-Ti alloys by controlling grain size, volume fraction of Gamma phase, and test temperature.

Heat treatment studies of the alloys is suggested to determine whether inhomogeneities can be eliminated and a single phase Gamma alloy produced with improved ductility. By controlling grain size, volume fraction of Gamma phase, test temperature and reducing the inhomogeneities and porosity it is envisioned that a totally single phase, high carbon content off stoichiometric material can be produced with desired high temperature properties and ductility.



#### IIV. CONCLUSION

The following conclusions were drawn from the experiment and analysis:

- The yield stress increases with increasing volume fraction of Gamma phase.
- The true failure strain decreases as volume fraction of Gamma phase increases.
- The true maximum flow stress and yield stress decreases as the test temperature increases at constant volume fraction of Gamma phase.
- The true failure strain decreases with decreasing test temperature at constant volume fraction of Gamma phase.
- A transition in the controlling deformation mechanism was found to occur over the temperature range of 460°C to 525°C.
- The transition temperature increases linearly with increasing volume fraction of Gamma phase.
- Fracture surfaces shows a mixed mode of failure. Regions of cleavage appear to be the result of failure at the Gamma-Alpha phase boundary.
- A relation between yield stress ( $\sigma_y$ ), grain size ( $d$ ), volume fraction of Gamma phase ( $X_r$ ), and test temperature ( $T$ ) was developed to describe the behavior of all alloys tested

$$\sigma_y = A (d^{-1/2}) * [\exp(B * X_r)] * [\exp(Q/RT)]$$

## REFERENCES

1. F. J. Homann, "Fueled Graphite Development", Gas Cooled Reactor Program, Annual Progress Report, ONRL-5753, August (1981), p. 19.
2. N. S. Stoloff and R. G. David, "The Mechanical Properties of Ordered Alloys, Progress in Material Science, Vol. 13, (1), (1966), p 1.
3. B. H. Kear, C. F. Sims, N. S. Stoloff and J. H. Westbrook, Eds., Ordered Alloys Structure and Physical Metallurgy, Proc. 3rd., Bolton Landing Conf., Lake George, N.Y., Claiter's Pub. Div. (1970).
4. M. A. Krivoglaz and A. A. Smirnov, The Theory of Ordered-Disorder in Alloys, American Elsevier Pub. Co., New York (1964).
5. F. Muto and Y. Takagi, The Theory of Order-Disorder Transformation in Alloys, Academic Press, New York (1956).
6. L. E. Popov and N. A. Koneva, Order Disorder Transformation in Alloys, J. Warlimont, Ed., Springer-Verlag, New York (1974), p. 404.
7. M. J. Marcinkowski, Order Disorder Transformations in Alloys, J. Warlimant, Ed., Springer-Verlag, New York (1974), p. 364.
8. A. E. Vidoz, D. P. Lazarenio and R. W. Chan, Acta Met, Vol. 11 (1963), p. 17.
9. B. H. Kear and H. Wilsdorf, Trans AIME, Vol. 224 (1962), p. 382.
10. R. C. Boettner, N. S. Stoloff and R. G. Davis, Trans AIME, Vol. 236 (1966), p. 131.
11. E. M. Schulson, "Order Strengthening as a Method for Reducing Irradiation Creep: An Hypothesis", Journal of Nuclear Materials, Vol. 66, (1977), p. 322.
12. C. T. Liu, "Development of Iron-Base Alloys with Long Range Ordered Crystal Structure", ADIP Quarterly Progress Report, Doe/er-0045/1, April (1980), p. 72.

13. D. N. Braski, "Resistance of  $(\text{Fe,Ni})_3\text{V}$  Long Range Ordered Alloys to Radiation Damage", Alloy Development for Irradiation Performance, Proceedings of DOE Program Review Meeting, Sept. 30 - Oct. 1 (1980), p. 367.
14. R. W. Carpenter and E. A. Kenik, "Stability of Chemical Order in NiMo Alloy Under Fast Electron Irradiation", in Proceedings of 35th Electron Microscopy Society, Claitor's Publishing, Baton Rouge, LA. (1977).
15. G. J. E. Carpenter and E. M. Schulson, J. Nuclear Materials, Vol. 23 (1978), p. 180.
16. E. M. Schulson, J. Nuclear Material, Vol. 56 (1975), p. 38.
17. E. M. Schulson and M. H. Stewart, Met Trans B., Vol. 78 (1976), p. 363.
18. L. E. Tranner, P. Stark, E. T. Petters, J. J. Ryan, I. Vilks, and S. V. Radcliffe, AST-TDR62-1087 Man Labs Inc., Cambridge, MA (1963).
19. D. T. Liu, "Development of Long Range Ordered Alloys", Alloy Development for Irradiation Performance, Proceedings of Program Review Meeting, Sept. 30 - Oct. 1. (1980), p. 354.
20. C. T. Liu and H. Imouye, "Control of Ordered Structure and Ductility of  $(\text{Fe,Co,Ni})_3\text{V}$  Alloys", Met. Trans A., Vol. 10 (1979), p. 1515.
21. C. T. Liu, "Development of Alloys with Long Range Order", ADIP Quarterly Progress Report, DOE/ET-0058/1, Aug. (1978).
22. M. Hansen, Constitution of Binary Alloys, McGraw-Hill, New York (1958), p. 370.
23. T. Lyman, ed., "Metallography, Structures and Phase Diagrams", Metals Handbook, Vol. 8, p. 279.
24. R. Kikuchi, Acta Metall. Vol. 25 (1977), p. 195.
25. G. Tammann, Z. anorg. Chem. (1919), p. 107.
26. T. Muto and Y. Takagi, The Theory of Order-Disorder Transition in Alloys, Academic Press, New York, Solid State Reprints. (1955).



27. W. L. Bragg, and E. J. Williams, Proc. Roy. Soc. Vol. A145 (1934); p. 699; Vol. A151 (1935); p. 540; E. J. Williams, Proc. Roy. Soc., Vol. A152 (1935), p. 231.
28. H. Bethe, Proc. Roy. Soc. Vol. A150 (1935), p. 552.
29. J. G. Kirkwood, J. Chem. Phys. Vol. 6 (1938), p. 70.
30. E. A. Guggenheim, Proc. Roy. Soc. Vol. A148 (1935), p. 304.
31. R. H. Fowler and E. A. Guggenheim, Proc. Roy. Soc., Vol. A174 (1940), p. 189, E. A. Guggenheim, Proc. Roy. Soc., Vol. A184 (1944), p. 221.
32. Y. Takagi, Proc. Phys-Math., Soc. Japan, Vol. 23 (1941), p. 44.
33. R. Kikuchi, Phys. Rev., Vol. 81 (1951), p. 988.
34. C. N. Yang, J. Chem. Phys. Vol. 13 (1945), p. 66; C. N. Yang and Y. Y. Li, Chinese Phys. Vol. 7 (1947), p. 59; Y. Y. Li, J. Chem. Phys., Vol. 17 (1949), p. 447.
35. T. L. Hill, J. Chem. Phys. Vol. 18 (1950), p. 988.
36. A. G. Khachaturyam, Physics Metals Mettlog. Vol. 13, (1962), p. 493; Sov. Phys. Solids St. Vol. 5 (1963), p. 16; Sov. Phys. Solid St., Vol. 5 (1963), p. 548.
37. R. C. Kittler and L. M. Falicov, Phys. Rev. B, Vol. 18 (1978), p. 2506.
38. L. D. Fosdick, Phys. Rev. Vol. 116 (1959), p. 565.
39. R. Kikuchi, J. of Chem. Phys, Vol. 60 (1974) p. 1071.
40. M. Kurata and R. Kikuchi, J. Chem. Phys., Vol. 21 (1953), p. 434.
41. N. S. Golosov, L. E. Popov, L. W. Pudan, J. Phys. Chem. Solids, Vol. 34 (1973), p. 1149, p. 1157.
42. R. Kikuchi, Acta Metallurgica, Vol. 25 (1977), p. 195.
43. S. M. Shapiro, SD Axe, G. Shifame, Phys. Rev. B. Vol. 6 (1972), p.4332.
44. L. D. Landau, Sov. Phys., Vol. 11 (1937), p. 26, p. 545.
45. E. M. Lifshitz, Fig. Zh. Vol. 7 (1942), p. 61, p. 251.

46. A. G. Khachaturyan, Progress in Materials Science, Vol. 22 (1978), p. 1.
47. L. Guttman, J. Chem. Phys, Vol. 34 (1961), p. 1024.
48. P. C. Clapp in Long Range Order in Solids, Academic Press Inc.
49. P. C. Clappy, Phy. Rev. Letters, Vol. 16 (1966), p. 687.
50. J. Friedel, Phil. Mag. Vol. 43 (1952), p. 153.
51. J. S. Langer and S. H. Vosko, J.P.C.S., Vol 12 (1959), p. 186
52. A. J. Harrison and A. Paskin, J. Phys. Soc. Japan, Vol. 15 (1960). p. 1902.
53. F. Ducastelle and F. Gautier, J. Phys. F., Vol 6 (1976), p. 2039.
54. T. L. Cottrell, The Strenght of Chemical Bonds, Buttrworths Scientific Publ., London (1854).
55. V. I. Vedeneyen, et al., Bond Energies, Ionization Potentials and Electron Affinities. Edward Arnold Publ. LTD, London (1966).
56. Handbook of Chemistry and Physics, 66th ed. (1985-1986), pp. F-174, F-179.
57. Irving Cadoff and John P. Nielson, J. of Metals, Feb. (1953), pp. 248-252.
58. F. C. Wanger, E. J. Bucur and M. A. Steinberg, "The Rate of Diffusion of Carbon In Alpha and Beta Titanium", Trans. of The ASM (1956), pp. 742-761.
59. H. R. Odgen, R. I. Jaffee and F. C. Holden, Trans. AIME, Journal of Metals, Jan. (1955), pp. 73-80.
60. W. S. Williams and R. D. Schaal, "Elastic Deformation, Plastic Flow, and Dislocations in Single Crystals of Titanium Carbide," Journal of Applied Physics, Vol. 33, No. 3, March (1962), pp. 955-962.

61. D. K. Chatterjee, M. G. Mendiratta and H. A. Lipsitt, "Deformation Behavior of Single Crystals of Titanium Carbide," Journal of Materials Science, 14 (1979), pp. 2151-2156.
62. Y. Kumashiro, A. Itoh, T. Kinoshita and M. Sobajima, "The Micro-Vickers Hardness of TiC Single Crystals Up To 1500°C," Journal of Materials Science, 12 (1977), pp. 595-601.
63. D. J. Rowcliffe and G. E. Hollox, "Plastic Flow and Fracture of Tantalum Carbide and Hafnium Carbide at Low Temperatures," Journal of Materials Science, 6 (1971), pp. 1261-1269.
64. W. S. Williams, "Influence of Temperature, Strain Rate, Surface Condition, and Composition on the Plasticity of Transition-Metal Carbide Crystals," J. of Applied Physics, Vol. 35, No. 4, April (1964), pp. 1329-1338.
65. F. Keihn and R. Kebler, "High-Temperature Ductility of Large-Grained TiC," J. Less-Common Metals, Union Carbide Research Inst., Tarrytown, NY, 6 (1964), pp. 484-485.
66. A. P. Katz, H. A. Lipsitt, T. Mah and M. G. Mendiratta, "Mechanical Behavior of Polycrystalline TiC," J. of Materials Science, 18 (1983), pp. 1983-1992.
67. D. B. Miracle, H. A. Lipsitt, "Mechanical Properties of Fine-Grained Substoichiometric Titanium Carbide," J. of the American Ceramics Society, Vol. 66, No. 8 (1982), pp. 592-596.
68. G. Das, K. S. Mazdiasni and H. A. Lipsitt, "Mechanical Properties of Polycrystalline TiC," J. Amer. Ceramic Soc., Vol. 65 (1982), pp. 104-110.
69. E. O. Hall, "The Deformation and Aging of Mild Steel: I," Proc. Phys. Soc., Sec. B, 64 (1951), pp. 747-753.
70. A. Kelly and D. J. Rowcliffe, "Deformation of Polycrystalline Transition Metal Carbides," J. Ame. Ceramic Soc., 50[5] (1967), pp. 253-256.
71. ASm Metal Handbook, Vol. 8, 9th ed., p. 382
72. ASM Metal Handbook, Vol. 2, 9th ed., pp. 814-816.
73. C. Severac, C. Quesne et P. Lacombe, "Comportement Mécanique en Traction et en Fluage du Titane Commercial T

40 Entre 25<sup>0</sup>C et 600<sup>0</sup>C," J. of the Less-Common Metal, Vol.  
56 (1977), pp. 253-261.

APPENDICES

APPENDIX A

DIMENSIONAL MEASUREMENTS OF COMPRESSION SPECIMENS

Specimen	Gage Length (inches)	Diameter	Cross Section Area (in <sup>2</sup> )
W1	.285	.172	.023
W2	.274	.173	.023
W3	.265	.170	.023
W4	.274	.172	.023
I1	.271	.175	.024
I2	.272	.179	.025
I3	.274	.176	.024
I4	.263	.174	.024
I5	.259	.165	.021
I6	.273	.172	.023
I7	.254	.170	.023
I8	.260	.172	.023
I9	.260	.180	.025
I10	.264	.170	.022
I11	.275	.175	.024
I12	.269	.172	.023
I13	.253	.179	.024
I14	.269	.172	.023
I15	.264	.173	.024
I16	.273	.175	.024

(Continued)

Specimen	Gage Length	Diameter	Cross Section Area
	(inches)		(in <sup>2</sup> )
I17	.268	.172	.023
I18	.283	.171	.023
I19	.278	.159	.020
I20	.261	.175	.024
I21	.260	.172	.023
I22	.268	.170	.023
I23	.272	.170	.023
I24	.274	.168	.022
I25	.269	.173	.023
I26	.276	.172	.023
I27	.279	.159	.020
I28	.278	.167	.022
HA1	.258	.173	.024
HA2	.279	.174	.024
HA3	.273	.169	.022
HA4	.298	.172	.023
HA5	.273	.174	.024
HB1	.296	.168	.022
HB2	.286	.171	.023
HB3	.256	.158	.022



(Continued)

Specimen	Gage Length	Diameter	Cross Section Area
	(inches)		(in <sup>2</sup> )
HB4	.266	.171	.023
HB5	.265	.175	.024
HB6	.276	.165	.021
HB7	.25	.171	.023
HC1	.256	.171	.023
HC2	.293	.172	.023
HC3	.256	.162	.021
HC4	.260	.172	.023
HC5	.281	.173	.023
HC6	.272	.169	.023
HC7	.286	.171	.023
HD1	.242	.173	.024
HD2	.291	.174	.024
HD3	.282	.172	.023
HD4	.277	.175	.024
HD5	.252	.173	.023
HD6	.282	.172	.023
HD7	.293	.174	.024
HE1	.268	.172	.023
HE2	.270	.174	.024

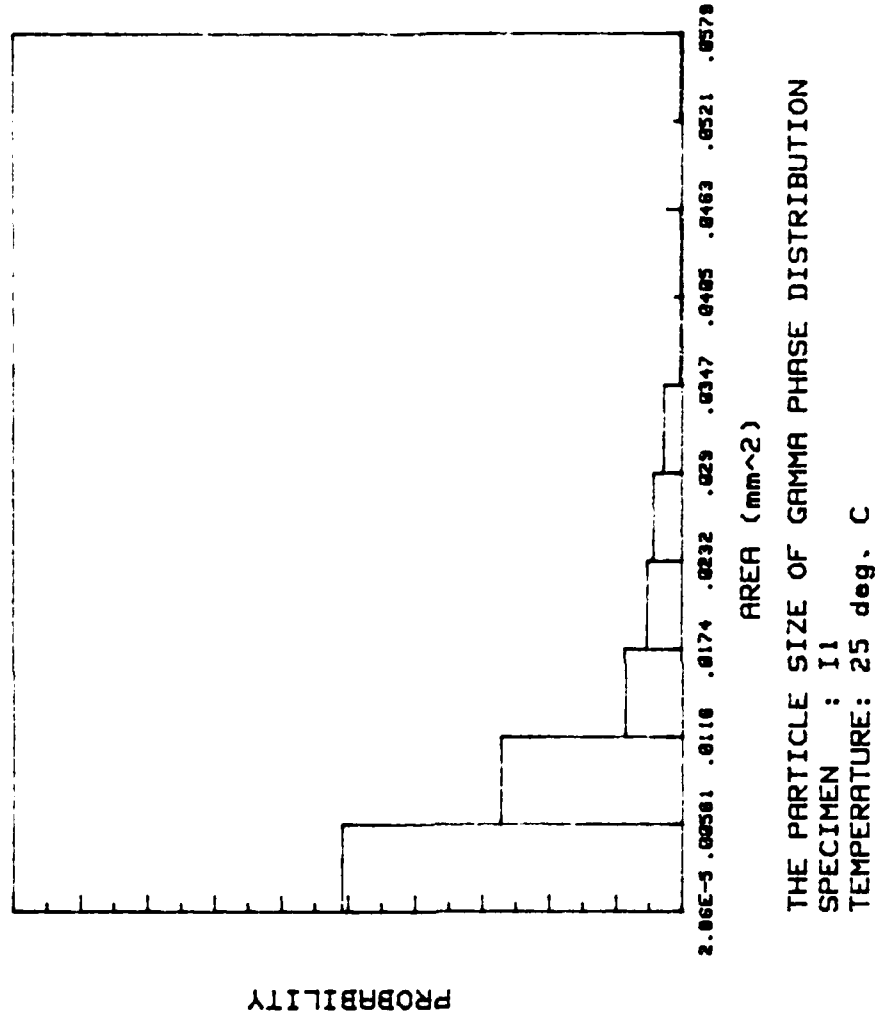
(Continued)

Specimen	Gage Length	Diameter	Cross Section Area
	(inches)		(in <sup>2</sup> )
HE3	.281	.180	.025
HE4	.287	.168	.022
HE5	.288	.170	.023

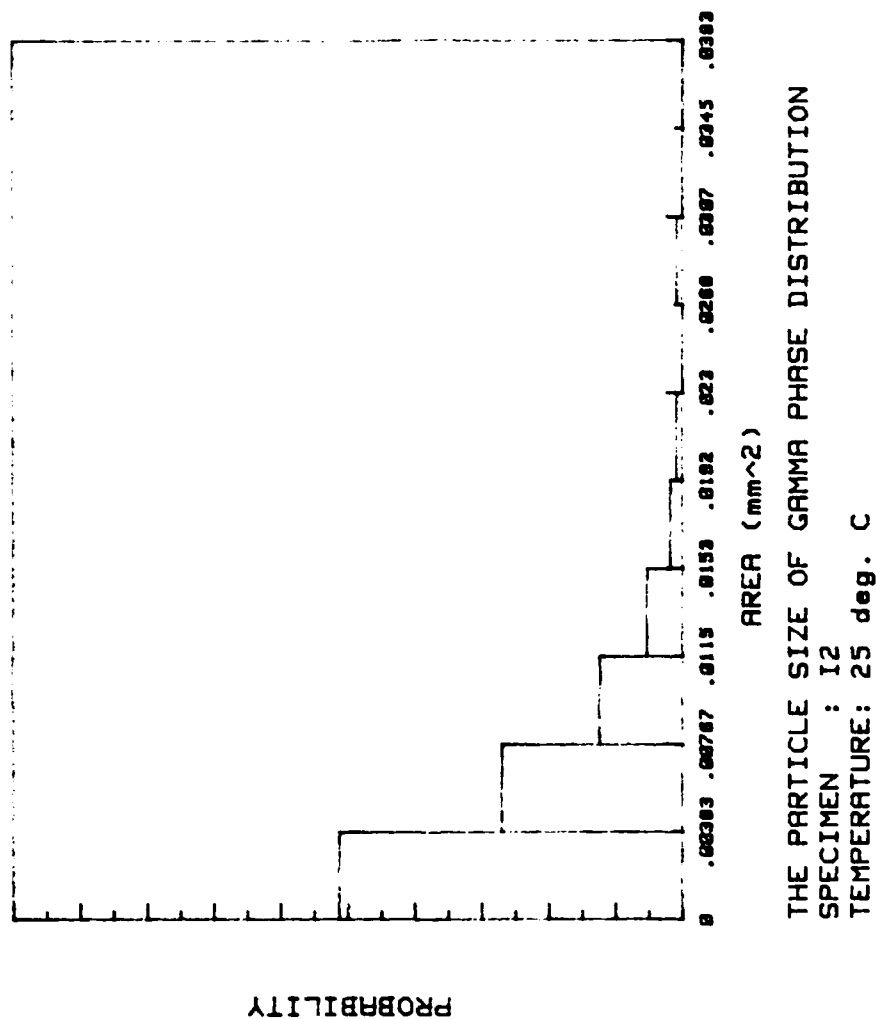
APPENDIX B

GAMMA PHASE PARTICLE DISTRIBUTION FOR

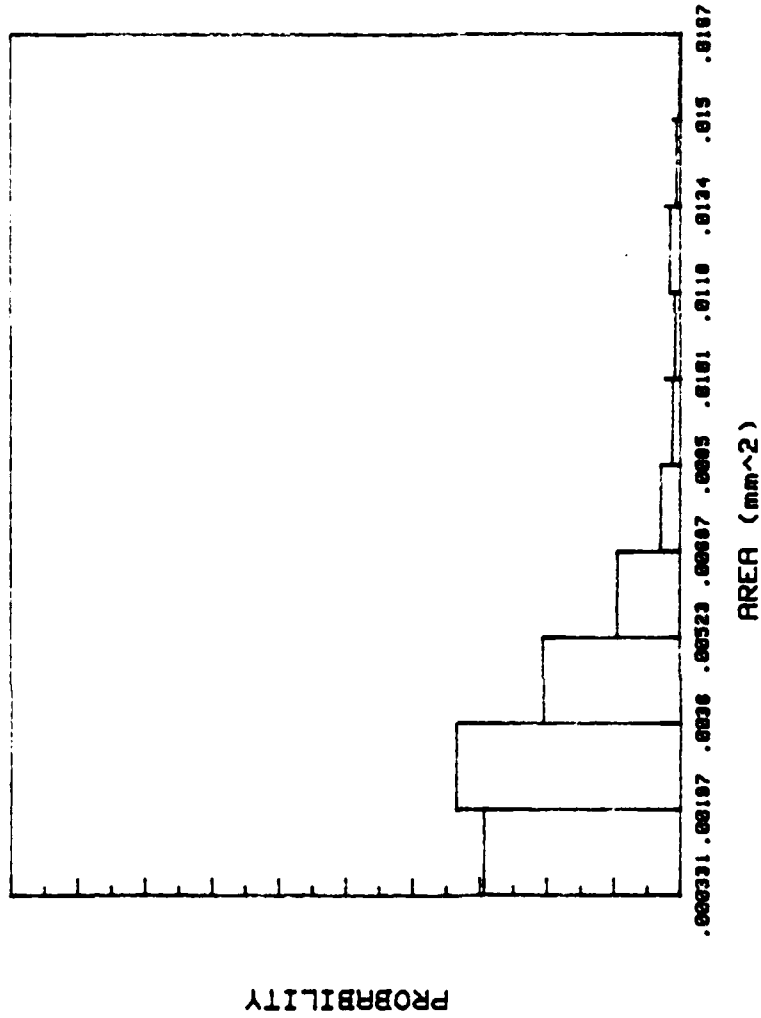
ALL COMPRESSION SPECIMENS

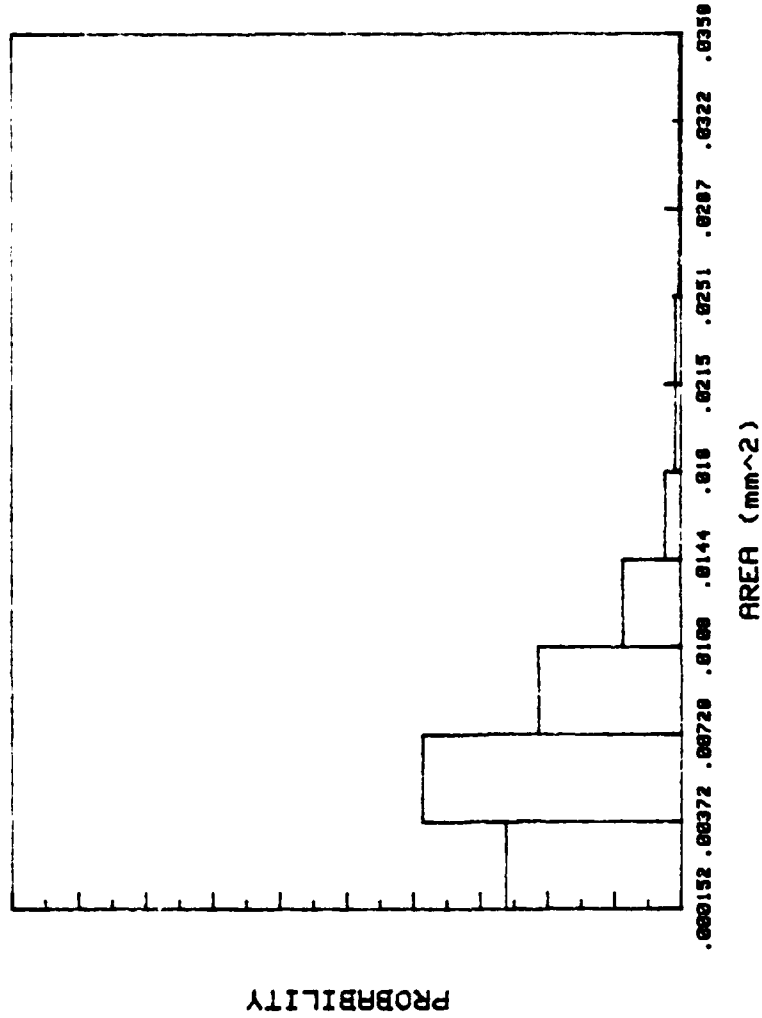


PARTICLE FRACTION : 49.29 %  
Alpha-T1 PHASE FRACTION : 50.71 %  
TOTAL PARTICLE NO. : 328  
AVERAGE OF AREA: .008312794 (mm<sup>2</sup>)



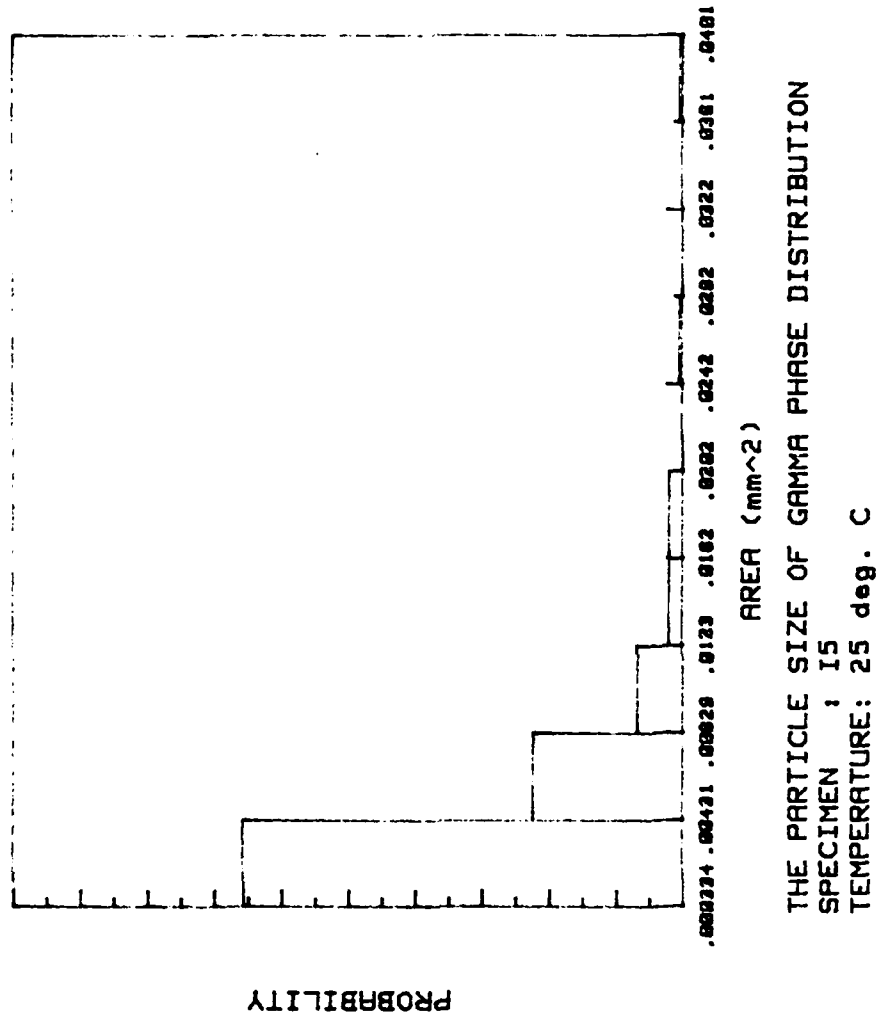
PARTICLE FRACTION : 43.35 %  
 Alpha-11 PHASE FRACTION : 56.65 %  
 TOTAL PARTICLE NO. : 340  
 AVERAGE OF AREA: .006525633 (mm<sup>2</sup>)





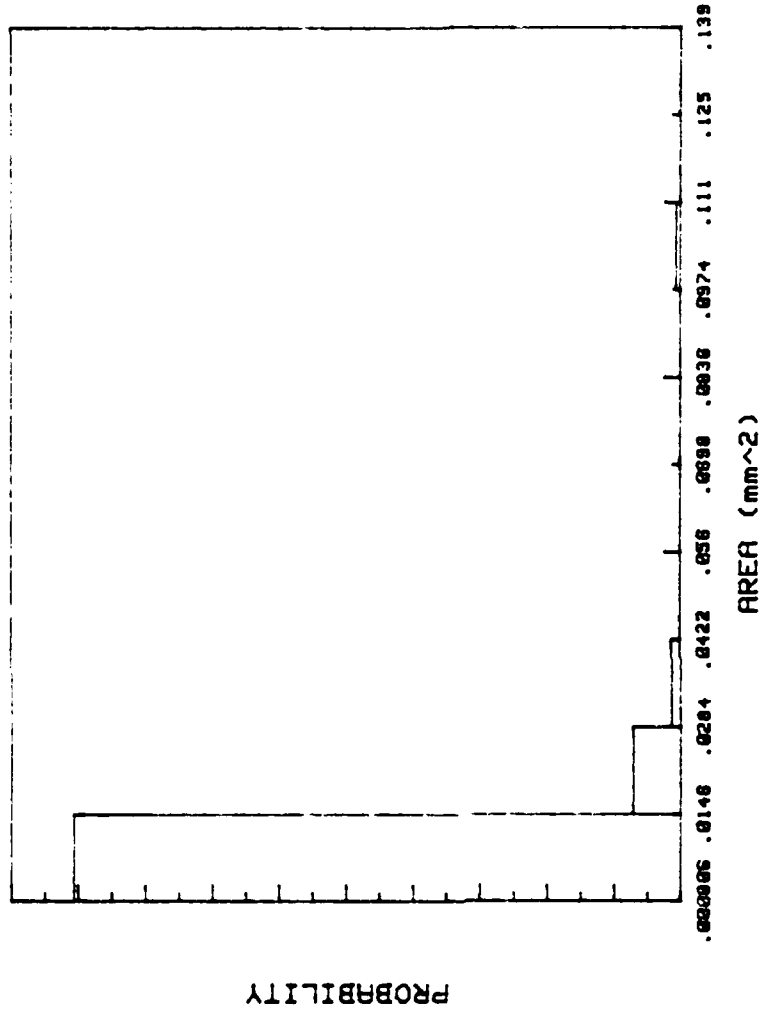
THE PARTICLE SIZE OF GAMMA PHASE DISTRIBUTION  
SPECIMEN : 14  
TEMPERATURE: 25 deg. C

PARTICLE FRACTION : 41.29 %  
ALPHA-11 PHASE FRACTION : 58.71 %  
TOTAL PARTICLE NO. : 347  
AVERAGE OF AREA: .006694694 (mm<sup>2</sup>)



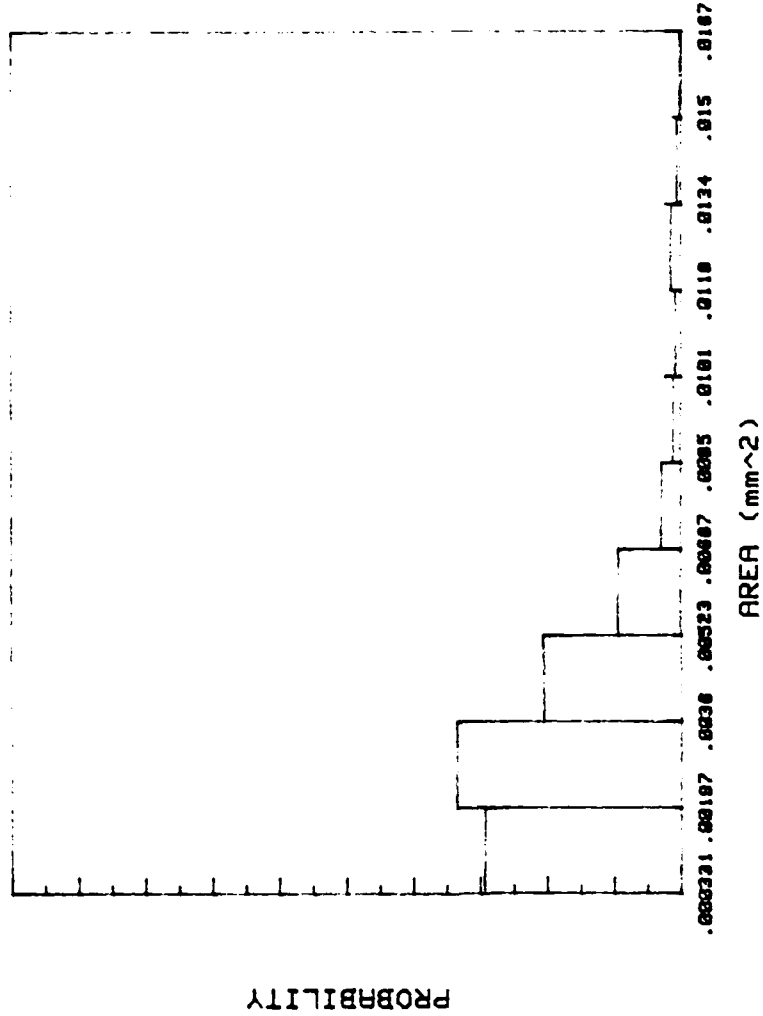
PARTICLE FRACTION : 55.08 %  
 ALPHA-T1 PHASE FRACTION: 44.92 %  
 TOTAL PARTICLE NO. : 358  
 AVERAGE OF AREA: .004338331 (mm<sup>2</sup>)





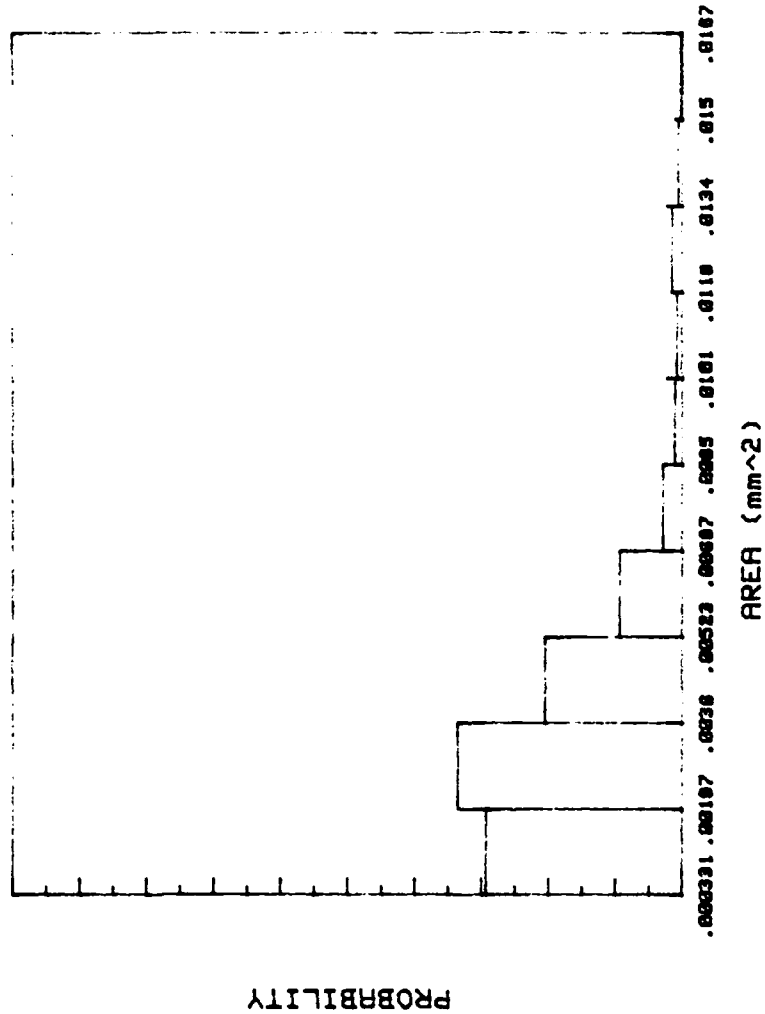
THE PARTICLE SIZE OF GAMMA PHASE DISTRIBUTION  
 SPECIMEN : 16  
 TEMPERATURE: 25 deg. C

PARTICLE FRACTION : 46.25 %  
 Alpha-T1 PHASE FRACTION : 53.75 %  
 TOTAL PARTICLE NO. : 310  
 AVERAGE OF AREA: .00840378 (mm<sup>2</sup>)



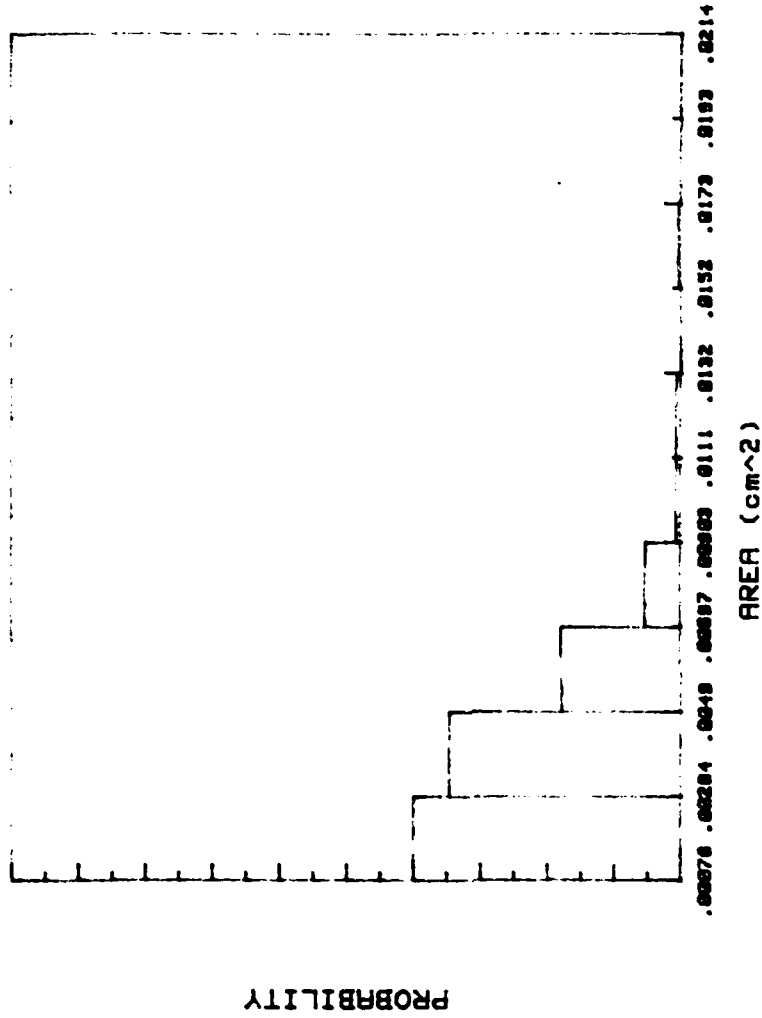
THE PARTICLE SIZE OF GAMMA PHASE DISTRIBUTION  
 SPECIMEN : I7  
 TEMPERATURE: 25 deg. C

PARTICLE FRACTION : 36.12 %  
 ALPHA-1 PHASE FRACTION : 63.88 %  
 TOTAL PARTICLE NO. : 480  
 AVERAGE OF AREA: .004023645 (mm<sup>2</sup>)



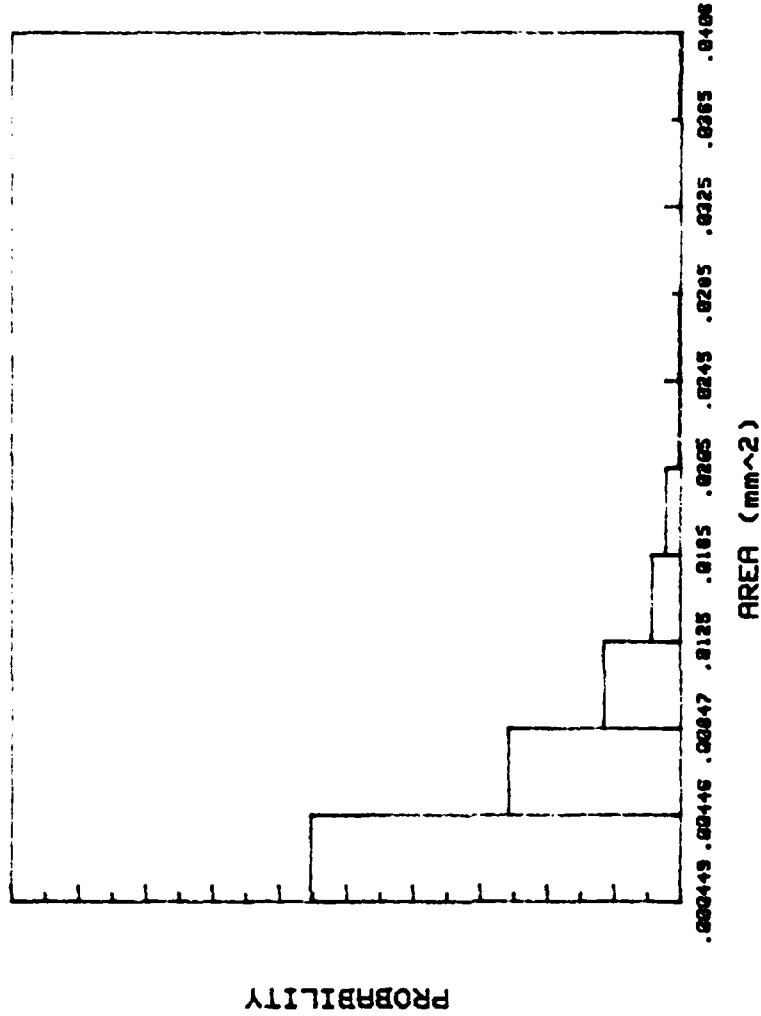
THE PARTICLE SIZE OF GAMMA PHASE DISTRIBUTION  
 SPECIMEN : 18  
 TEMPERATURE: 25 deg. C

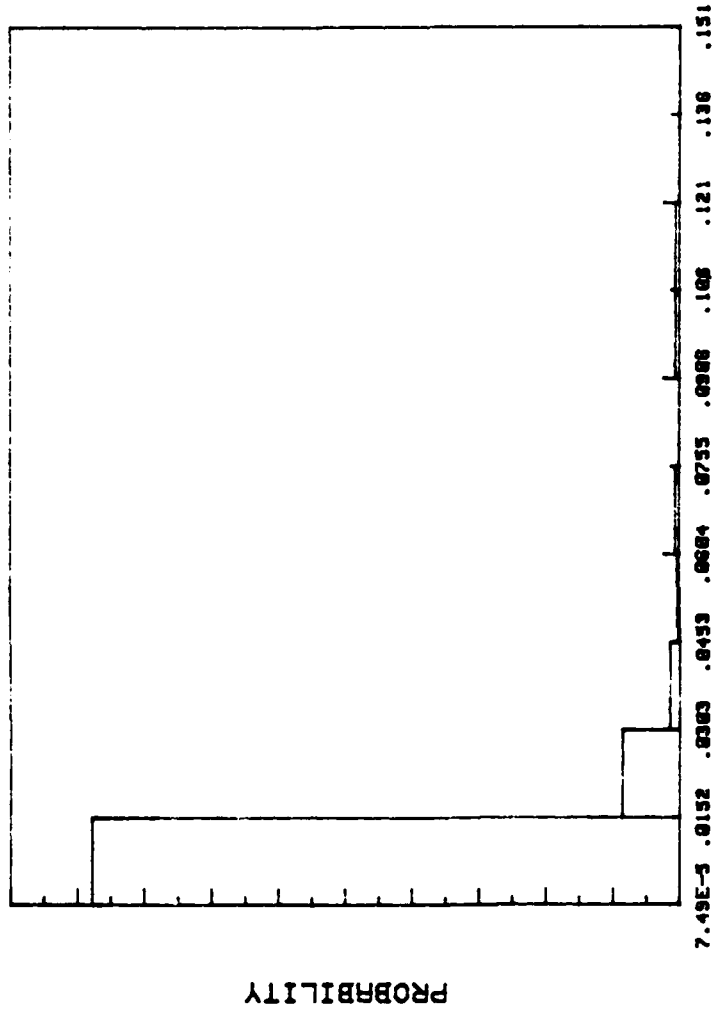
PARTICLE FRACTION : 38.79 %  
 Alpha-T1 PHASE FRACTION : 61.21 %  
 TOTAL PARTICLE NO. : 446  
 AVERAGE OF AREA: .004105641 (mm<sup>2</sup>)



THE PARTICLE SIZE OF GAMMA PHASE DISTRIBUTION  
SPECIMEN : 19  
TEMPERATURE: 25 deg. C

PARTICLE FRACTION : 67.63 %  
Alpha-Ti PHASE FRACTION : 32.37 %  
TOTAL PARTICLE NO. : 301  
AVERAGE OF AREA: .004473999 (cm<sup>2</sup>)





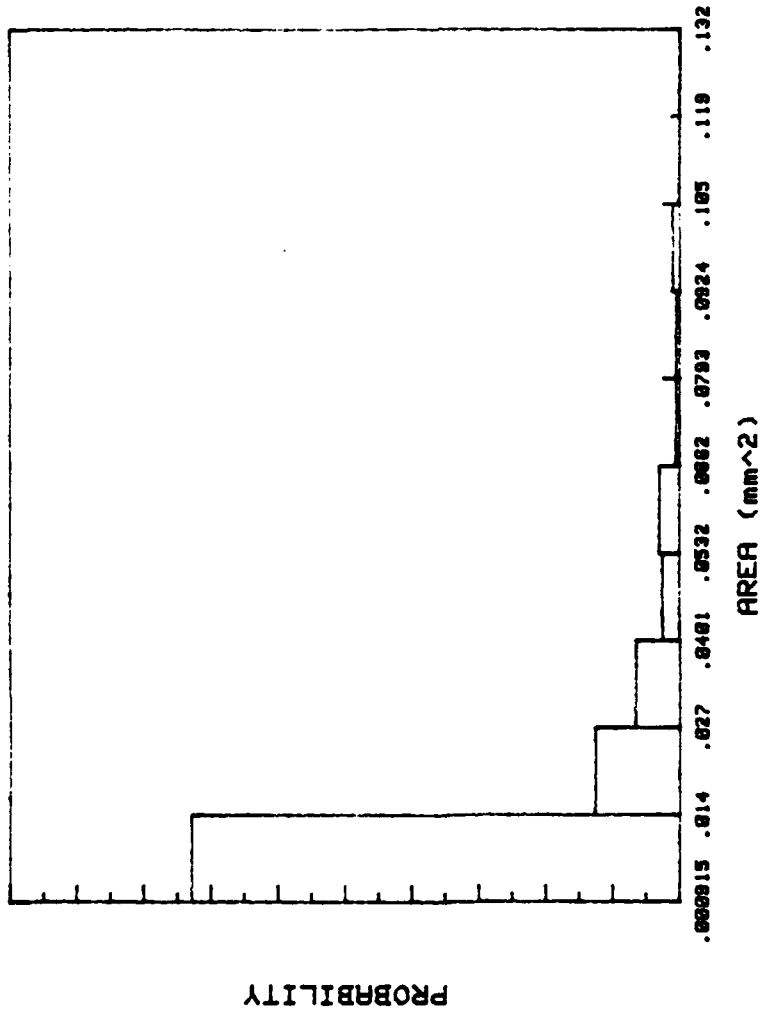
AREA (mm<sup>2</sup>)

THE PARTICLE SIZE OF GAMMA PHASE DISTRIBUTION

SPECIMEN : I11

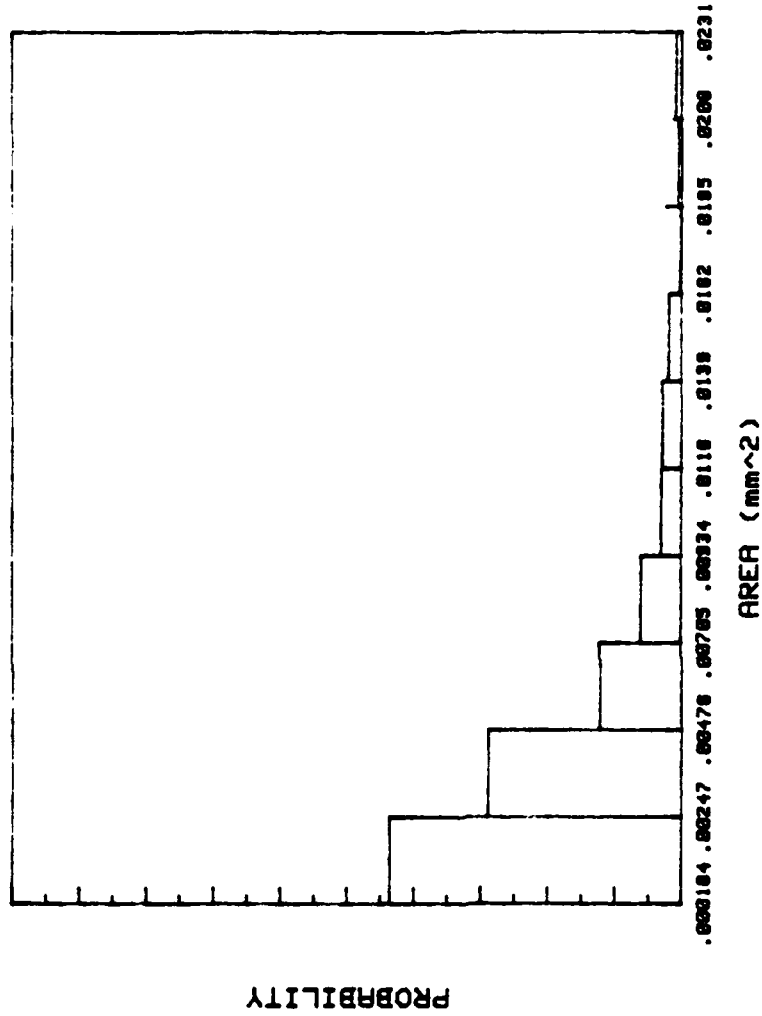
TEMPERATURE: 25 deg. C

PARTICLE FRACTION : 70.48 %  
 Alpha-Ti PHASE FRACTION : 29.52 %  
 TOTAL PARTICLE NO. : 353  
 AVERAGE OF AREA: .009659743 (mm<sup>2</sup>)



THE PARTICLE SIZE OF GAMMA PHASE DISTRIBUTION  
 SPECIMEN : I12  
 TEMPERATURE: 25 deg. C

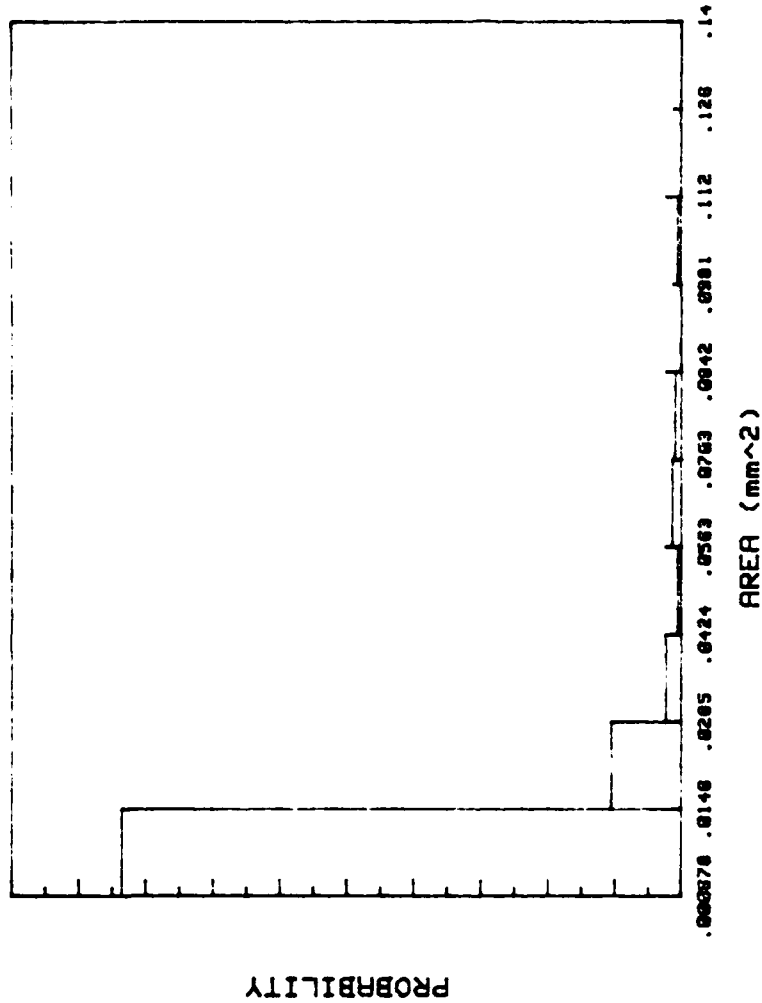
PARTICLE FRACTION : 35.84 %  
 Alpha-T1 PHASE FRACTION : 64.16 %  
 TOTAL PARTICLE NO. : 199  
 AVERAGE OF AREA: .01700092 (mm<sup>2</sup>)



THE PARTICLE SIZE OF GAMMA PHASE DISTRIBUTION  
SPECIMEN : I13  
TEMPERATURE: 25 deg. C

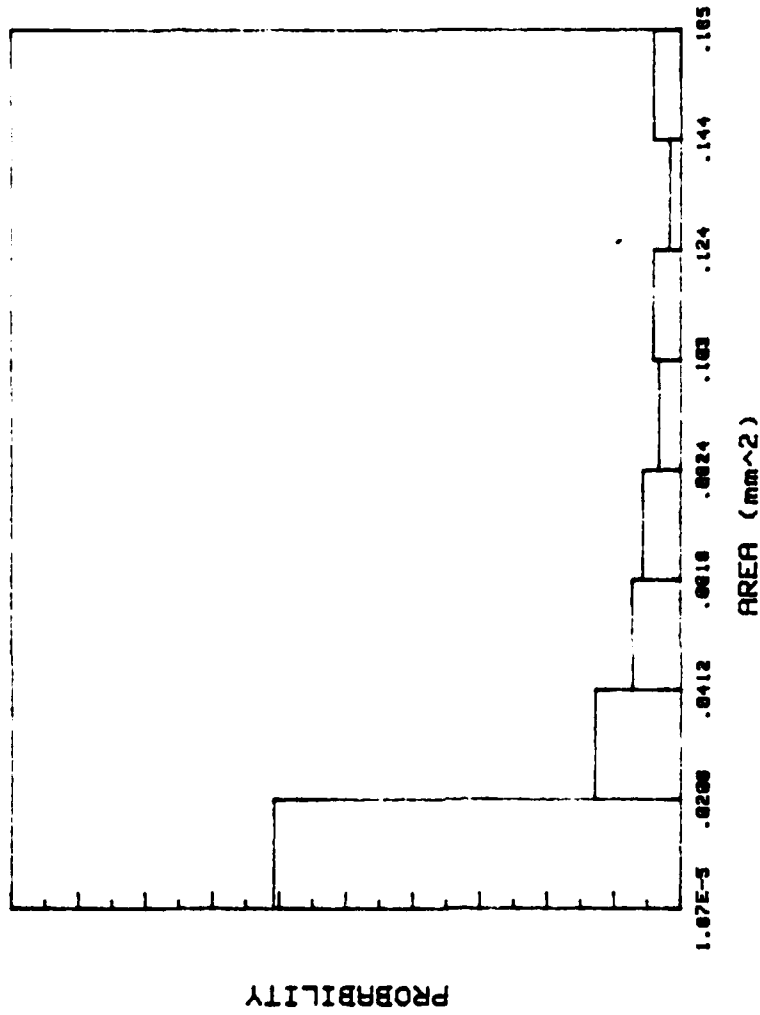
PARTICLE FRACTION : 43.77 %  
ALPHA-TI PHASE FRACTION : 56.23 %  
TOTAL PARTICLE NO. : 599  
AVERAGE OF AREA: .004145844 (mm<sup>2</sup>)





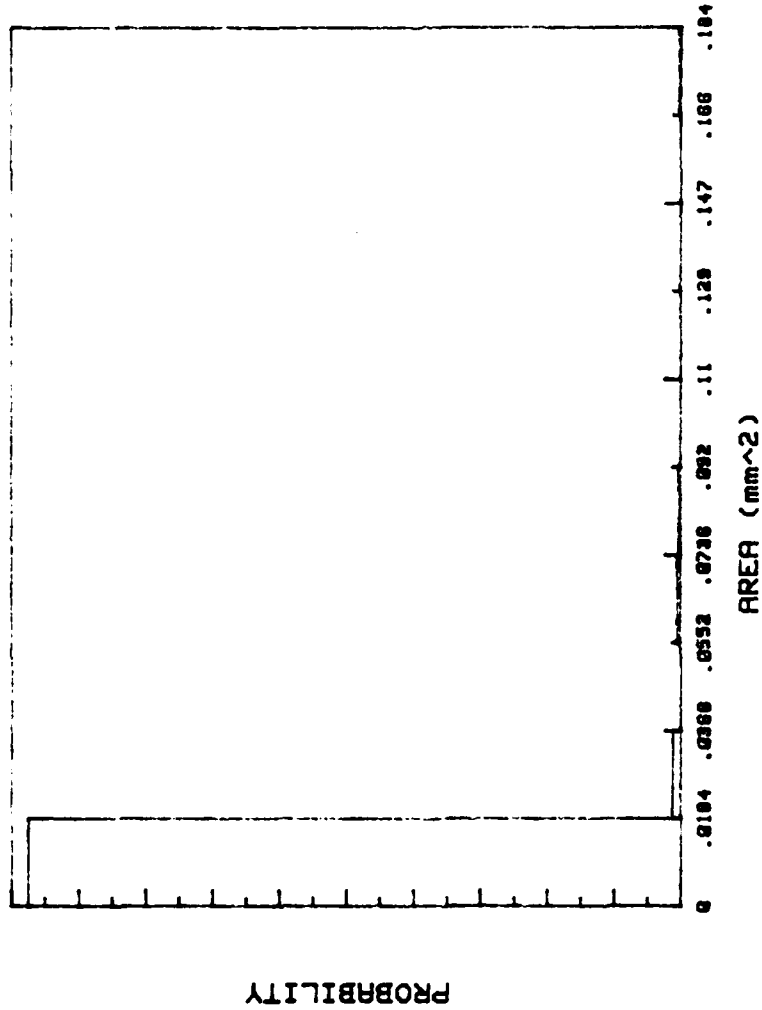
THE PARTICLE SIZE OF GAMMA PHASE DISTRIBUTION  
SPECIMEN : I14  
TEMPERATURE: 25 deg. C

PARTICLE FRACTION : 46.02 %  
Alpha-Ti PHASE FRACTION : 53.98 %  
TOTAL PARTICLE NO. : 220  
AVERAGE OF AREA: .011727 (mm<sup>2</sup>)



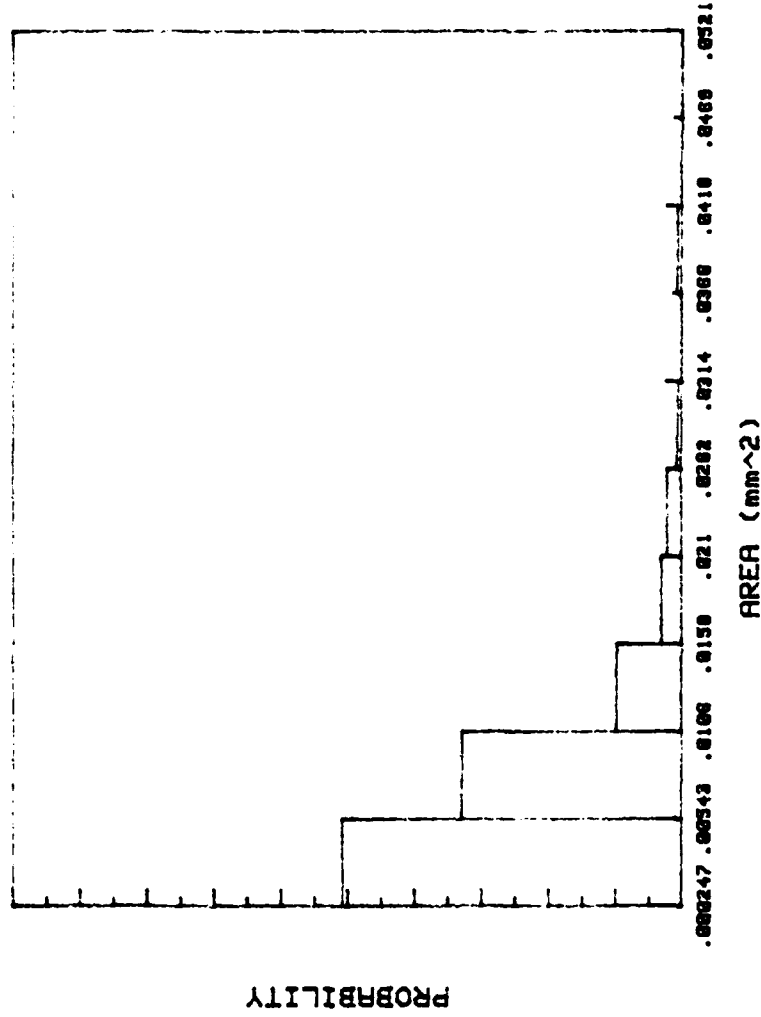
THE PARTICLE SIZE OF GAMMA PHASE DISTRIBUTION  
 SPECIMEN : I15  
 TEMPERATURE: 25 deg. C

PARTICLE FRACTION : 39.87%  
 Alpha-T1 PHASE FRACTION : 60.13%  
 TOTAL PARTICLE NO. : 125  
 AVERAGE OF AREA: .03382799 (mm<sup>2</sup>)



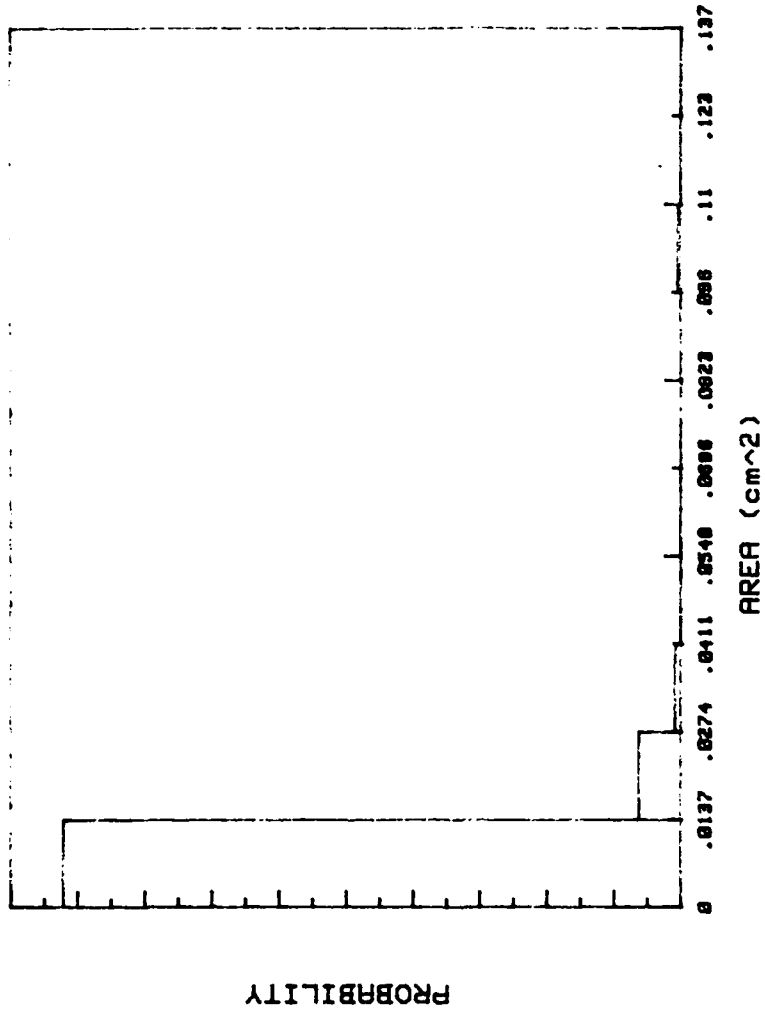
THE PARTICLE SIZE OF GAMMA PHASE DISTRIBUTION  
SPECIMEN : I16  
TEMPERATURE: 25 deg. C

PARTICLE FRACTION : 36.23 %  
Alpha-1 PHASE FRACTION : 63.77 %  
TOTAL PARTICLE NO. : 406  
AVERAGE OF AREA: .004832212 (mm<sup>2</sup>)



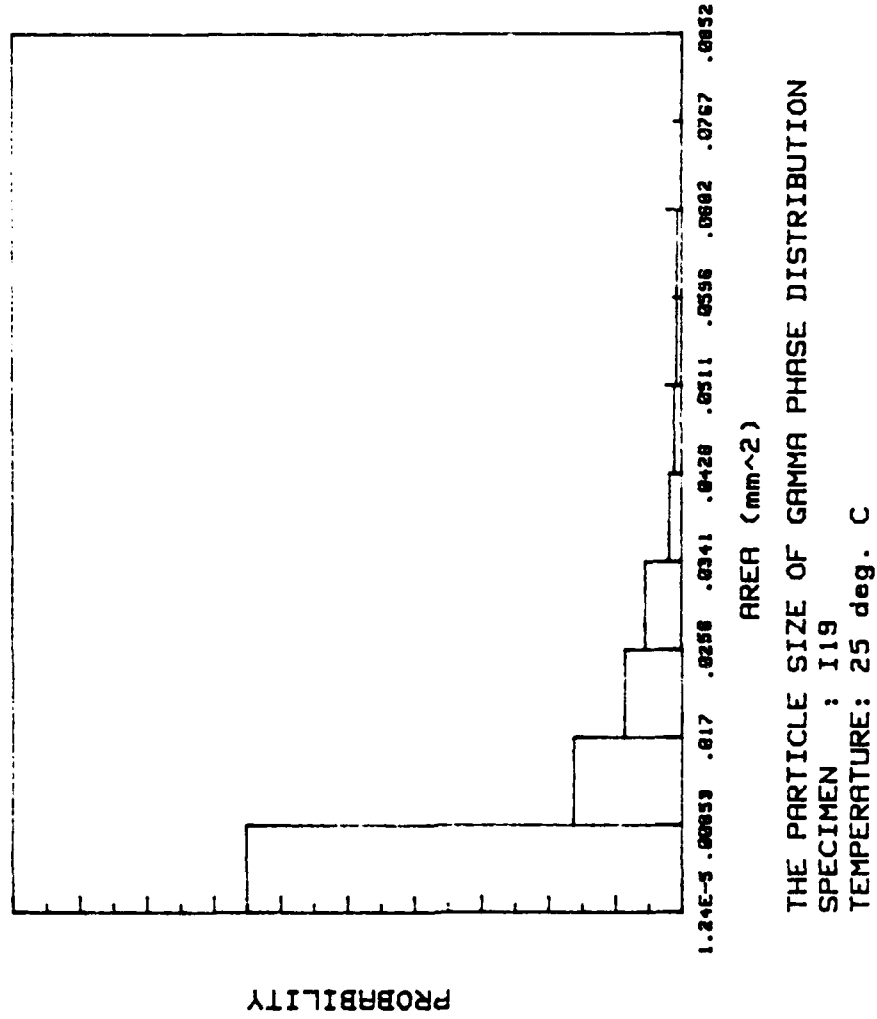
THE PARTICLE SIZE OF GAMMA PHASE DISTRIBUTION  
SPECIMEN : I17  
TEMPERATURE: 25 deg. C

PARTICLE FRACTION : 30.32%  
Alpha-T1 PHASE FRACTION : 69.68%  
TOTAL PARTICLE NO. : 329  
AVERAGE OF AREA: .008408931 (mm<sup>2</sup>)

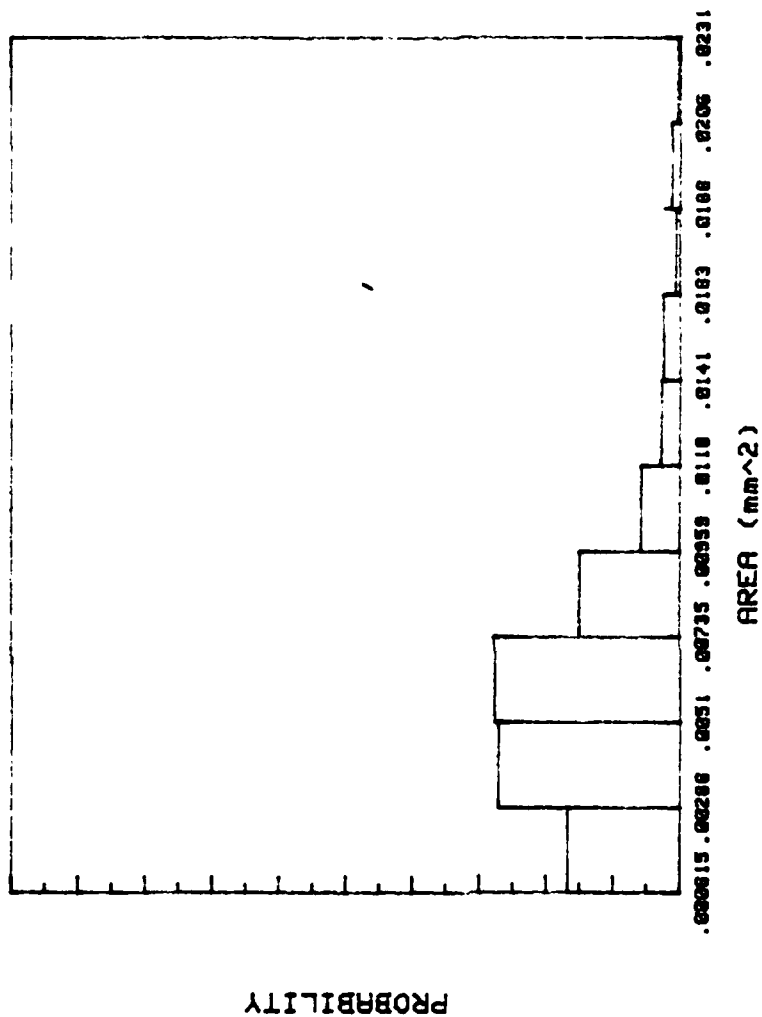


THE PARTICLE SIZE OF GAMMA PHASE DISTRIBUTION  
 SPECIMEN : I18  
 TEMPERATURE: 25 deg. C

PARTICLE FRACTION : 68.02 %  
 Alpha-1 PHASE FRACTION : 31.98 %  
 TOTAL PARTICLE NO. : 289  
 AVERAGE OF AREA: .002116405 (cm<sup>2</sup>)

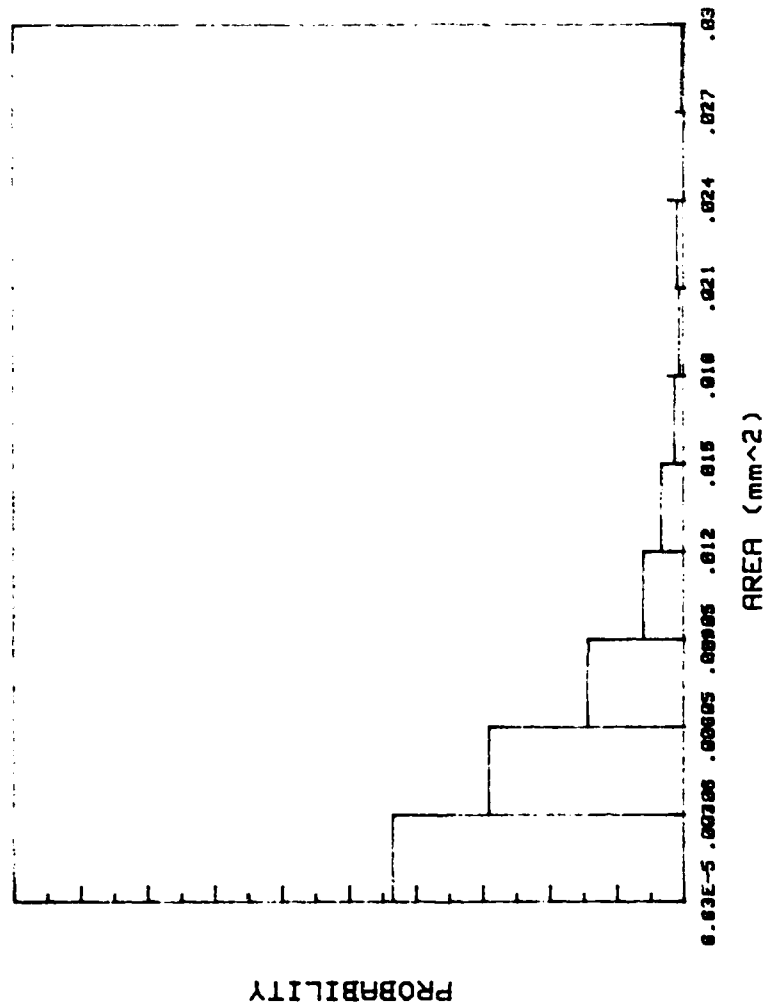


PARTICLE FRACTION : 58 %  
Alpha-T1 PHASE FRACTION : 42 %  
TOTAL PARTICLE NO. : 278  
AVERAGE OF AREA: .01188863 (mm<sup>2</sup>)



THE PARTICLE SIZE OF GAMMA PHASE DISTRIBUTION  
 SPECIMEN : 120  
 TEMPERATURE: 25 deg. C

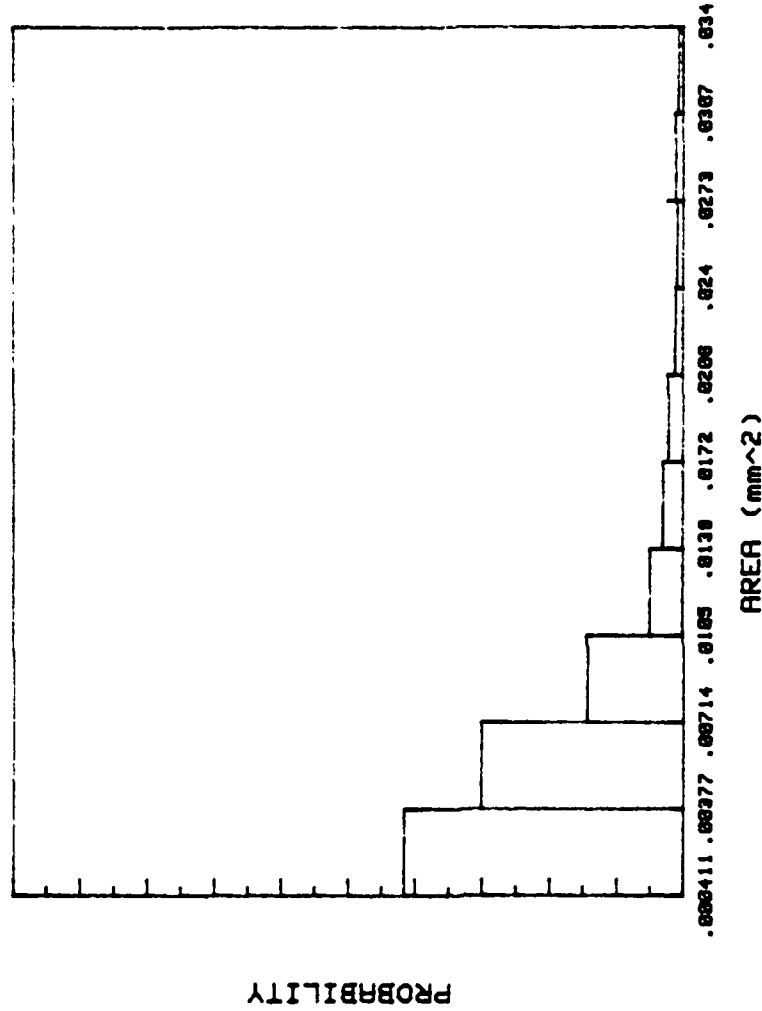
PARTICLE FRACTION : 35.66 %  
 Alpha-11 PHASE FRACTION : 64.34 %  
 TOTAL PARTICLE NO. : 328  
 AVERAGE OF AREA: .006125998 (mm<sup>2</sup>)

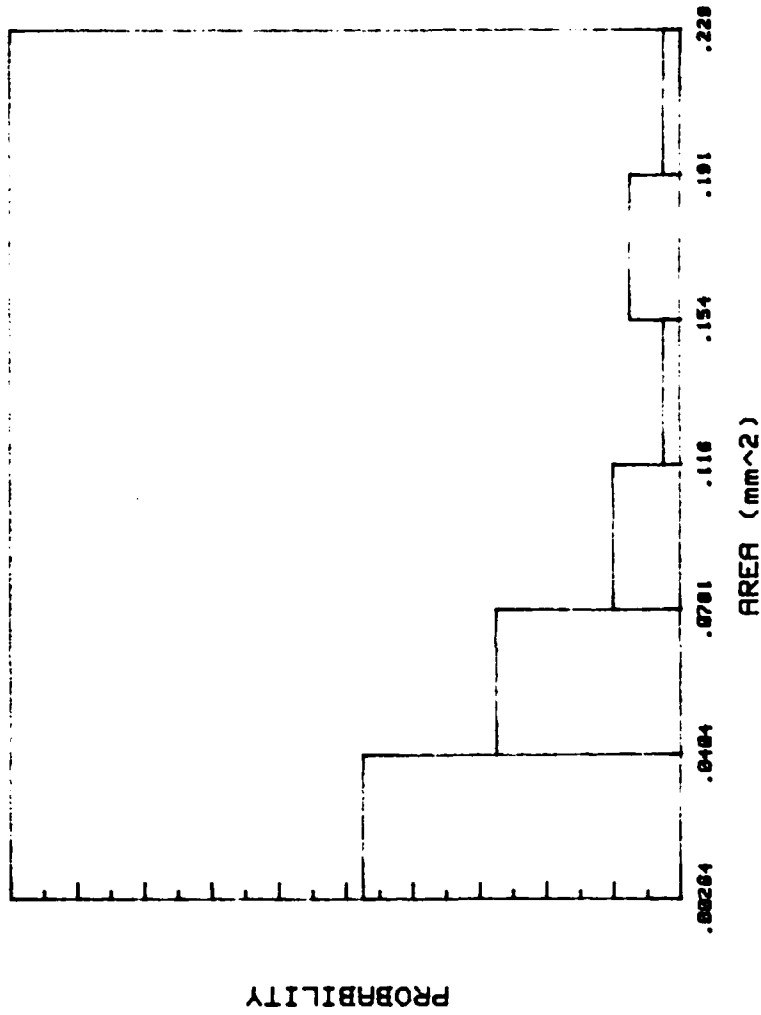


THE PARTICLE SIZE OF GAMMA PHASE DISTRIBUTION  
 SPECIMEN : I21  
 TEMPERATURE: 25 deg. C

PARTICLE FRACTION : 36.24 %  
 Alpha-Ti PHASE FRACTION: 63.76 %  
 TOTAL PARTICLE NO. : 299  
 AVERAGE OF AREA: .004863783 (mm<sup>2</sup>)

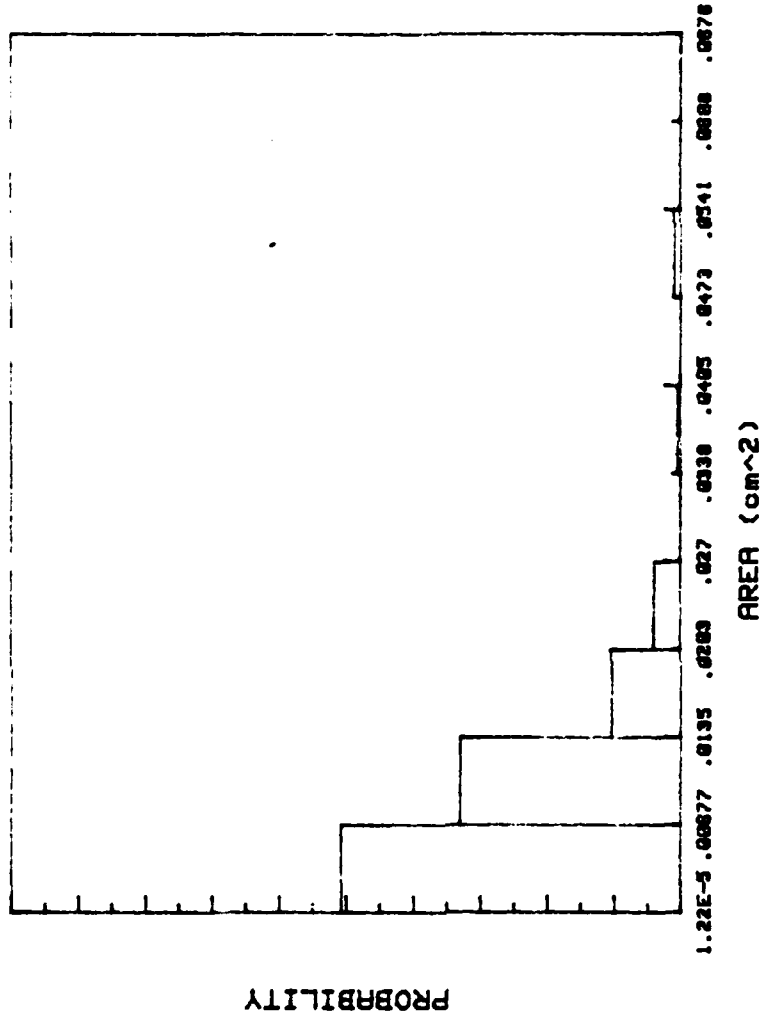






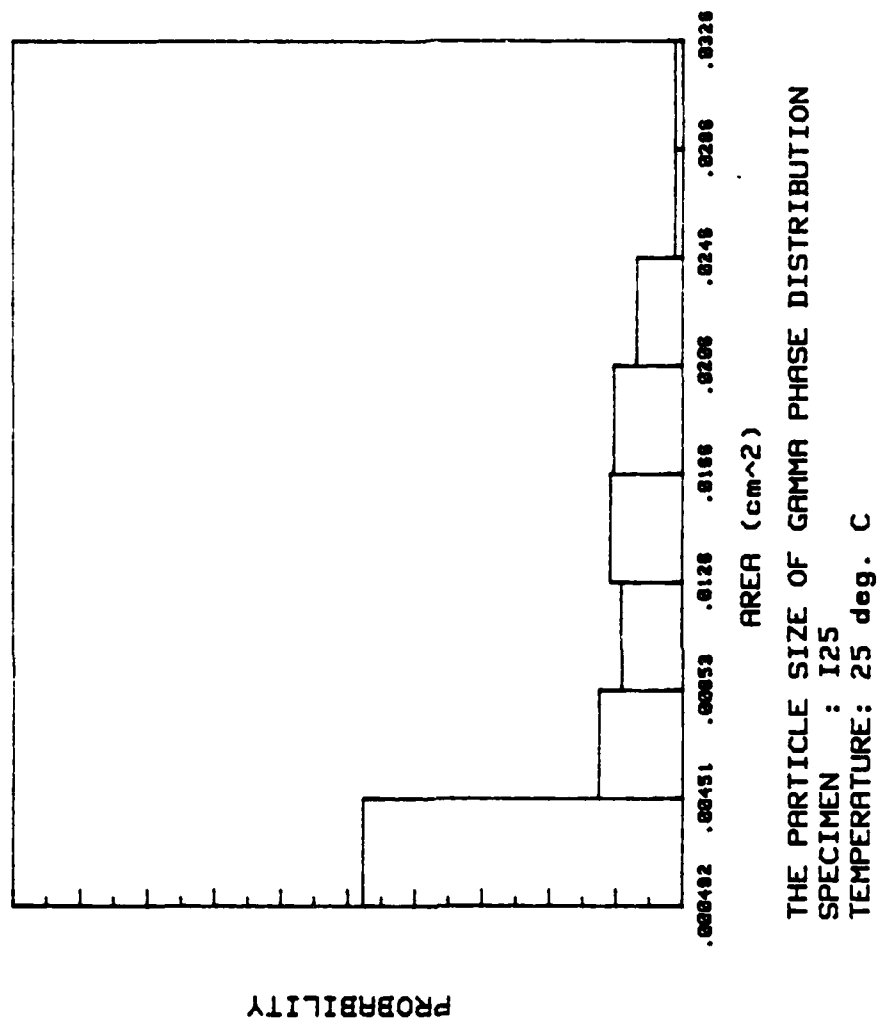
THE PARTICLE SIZE OF GAMMA PHASE DISTRIBUTION  
SPECIMEN : I23  
TEMPERATURE: 25 deg. C

PARTICLE FRACTION : 66.85 %  
Alpha-Ti PHASE FRACTION: 33.15 %  
TOTAL PARTICLE NO. : 289  
AVERAGE OF AREA: .05511086 (mm<sup>2</sup>)

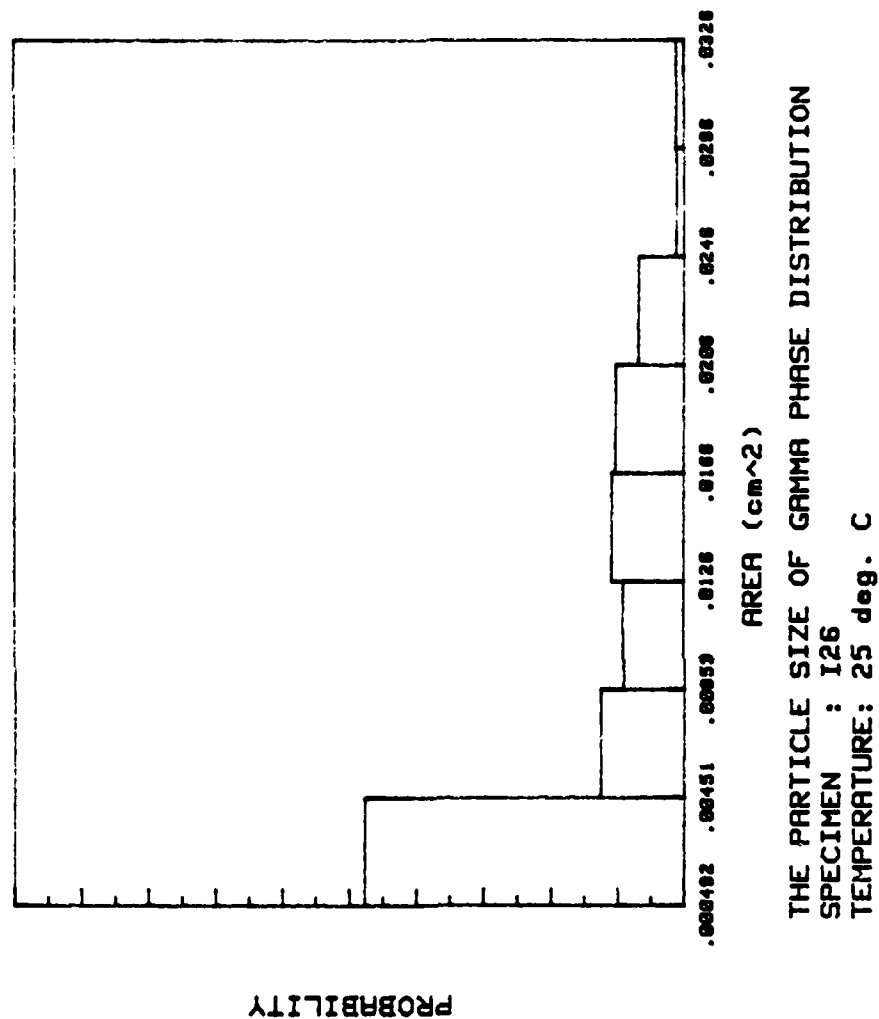


THE PARTICLE SIZE OF GAMMA PHASE DISTRIBUTION  
 SPECIMEN : I24  
 TEMPERATURE: 25 deg. C

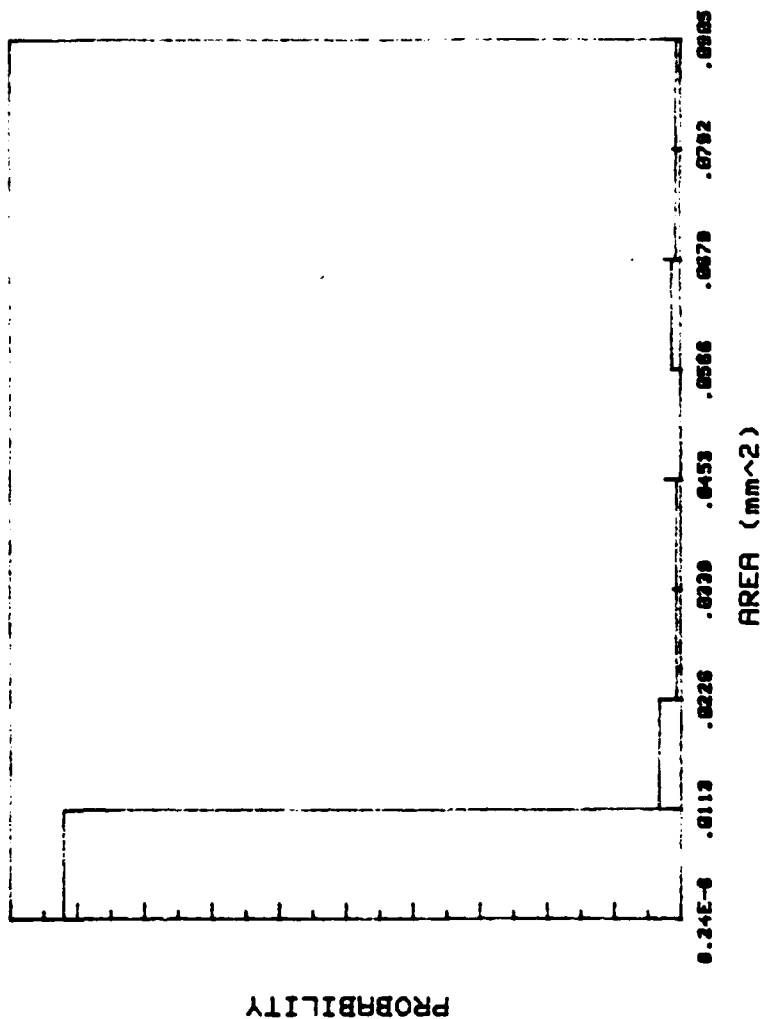
PARTICLE FRACTION : 38.37 %  
 Alpha-1 PHASE FRACTION : 69.63 %  
 TOTAL PARTICLE NO. : 203  
 AVERAGE OF AREA: .01081276 (cm<sup>2</sup>)



PARTICLE FRACTION : 26.96 %  
Alpha-Ti PHASE FRACTION : 73.04 %  
TOTAL PARTICLE NO. : 176  
AVERAGE OF AREA: .008530059 (cm<sup>2</sup>)

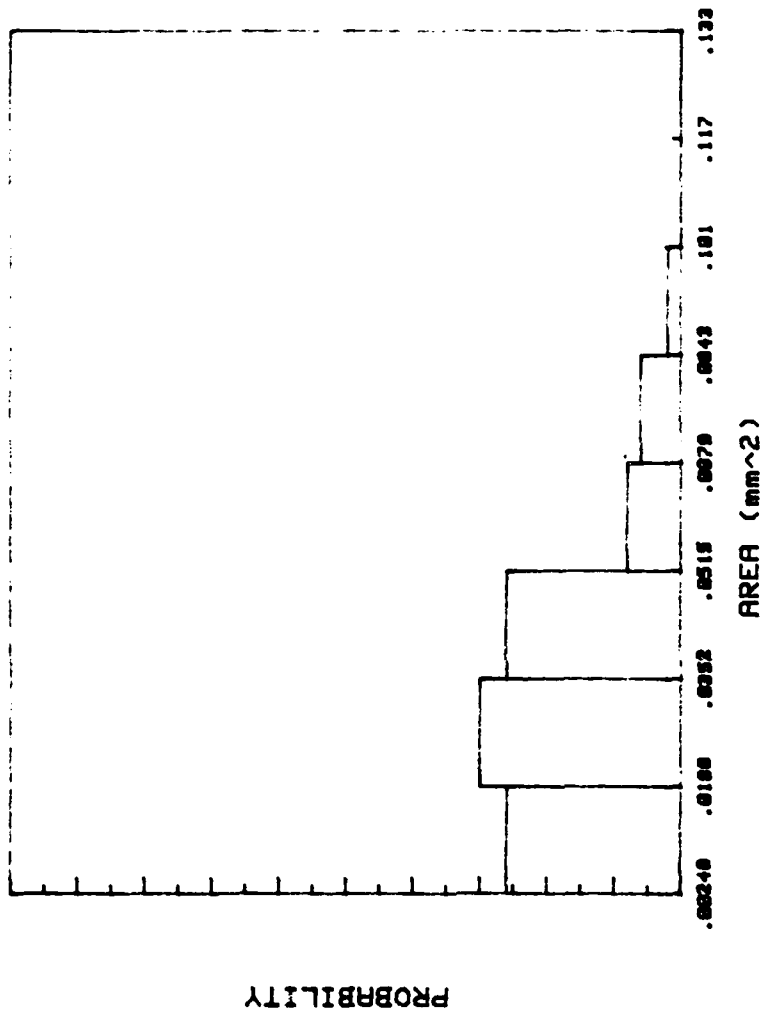


PARTICLE FRACTION : 26.96 %  
Alpha-1 PHASE FRACTION : 73.04 %  
TOTAL PARTICLE NO. : 176  
AVERAGE OF AREA: .008530059 (cm<sup>2</sup>)



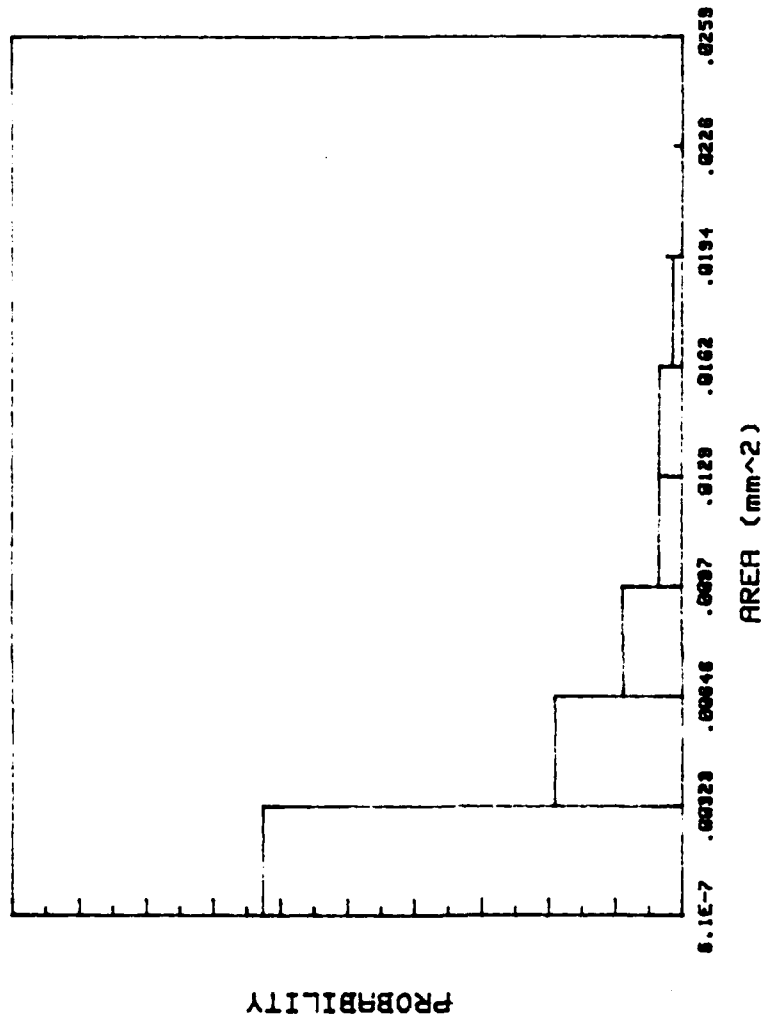
THE PARTICLE SIZE OF GAMMA PHASE DISTRIBUTION  
 SPECIMEN : I27  
 TEMPERATURE: 25 deg. C

PARTICLE FRACTION : 10.23 %  
 Alpha-T1 PHASE FRACTION : 89.77 %  
 TOTAL PARTICLE NO. : 151  
 AVERAGE OF AREA: .005141561 (mm<sup>2</sup>)



THE PARTICLE SIZE OF GAMMA PHASE DISTRIBUTION  
SPECIMEN : 128  
TEMPERATURE: 25 deg. C

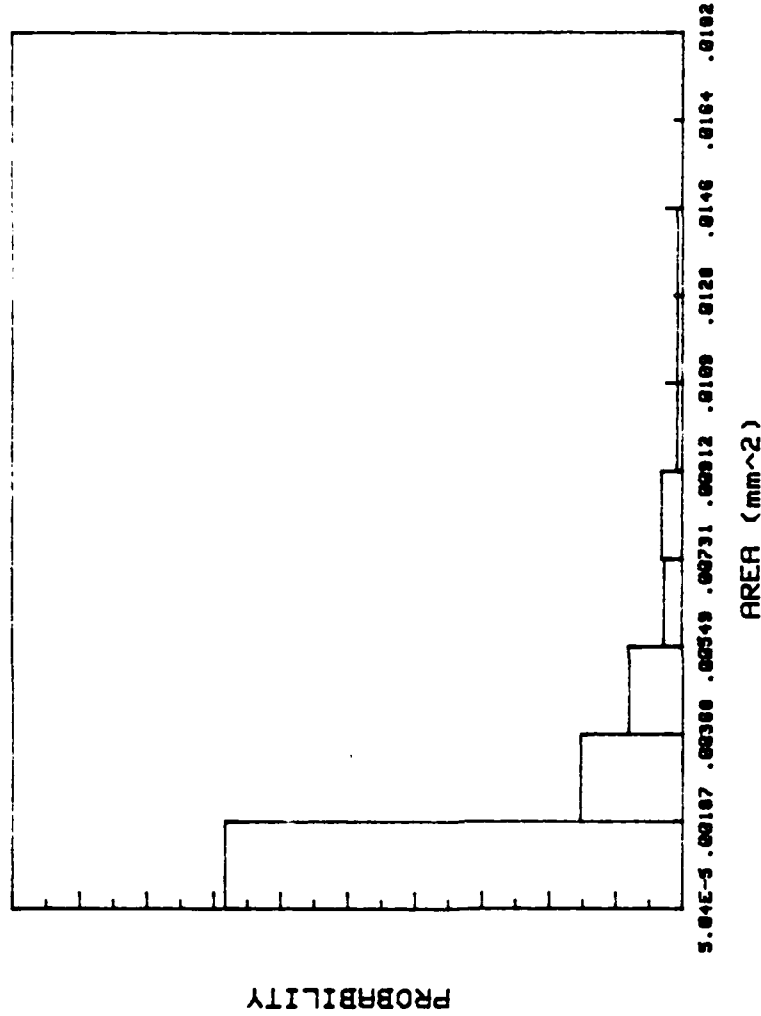
PARTICLE FRACTION : 20.39 %  
Alpha-11 PHASE FRACTION : 79.61 %  
TOTAL PARTICLE NO. : 143  
AVERAGE OF AREA: .005498753 (mm<sup>2</sup>)



THE PARTICLE SIZE OF GAMMA PHASE DISTRIBUTION  
SPECIMEN : W1  
TEMPERATURE: 25 deg. C

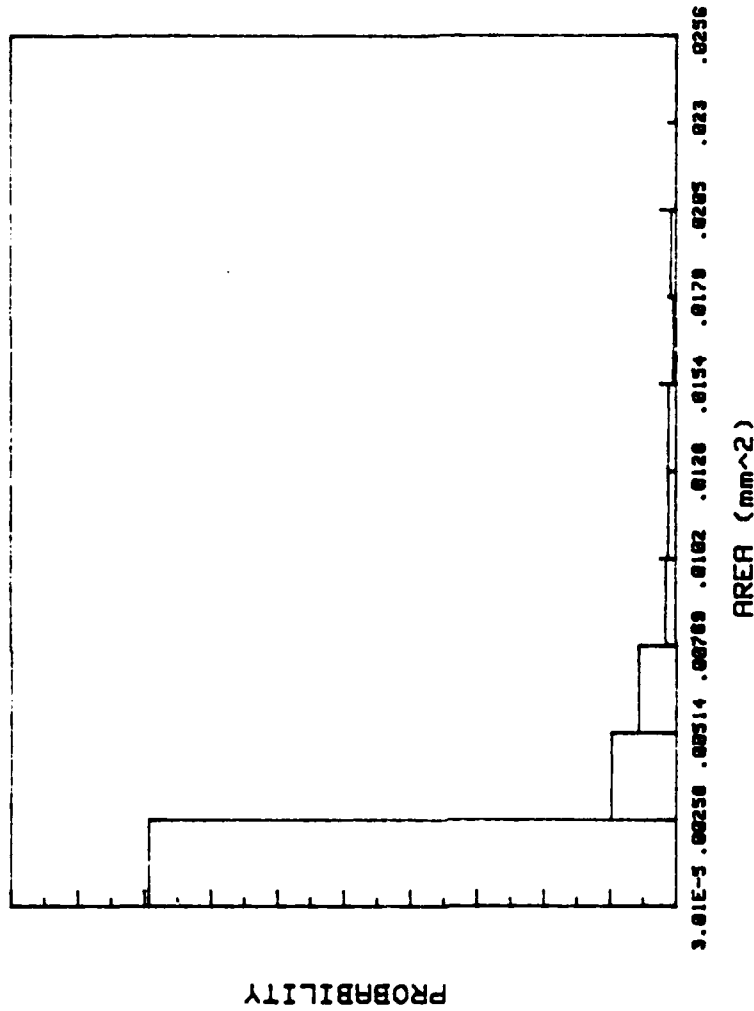
PARTICLE FRACTION : 81.39 %  
Alpha-11 PHASE FRACTION : 18.61 %  
TOTAL PARTICLE NO. : 147  
AVERAGE OF AREA: .004807768 (mm<sup>2</sup>)





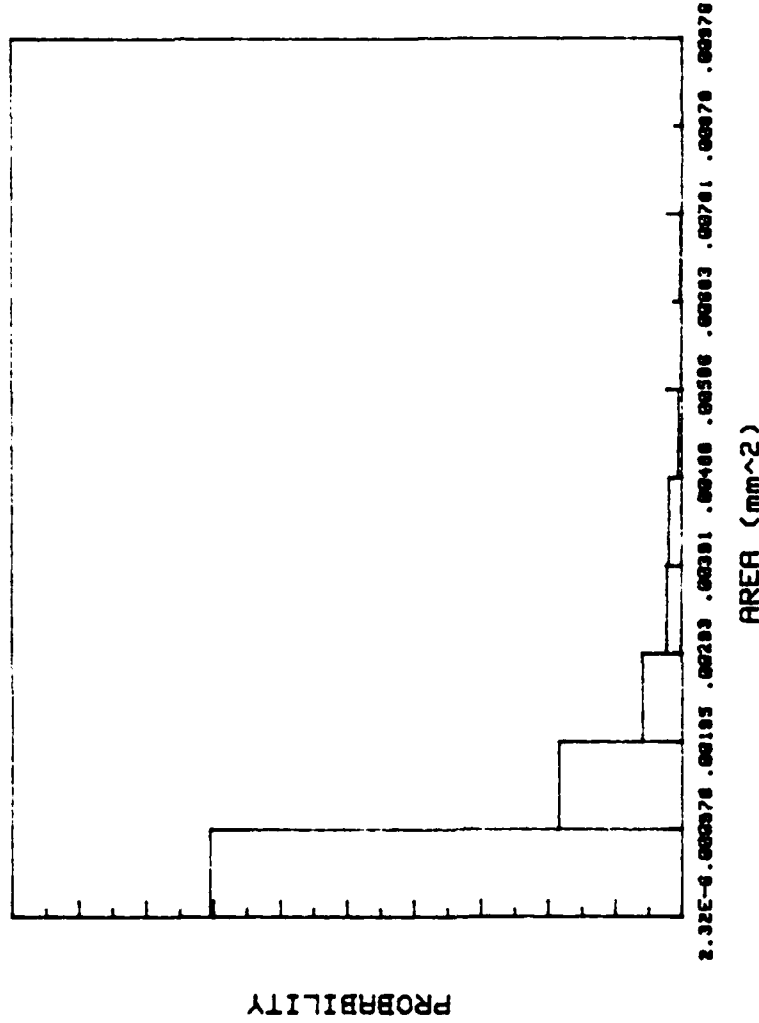
THE PARTICLE SIZE OF GAMMA PHASE DISTRIBUTION  
SPECIMEN : W2  
TEMPERATURE: 25 deg. C

PARTICLE FRACTION : 74.46 %  
Alpha-11 PHASE FRACTION : 25.54 %  
TOTAL PARTICLE NO. : 262  
AVERAGE OF AREA: .0025506092 (mm<sup>2</sup>)



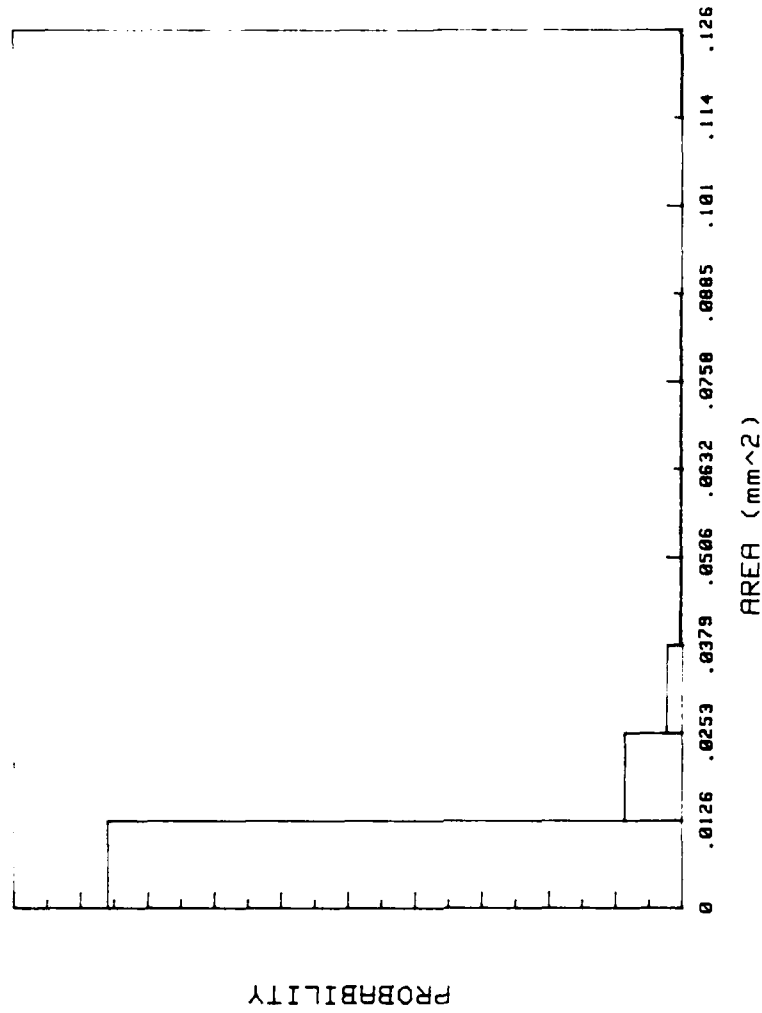
THE PARTICLE SIZE OF GAMMA PHASE DISTRIBUTION  
 SPECIMEN : W3  
 TEMPERATURE: 25 deg. C

PARTICLE FRACTION : 71.67 %  
 Alpha-1 PHASE FRACTION : 28.33 %  
 TOTAL PARTICLE NO. : 266  
 AVERAGE OF AREA: .002377672 (mm<sup>2</sup>)



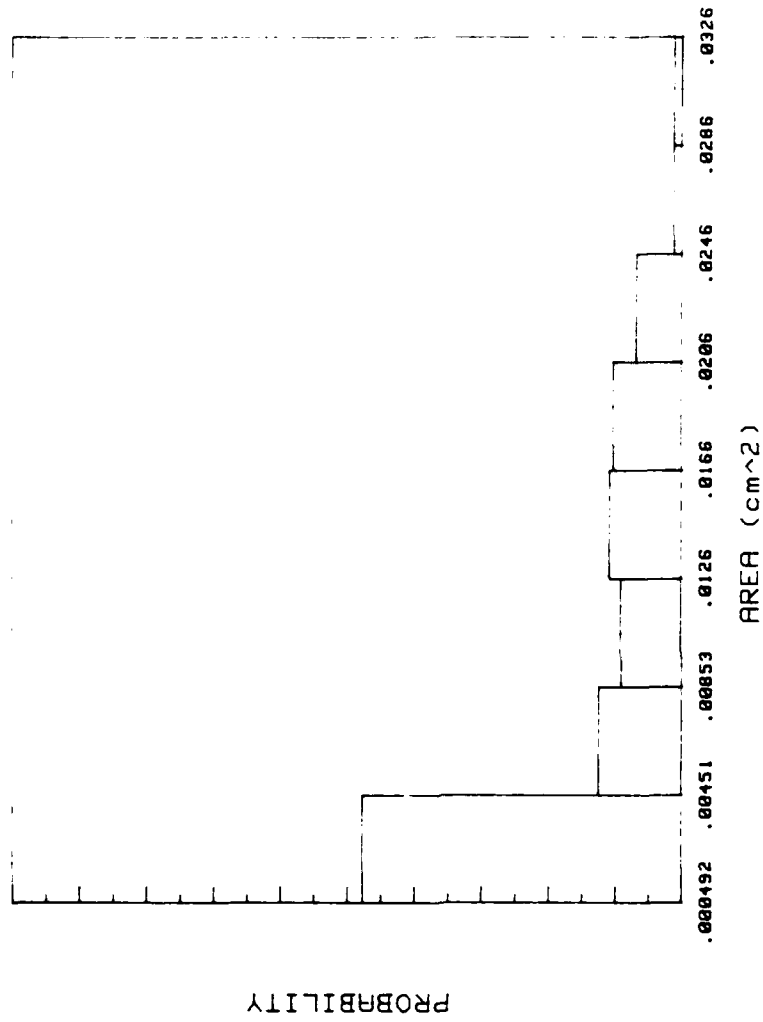
THE PARTICLE SIZE OF GAMMA PHASE DISTRIBUTION  
 SPECIMEN : W4  
 TEMPERATURE: 25 deg. C

PARTICLE FRACTION : 65.28 %  
 Alpha-11 PHASE FRACTION : 34.72 %  
 TOTAL PARTICLE NO. : 370  
 AVERAGE OF AREA: .001119364 (mm<sup>2</sup>)



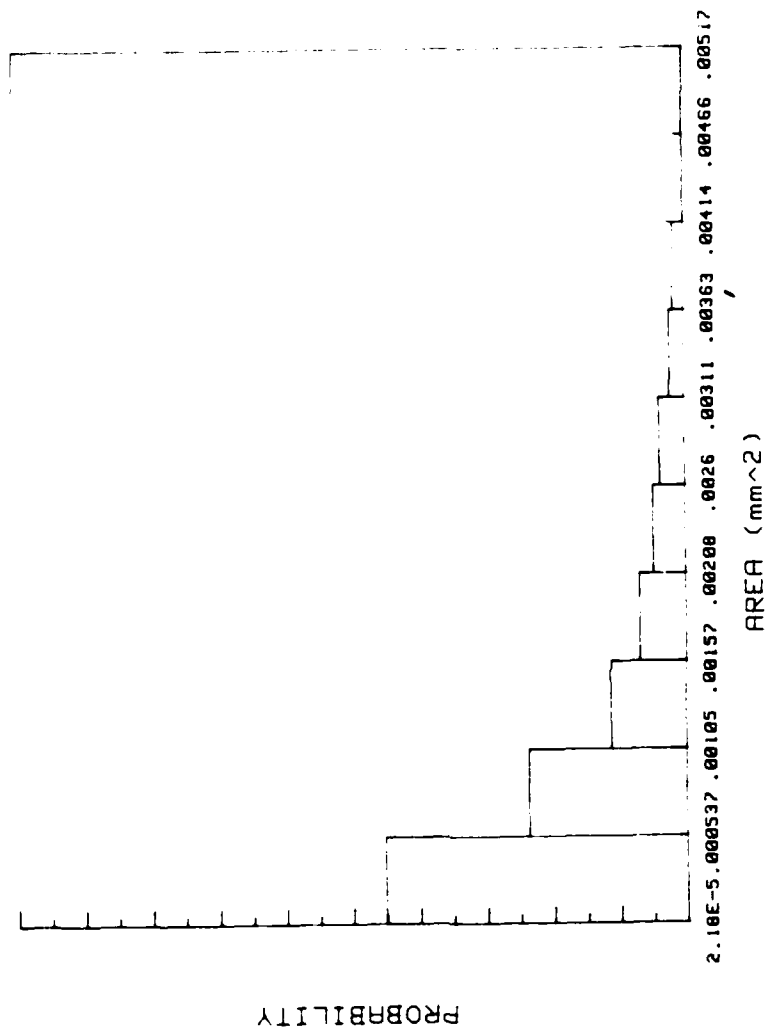
THE PARTICLE SIZE OF GAMMA PHASE DISTRIBUTION  
 SPECIMEN : HRI  
 TEMPERATURE: 150 deg. C

PARTICLE FRACTION : 12.15 %  
 Alpha-T1 PHASE FRACTION : 87.85 %  
 TOTAL PARTICLE NO. : 105  
 AVERAGE OF AREA: .006539226 (mm<sup>2</sup>)



THE PARTICLE SIZE OF GAMMA PHASE DISTRIBUTION  
SPECIMEN : HR2  
TEMPERATURE: 150 deg. C

PARTICLE FRACTION : 24.13 %  
Alpha-1<sub>1</sub> PHASE FRACTION : 75.87 %  
TOTAL PARTICLE NO. : 176  
AVERAGE OF AREA: .008530059 (cm<sup>2</sup>)

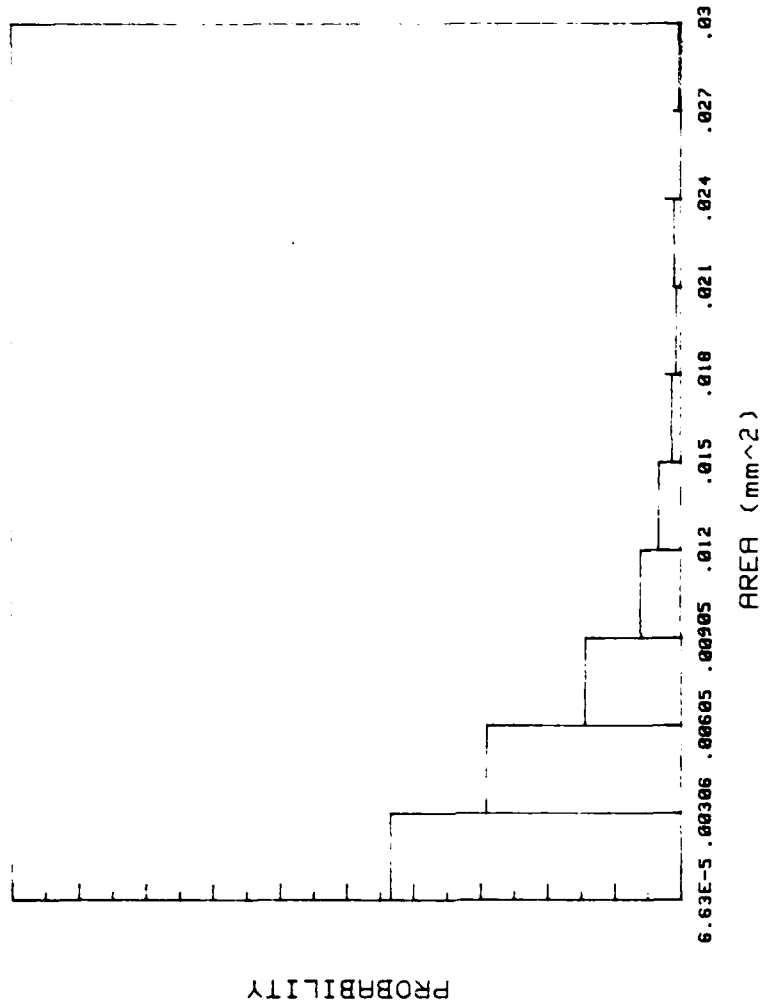


# THE PARTICLE SIZE OF GAMMA PHASE DISTRIBUTION

SPECIMEN : HA3

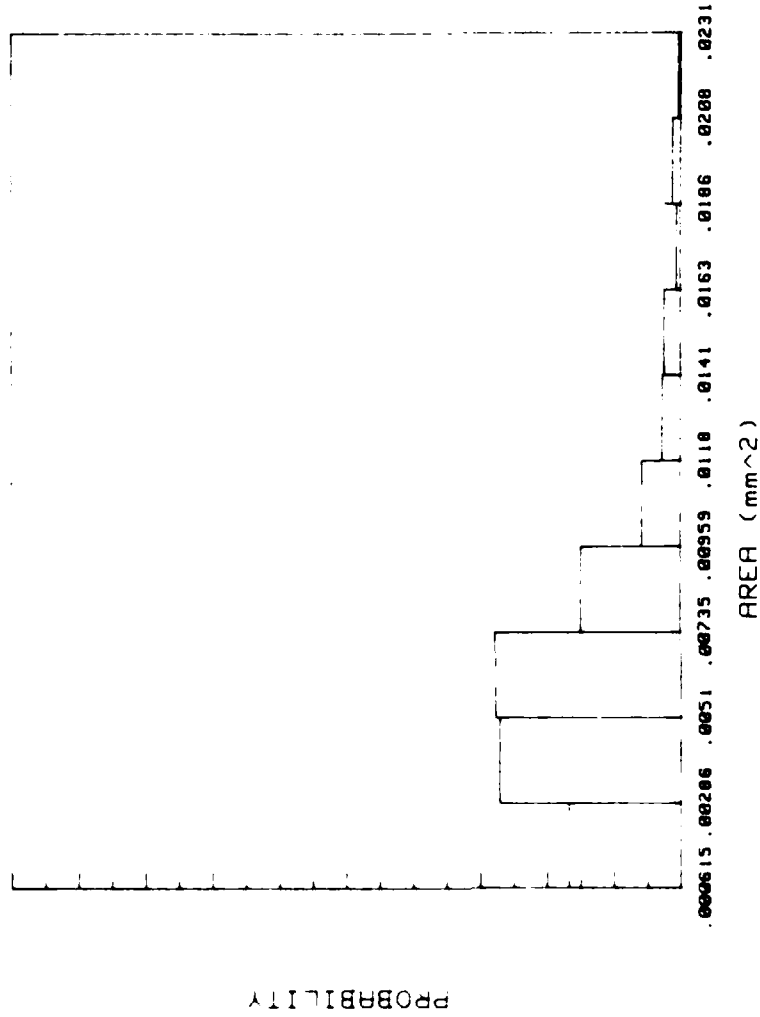
TEMPERATURE: 150 deg. C

PARTICLE FRACTION : 42.85 %  
 Alpha-11 PHASE FRACTION : 57.15 %  
 TOTAL PARTICLE NO. : 186  
 AVERAGE OF AREA: .001143929 (mm<sup>2</sup>)



THE PARTICLE SIZE OF GAMMA PHASE DISTRIBUTION  
 SPECIMEN : HA4  
 TEMPERATURE: 150 deg. C

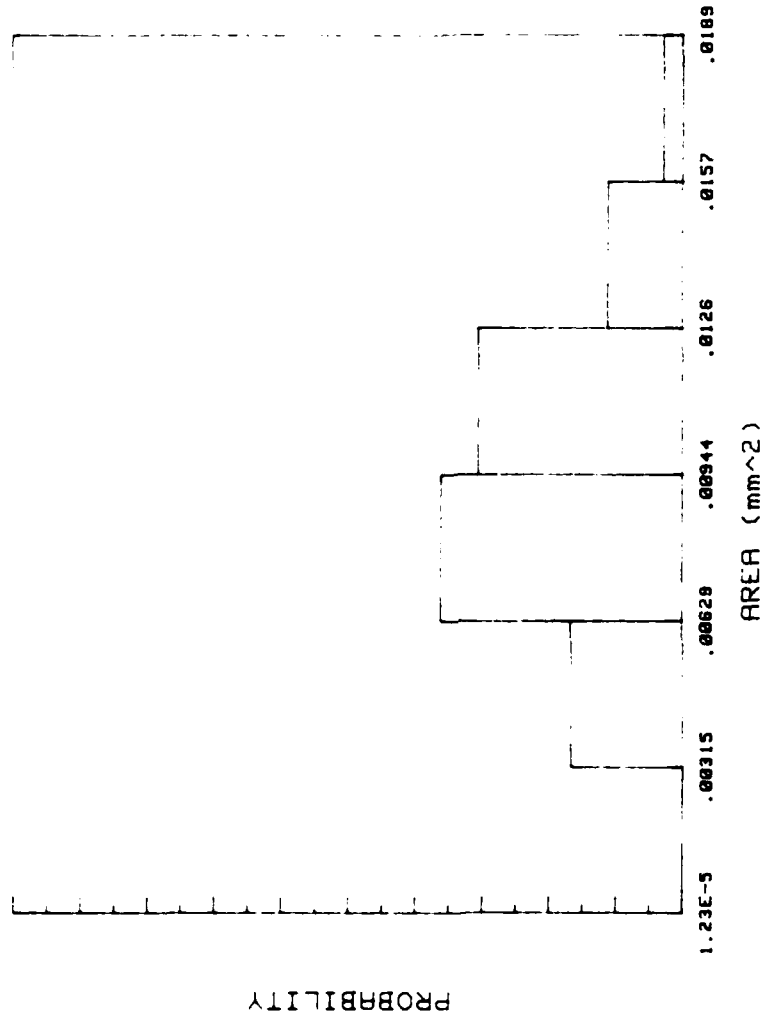
PARTICLE FRACTION : 51.43 %  
 Alpha-1<sub>1</sub> PHASE FRACTION: 48.57 %  
 TOTAL PARTICLE NO. : 299  
 AVERAGE OF AREA: .004863783 (mm<sup>2</sup>)



THE PARTICLE SIZE OF GAMMA PHASE DISTRIBUTION  
SPECIMEN : HAS  
TEMPERATURE: 150 deg. C

PARTICLE FRACTION : 62.14 %  
Gamma-1 PHASE FRACTION : 37.86 %  
TOTAL PARTICLE NO. : 328  
AVERAGE OF AREA: .008125998 (mm<sup>2</sup>)



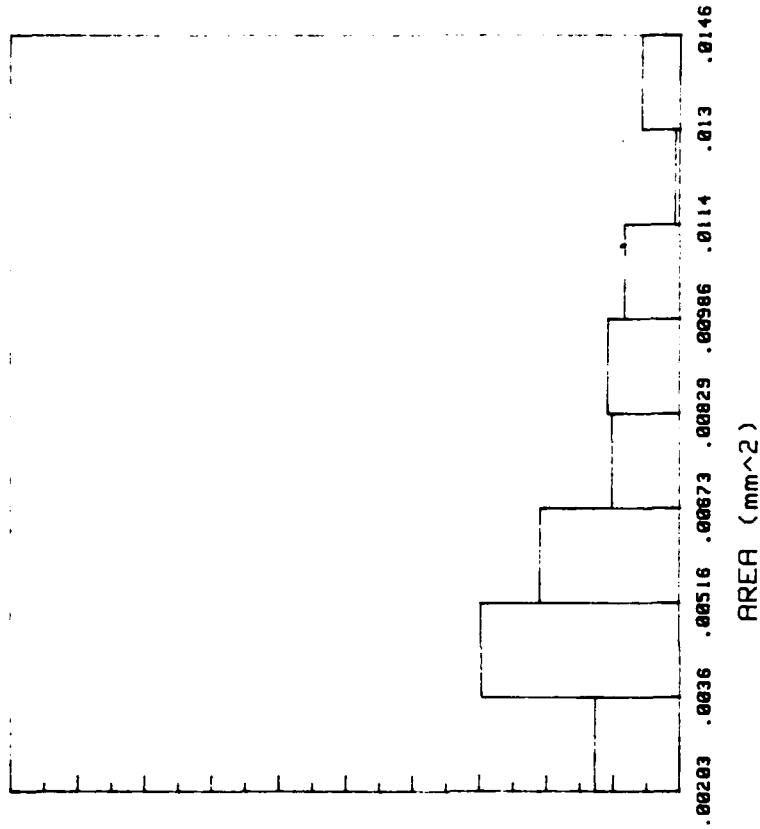


# THE PARTICLE SIZE OF GAMMA PHASE DISTRIBUTION

SPECIMEN : HB1

TEMPERATURE: 350 deg. C

PARTICLE FRACTION : 12.49 %  
 Alpha-1) PHASE FRACTION : 87.51 %  
 TOTAL PARTICLE NO. : 36  
 AVERAGE OF AREA: .009479142 (mm<sup>2</sup>)

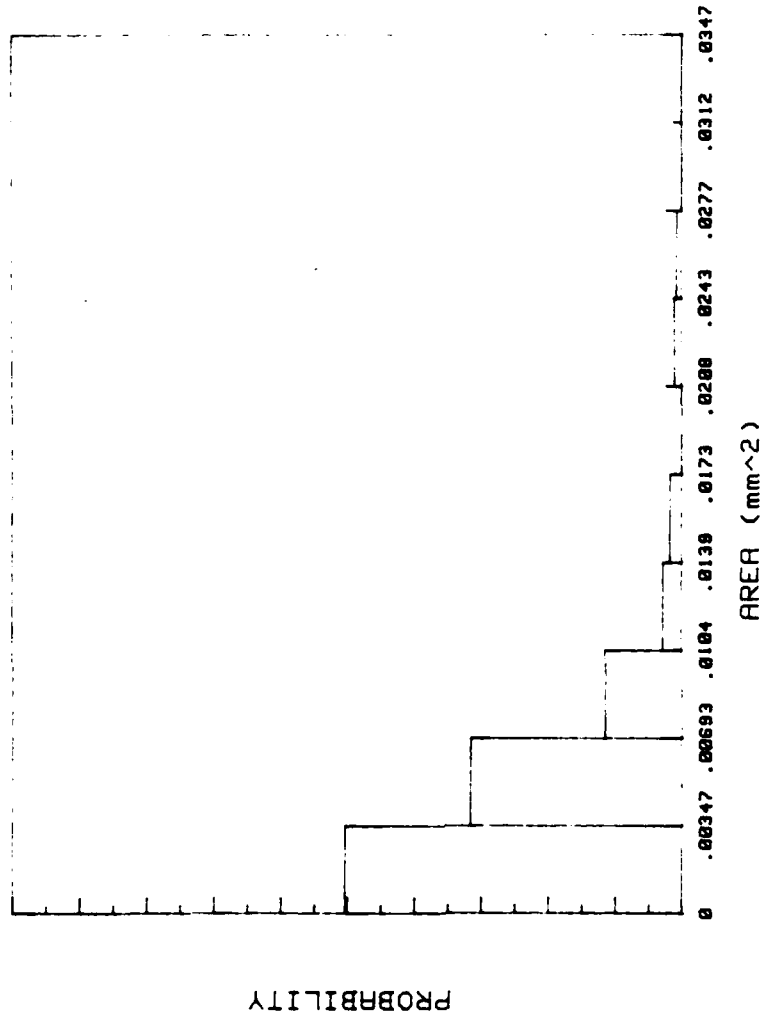


# THE PARTICLE SIZE OF GAMMA PHASE DISTRIBUTION

SPECIMEN : HB2

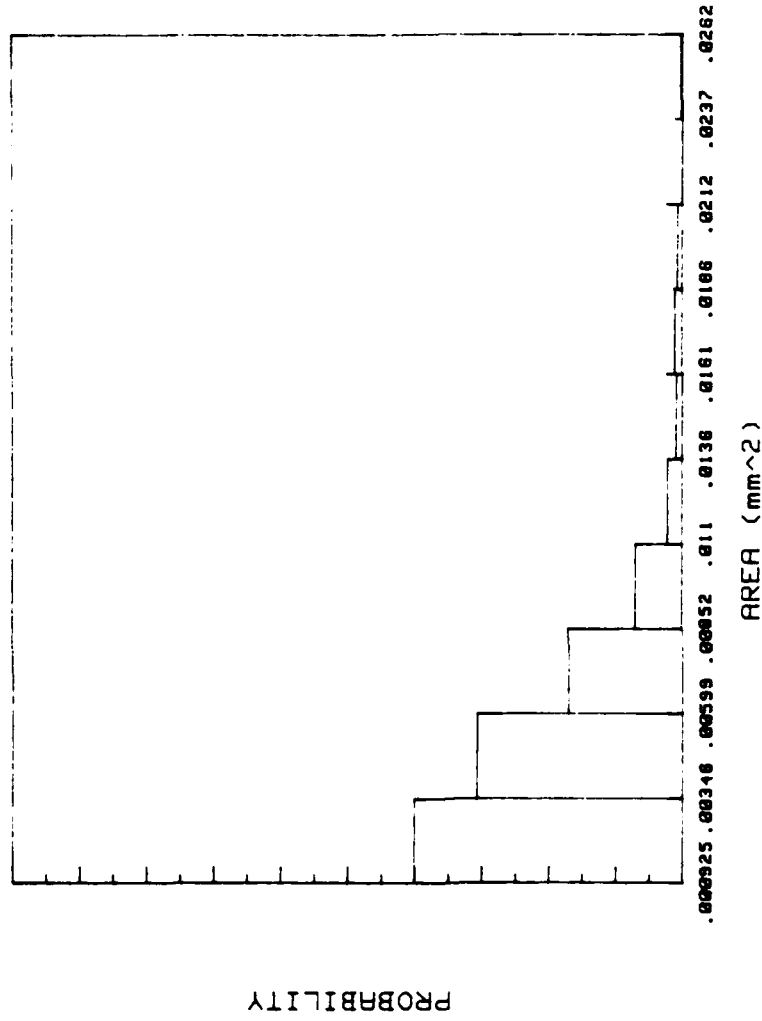
TEMPERATURE: 350 deg. C

PARTICLE FRACTION : 20.67 %  
 Alpha-1 PHASE FRACTION : 79.33 %  
 TOTAL PARTICLE NO. : 158  
 AVERAGE OF AREA: .006372362 (mm<sup>2</sup>)



THE PARTICLE SIZE OF GAMMA PHASE DISTRIBUTION  
 SPECIMEN : HB3  
 TEMPERATURE: 350 deg. C

PARTICLE FRACTION : 29.72 %  
 Alpha-11 PHASE FRACTION : 70.28 %  
 TOTAL PARTICLE NO. : 288  
 AVERAGE OF AREA: .005833552 (mm<sup>2</sup>)

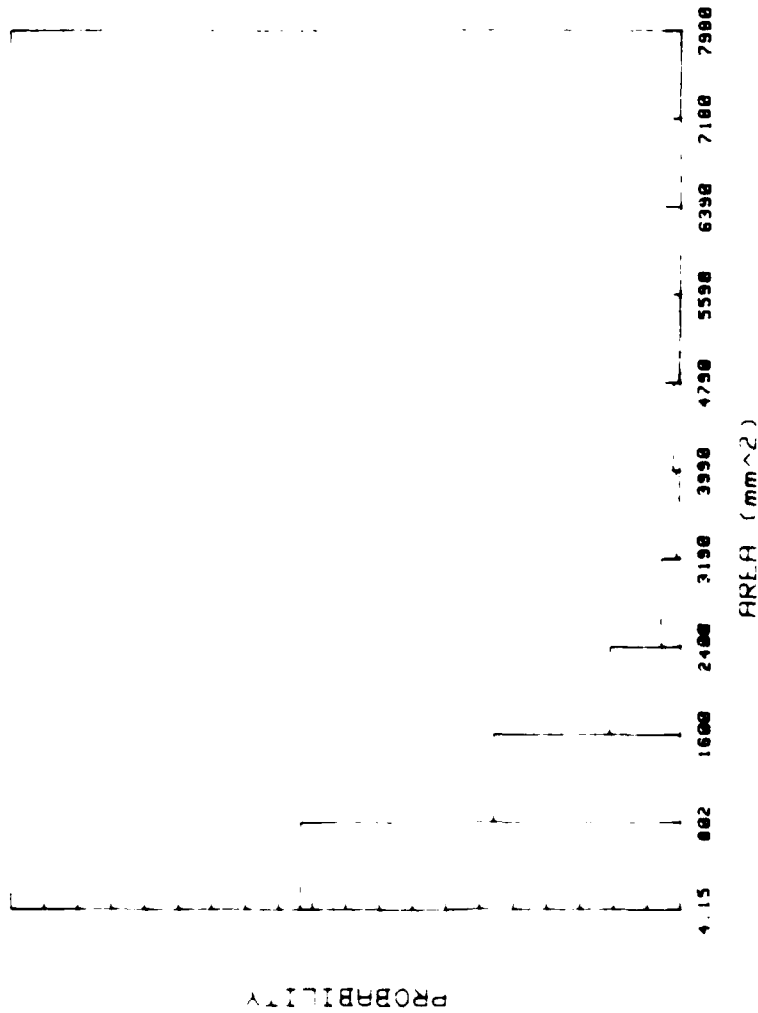


THE PARTICLE SIZE OF GAMMA PHASE DISTRIBUTION

SPECIMEN : HB4

TEMPERATURE: 350 deg. C

PARTICLE FRACTION : 40.31 %  
 Alpha-TI PHASE FRACTION : 59.69 %  
 TOTAL PARTICLE NO. : 459  
 AVERAGE OF AREA: .004983765 (mm<sup>2</sup>)

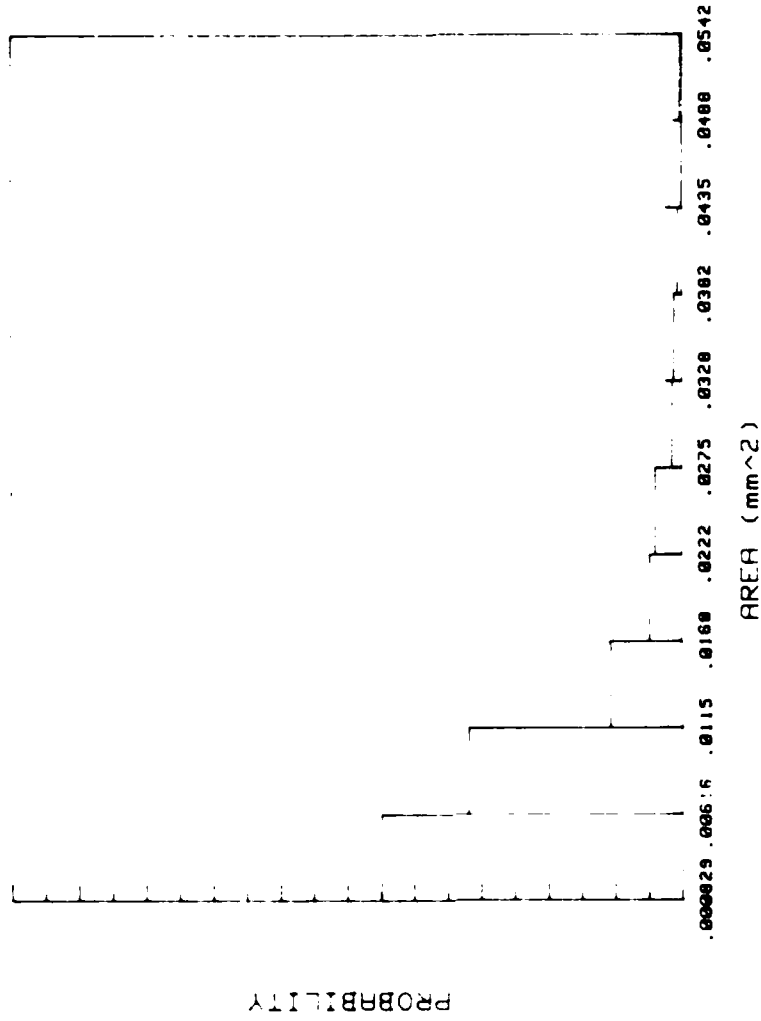


THE PARTICLE SIZE OF GAMMA PHASE DISTRIBUTION

SPECIMEN : HB5

TEMPERATURE : 350 deg. C

PARTICLE FRACTION : 43.38 %  
 ALPHA-1 PHASE FRACTION : 56.62 %  
 TOTAL PARTICLE NO. : 588  
 AVERAGE OF AREA: 937.4506 (mm<sup>2</sup>)

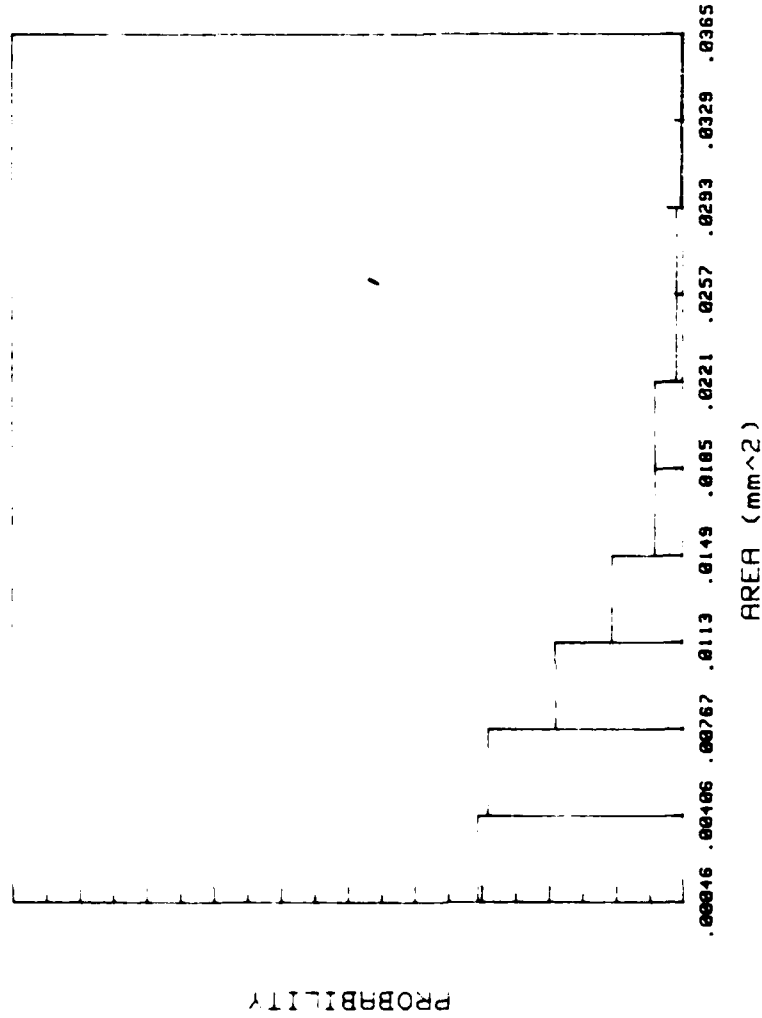


THE PARTICLE SIZE OF GAMMA PHASE DISTRIBUTION

SPECIMEN : HB6

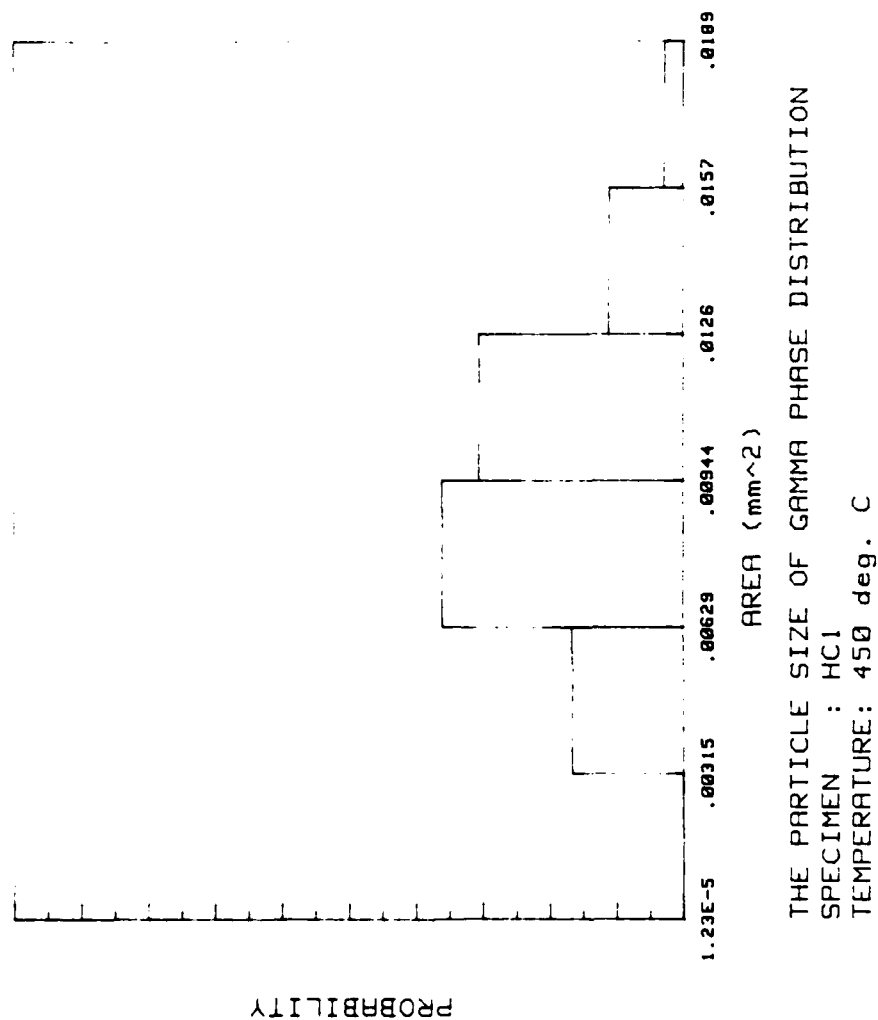
TEMPERATURE: 350 deg. C

PARTICLE FRACTION : 56.6 %  
 ALPHA-T<sub>1</sub> PHASE FRACTION : 43.4 %  
 TOTAL PARTICLE NO. : 354  
 AVERAGE OF AREA: .00903852 (mm<sup>2</sup>)



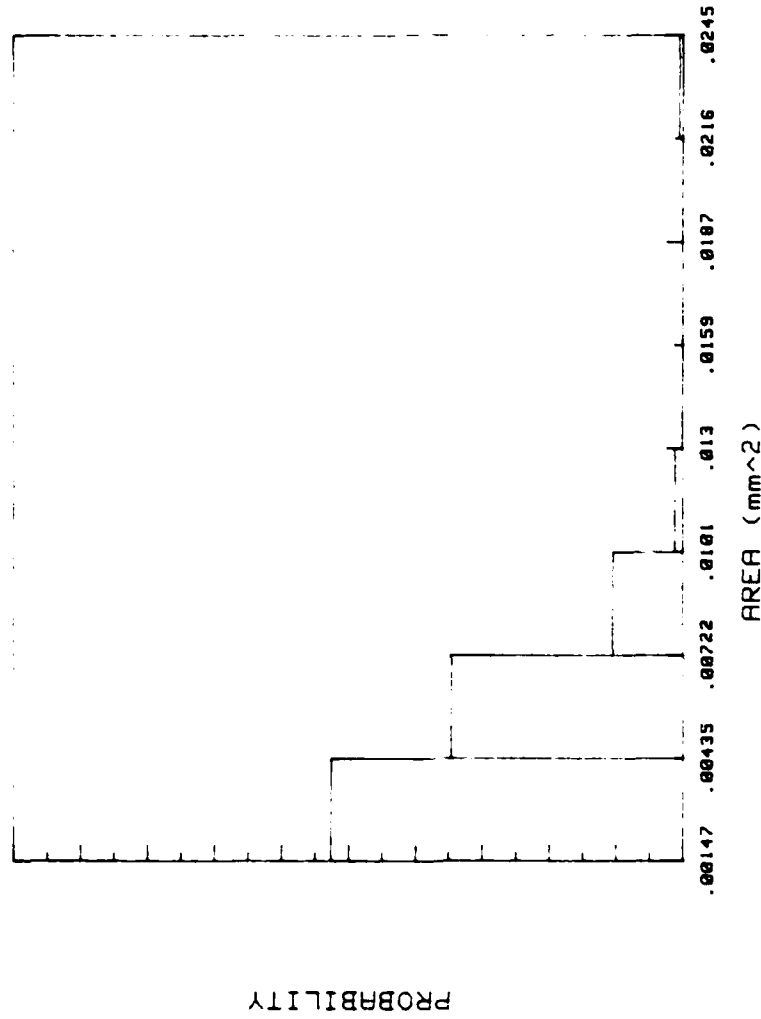
THE PARTICLE SIZE OF GAMMA PHASE DISTRIBUTION  
 SPECIMEN : HB7  
 TEMPERATURE: 350 deg. C

PARTICLE FRACTION : 59.17 %  
 Alpha-1) PHASE FRACTION : 40.83 %  
 TOTAL PARTICLE NO. : 437  
 AVERAGE OF AREA: .007671168 (mm<sup>2</sup>)



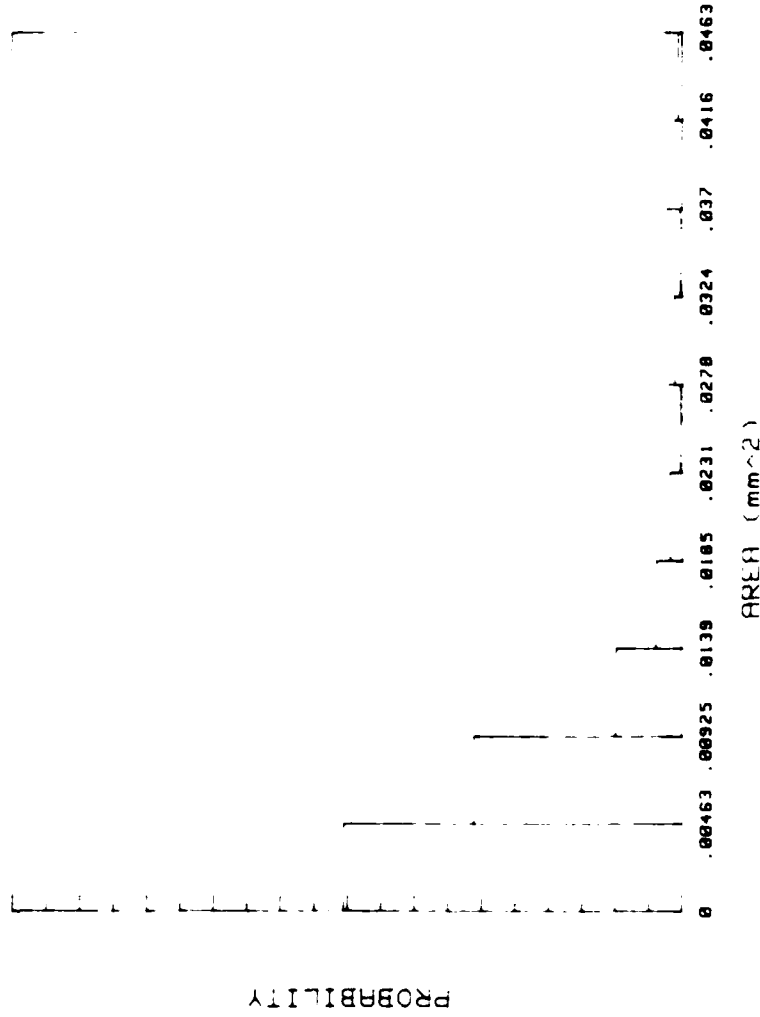
PARTICLE FRACTION : 12.49 %  
 Alpha-1 PHASE FRACTION : 87.51 %  
 TOTAL PARTICLE NO. : 36  
 AVERAGE OF AREA: .009479142 (mm<sup>2</sup>)





THE PARTICLE SIZE OF GAMMA PHASE DISTRIBUTION  
 SPECIMEN : HC2  
 TEMPERATURE: 450 deg. C

PARTICLE FRACTION : 24.39 %  
 Alpha-1 PHASE FRACTION : 75.61 %  
 TOTAL PARTICLE NO. : 173  
 AVERAGE OF AREA: .004667224 (mm<sup>2</sup>)

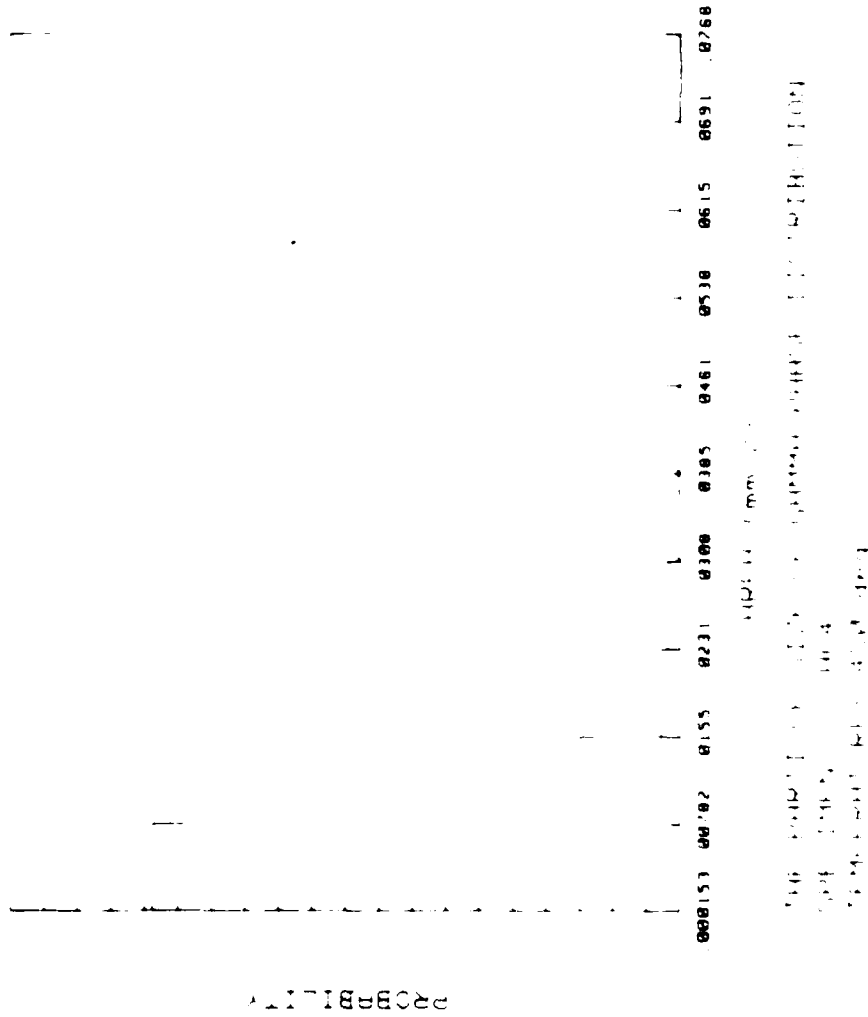


THE PARTICLE SIZE OF GAMMA PHASE DISTRIBUTION

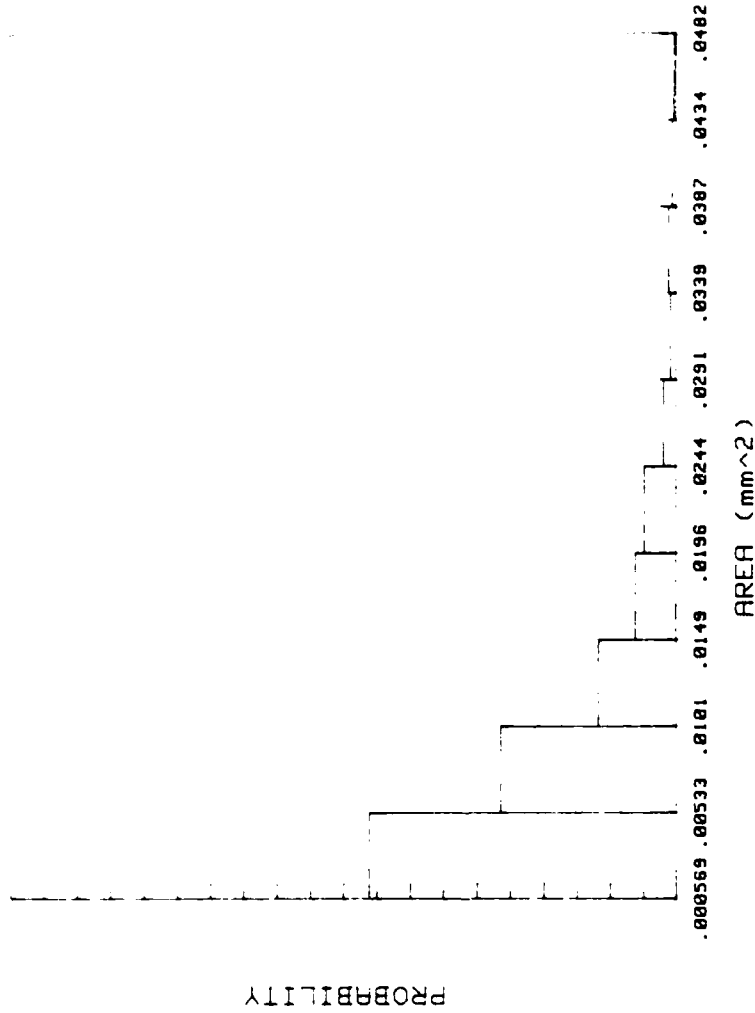
SPECIMEN : HC3

TEMPERATURE : 450 deg. C

PARTICLE FRACTION : 37.15 %  
 Alpha-1 PHASE FRACTION : 62.85 %  
 TOTAL PARTICLE NO. : 334  
 AVERAGE OF AREA: .006216656 (mm<sup>2</sup>)



PARTICLE FRACTION : 50.05 %  
 Alpha-1 PHASE FRACTION : 49.95 %  
 TOTAL PARTICLE NO. : 477  
 AVERAGE OF AREA: .025939362 (mm<sup>2</sup>)



THE PARTICLE SIZE OF GAMMA PHASE DISTRIBUTION  
 SPECIMEN : HC5  
 TEMPERATURE: 450 deg. C

PHASE FRACTION : 55.73 %  
 PHASE FRACTION : 44.27 %  
 PARTICLE NO. : 375  
 AREA OF AREA: .008372613 (mm<sup>2</sup>)

NO-A177 376

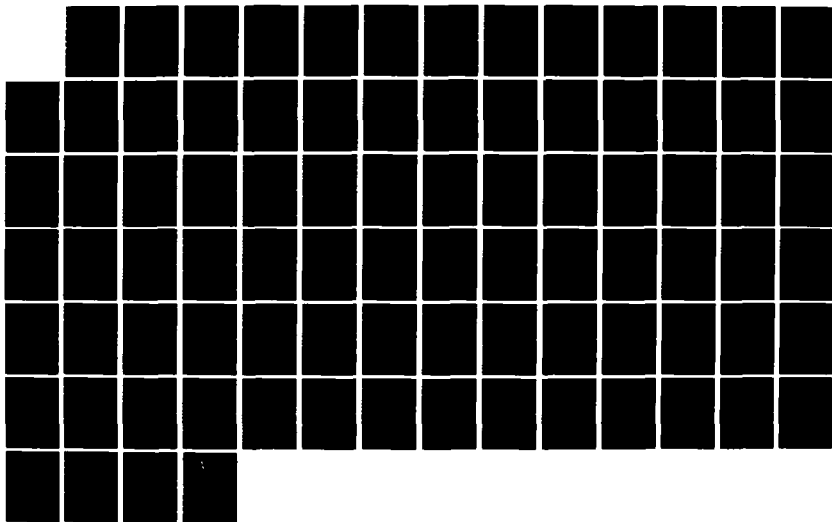
ORDERED CARBON - METAL ALLOYS FOR EXTRATERRESTRIAL  
POWER SYSTEMS(U) AUBURN UNIV AL DEPT OF MECHANICAL  
ENGINEERING B A CHIN ET AL 88 DEC 86 862BC2ETPS  
AFOSR-TR-87-0101 AFOSR-83-0168

3/3

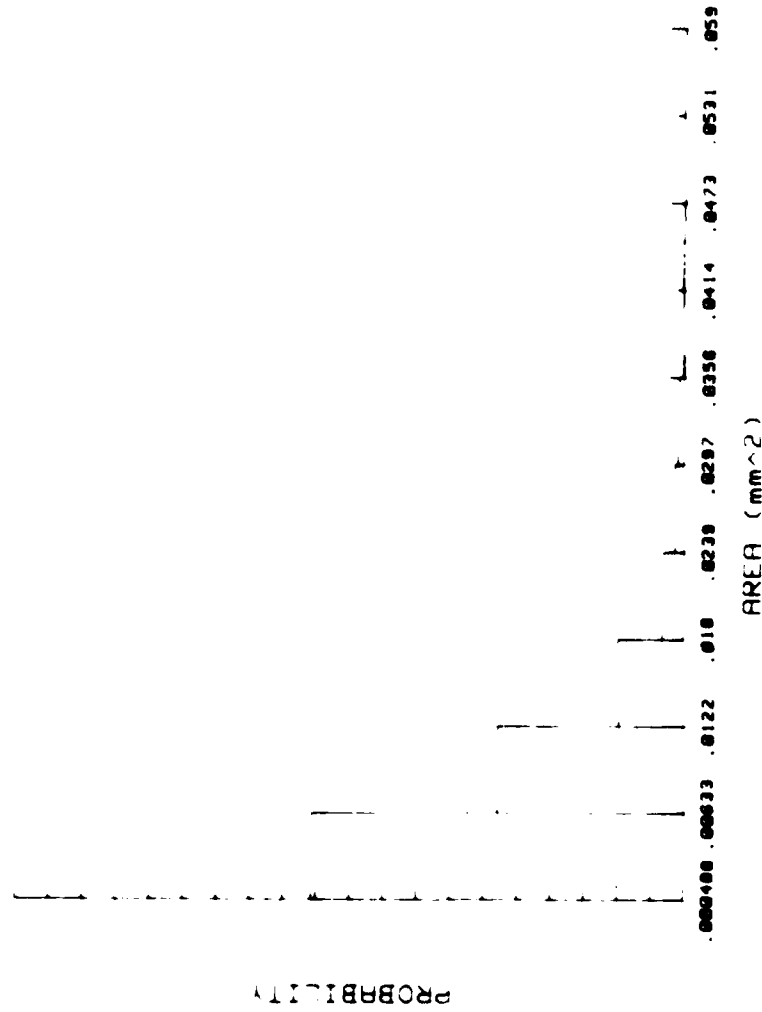
UNCLASSIFIED

F/G 11/6

NL

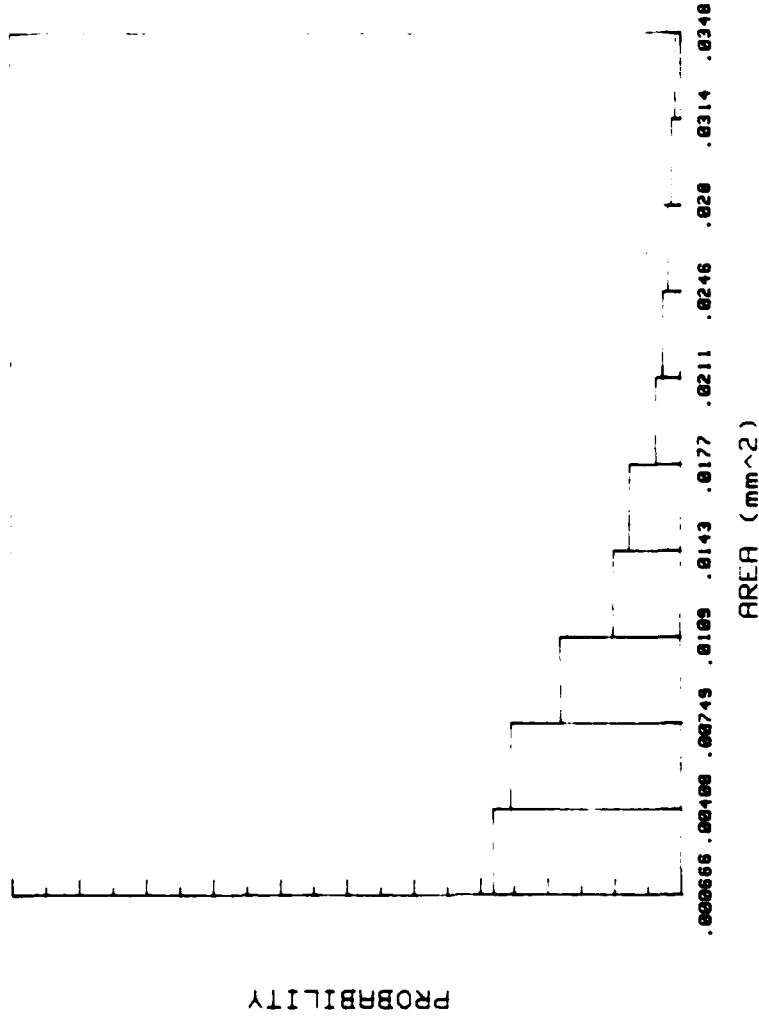






THE PARTICLE SIZE OF GAMMA PHASE DISTRIBUTION  
 SPECIMEN : HC6  
 TEMPERATURE: 450 deg. C

PARTICLE FRACTION : 52.38 %  
 ALPHA-T1 PHASE FRACTION : 42.62 %  
 TOTAL PARTICLE NO. : 436  
 AVERAGE OF AREA: .007415342 (mm<sup>2</sup>)



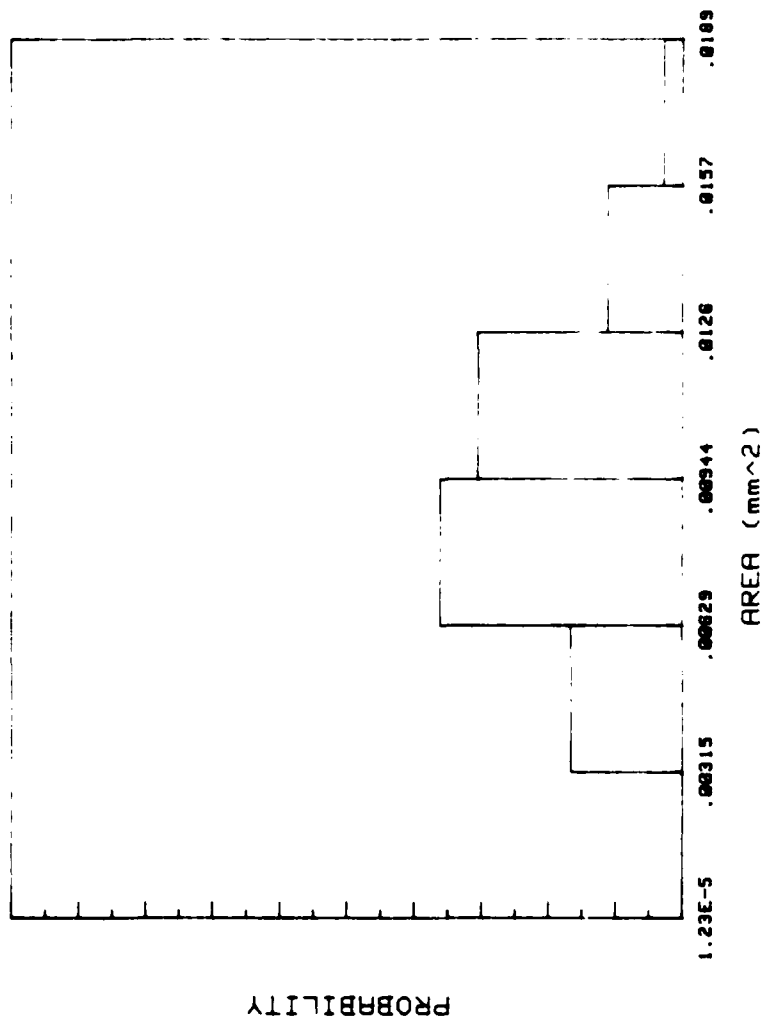
THE PARTICLE SIZE OF GAMMA PHASE DISTRIBUTION  
 SPECIMEN : HC7  
 TEMPERATURE: 450 deg. C

PARTICLE FRACTION : 58.17 %  
 ALPHA-T1 PHASE FRACTION : 41.83 %  
 TOTAL PARTICLE NO. : 372  
 AVERAGE OF AREA: .008709333 (mm<sup>2</sup>)

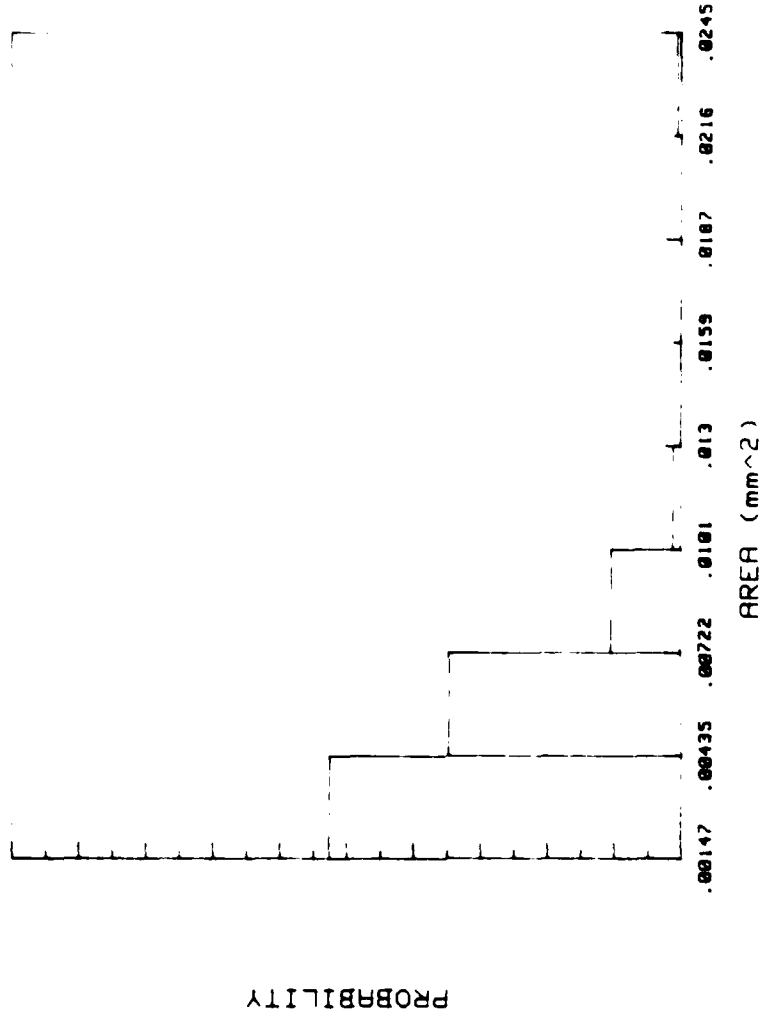


PARTICLE FRACTION : 11.23 %  
 Alpha-T1 PHASE FRACTION : 88.77 %  
 TOTAL PARTICLE NO. : 36  
 AVERAGE OF AREA: .009479142 (mm<sup>2</sup>)

186

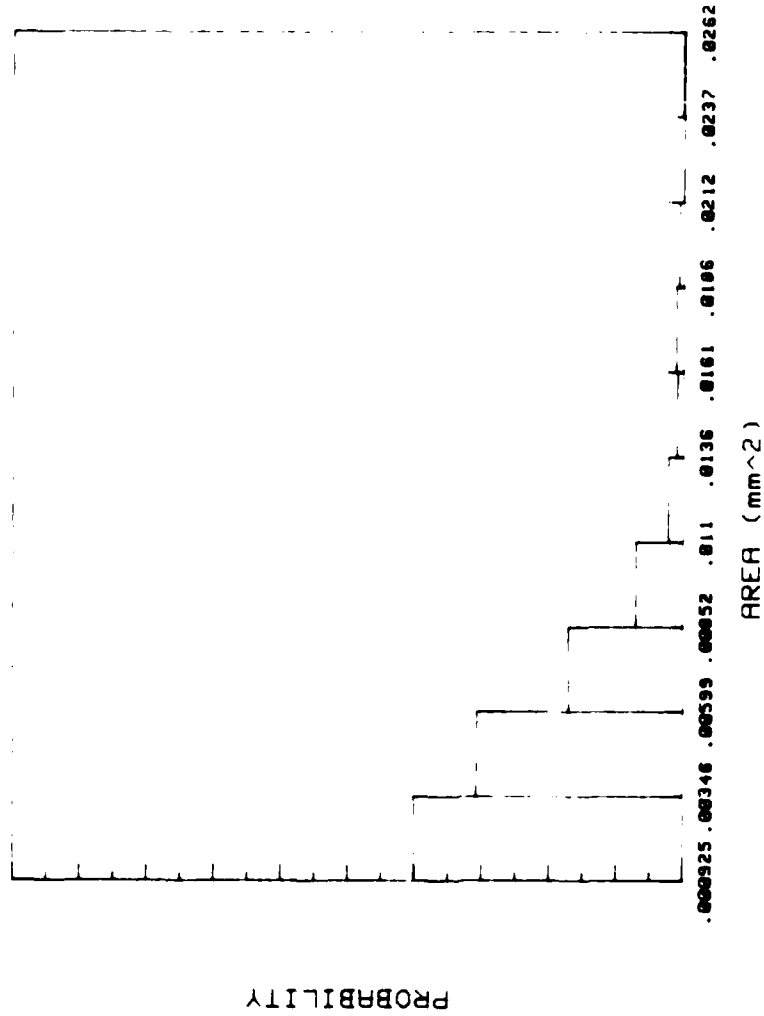


THE PARTICLE SIZE OF GAMMA PHASE DISTRIBUTION  
 SPECIMEN : HD1  
 TEMPERATURE: 550 deg. C



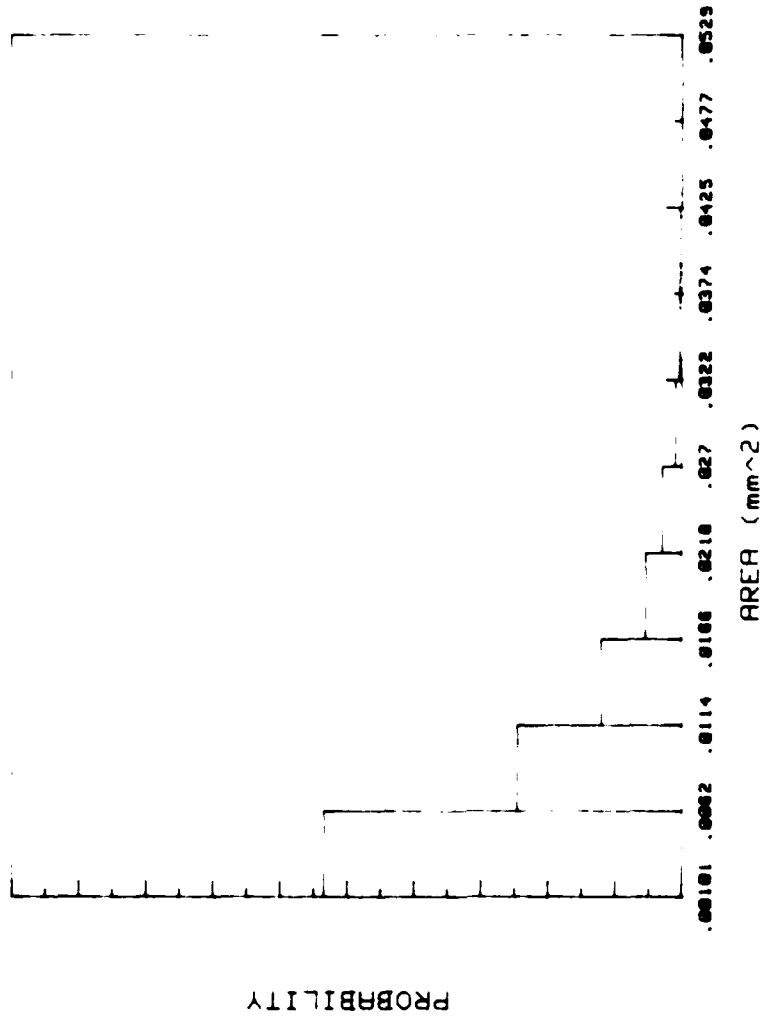
THE PARTICLE SIZE OF GAMMA PHASE DISTRIBUTION  
 SPECIMEN : HD2  
 TEMPERATURE: 550 deg. C

PARTICLE FRACTION : 24.39 %  
 Alpha-1 PHASE FRACTION : 75.61 %  
 TOTAL PARTICLE NO. : 173  
 AVERAGE OF AREA: .004667224 (mm<sup>2</sup>)



THE PARTICLE SIZE OF GAMMA PHASE DISTRIBUTION  
 SPECIMEN : HD3  
 TEMPERATURE: 550 deg. C

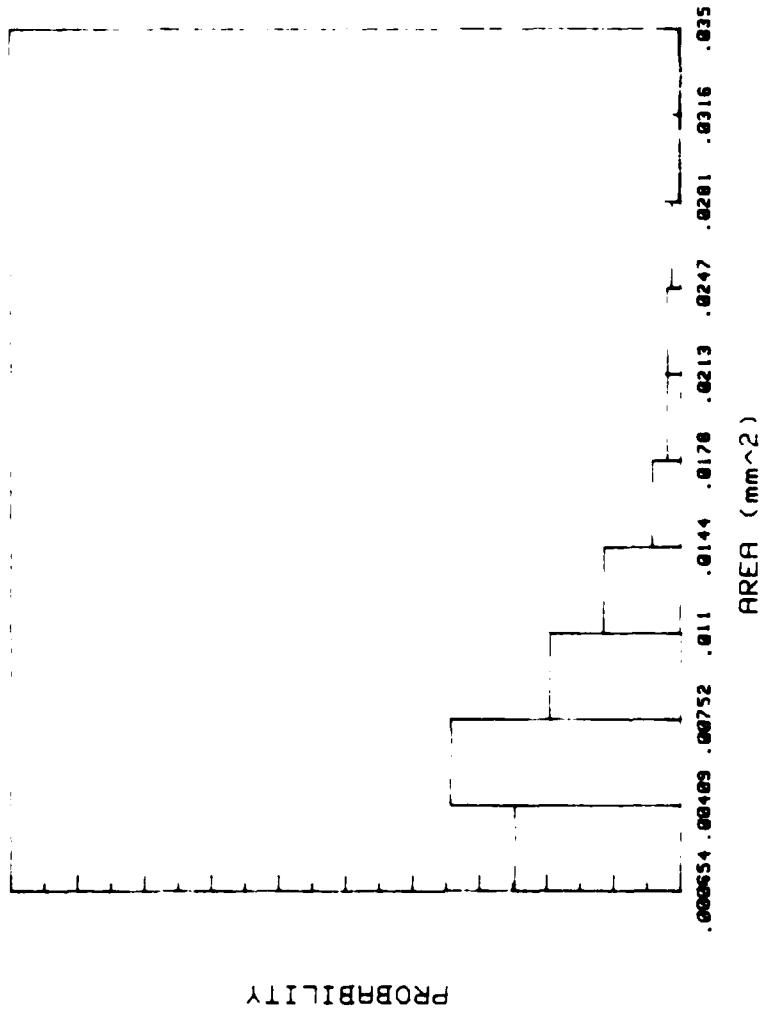
PARTICLE FRACTION : 40.31 %  
 Alpha-1 PHASE FRACTION : 59.69 %  
 TOTAL PARTICLE NO. : 459  
 AVERAGE OF AREA: .004983765 (mm<sup>2</sup>)



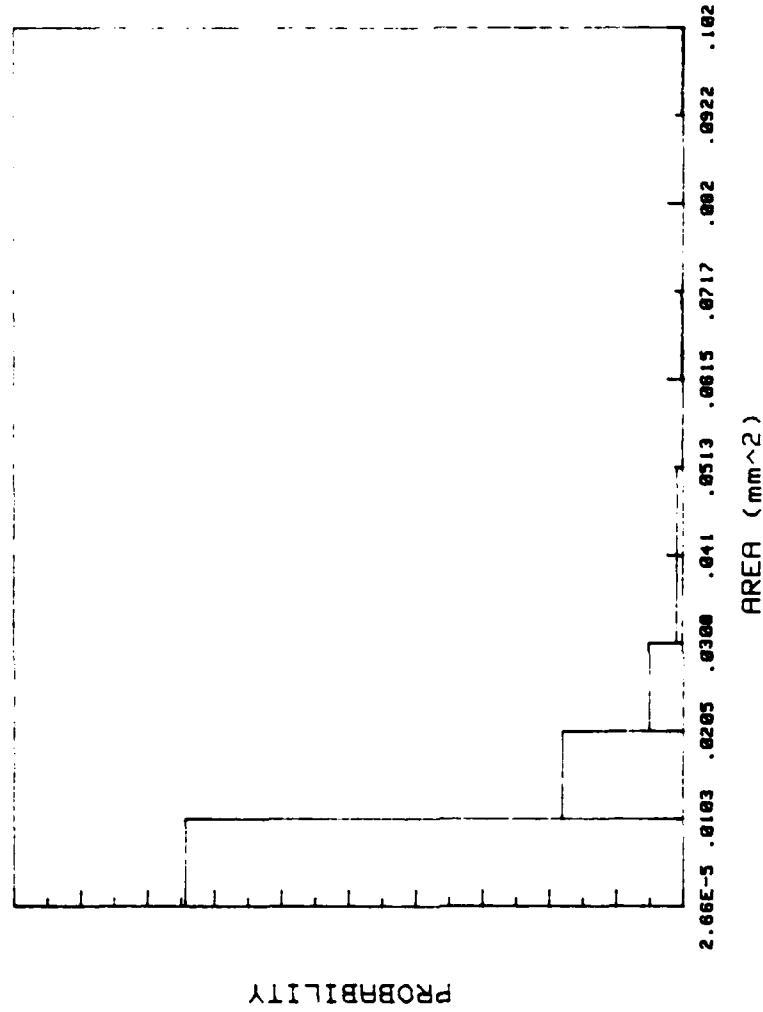
THE PARTICLE SIZE OF GAMMA PHASE DISTRIBUTION  
SPECIMEN : HD4  
TEMPERATURE: 550 deg. C

PARTICLE FRACTION : 55.05 %  
ALPHA-T) PHASE FRACTION : 44.95 %  
TOTAL PARTICLE NO. : 318  
AVERAGE OF AREA: .009703594 (mm<sup>2</sup>)

PARTICLE FRACTION : 57.12 %  
 Alpha-1 PHASE FRACTION : 42.88 %  
 TOTAL PARTICLE NO. : 405  
 AVERAGE OF AREA: .007946377 (mm<sup>2</sup>)

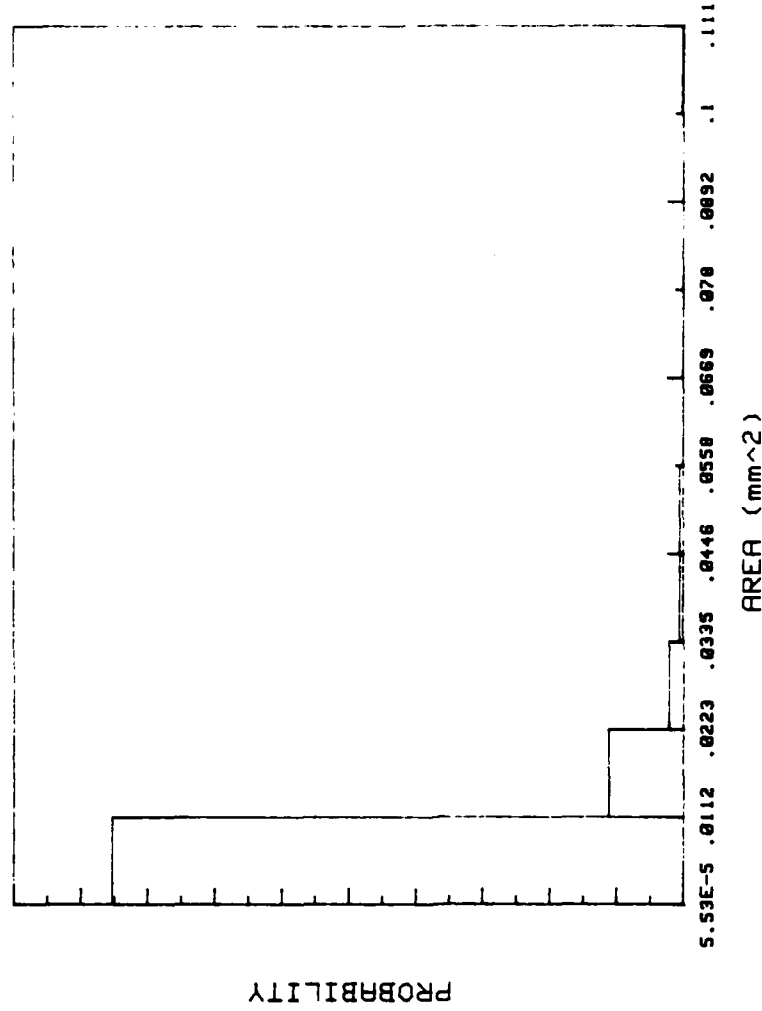


THE PARTICLE SIZE OF GAMMA PHASE DISTRIBUTION  
 SPECIMEN : HD5  
 TEMPERATURE: 550 deg. C



THE PARTICLE SIZE OF GAMMA PHASE DISTRIBUTION  
 SPECIMEN : HD6  
 TEMPERATURE: 550 deg. C

PARTICLE FRACTION : 63.91 %  
 Alpha-TI PHASE FRACTION : 36.09 %  
 TOTAL PARTICLE NO. : 433  
 AVERAGE OF AREA: .0082883 (mm<sup>2</sup>)



# THE PARTICLE SIZE OF GAMMA PHASE DISTRIBUTION

SPECIMEN : HD7

TEMPERATURE: 550 deg. C

PARTICLE FRACTION : 69.04 %  
 Alpha-1: PHASE FRACTION : 30.96 %  
 TOTAL PARTICLE NO. : 557  
 AVERAGE OF AREA: .006996822 (mm<sup>2</sup>)



THE PARTICLE SIZE OF GAMMA PHASE DISTRIBUTION  
 SPECIMEN : HE1  
 TEMPERATURE: 850 deg. C

PARTICLE FRACTION : 10.02 %  
 Alpha-Ti PHASE FRACTION : 89.98 %  
 TOTAL PARTICLE NO. : 89  
 AVERAGE OF AREA: .009479142 (mm<sup>2</sup>)





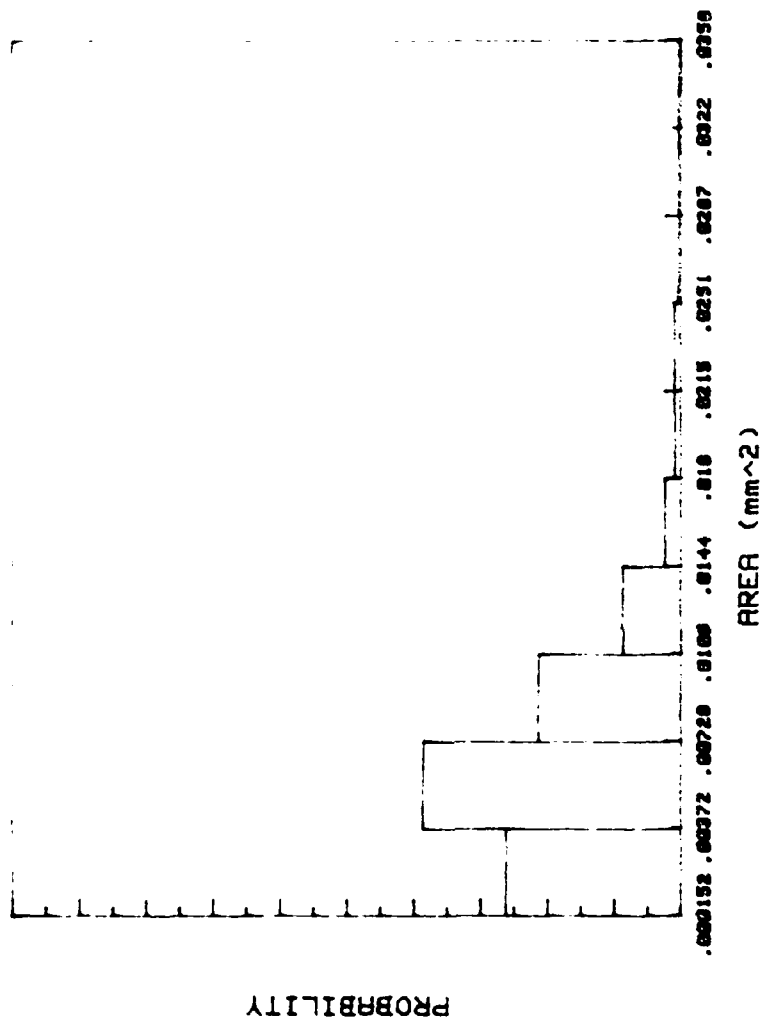
AREA (cm<sup>2</sup>)

THE PARTICLE SIZE OF GAMMA PHASE DISTRIBUTION

SPECIMEN : HE2

TEMPERATURE: 850 deg. C

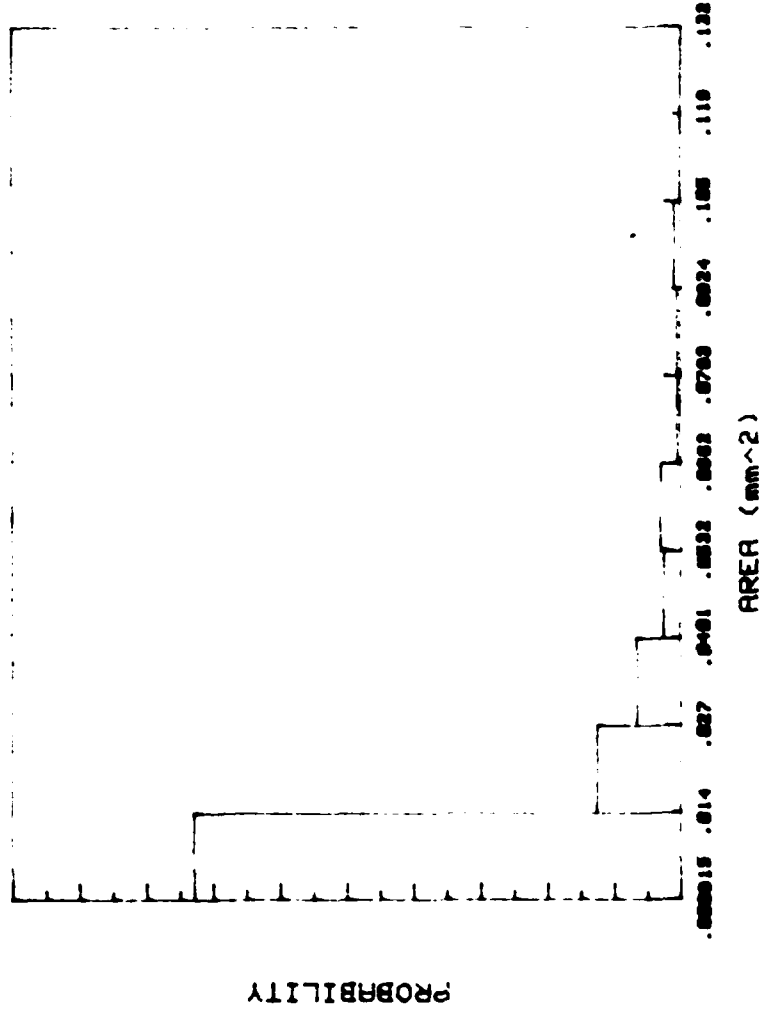
PARTICLE FRACTION : 21.53 %  
 Alpha-1 PHASE FRACTION : 78.47 %  
 TOTAL PARTICLE NO. : 176  
 AVERAGE OF AREA: .008530059 (cm<sup>2</sup>)



THE PARTICLE SIZE OF GAMMA PHASE DISTRIBUTION  
 SPECIMEN : HE3  
 TEMPERATURE: 850 deg. C

PARTICLE FRACTION : 41.29 %  
 Alpha-Ti PHASE FRACTION : 58.71 %  
 TOTAL PARTICLE NO. : 347  
 AVERAGE OF AREA: .006694694 (mm<sup>2</sup>)





THE PARTICLE SIZE OF GAMMA PHASE DISTRIBUTION  
 SPECIMEN : ME5  
 TEMPERATURE: 850 deg. C

PARTICLE FRACTION : 60.38 %  
 Alpha-TI PHASE FRACTION : 39.62 %  
 TOTAL PARTICLE NO. : 199  
 AVERAGE OF AREA: .01708092 (mm^2)

APPENDIX C

ROOM TEMPERATURE COMPRESSION PROPERTIES

Specimen	True MFS (Ksi)	YS	True $\epsilon_f$ (%)	%Gamma Phase
W1	189	166	1.8	82
W2	152	124	2.1	74
W3	183	136	3.2	72
W4	134	106	5.4	65
I1	142	60	10	49
I2	174	94	9.9	43
I3	160	74	10.5	33
I4	170	75	11.2	41
I5	116	94	7.5	55
I6	146	82	9.1	46
I7	176	90	14.7	36
I8	180	96	10.3	39
I9	144	99	7.0	68
I10	132	80	10.8	35
I11	150	104	4.9	70
I12	148	76	13.2	36
I13	138	86	7.3	44
I14	156	96	8.0	46
I15	144	74	11.3	40
I16	114	85	11.3	36

(Continued)

Specimen	True MFS	YS	True $\epsilon_f$	%Gamma Phase
	(Ksi)		(%)	
I17	140	62	13.8	30
I18	166	103	7.8	68
I19	124	102	5.0	58
I20	174	78	13.7	36
I21	162	76	14.8	36
I22	124	84	8.3	51
I23	164	102	7.7	67
I24	183	63	16.6	30
I25	144	68	16.2	27
I26	164	66	17.1	27
I27	143	50	30.0	13
I28	154	60	25.0	20

APPENDIX D

ELEVATED TEMPERATURE COMPRESSION PROPERTIES

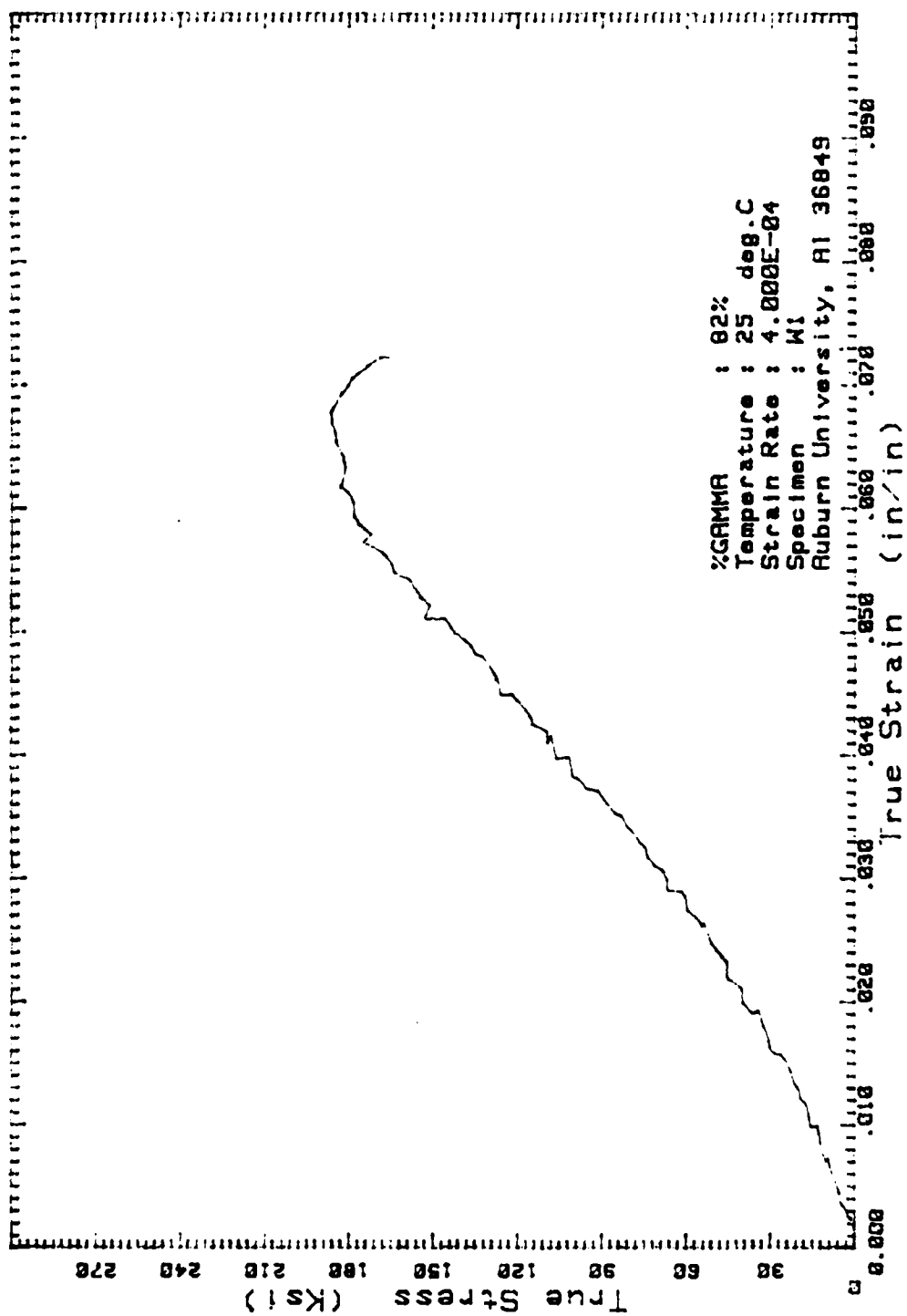


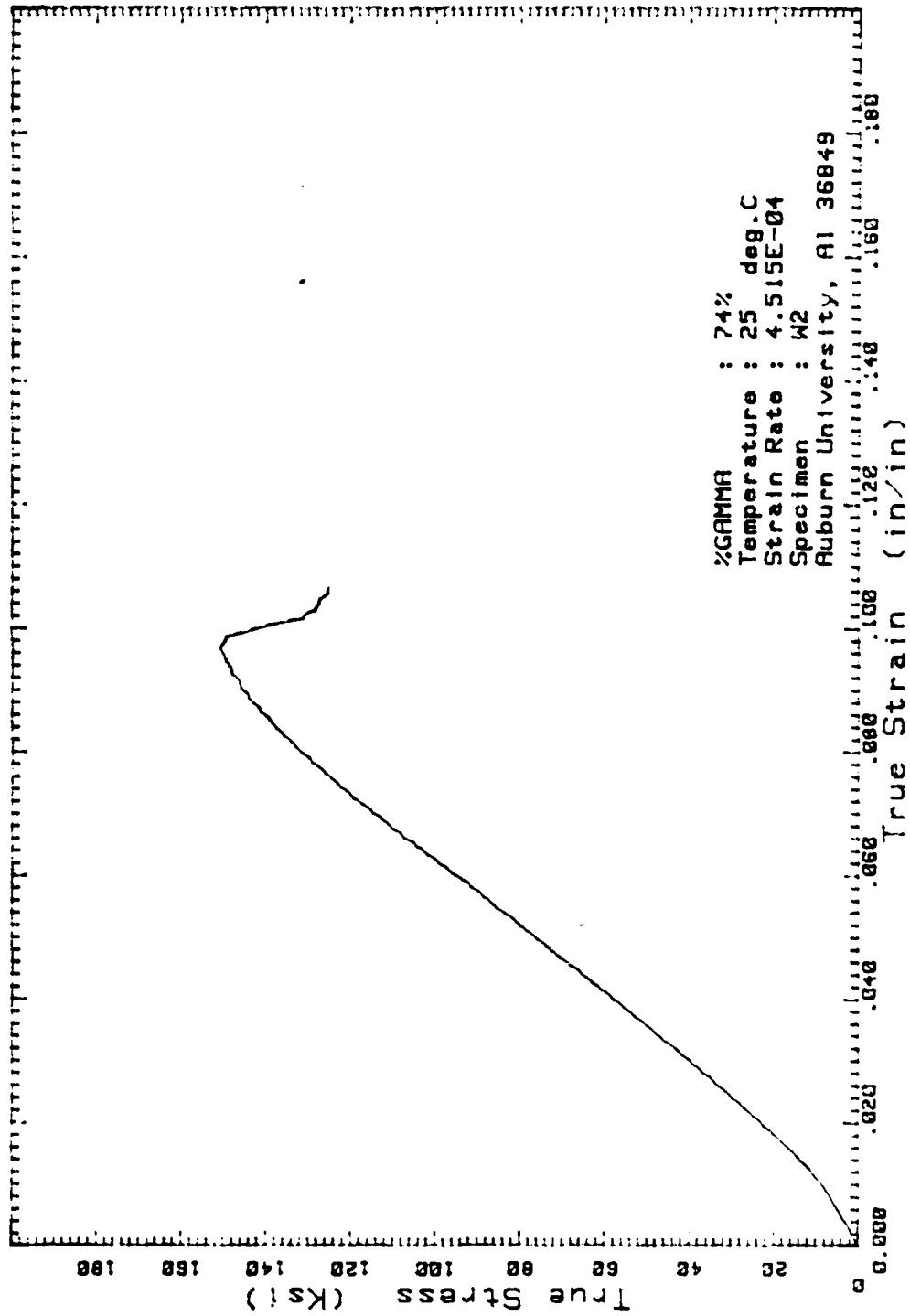
Specimen	True MFS (Ksi)	YS	True $\epsilon_f$ (%)	%Gamma Phase
HA1	62	29	18.2	10
HA2	89	38	14.8	22
HA3	108	60	8.6	40
HA4	160	65	6.8	57
HA5	156	90	4.9	60
HB1	50	18	23.9	10
HB2	41	33	17.4	22
HB3	86	34	16.6	30
HB4	82	47	10.4	40
HB5	95	55	9.5	43
HB6	116	66	9.1	57
HB7	122	82	5.4	59
HC1	34	18	24.7	10
HC2	53	23	23.9	22
HC3	84	35	17.4	37
HC4	79	50	15.7	50
HC5	99	61	14.0	56
HC6	103	64	13.1	57
HC7	106	70	11.3	58
HD1	30	10	27.8	10

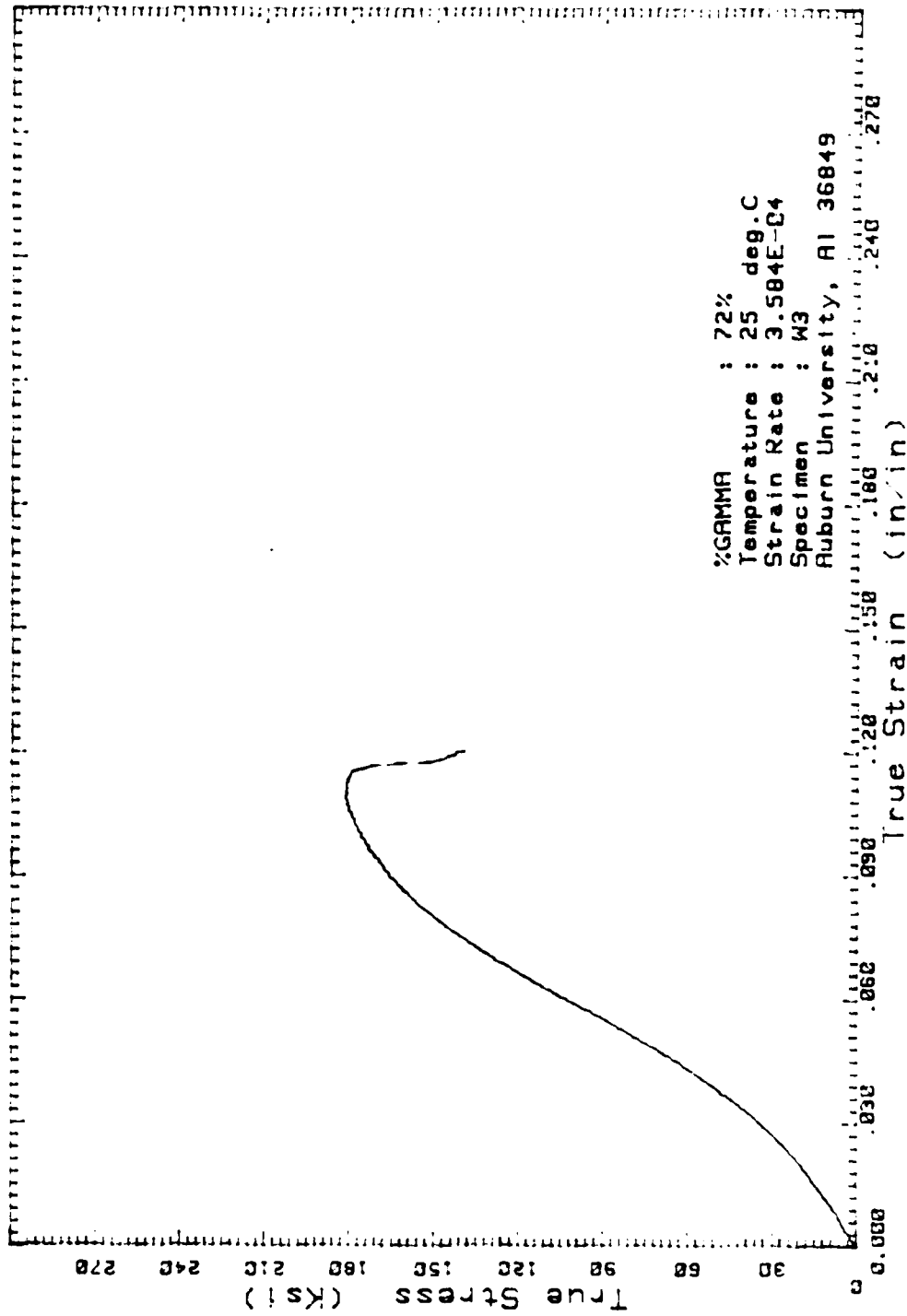
Specimen	True MFS (Ksi)	YS	True $\epsilon_f$ (%)	%Gamma Phase
HD2	26	16	23.9	22
HD3	60	34	18.2	40
HD4	57	47	15.7	55
HD5	63	50	11.3	57
HD6	77	51	9.5	64
HD7	88	53	9.4	69
HE1	10	5	37.4	10
HE2	28	7	34.2	22
HE3	30	14	31.1	40
HE4	30	21	26.2	57
HE5	35	25	23.5	60

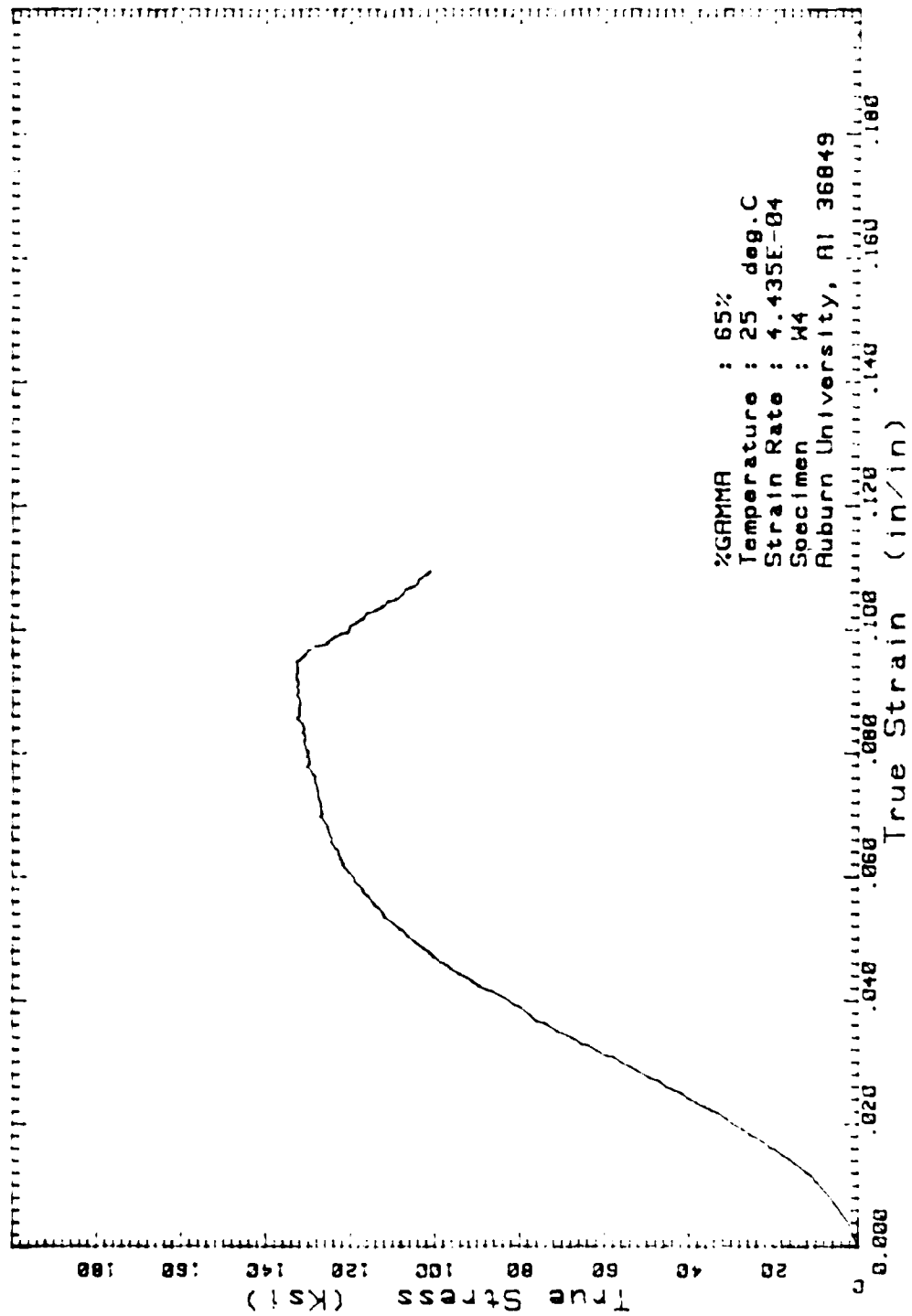
APPENDIX E

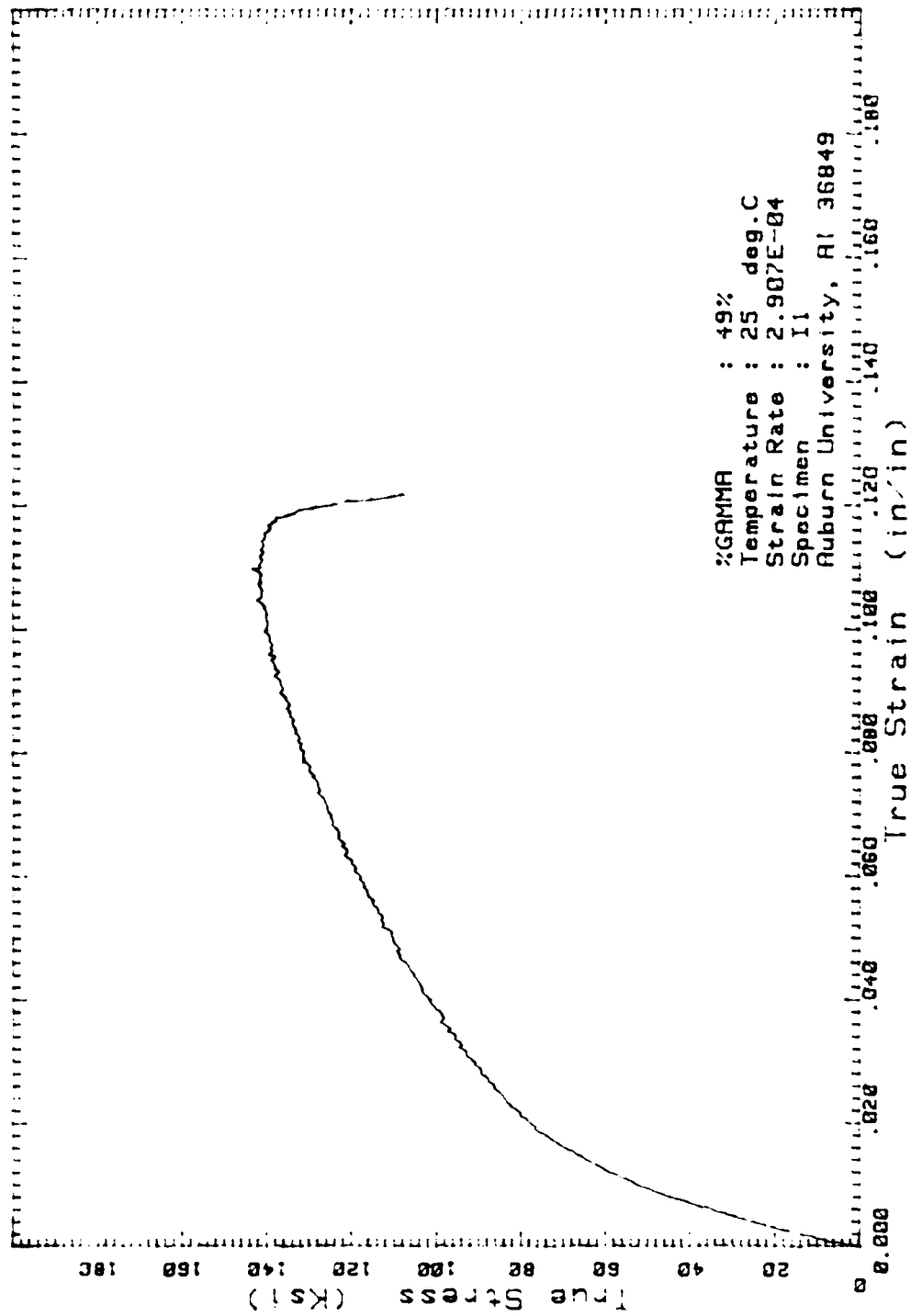
TRUE STRESS vs TRUE STRAIN CURVES FOR ALL COMPRESSION TESTS  
AT ROOM TEMPERATURE



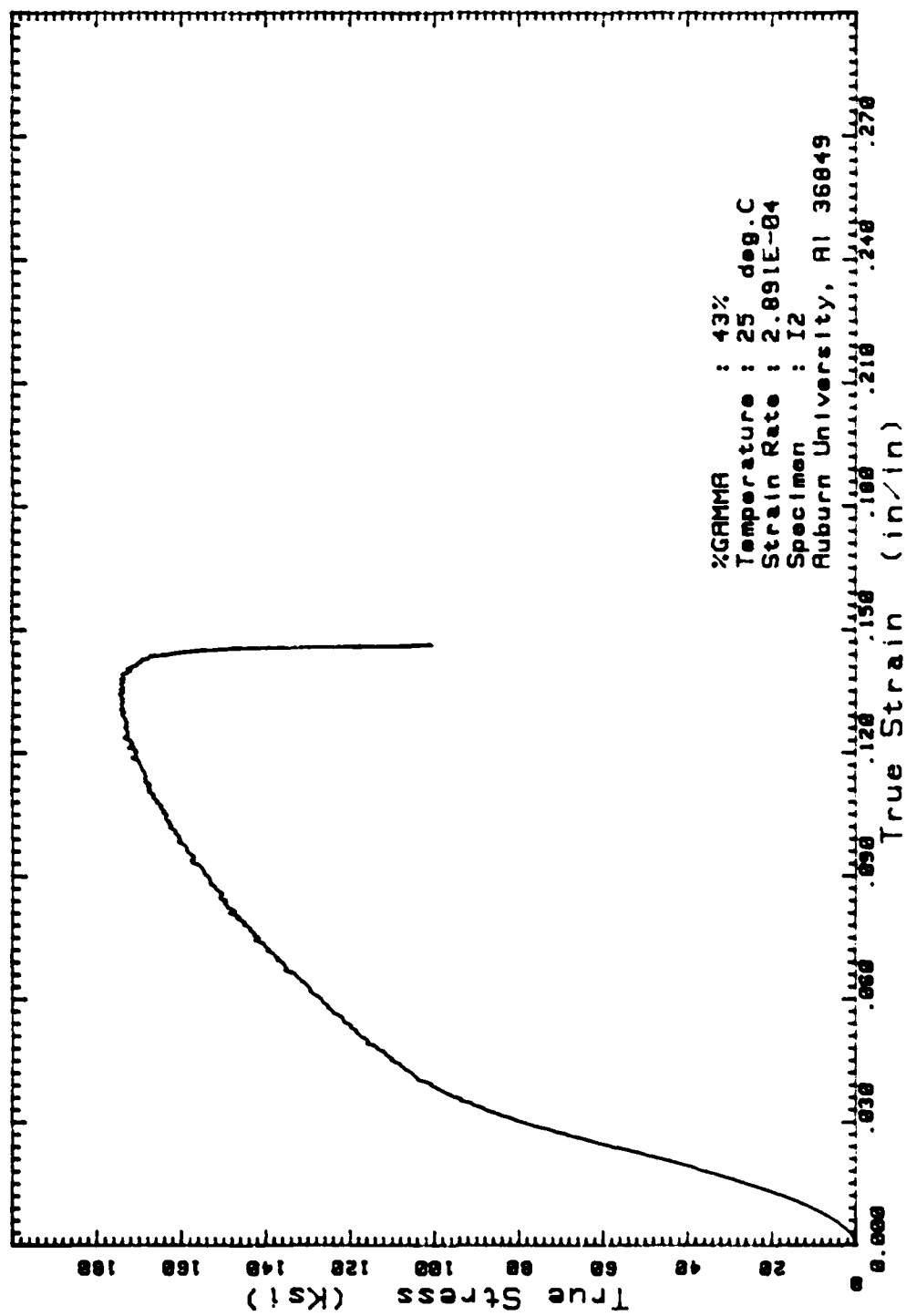


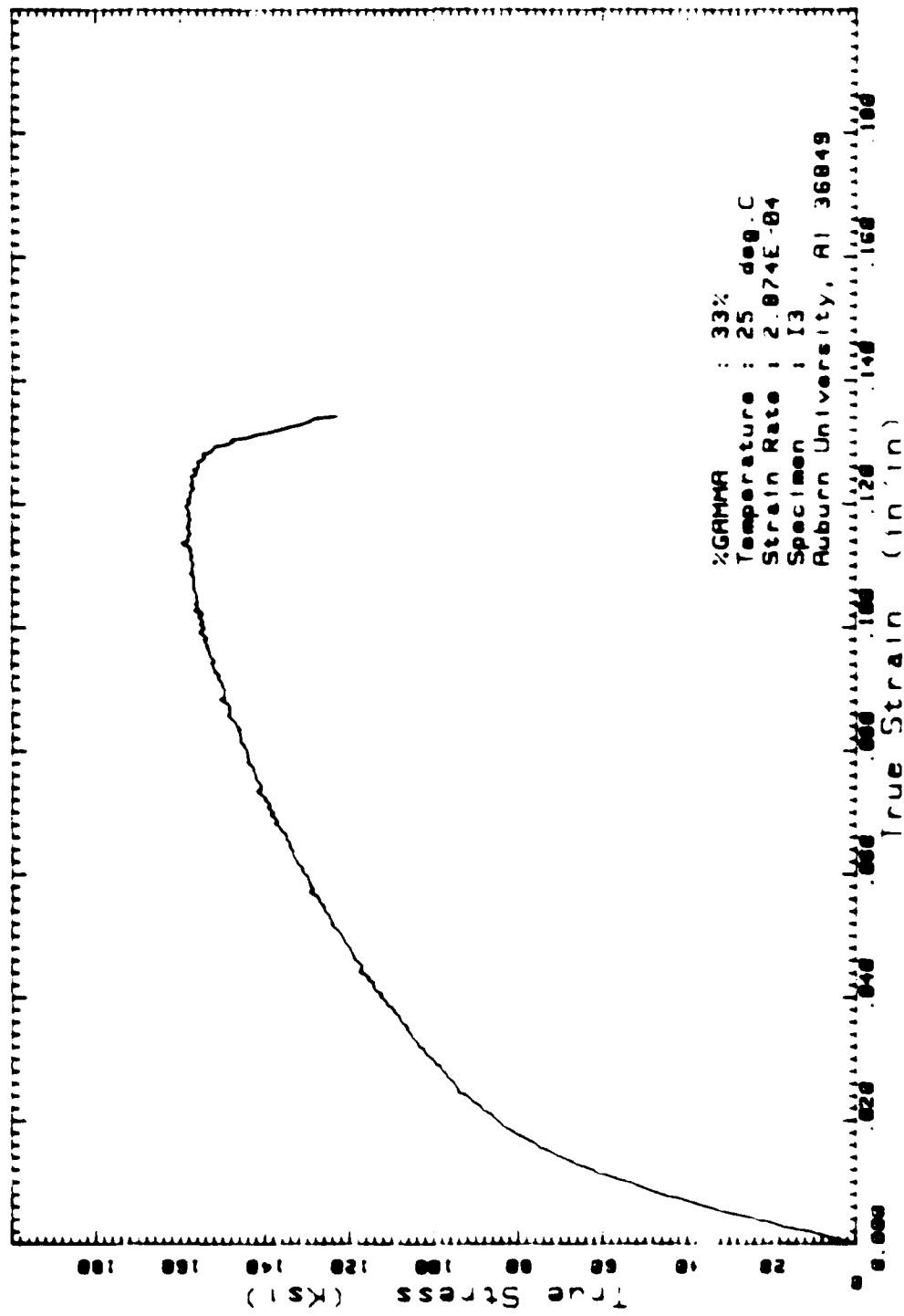


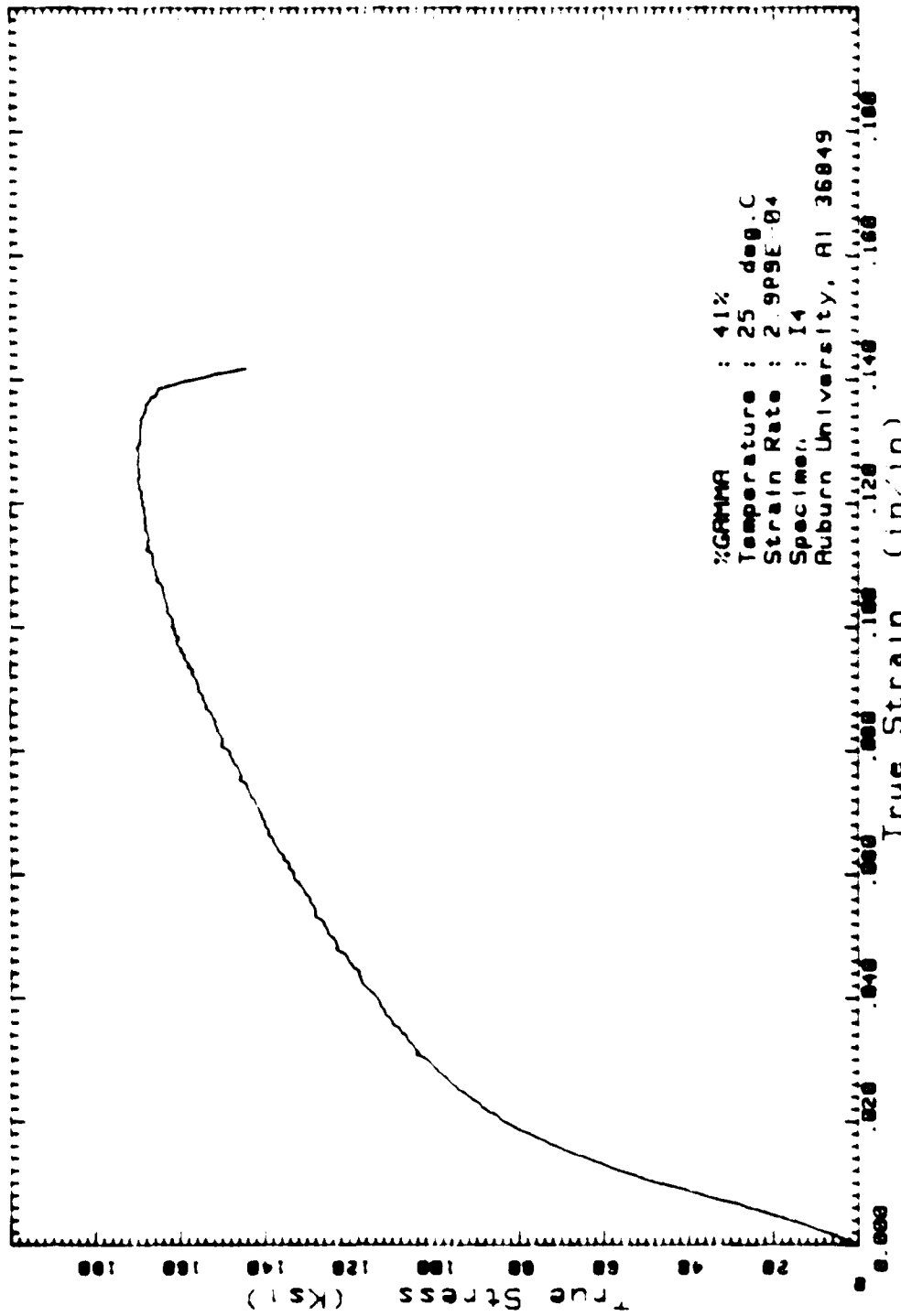




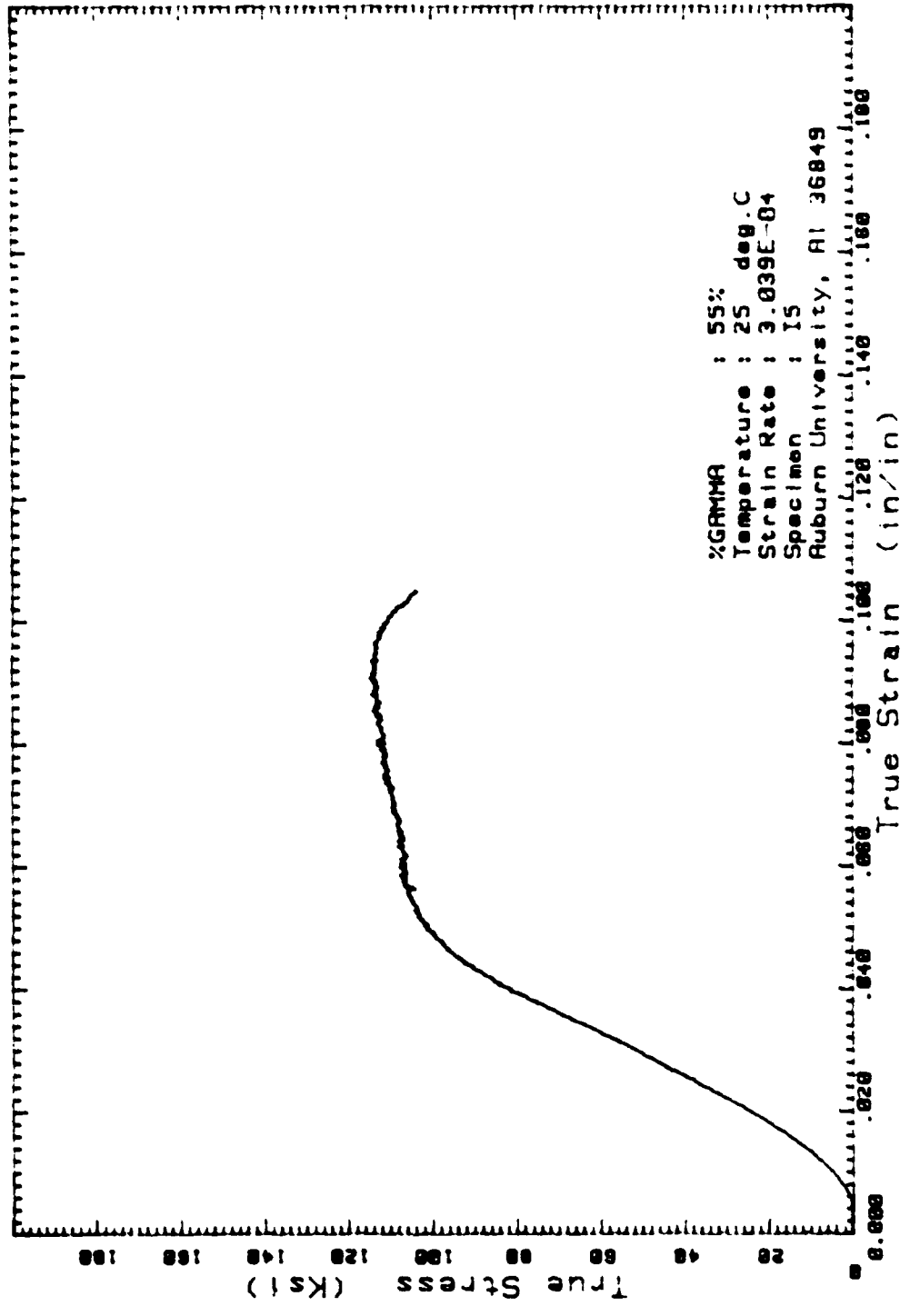


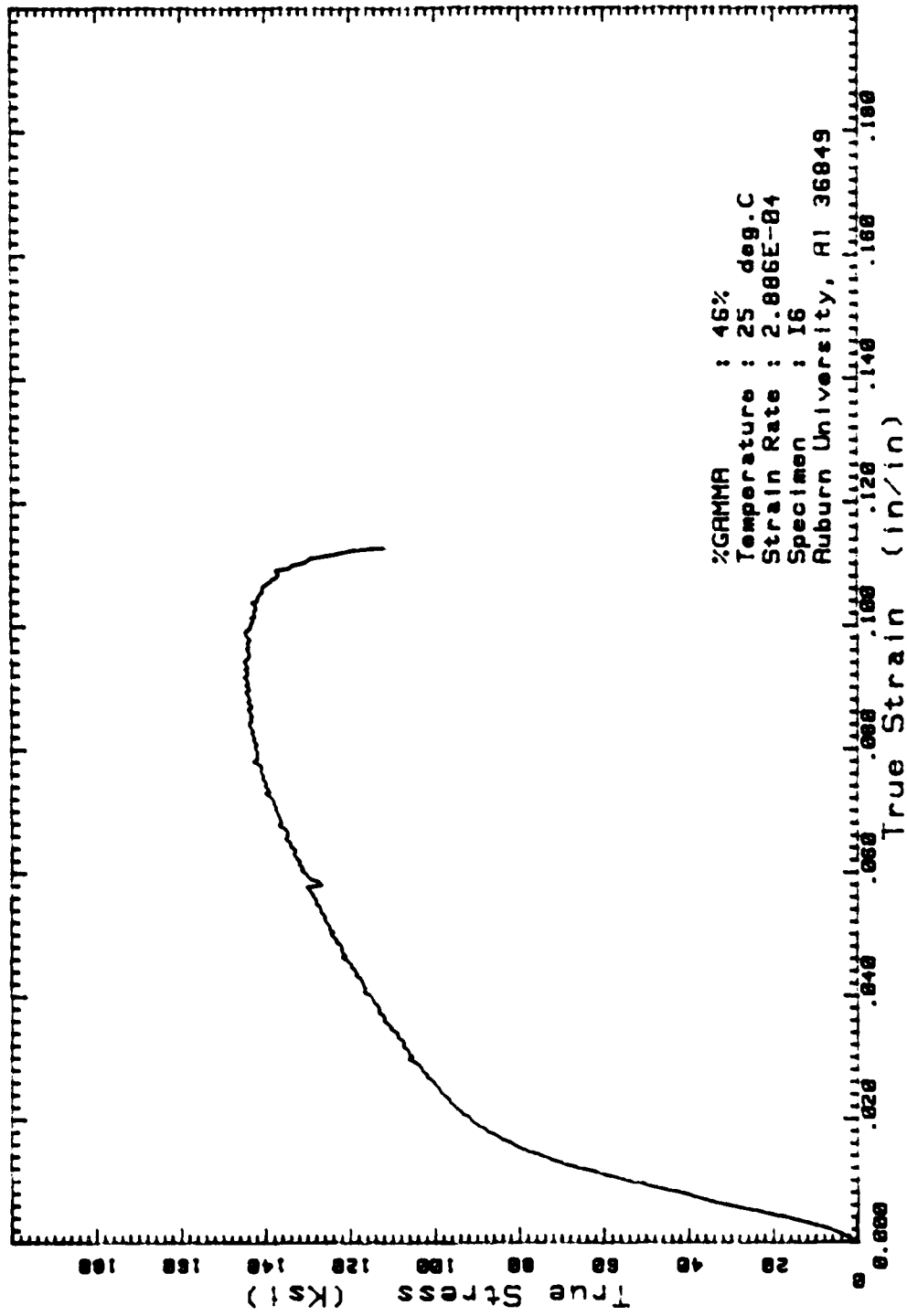


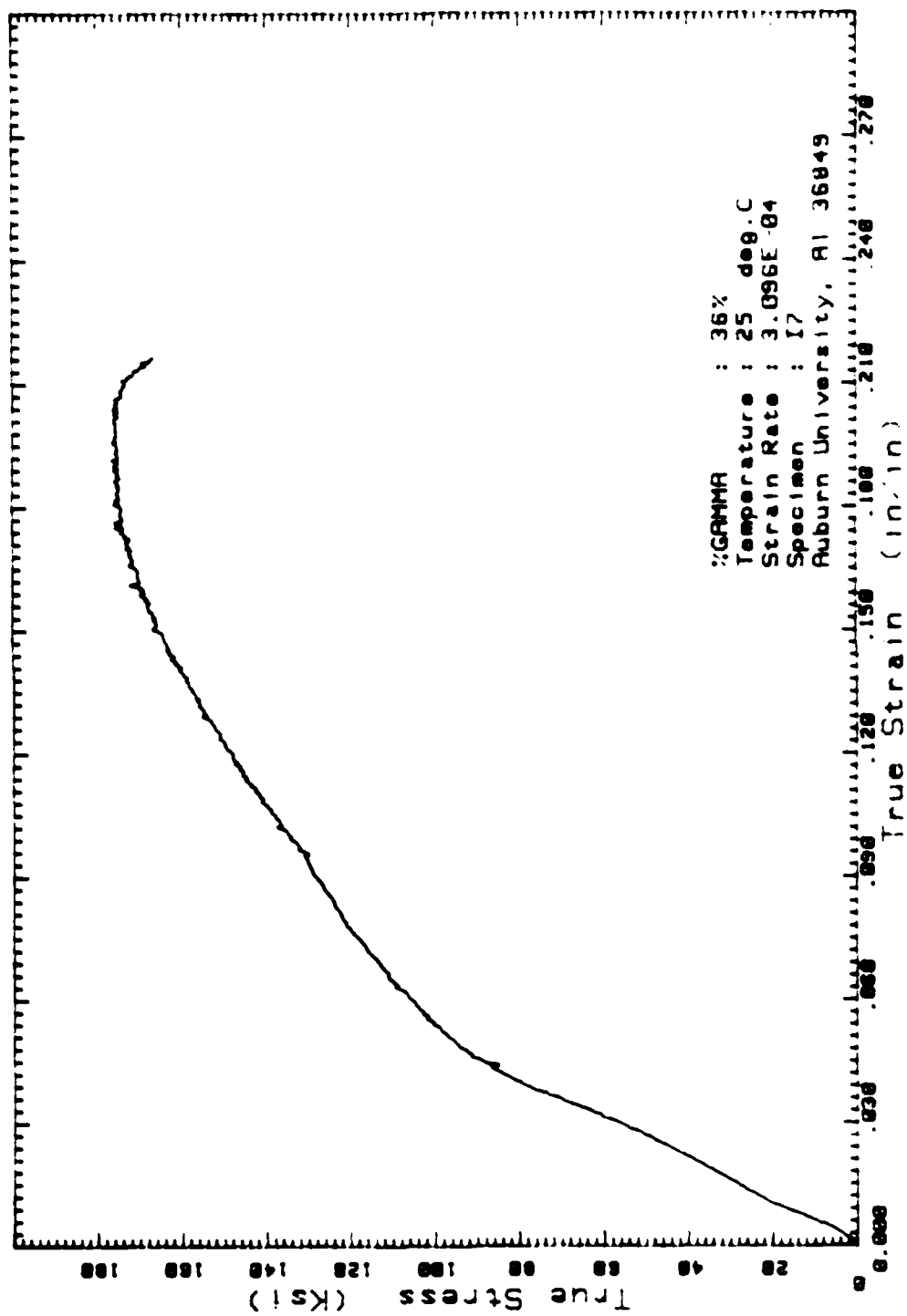


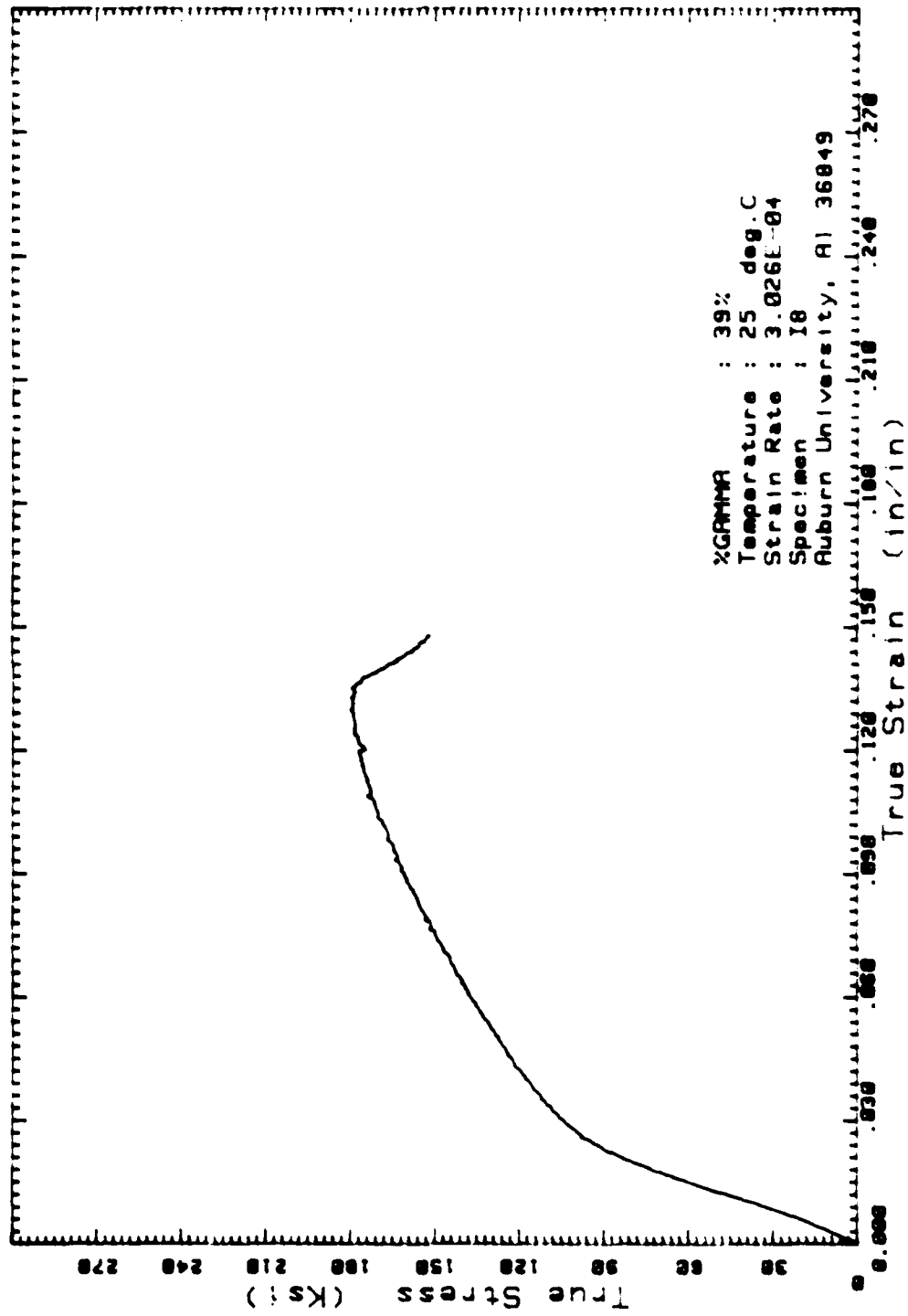


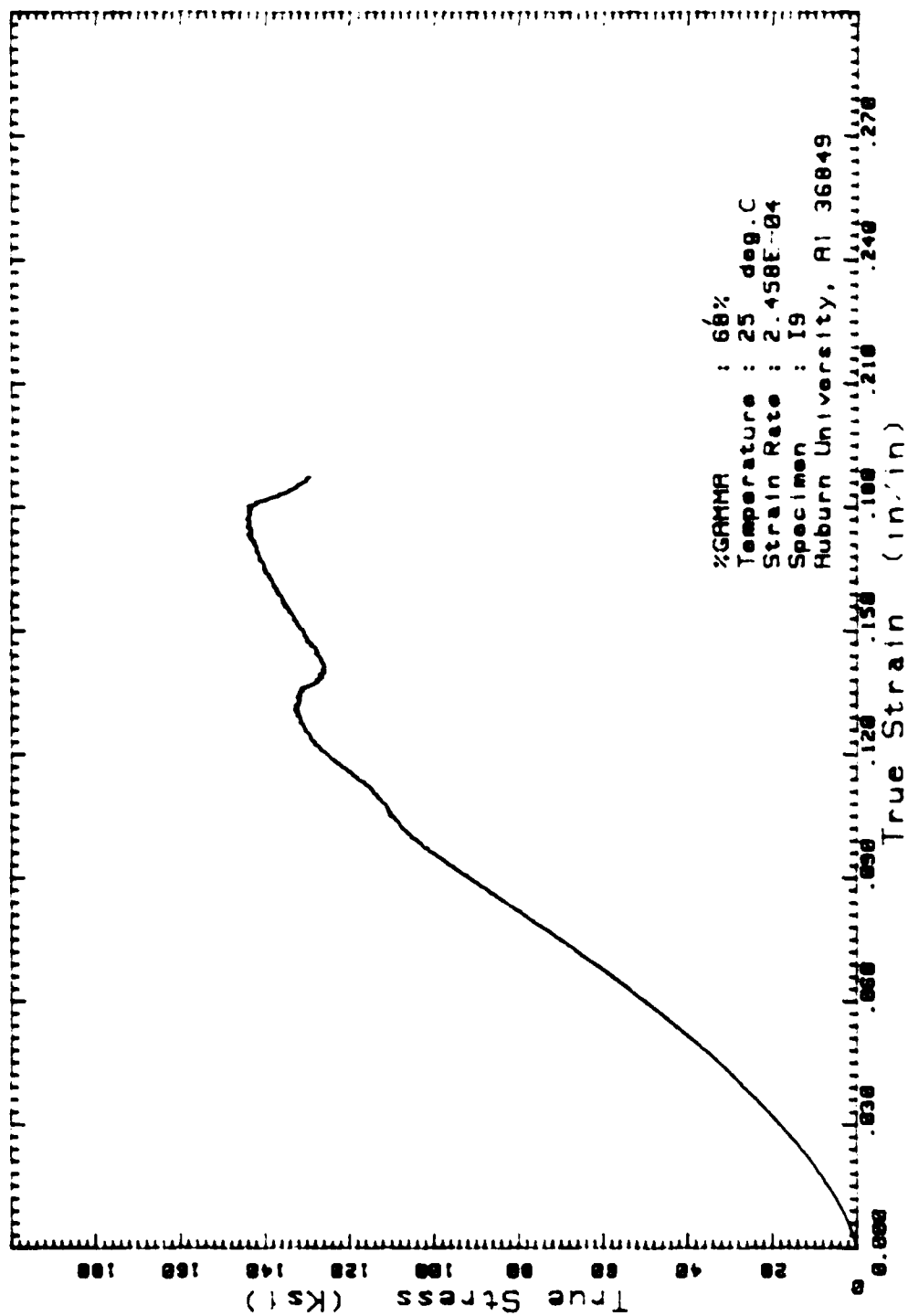
%GAMMA : 41%  
 Temperature : 25 deg.C  
 Strain Rate : 2.995E-04  
 Specimen : I4  
 Auburn University, AL 36849



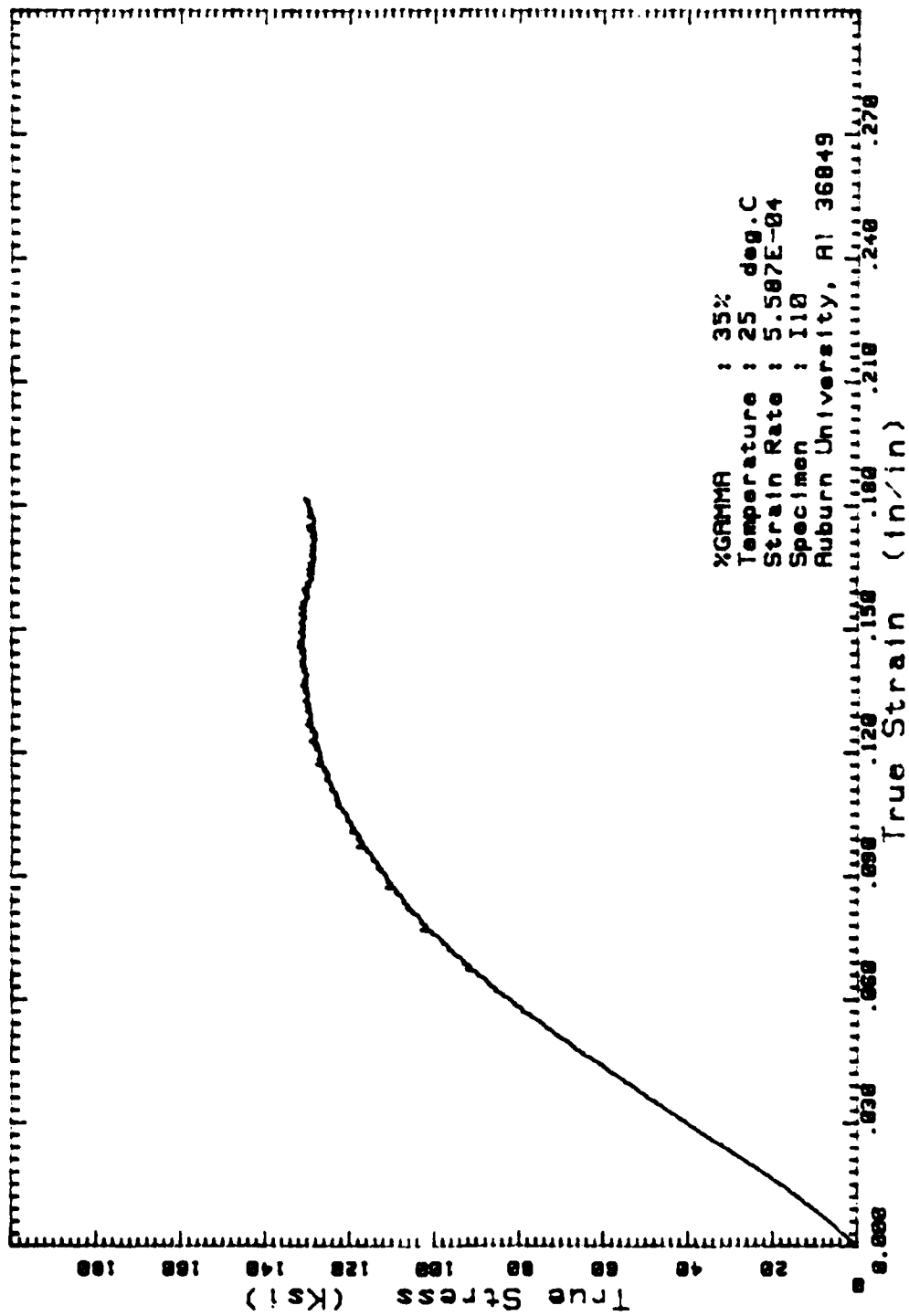


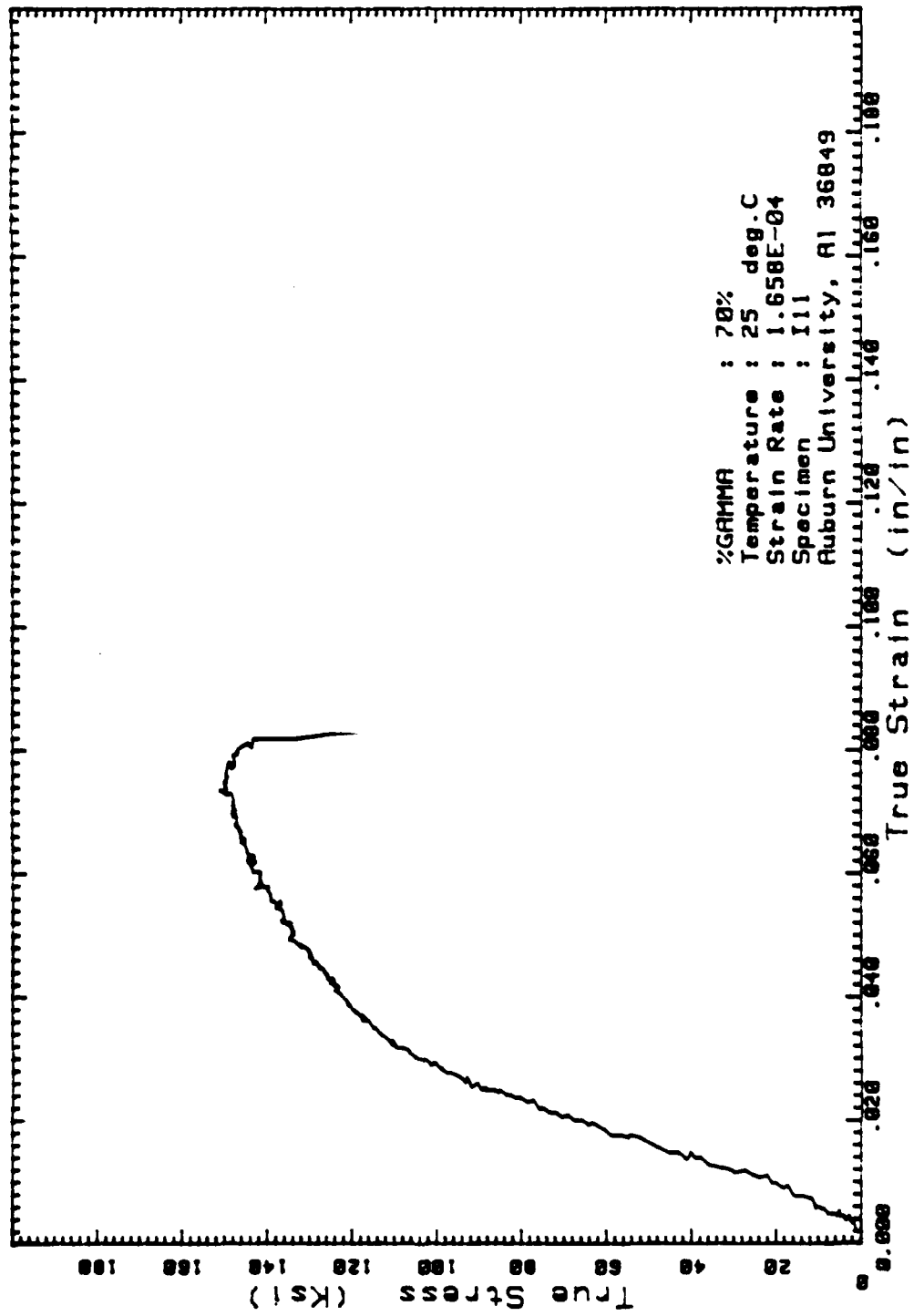


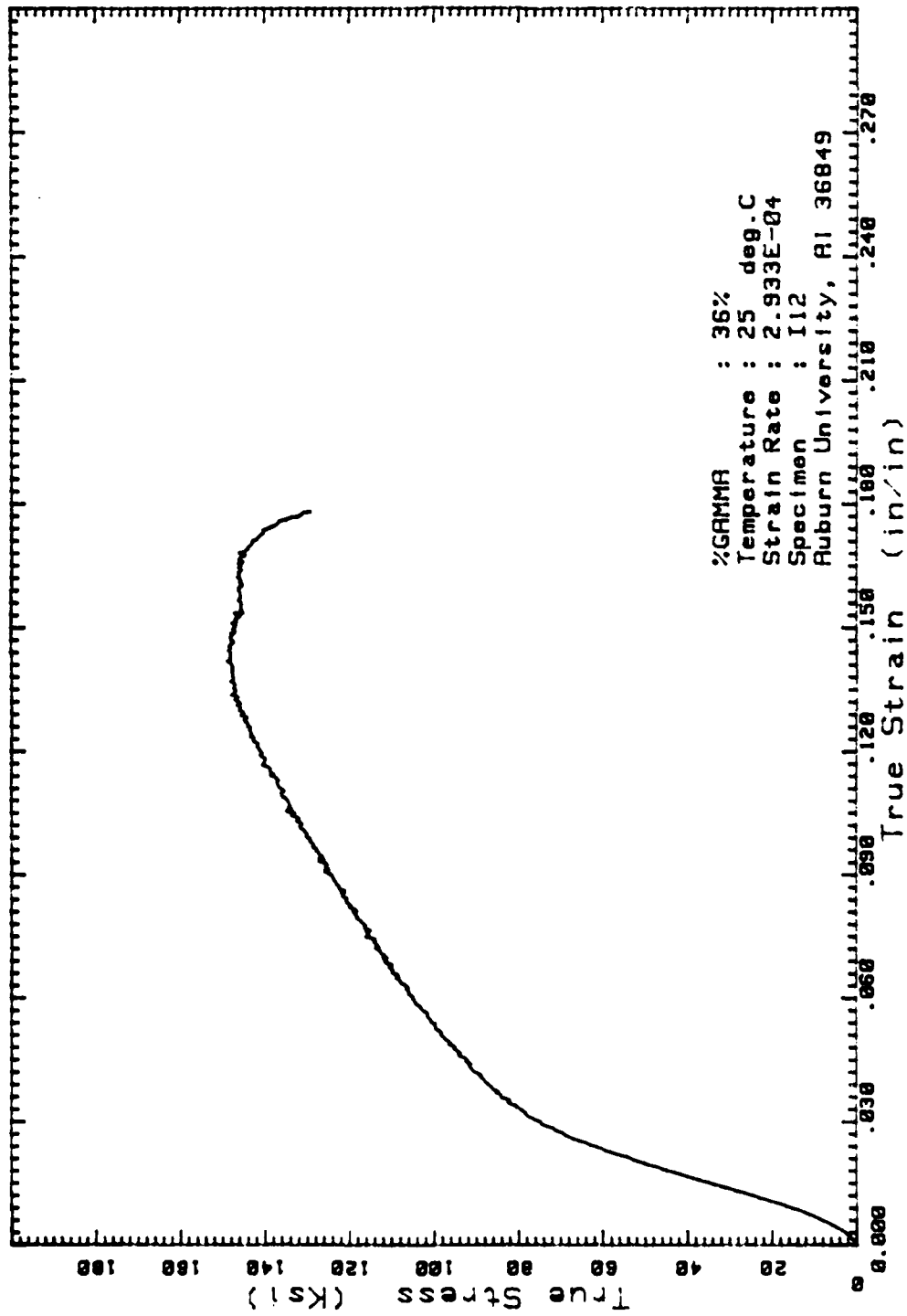


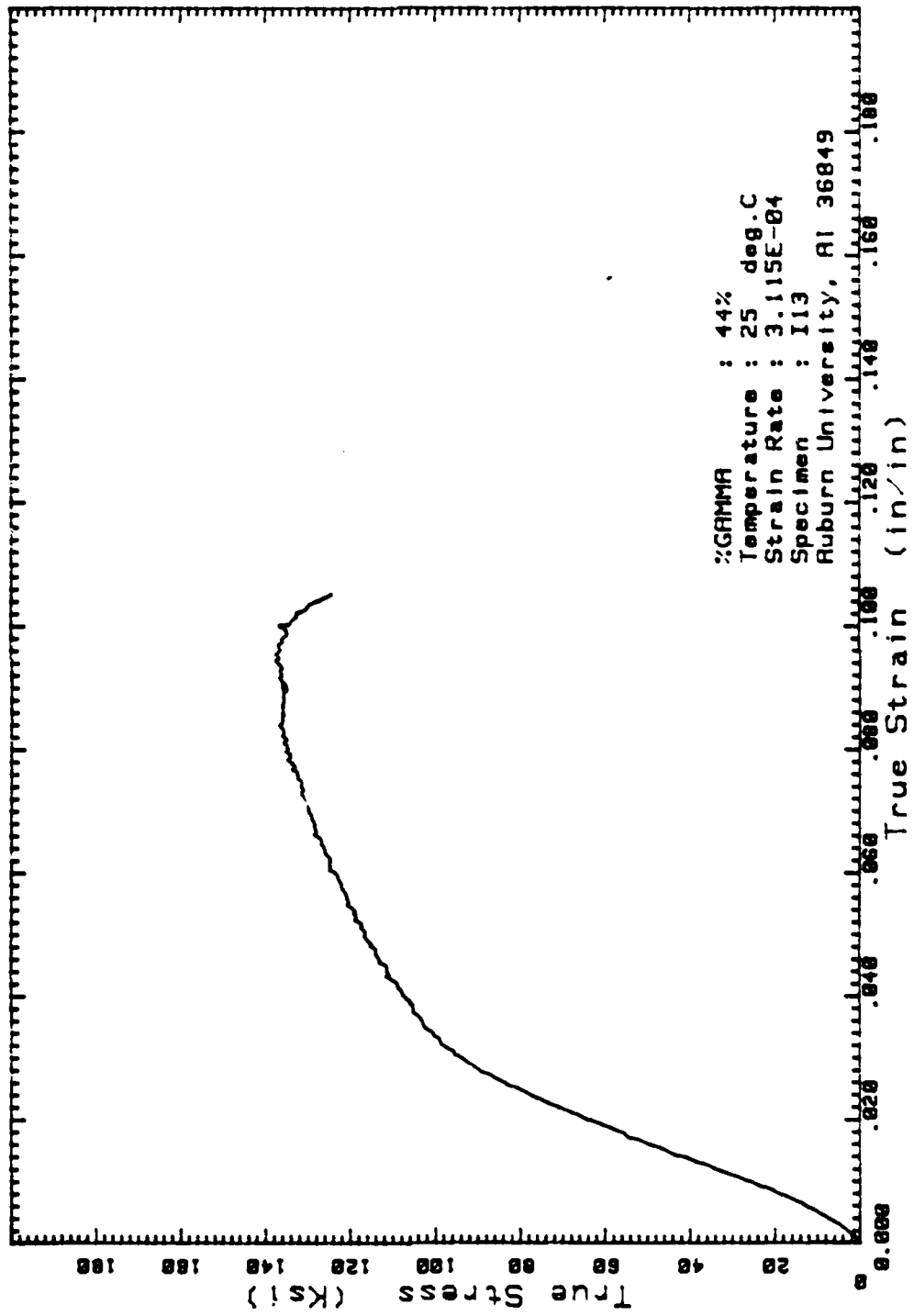


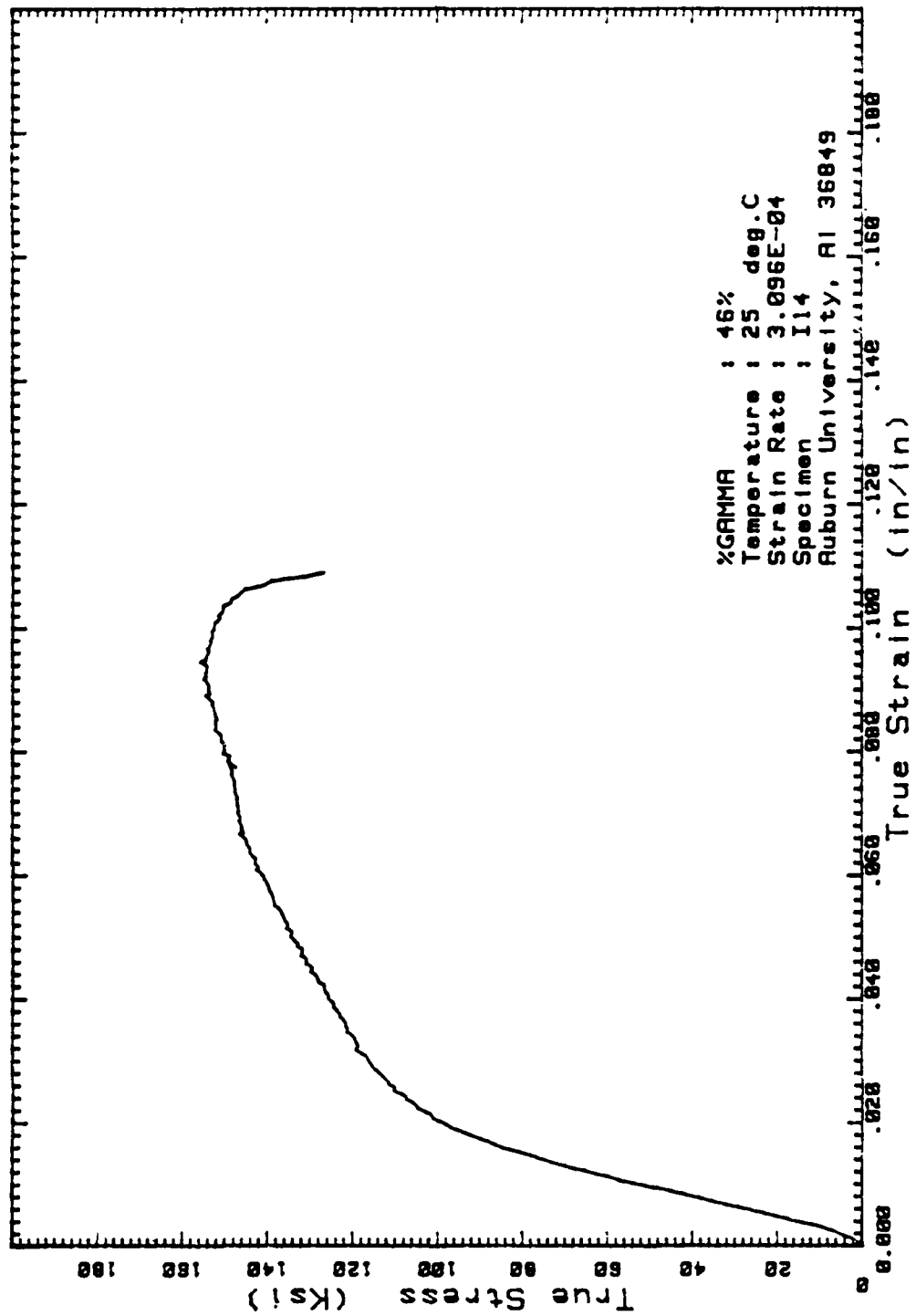


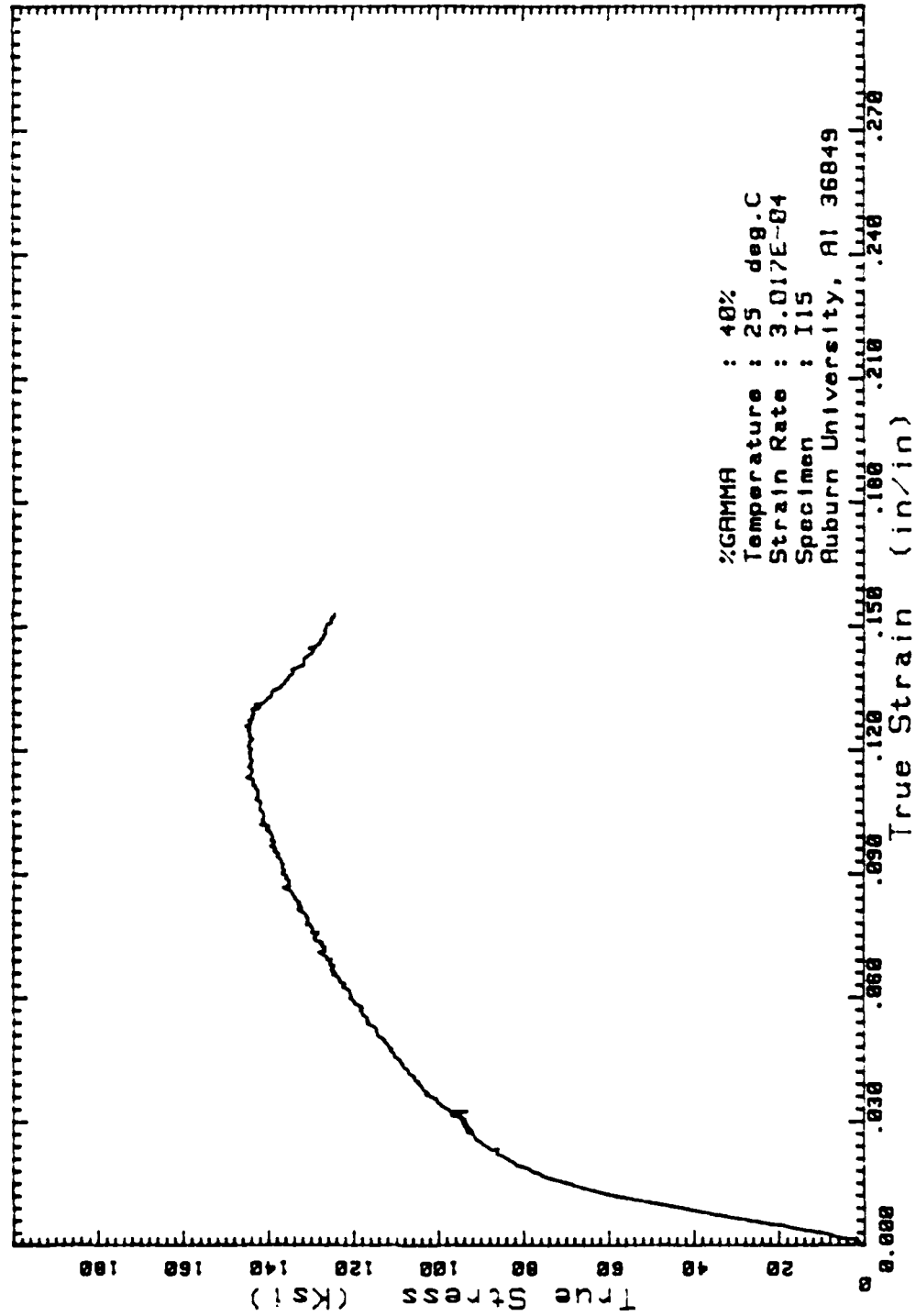


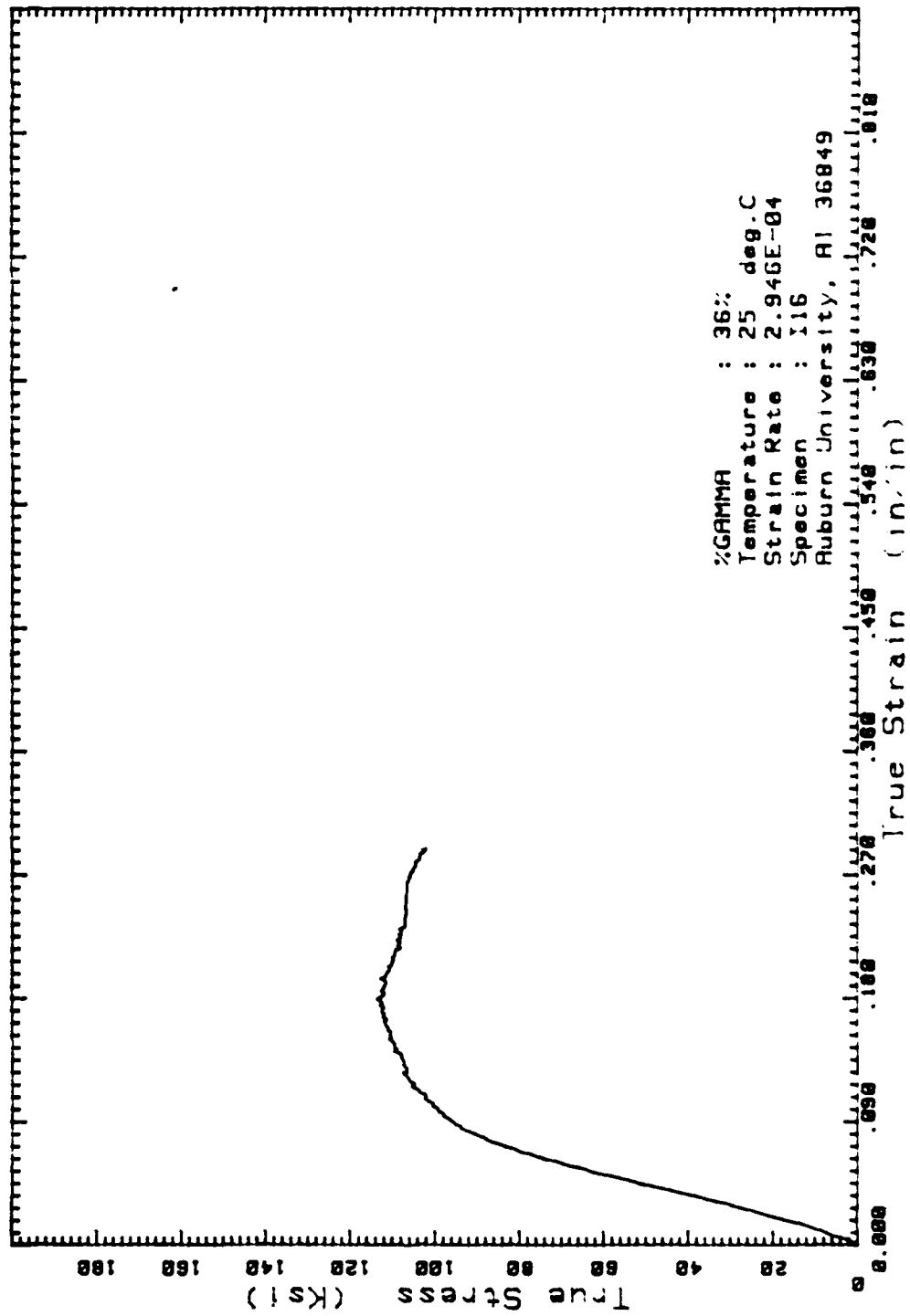


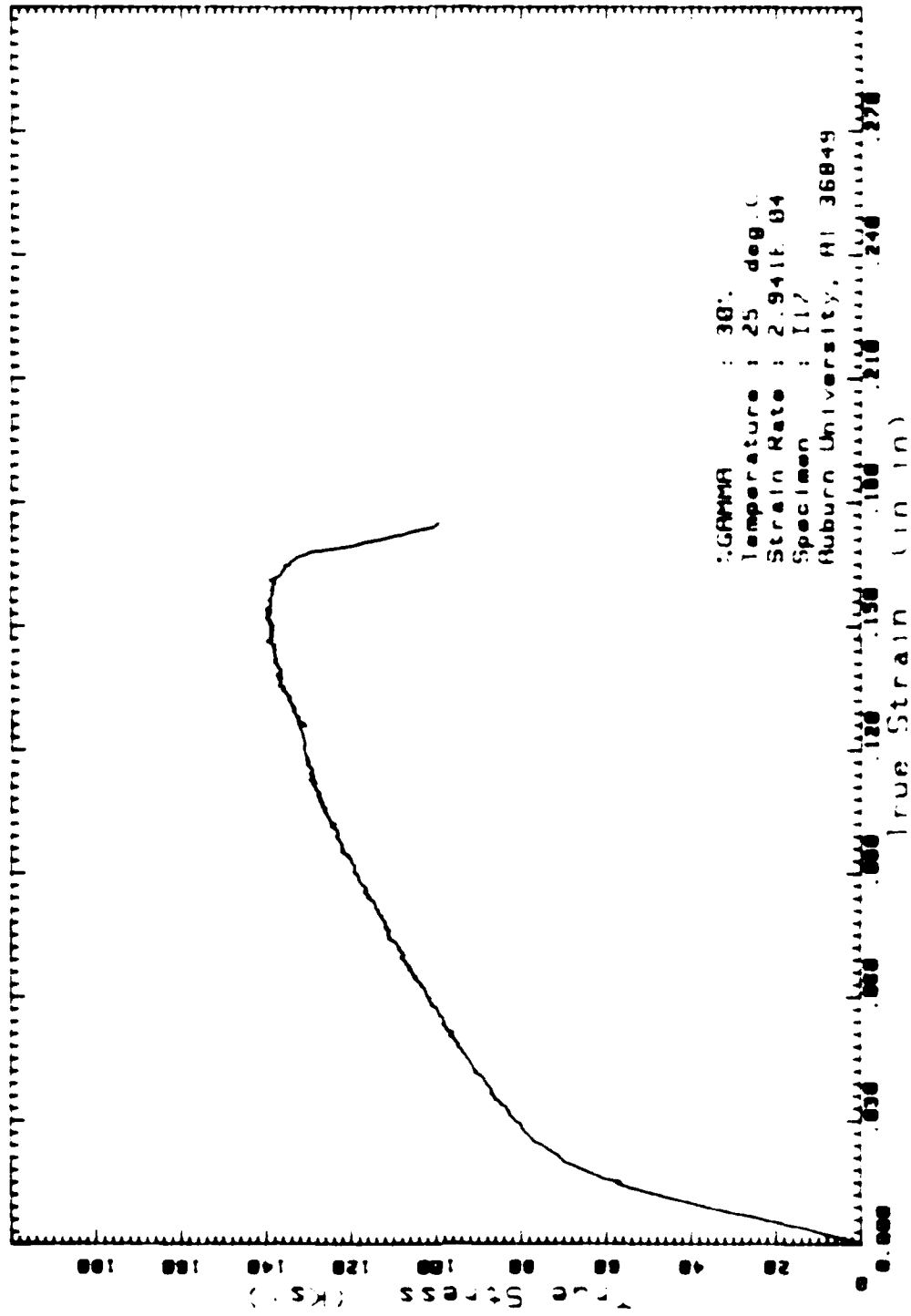




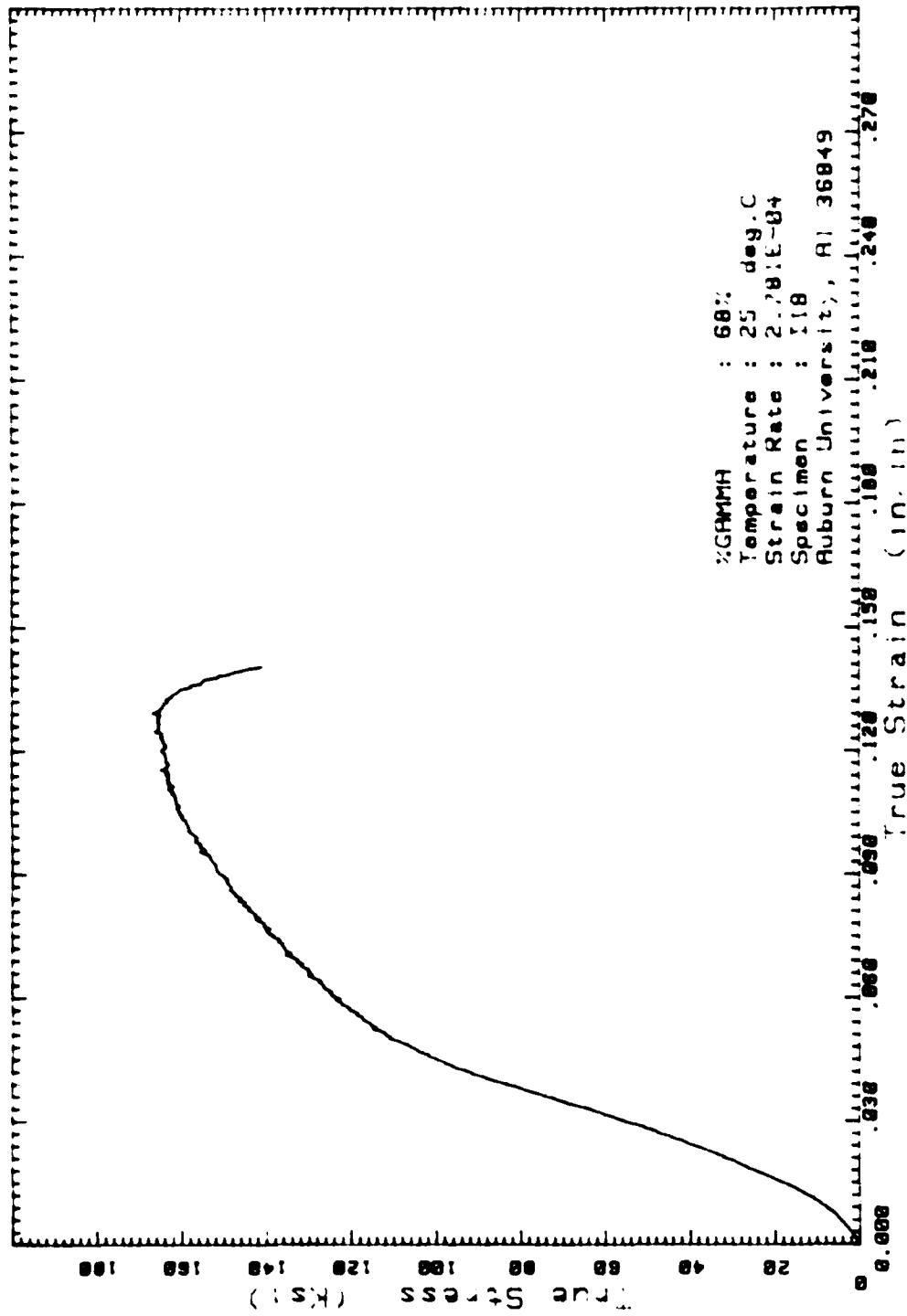


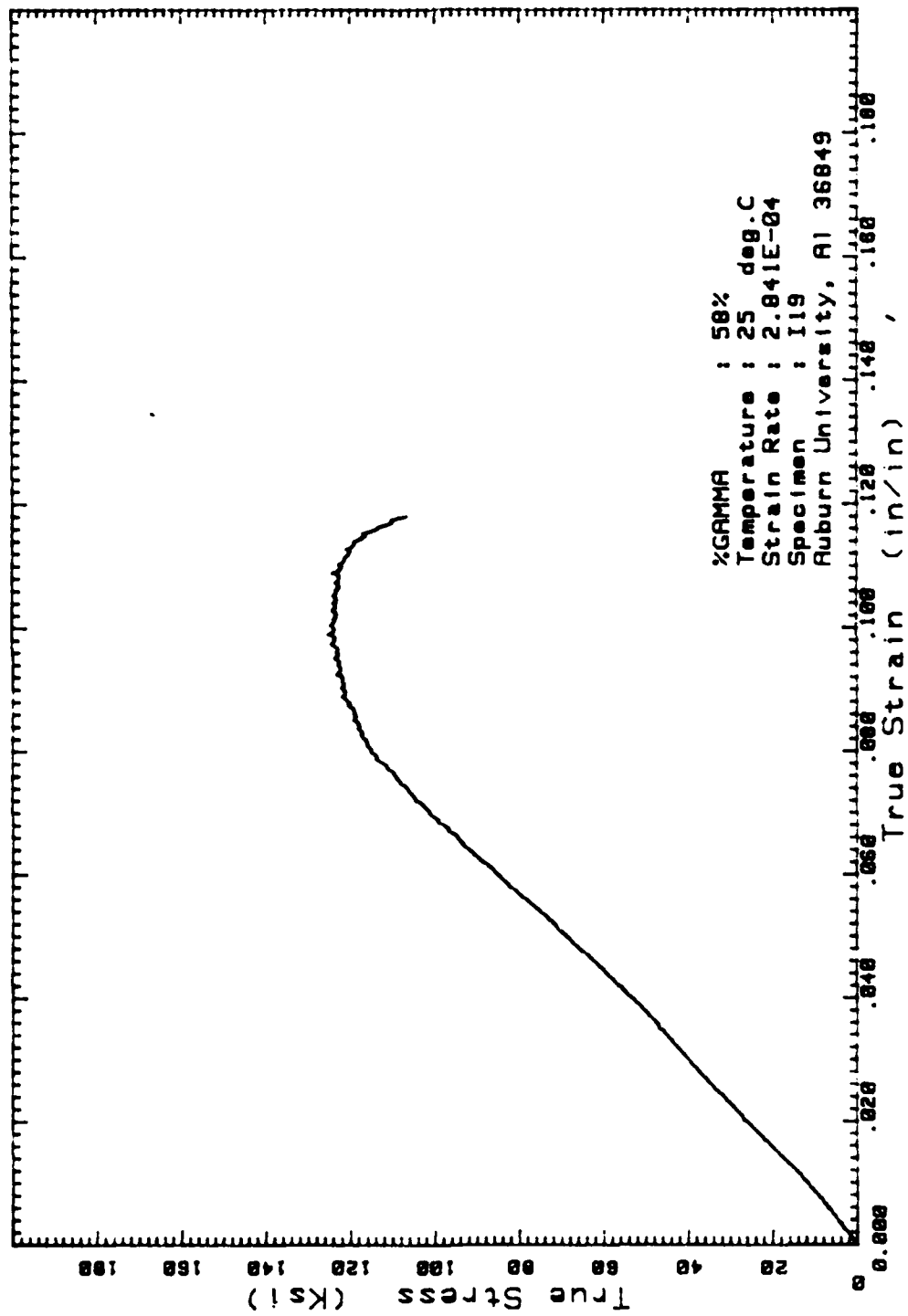


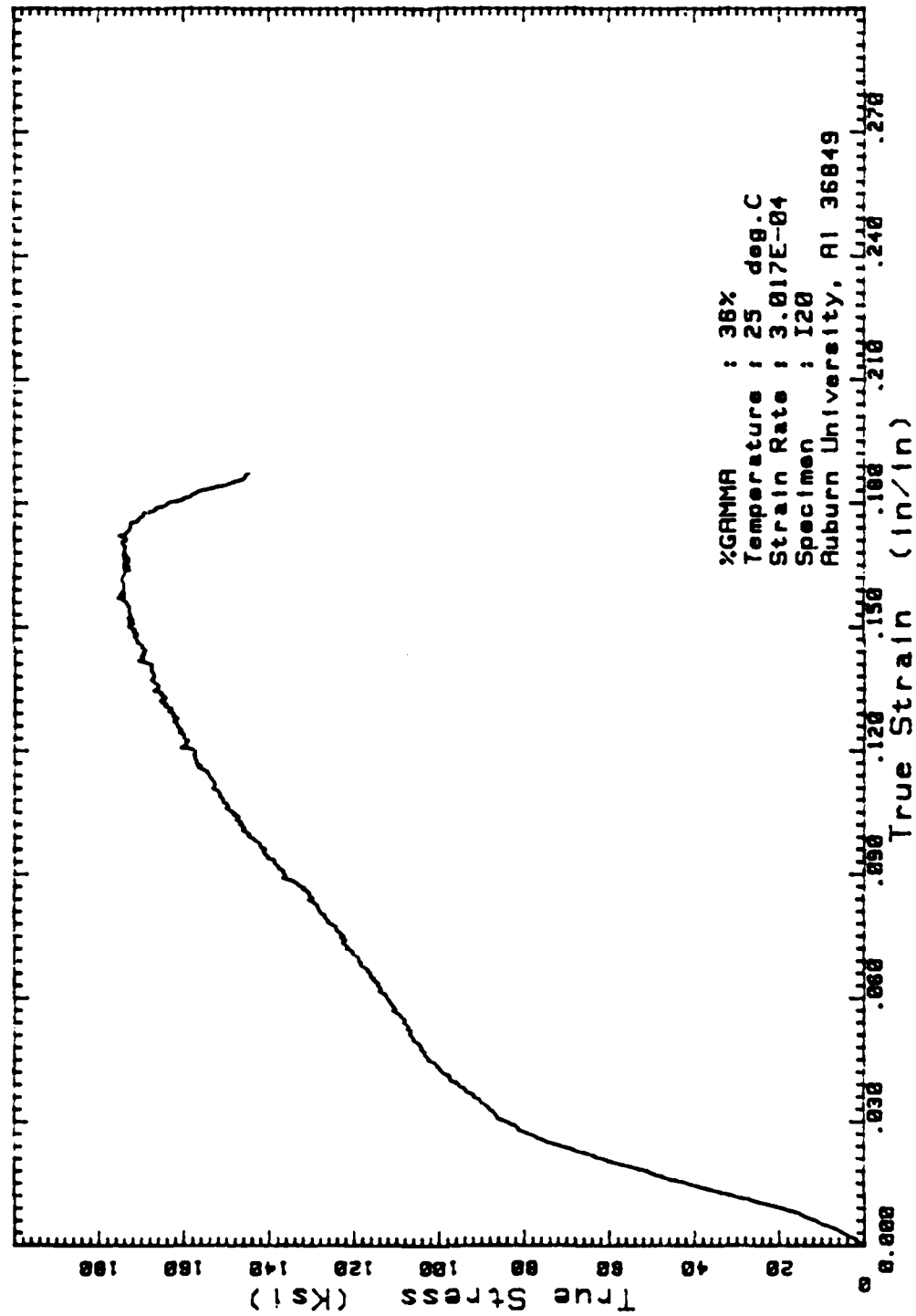


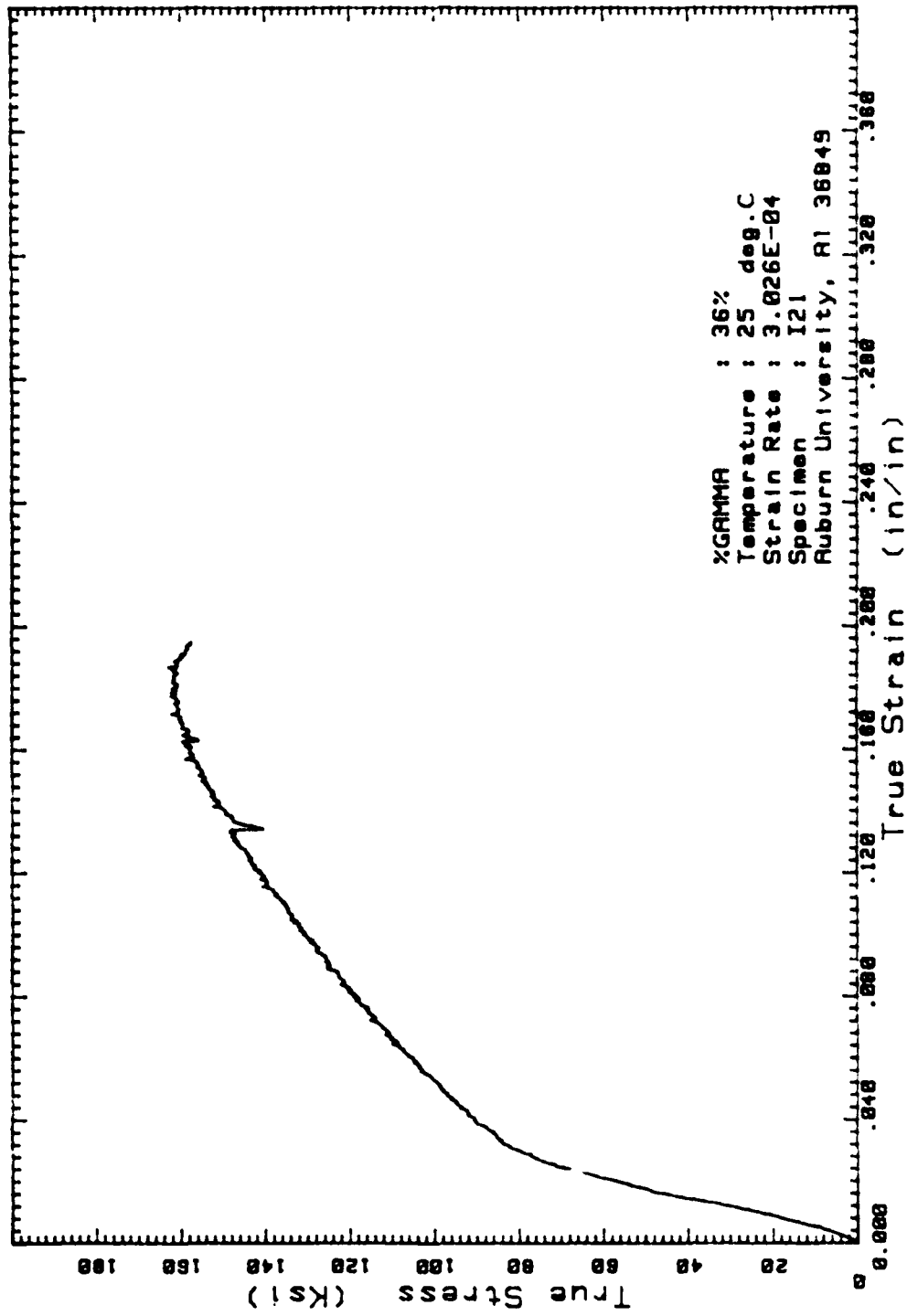


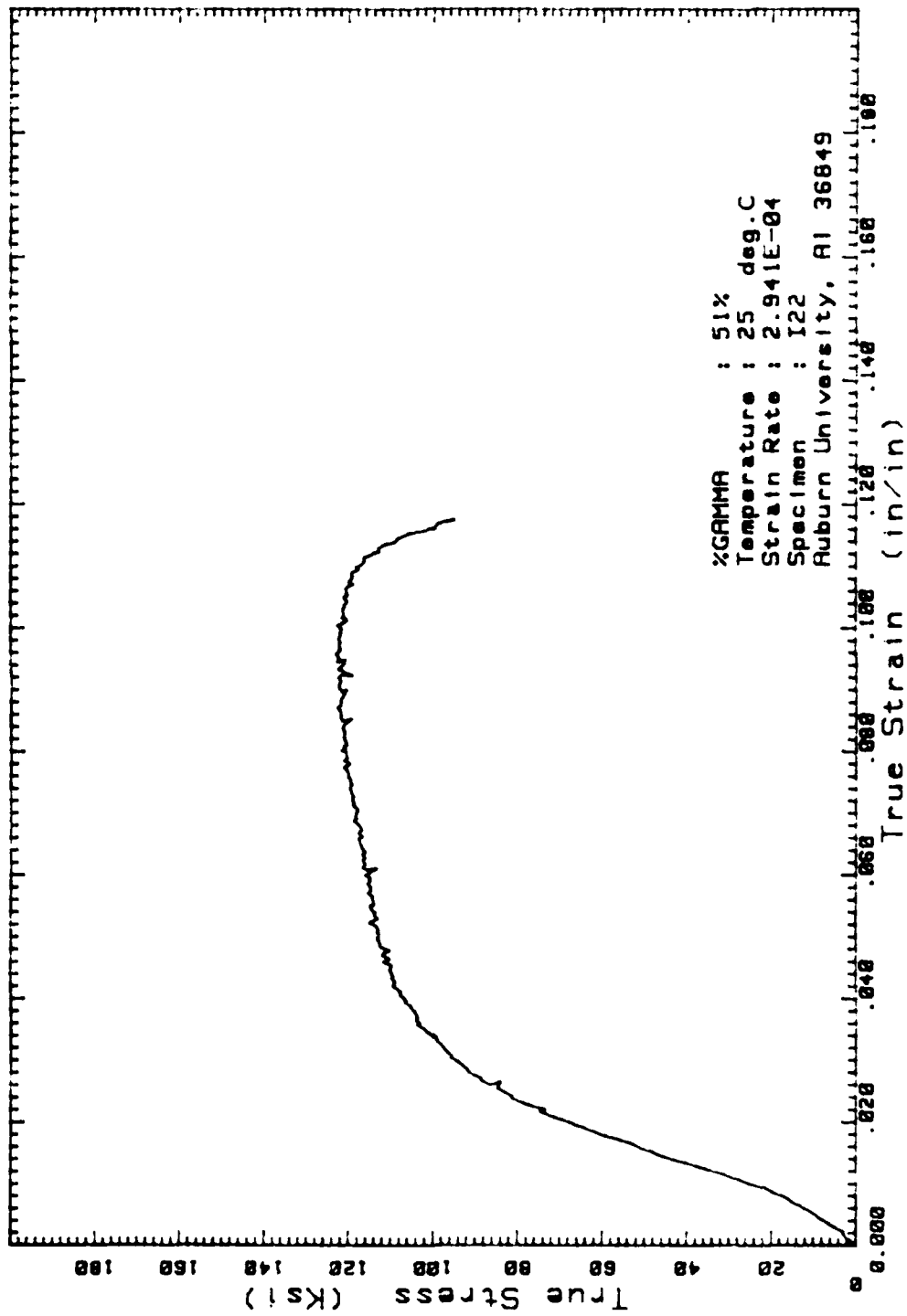


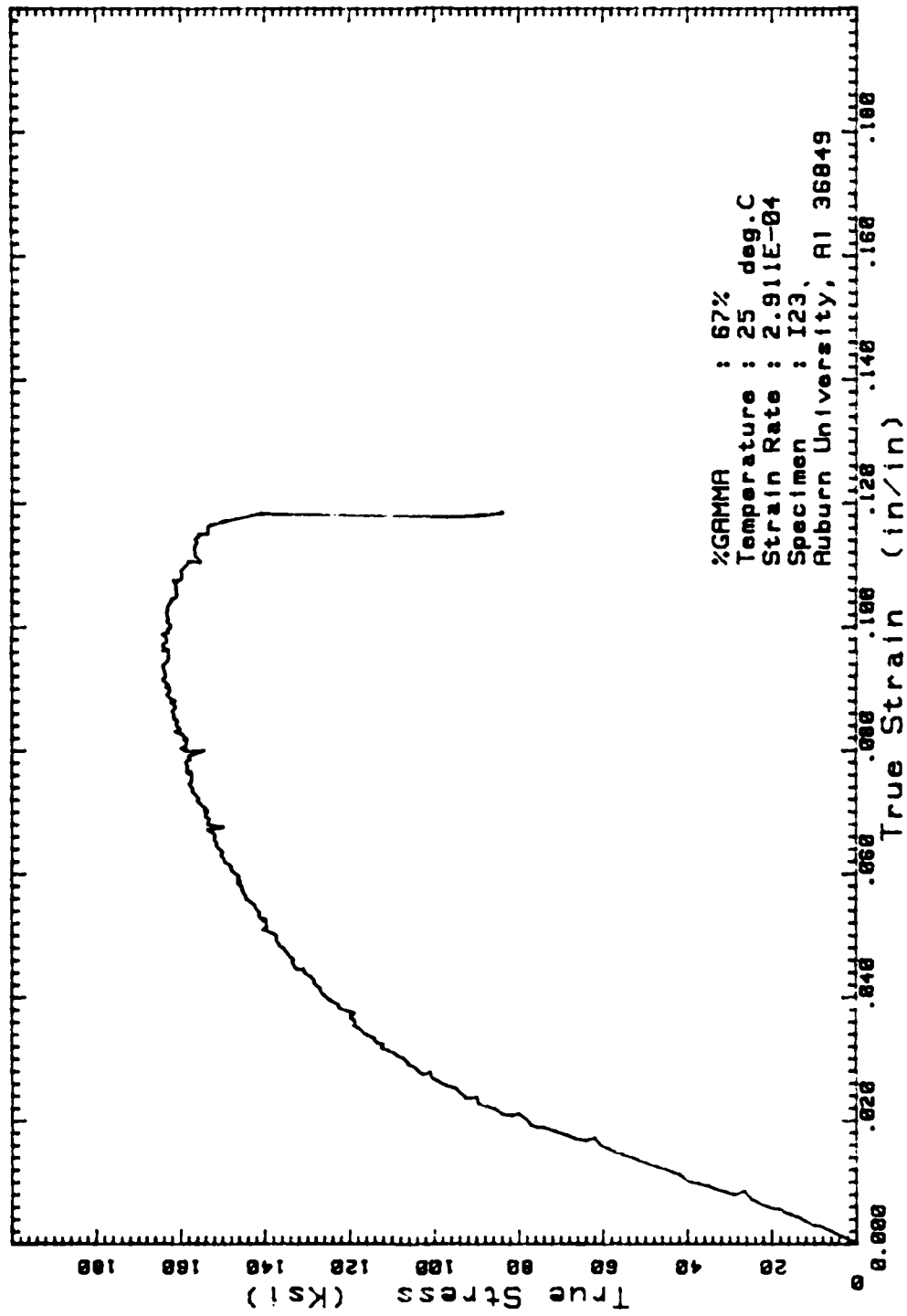


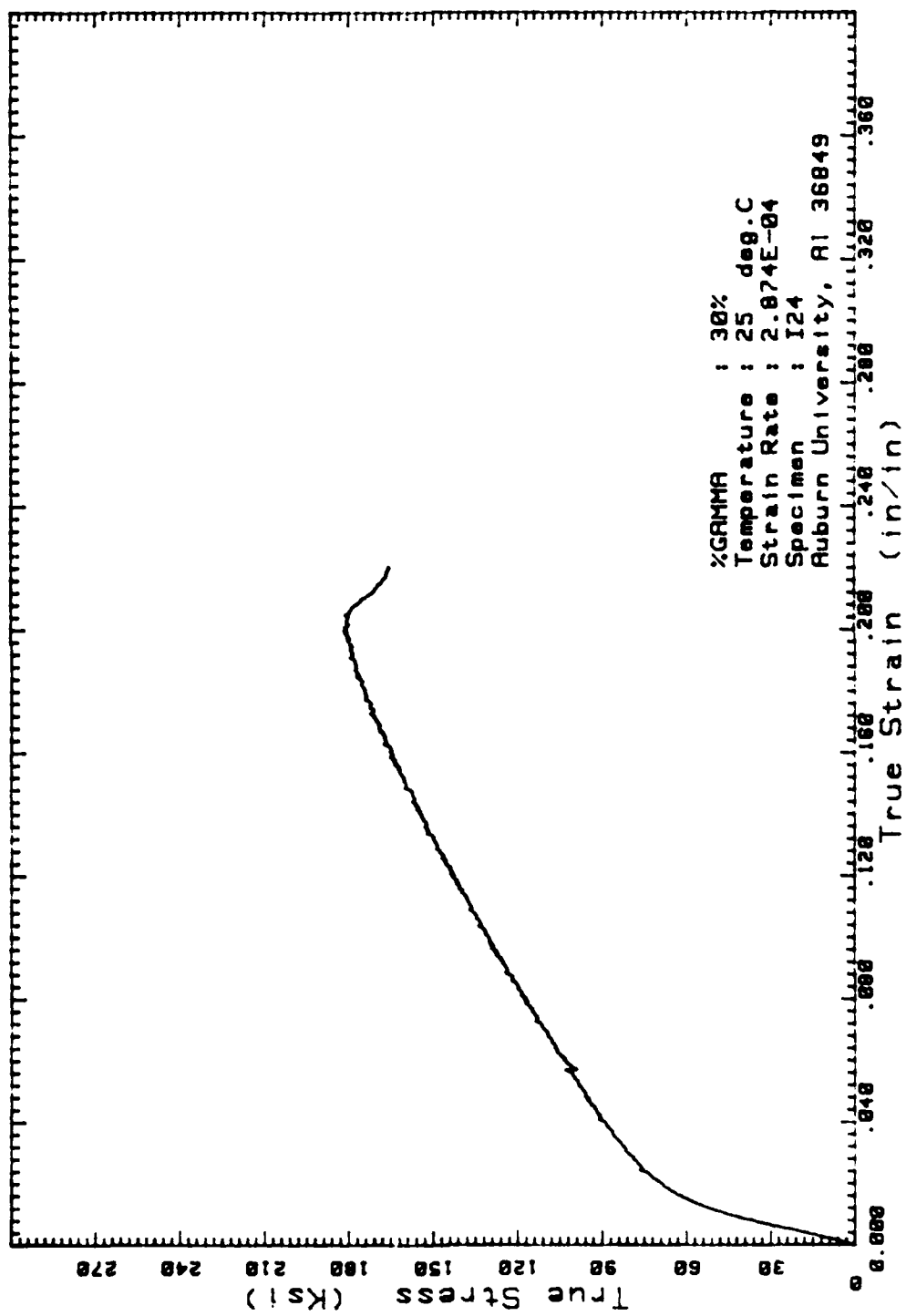


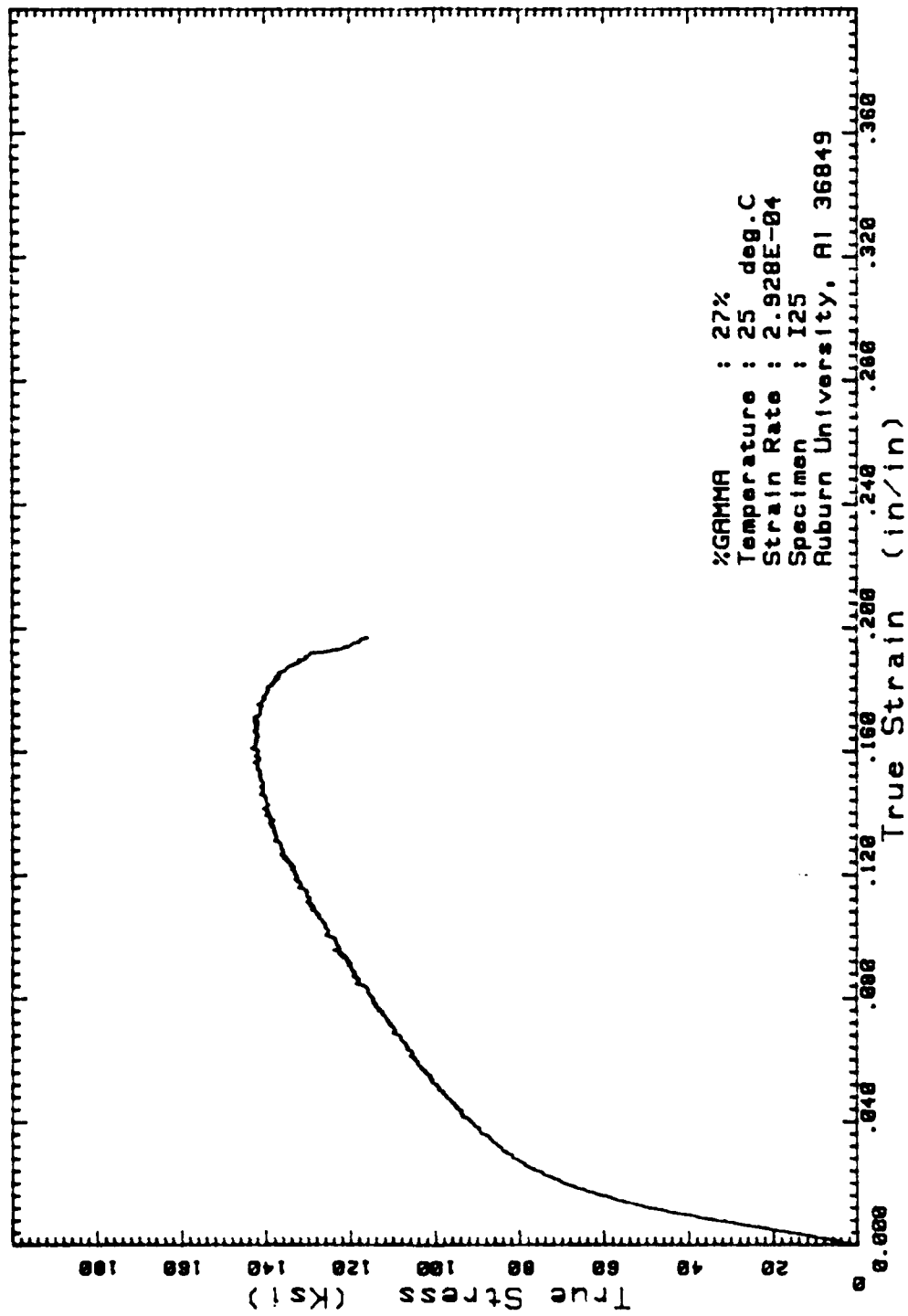




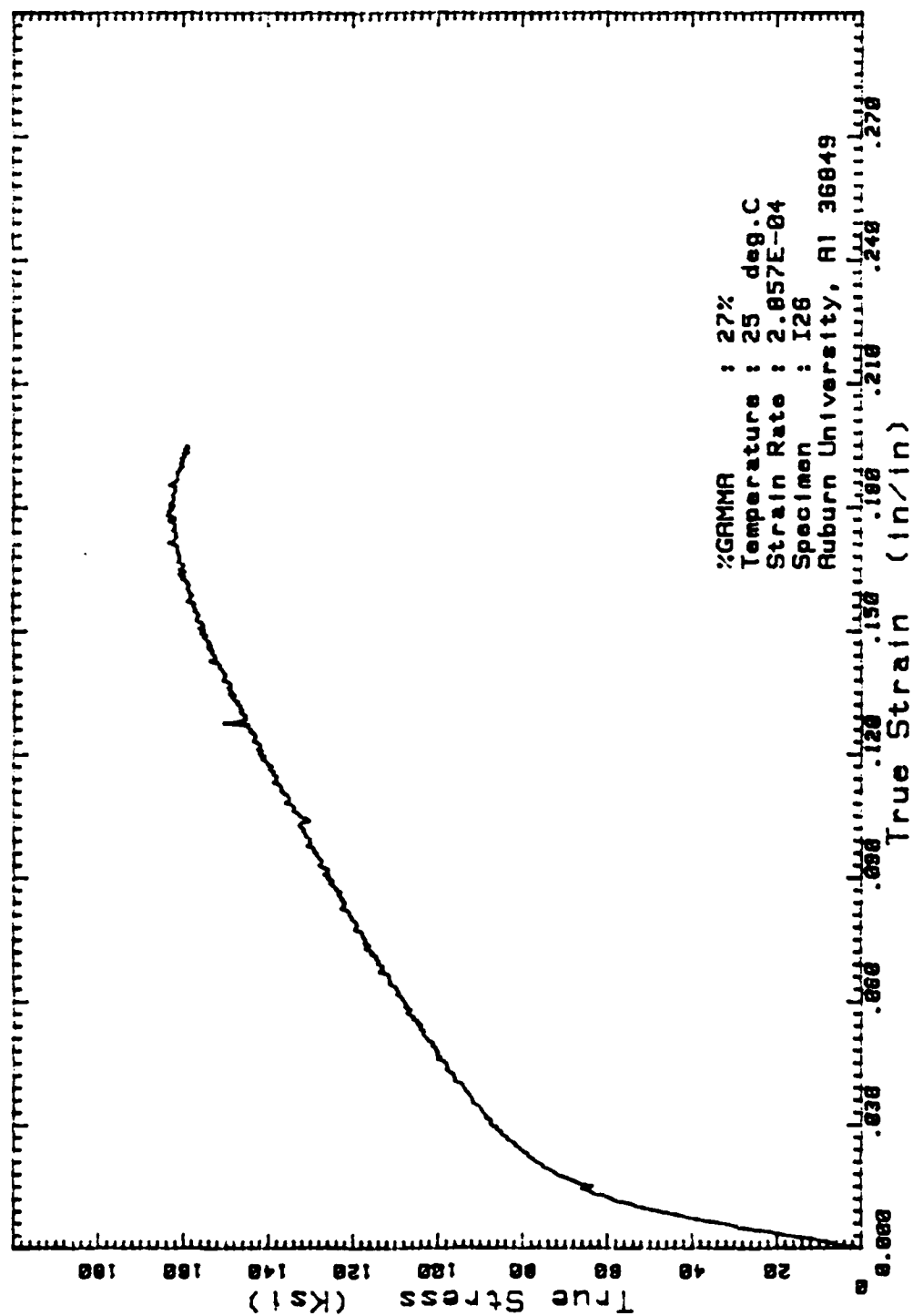


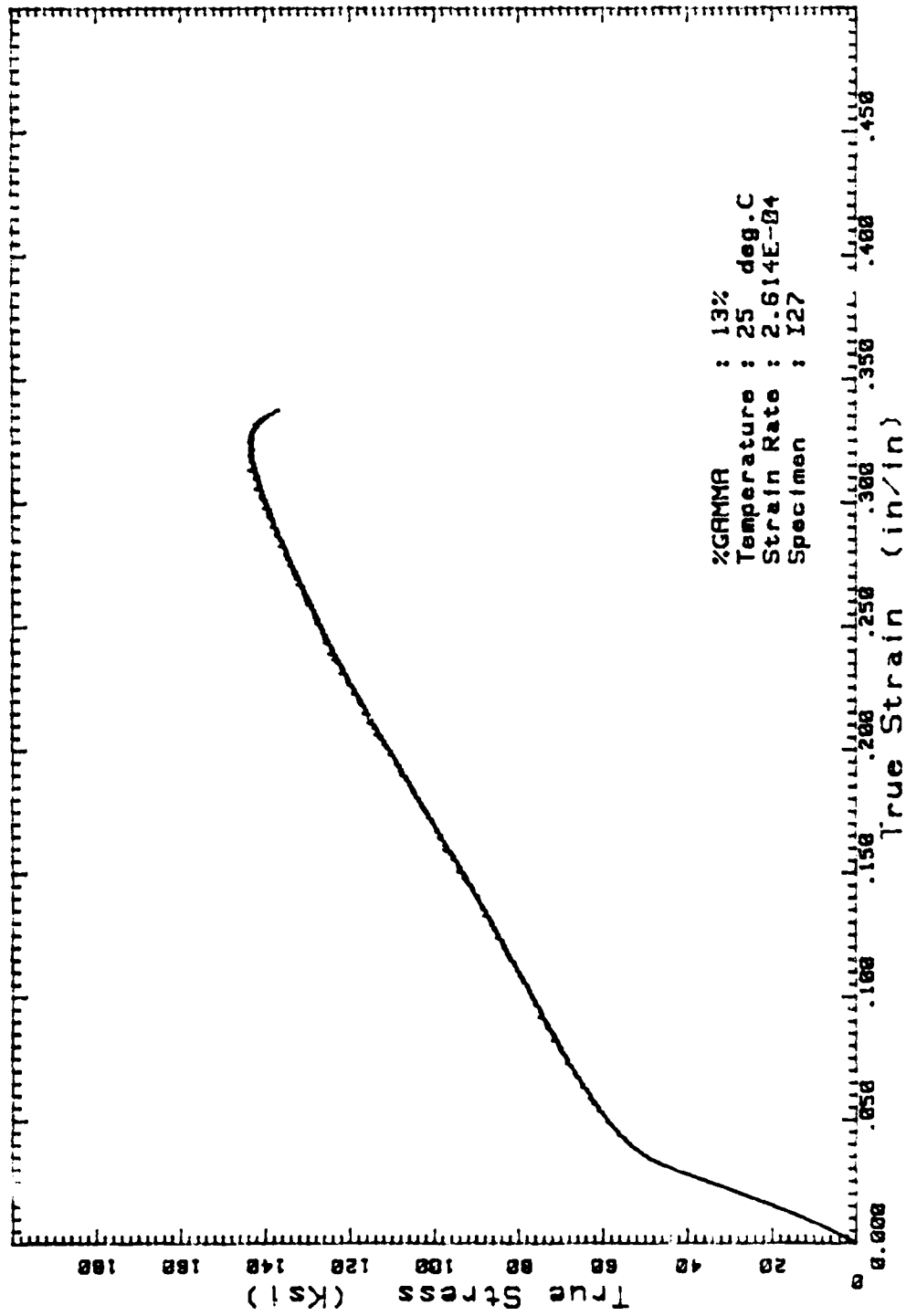


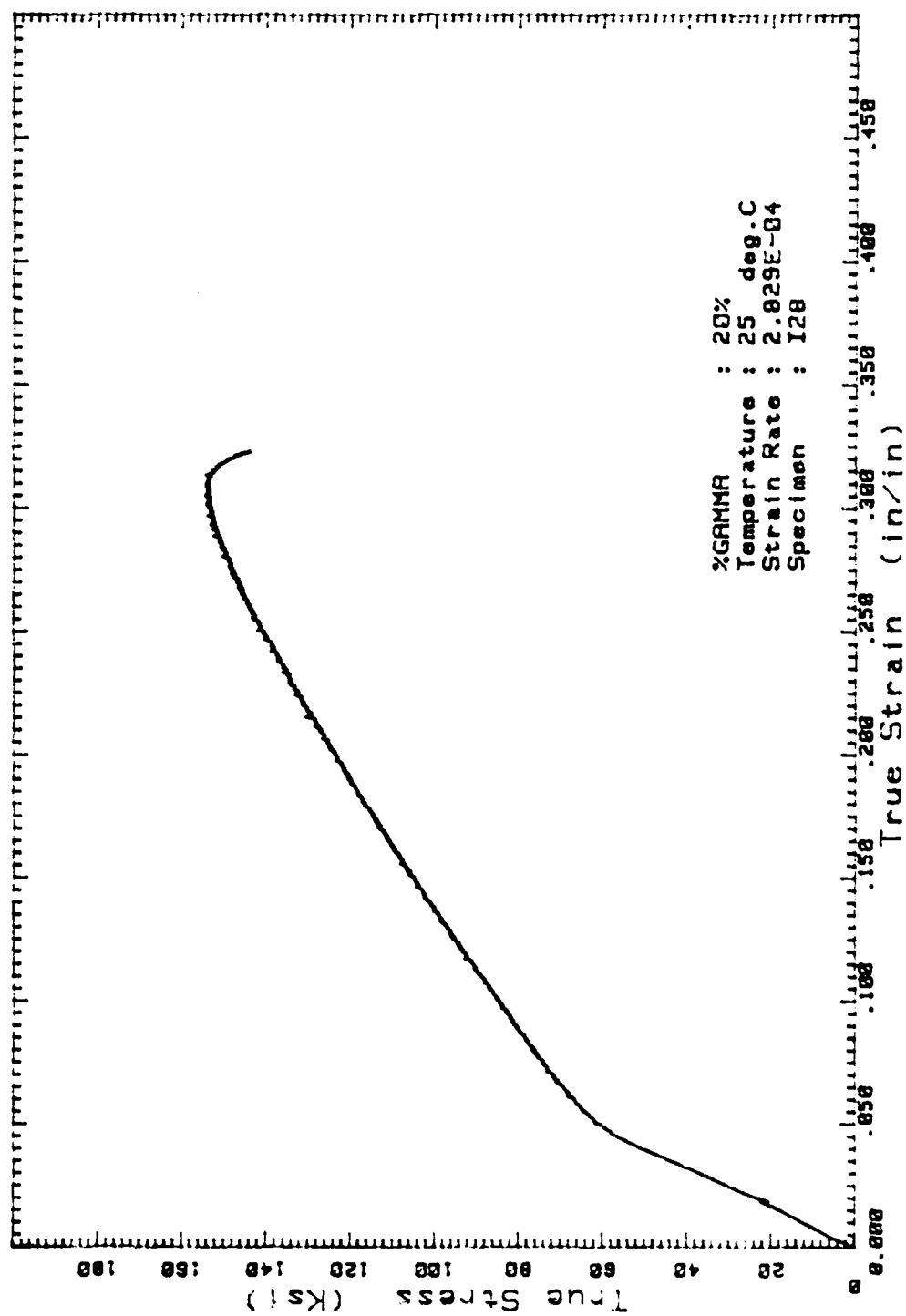






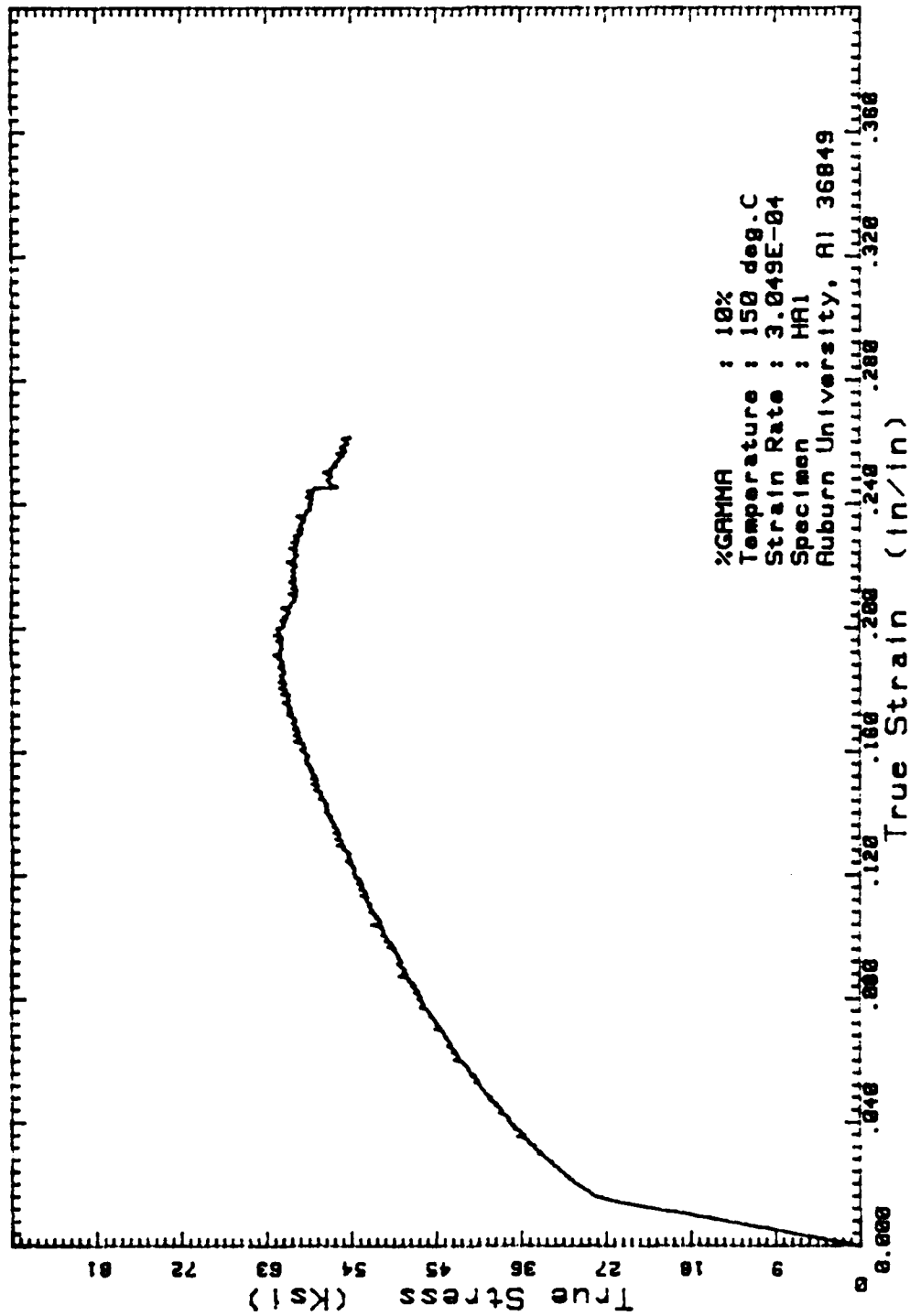


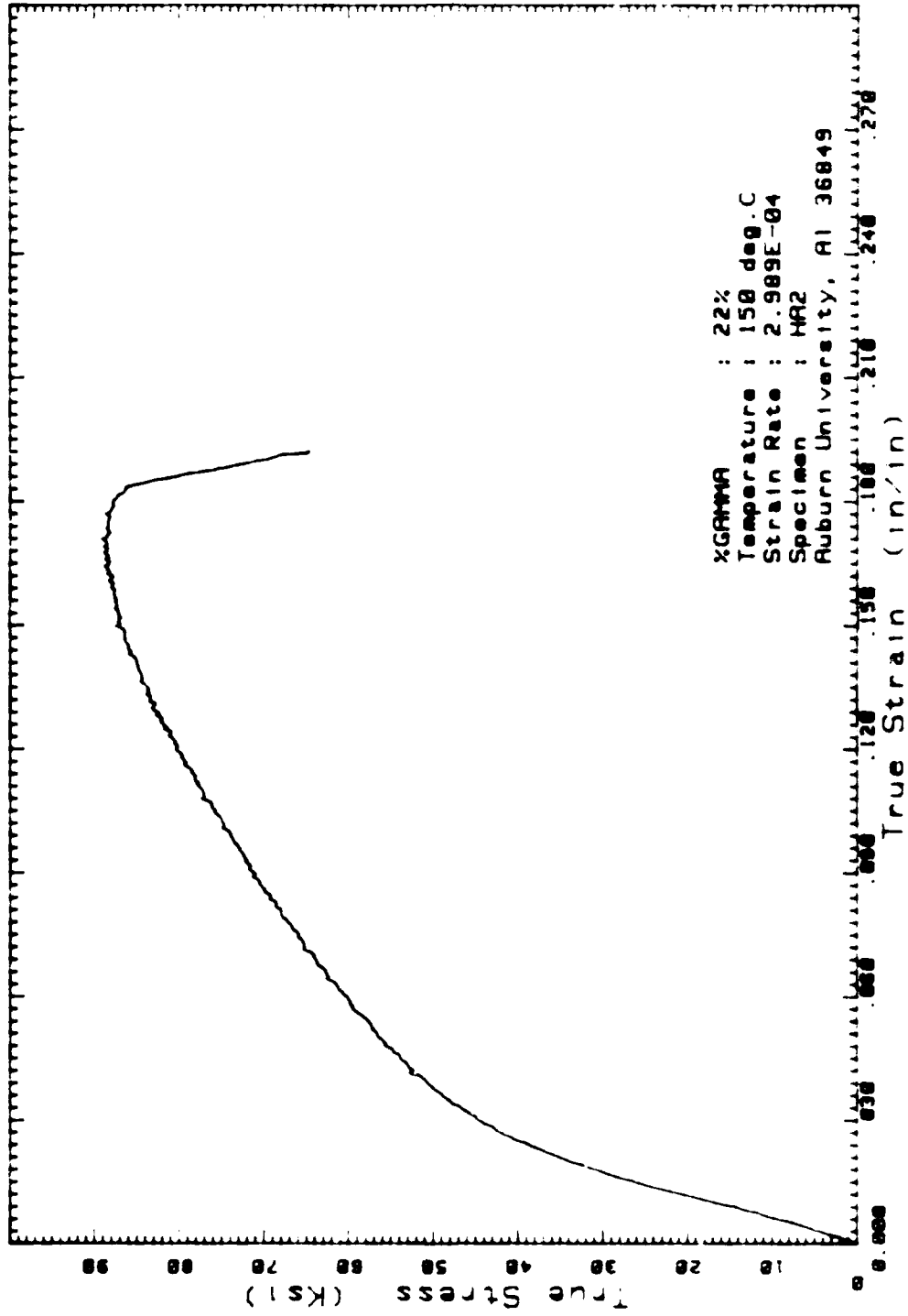


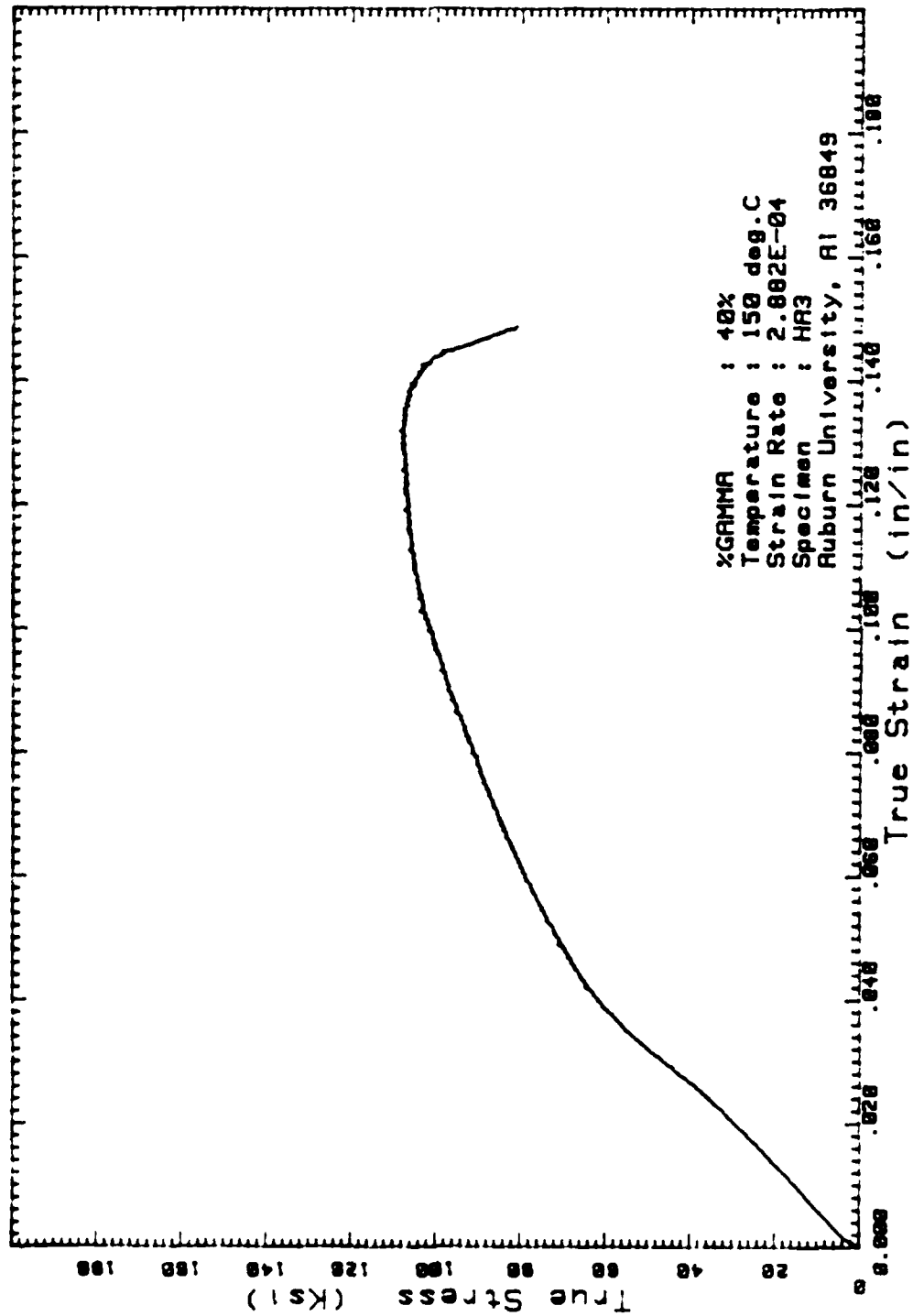


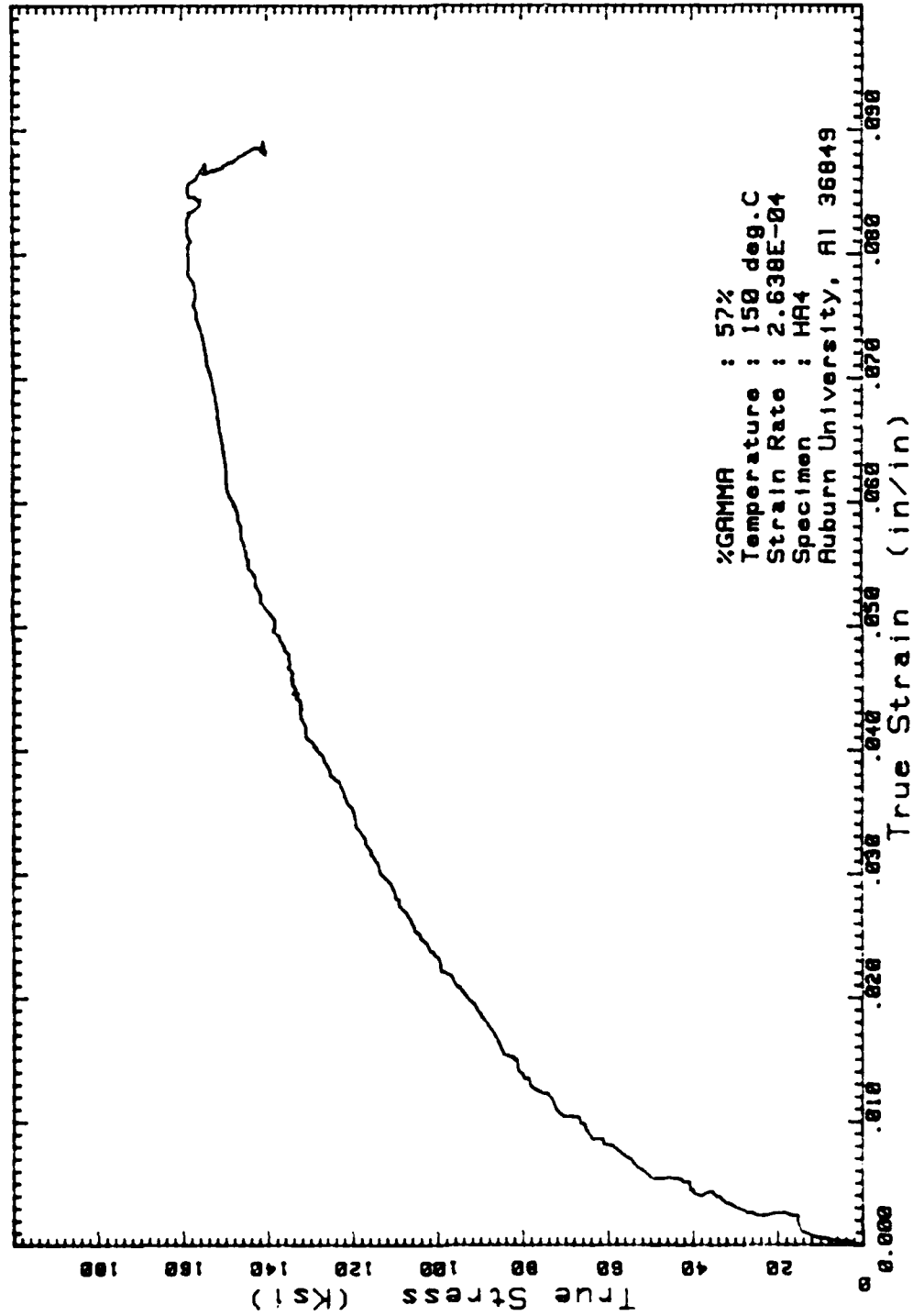
APPENDIX F

TRUE STRESS vs TRUE STRAIN CURVES FOR ALL COMPRESSION TESTS  
AT ELEVATED TEMPERATURE

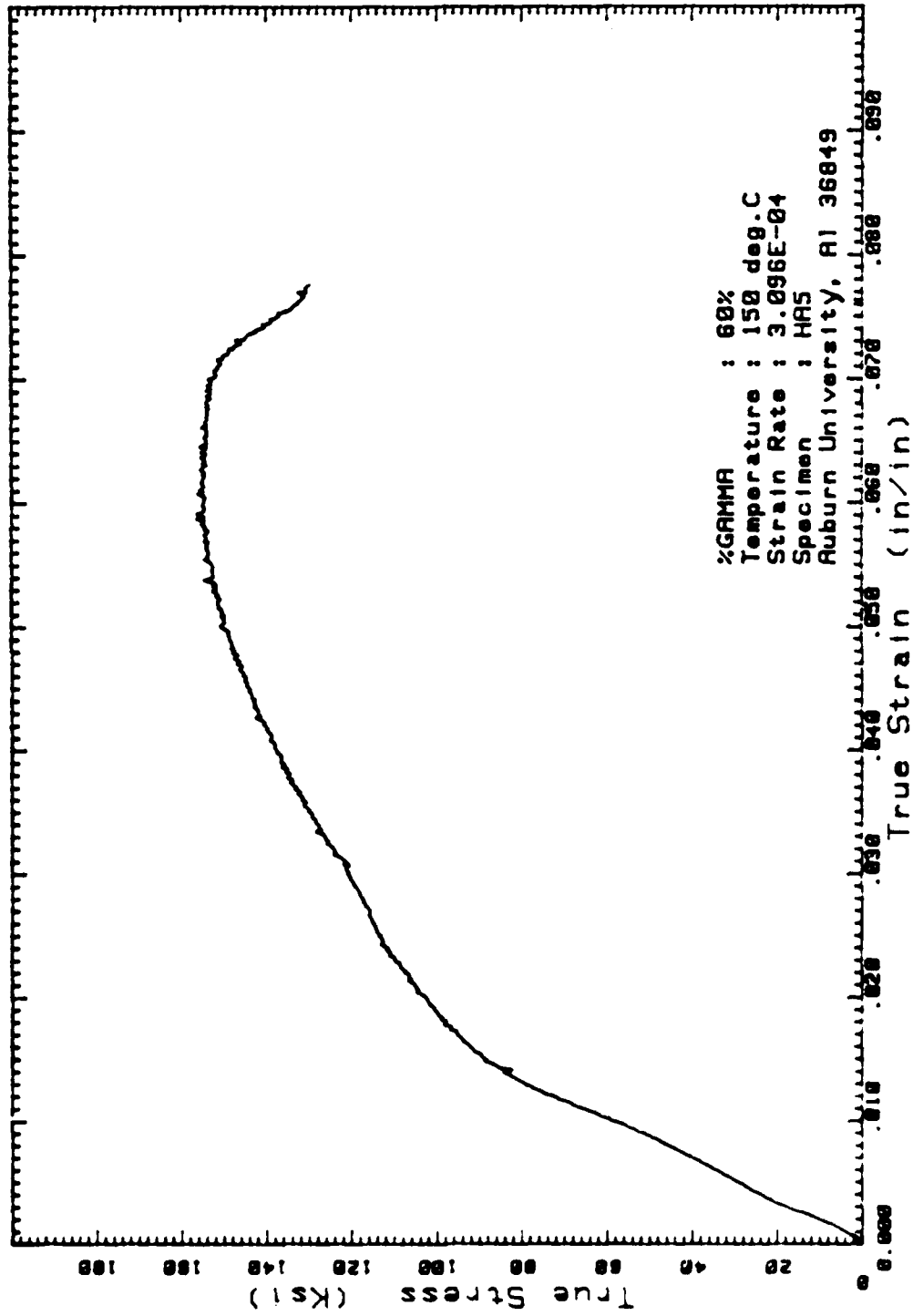


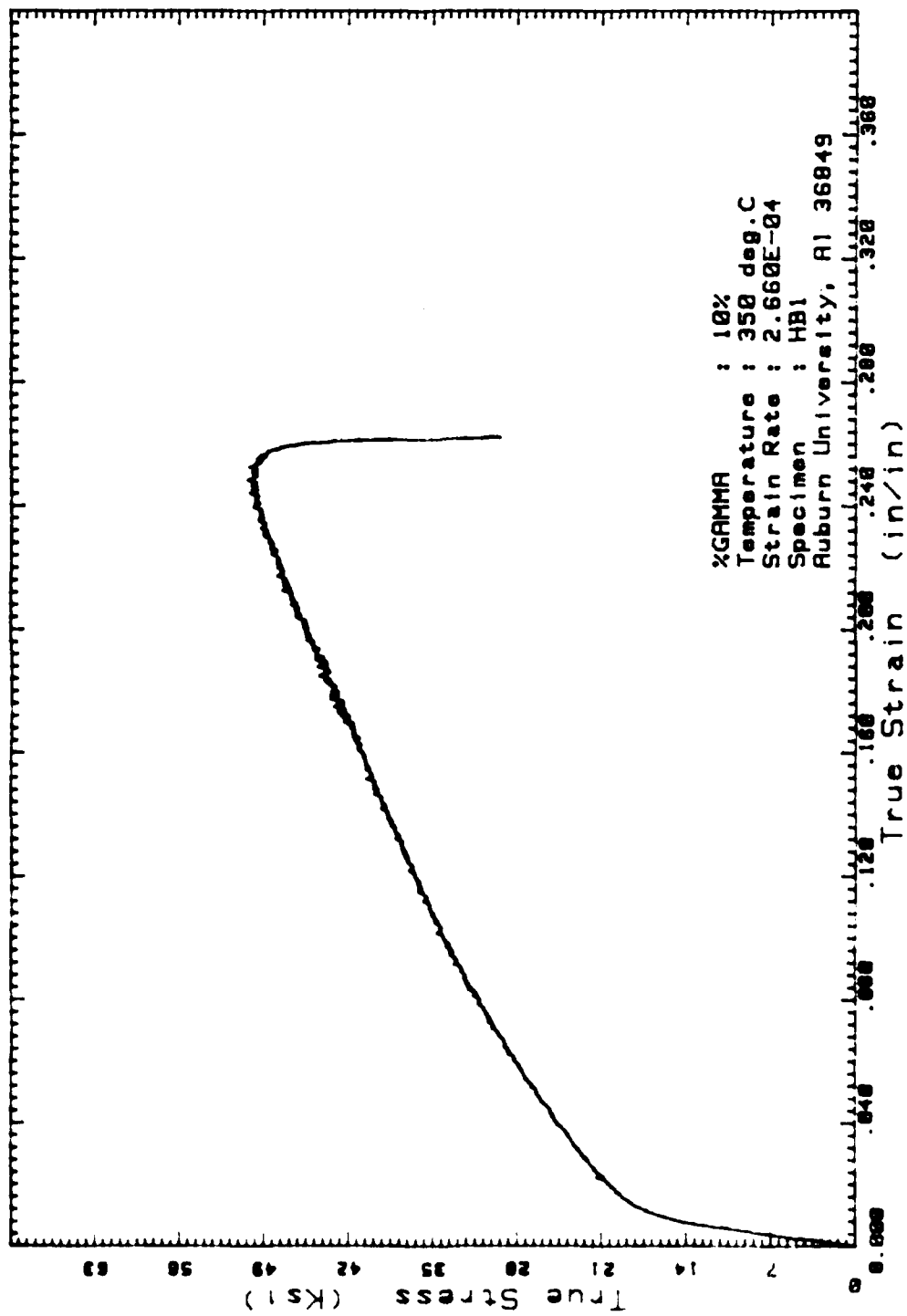


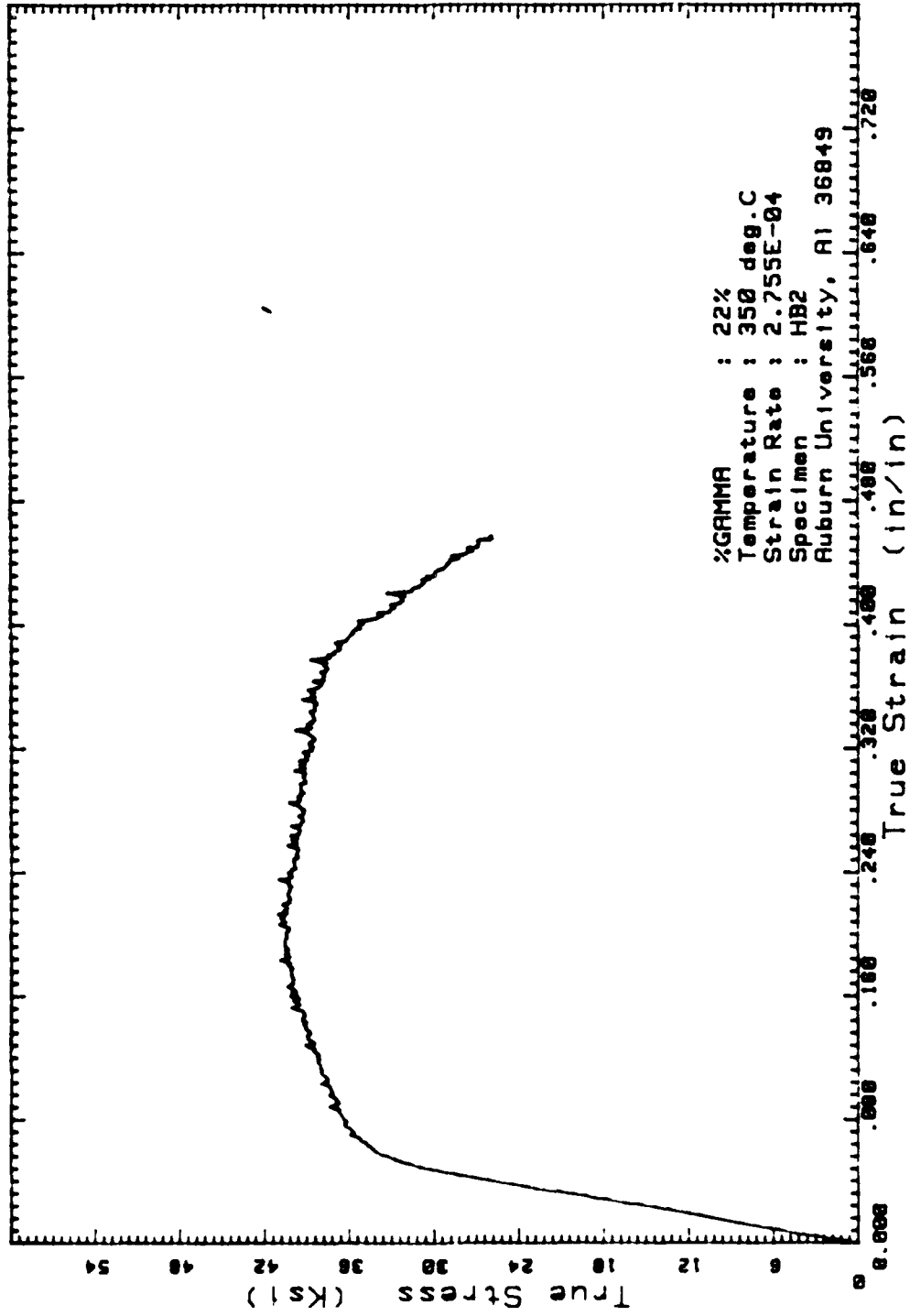


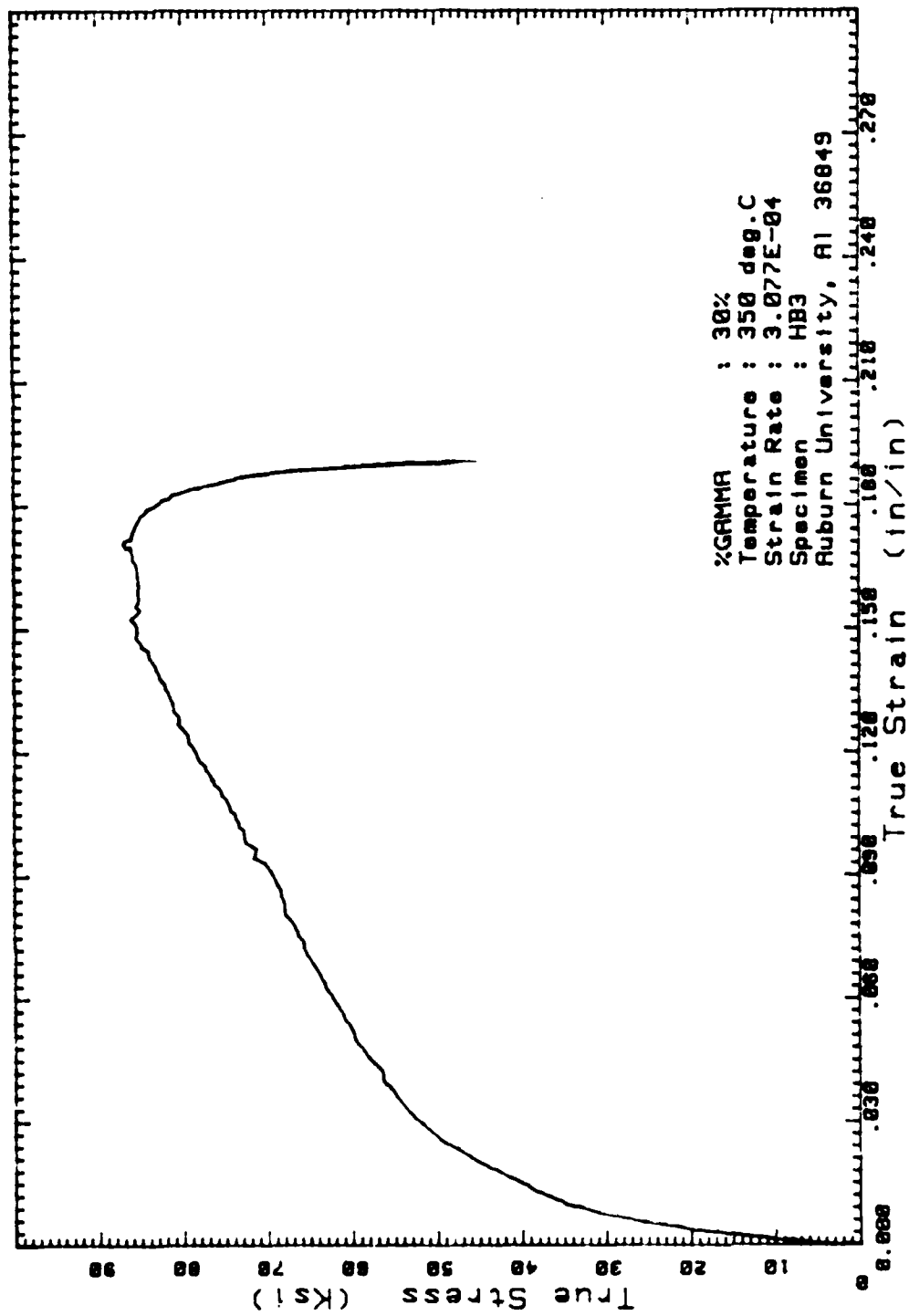


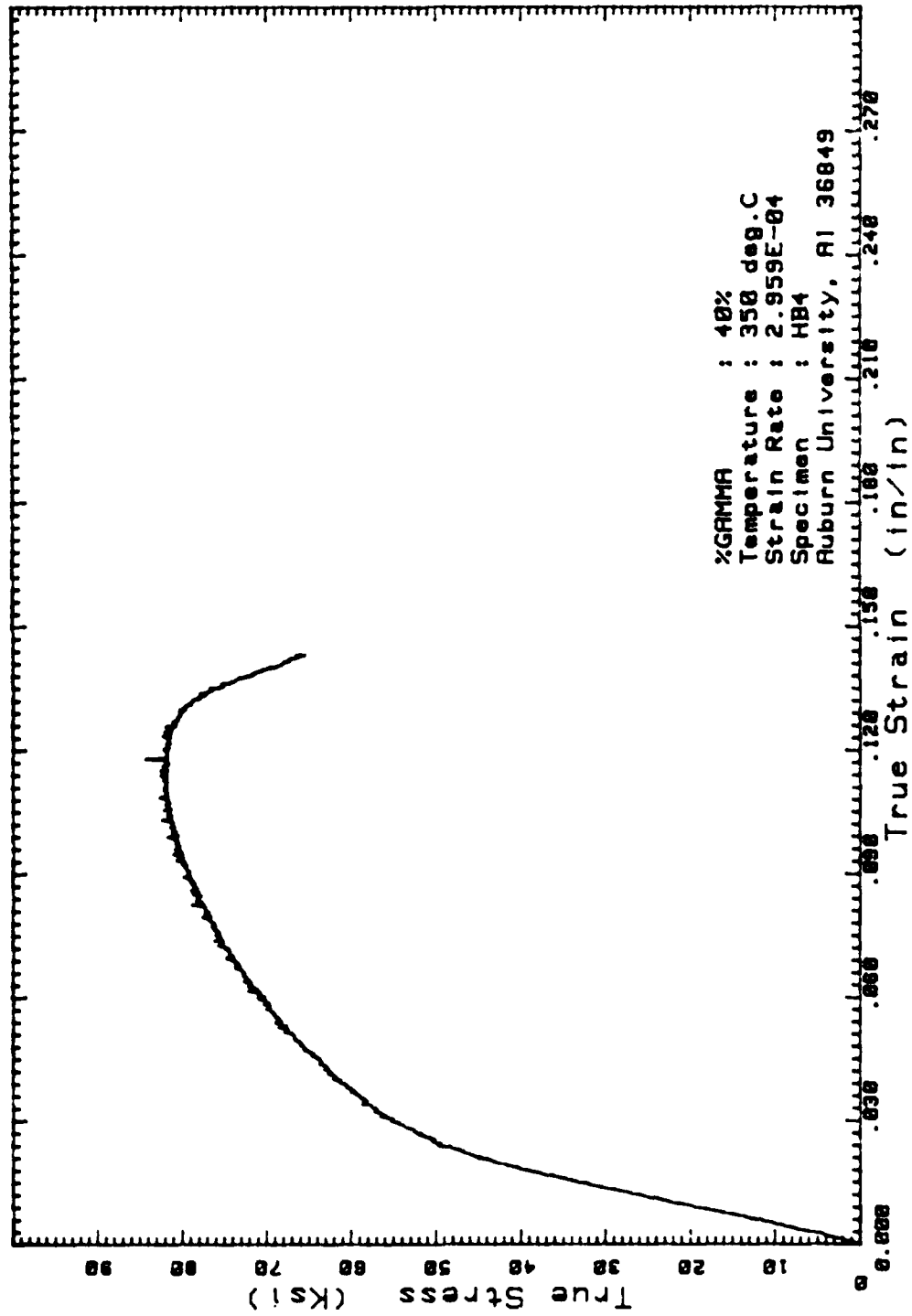


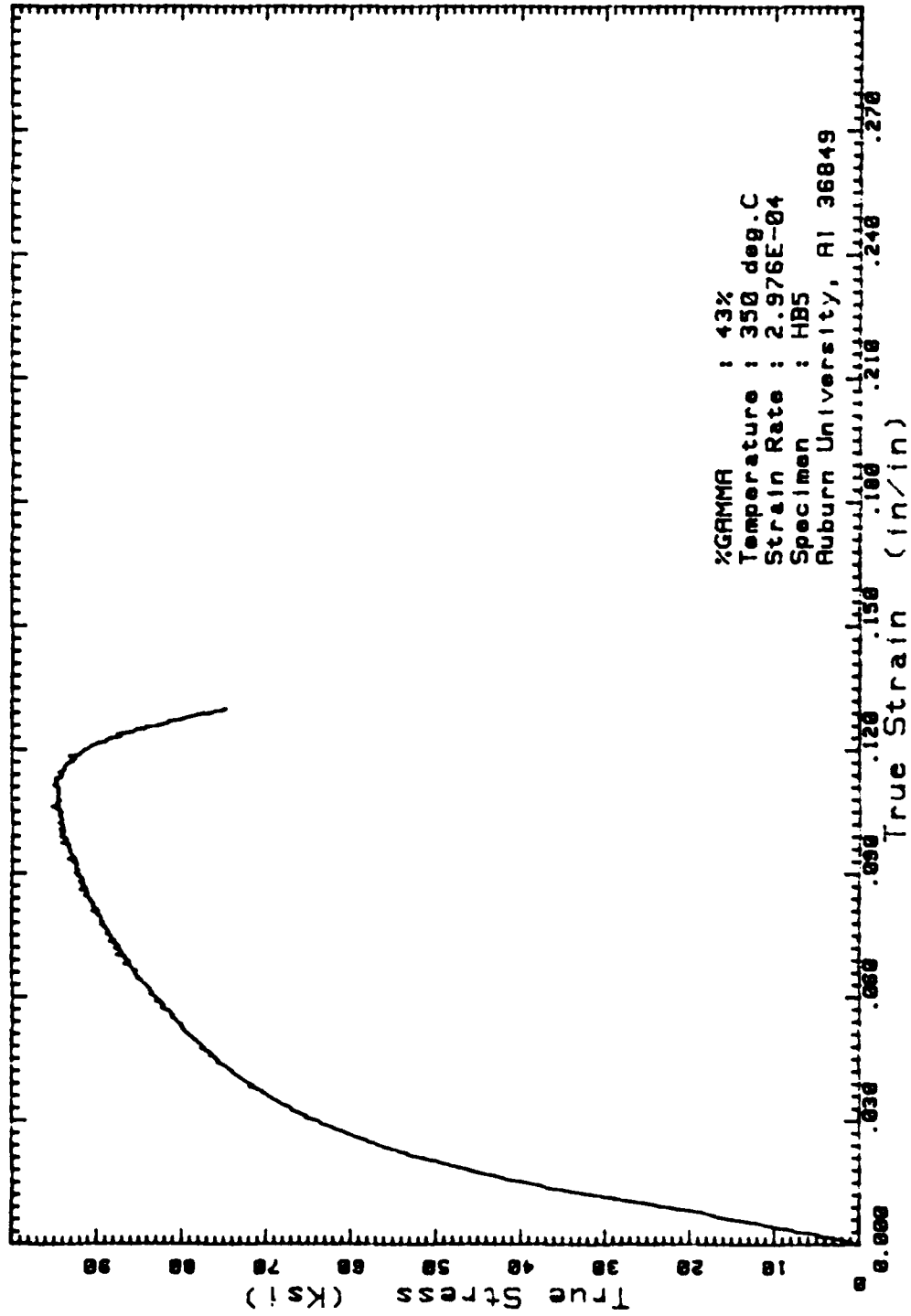


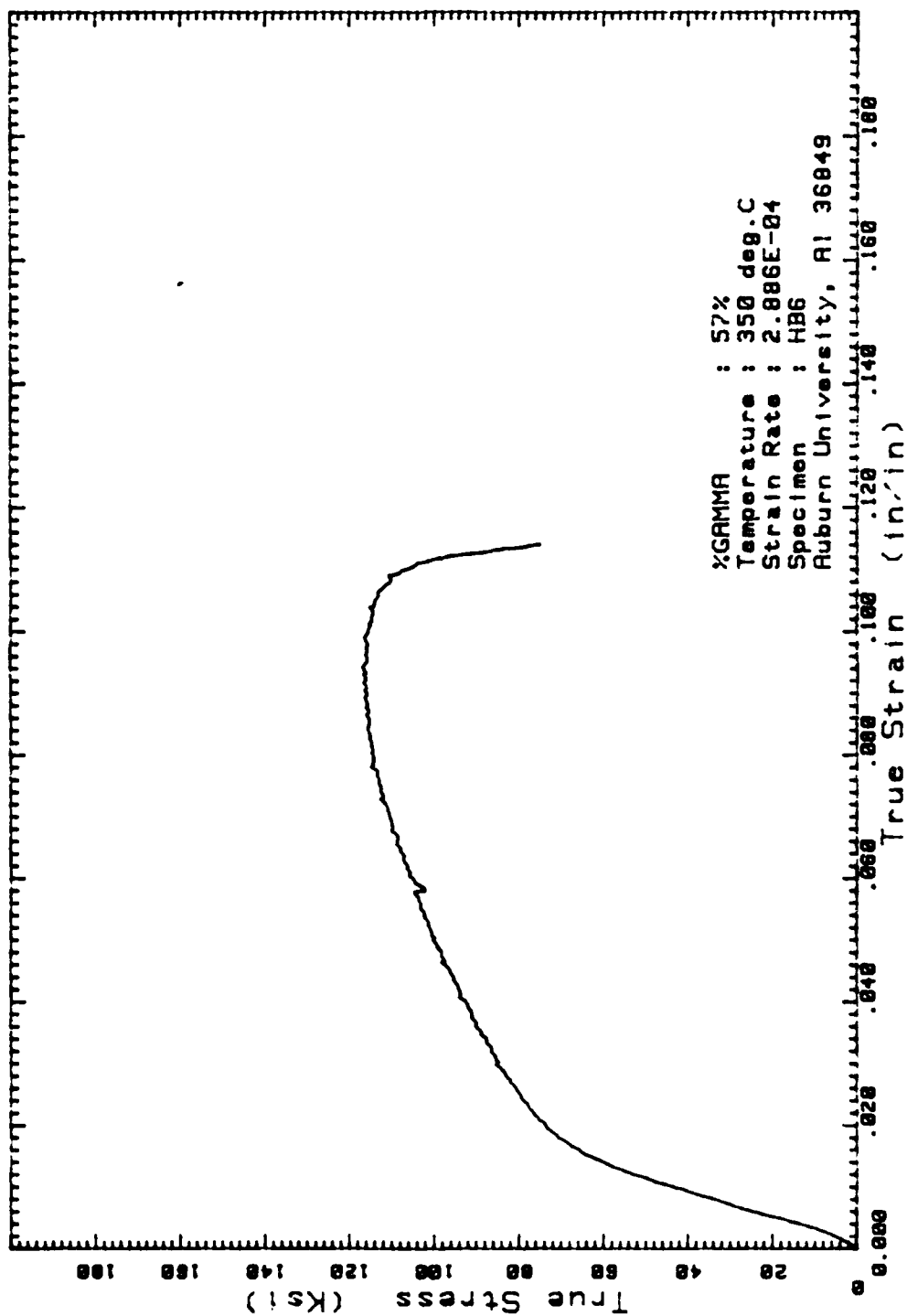


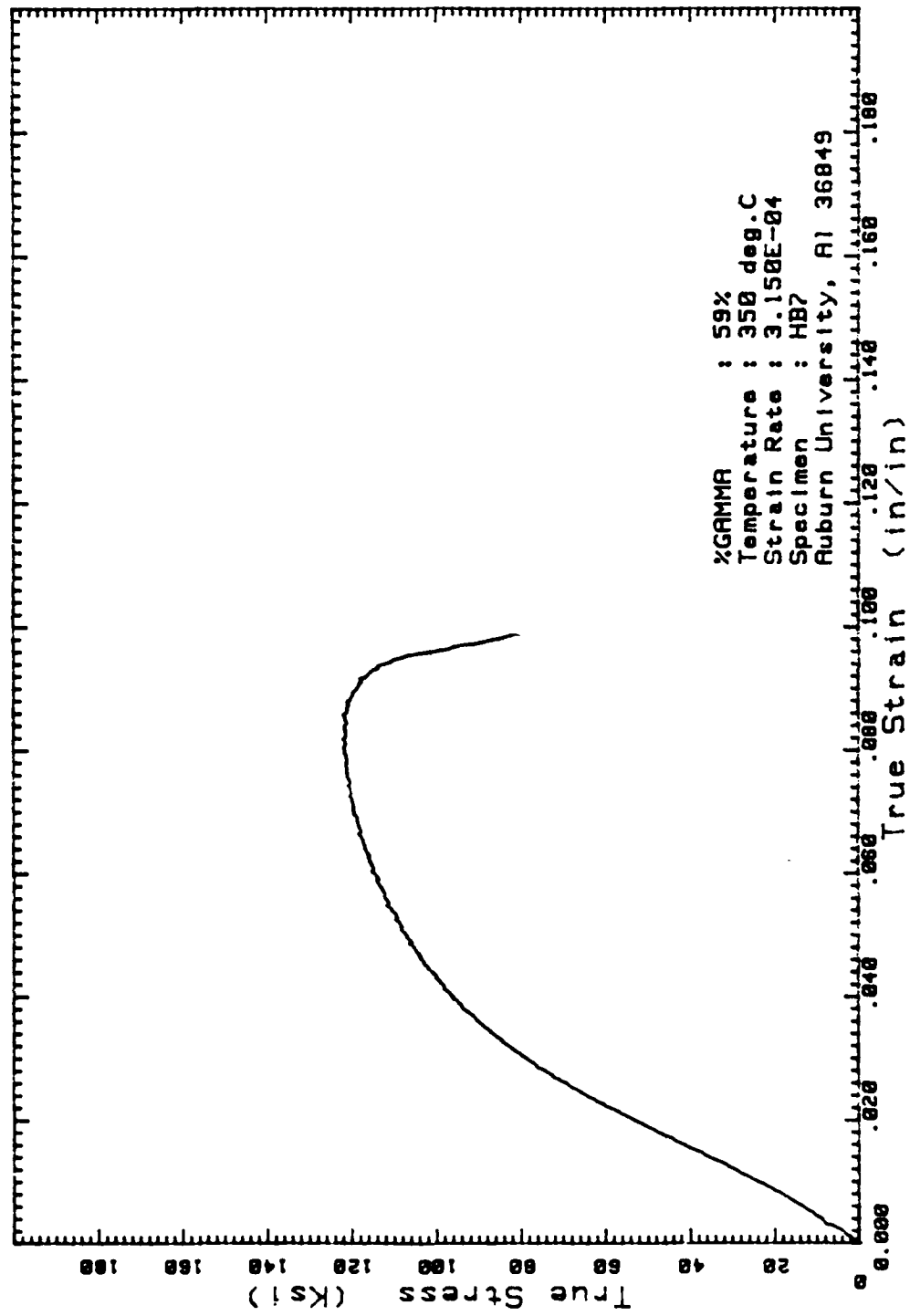




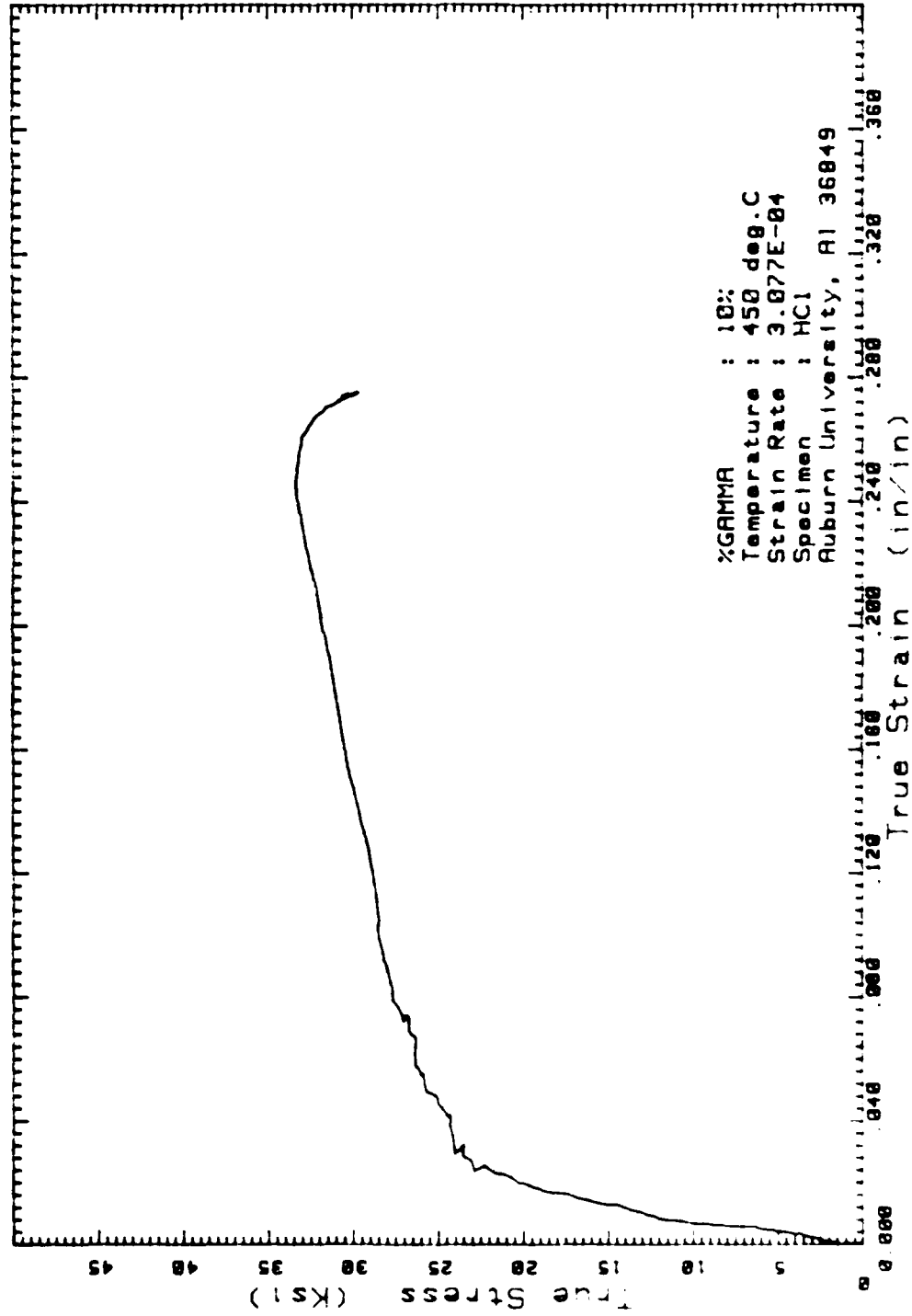


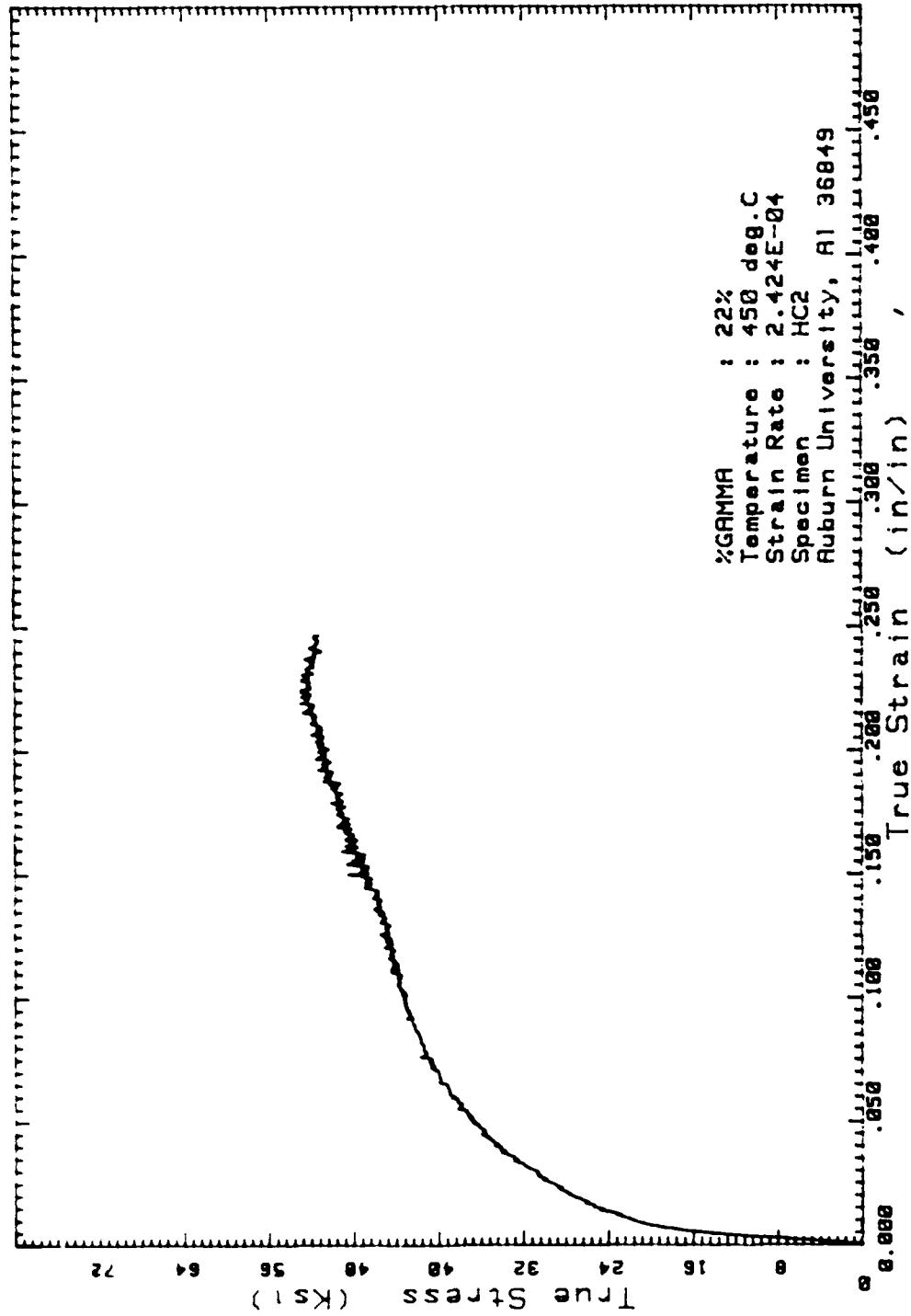


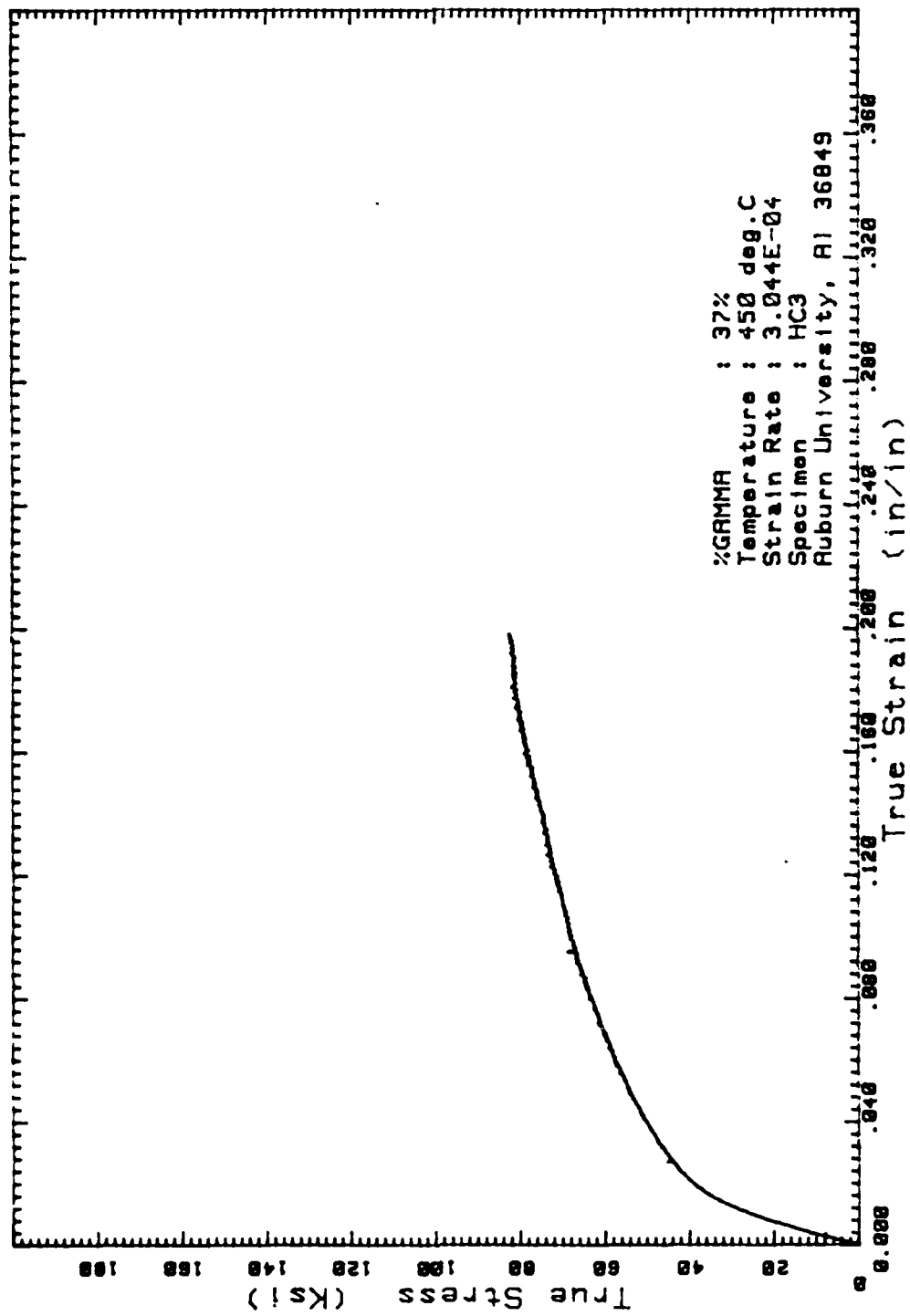


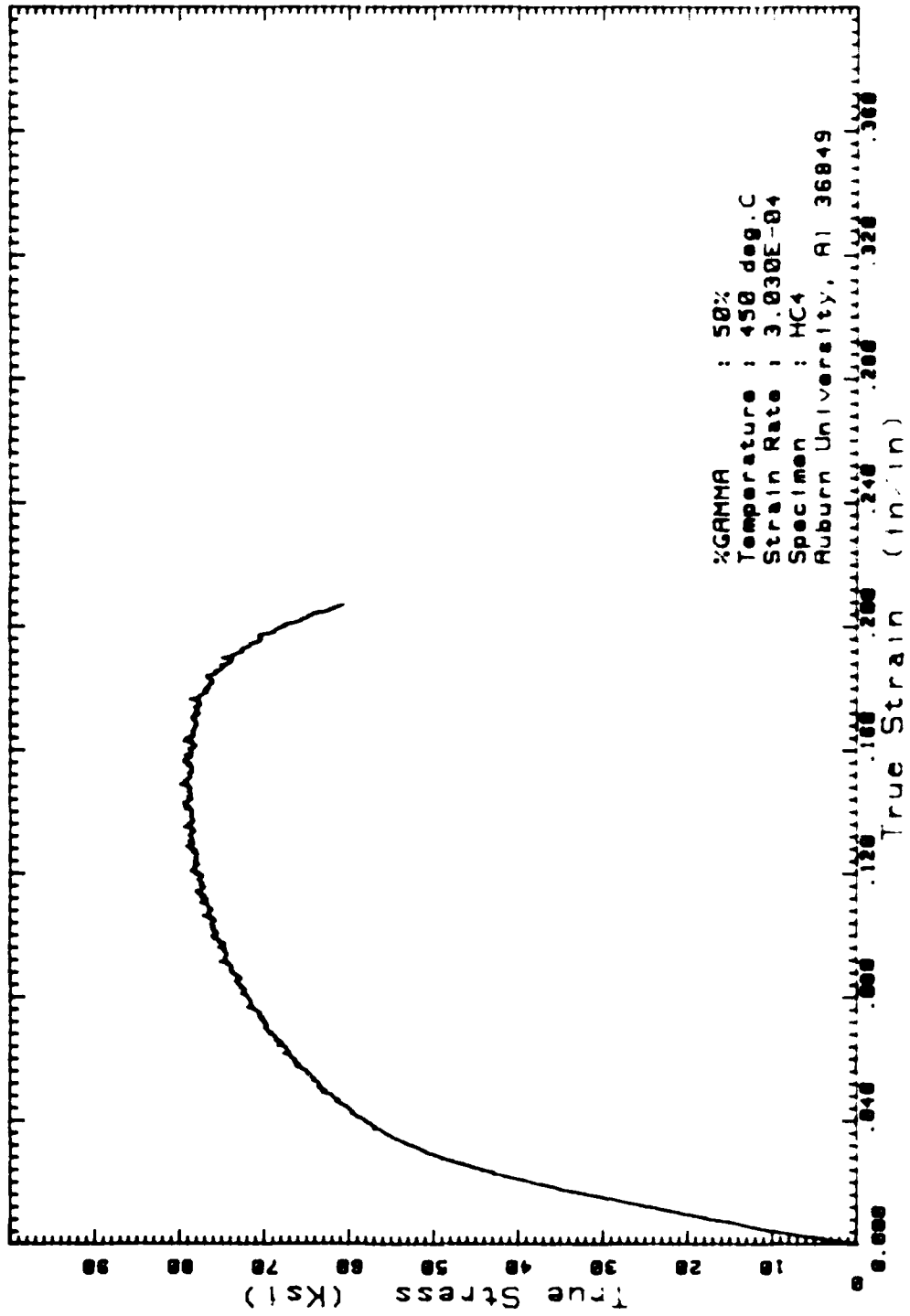


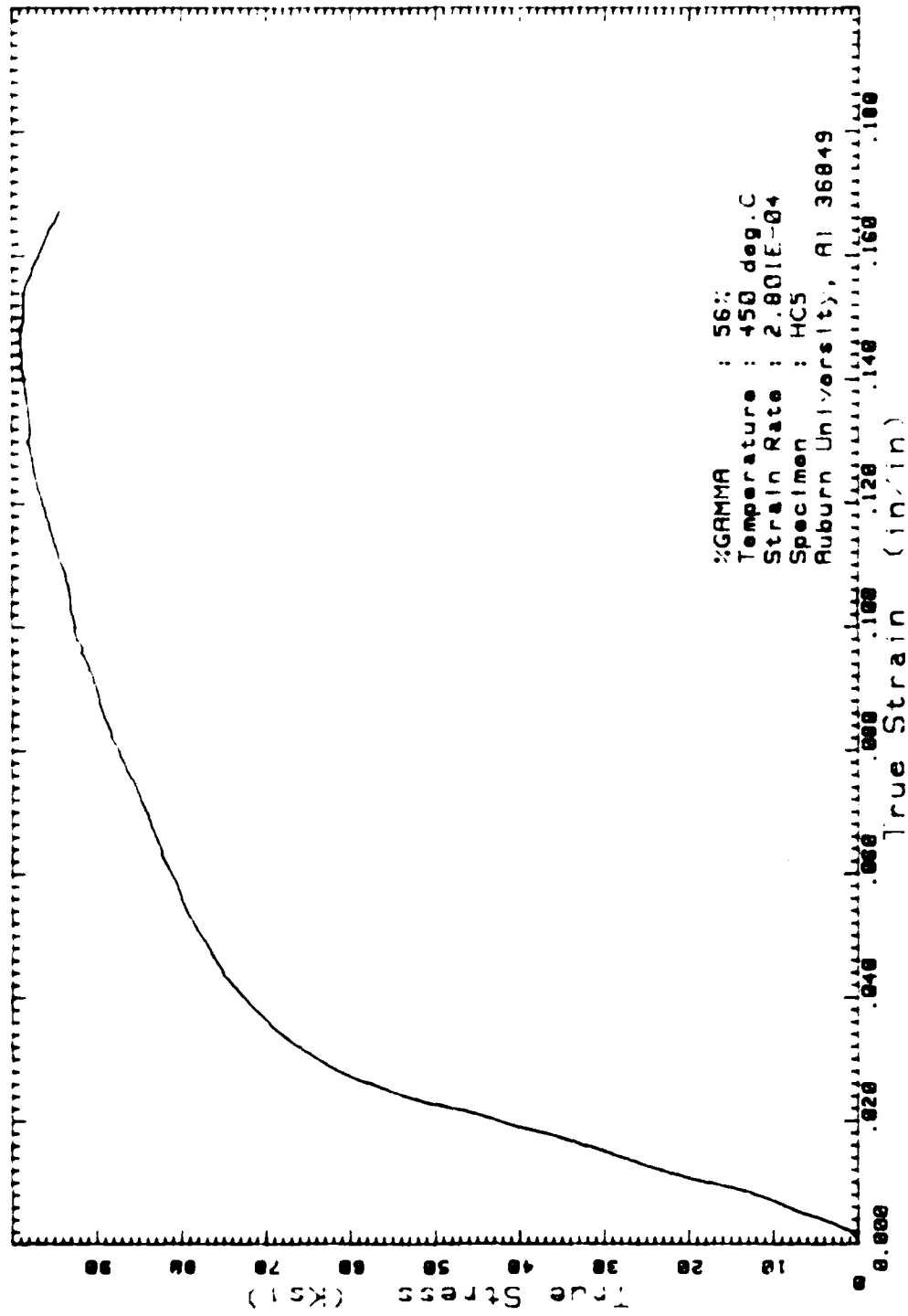


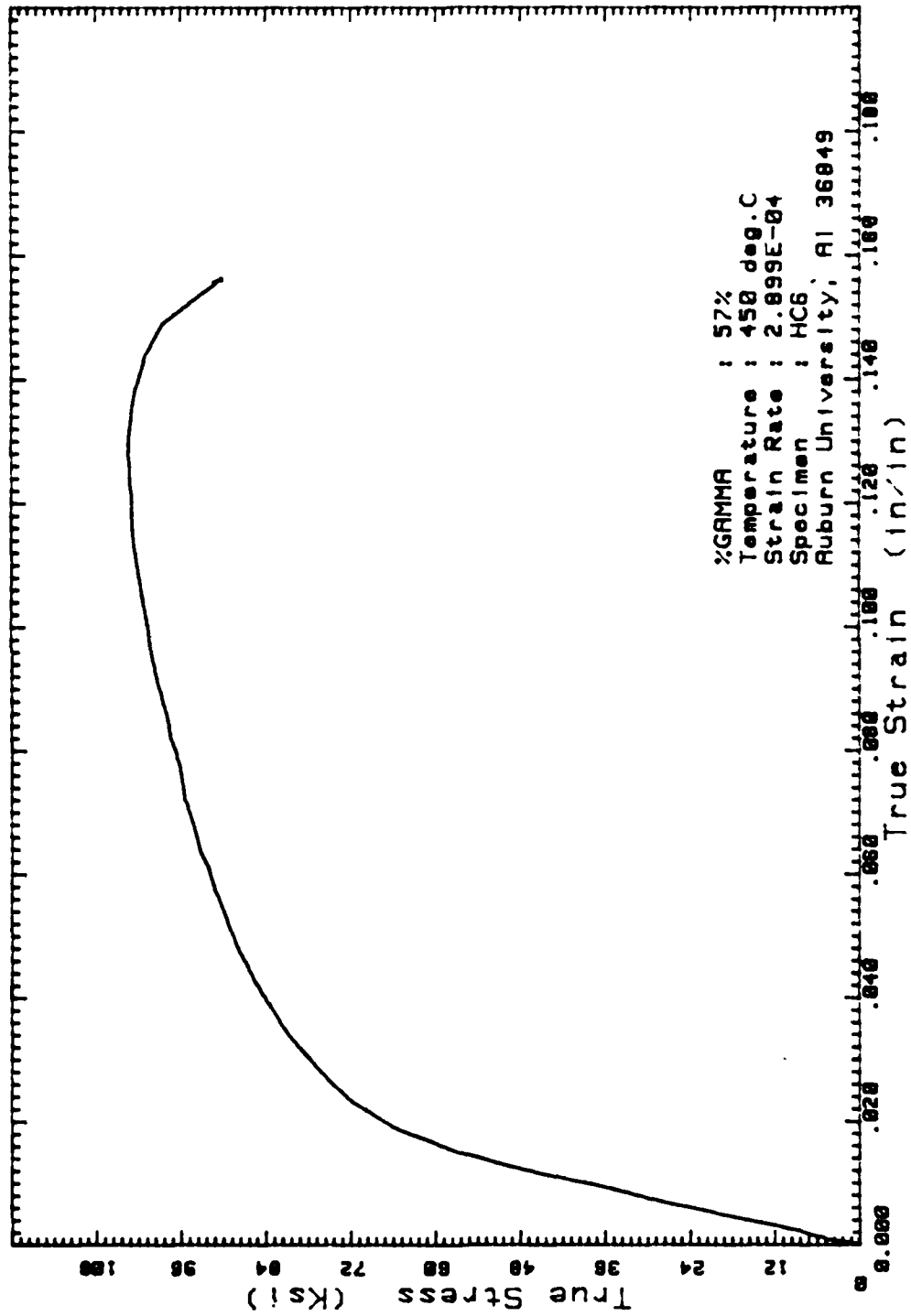


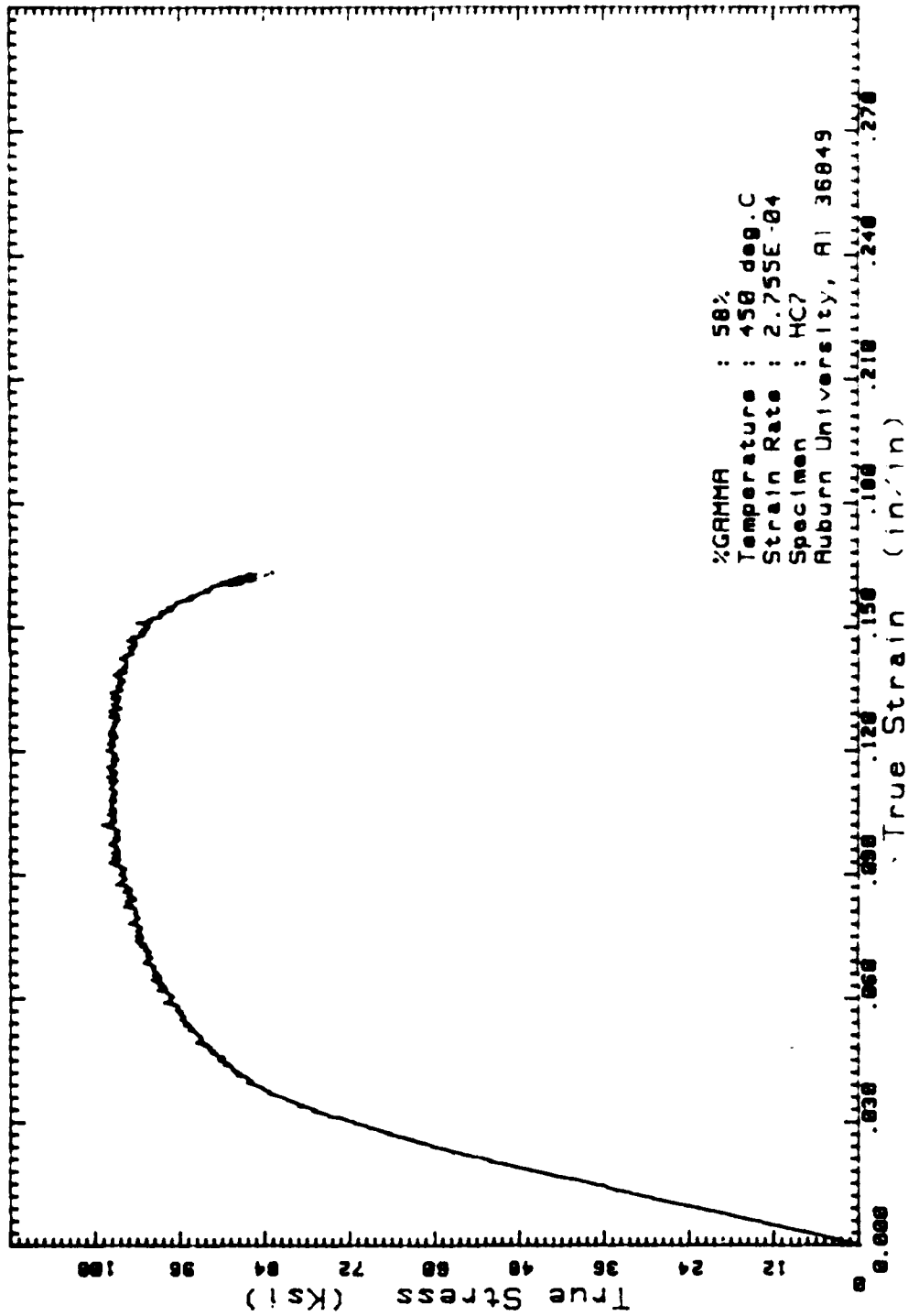


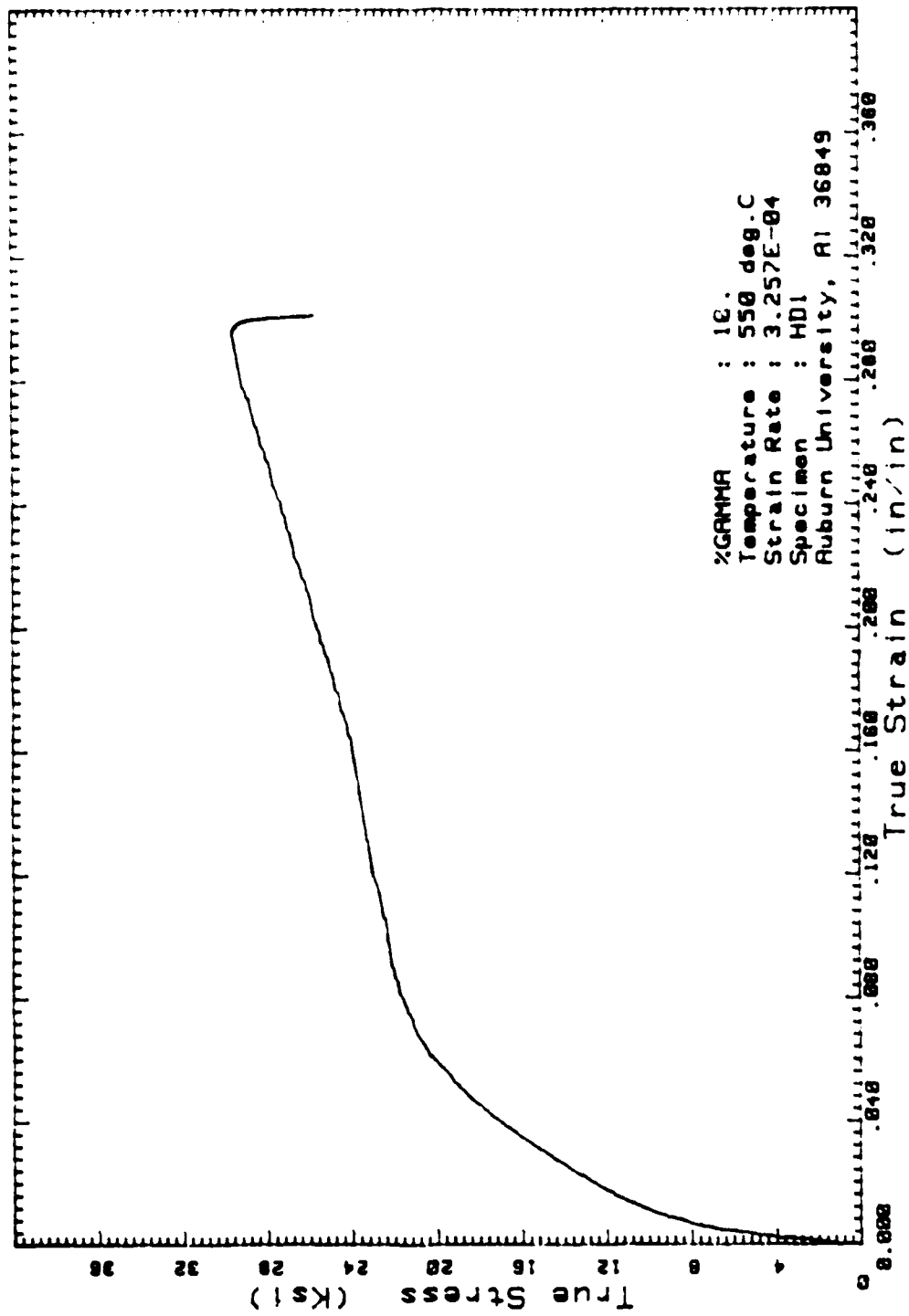




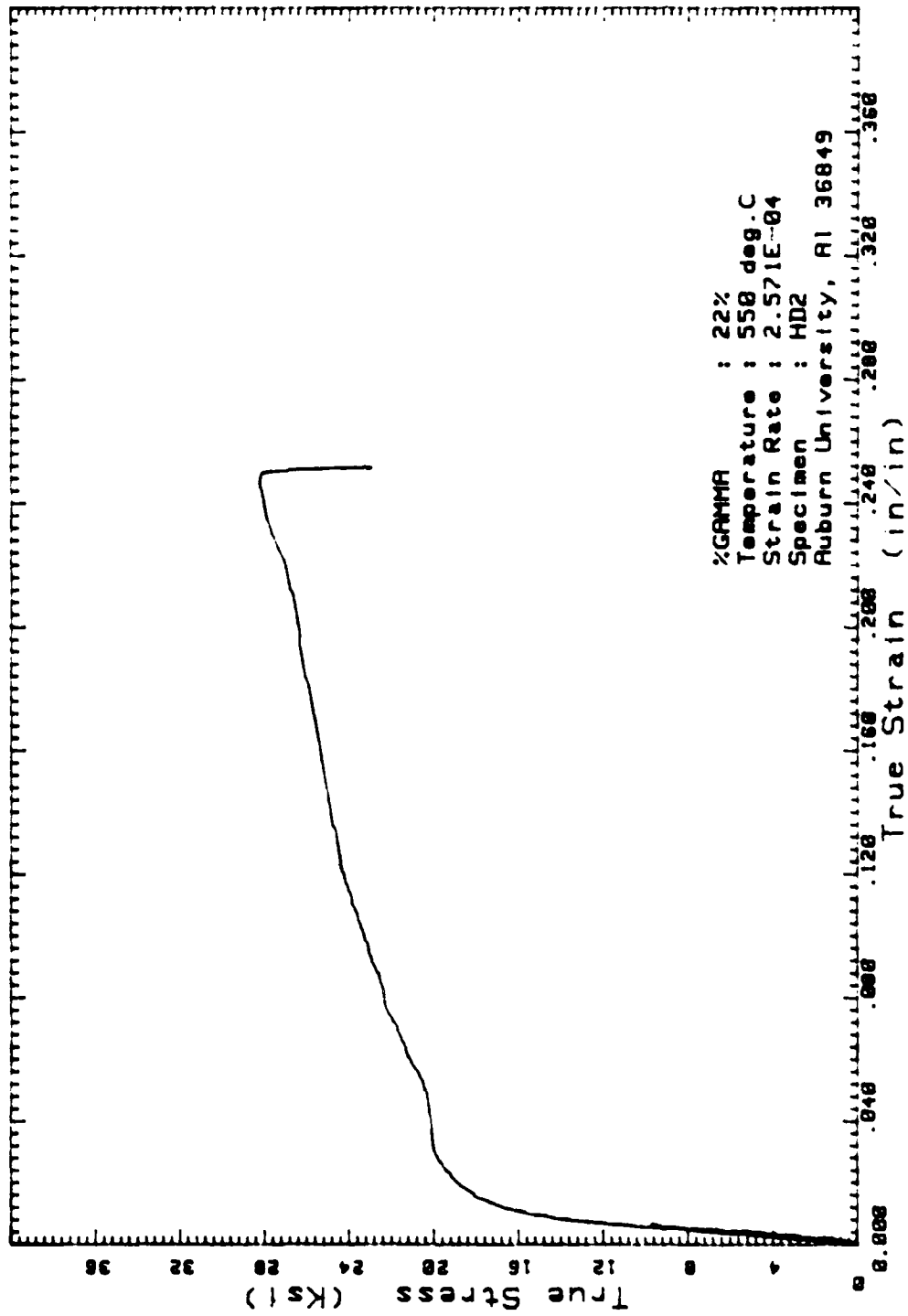


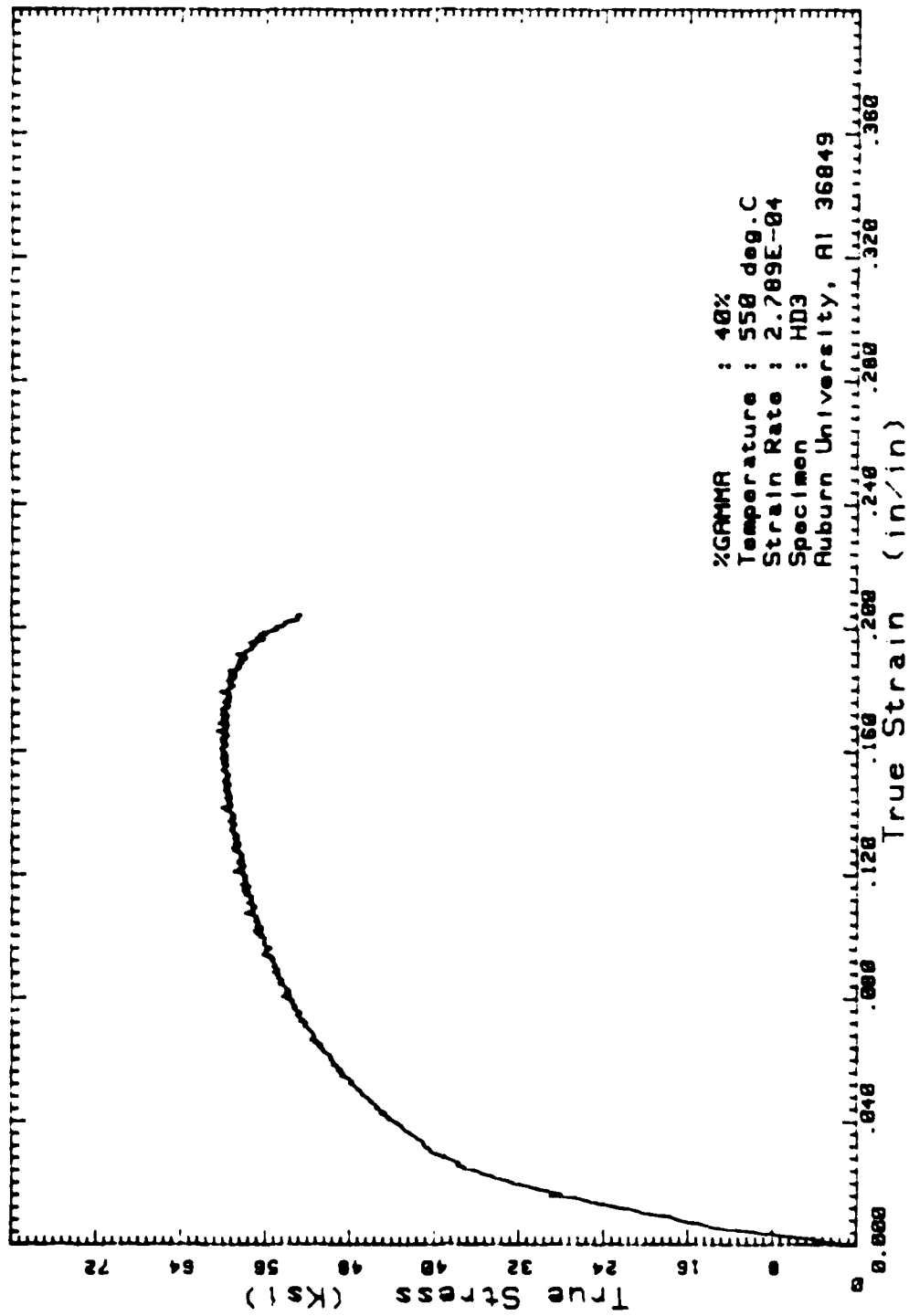


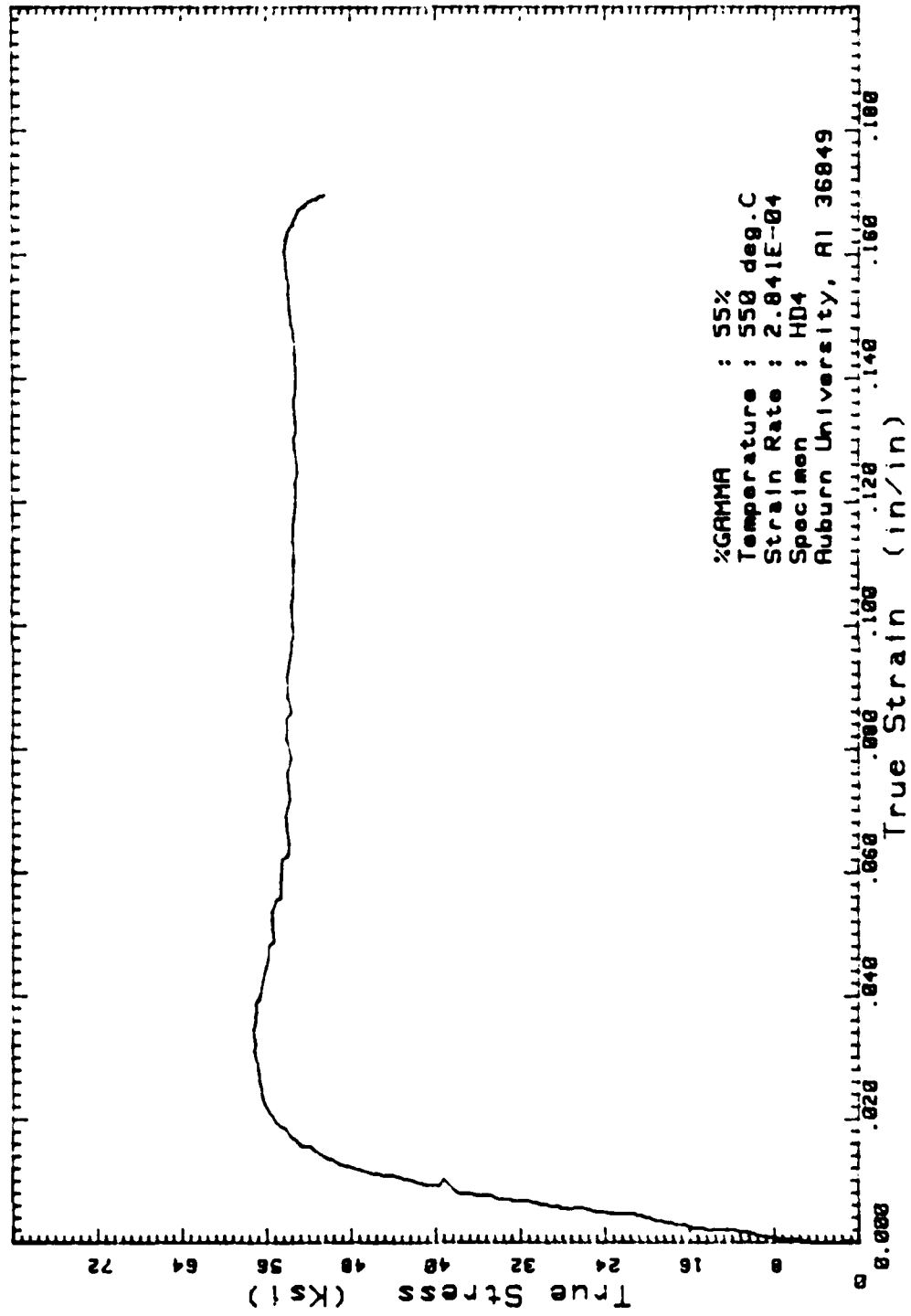


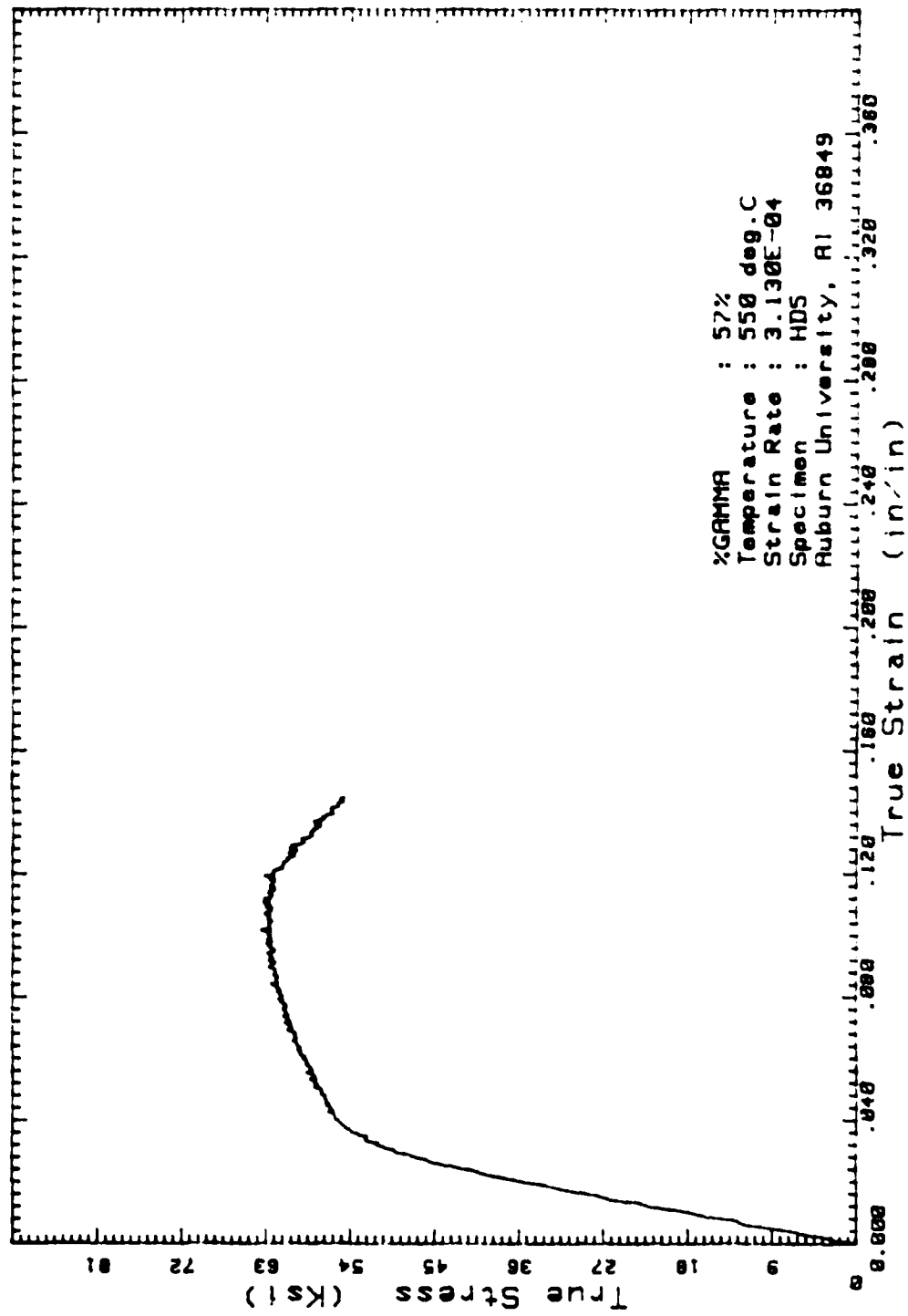


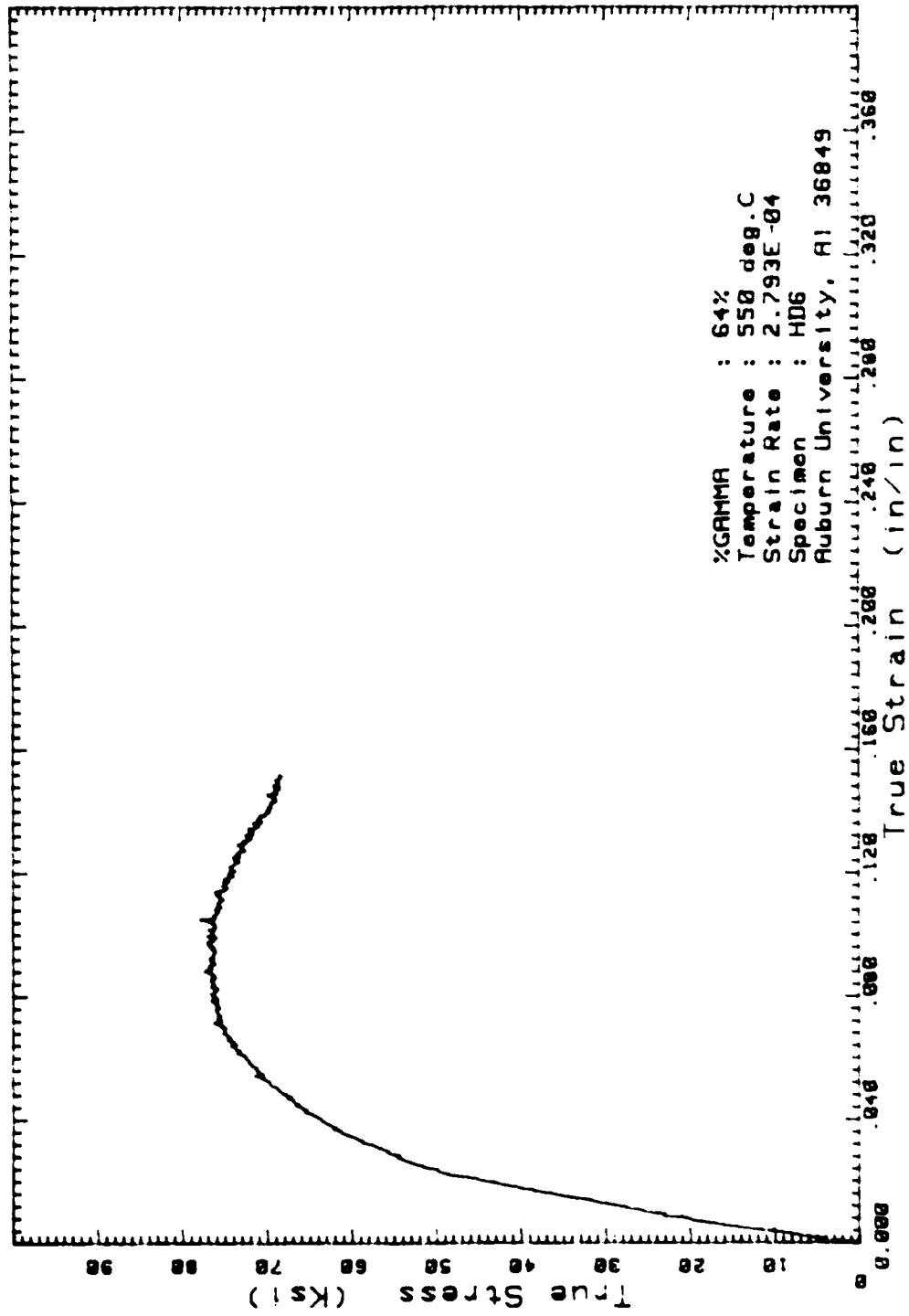


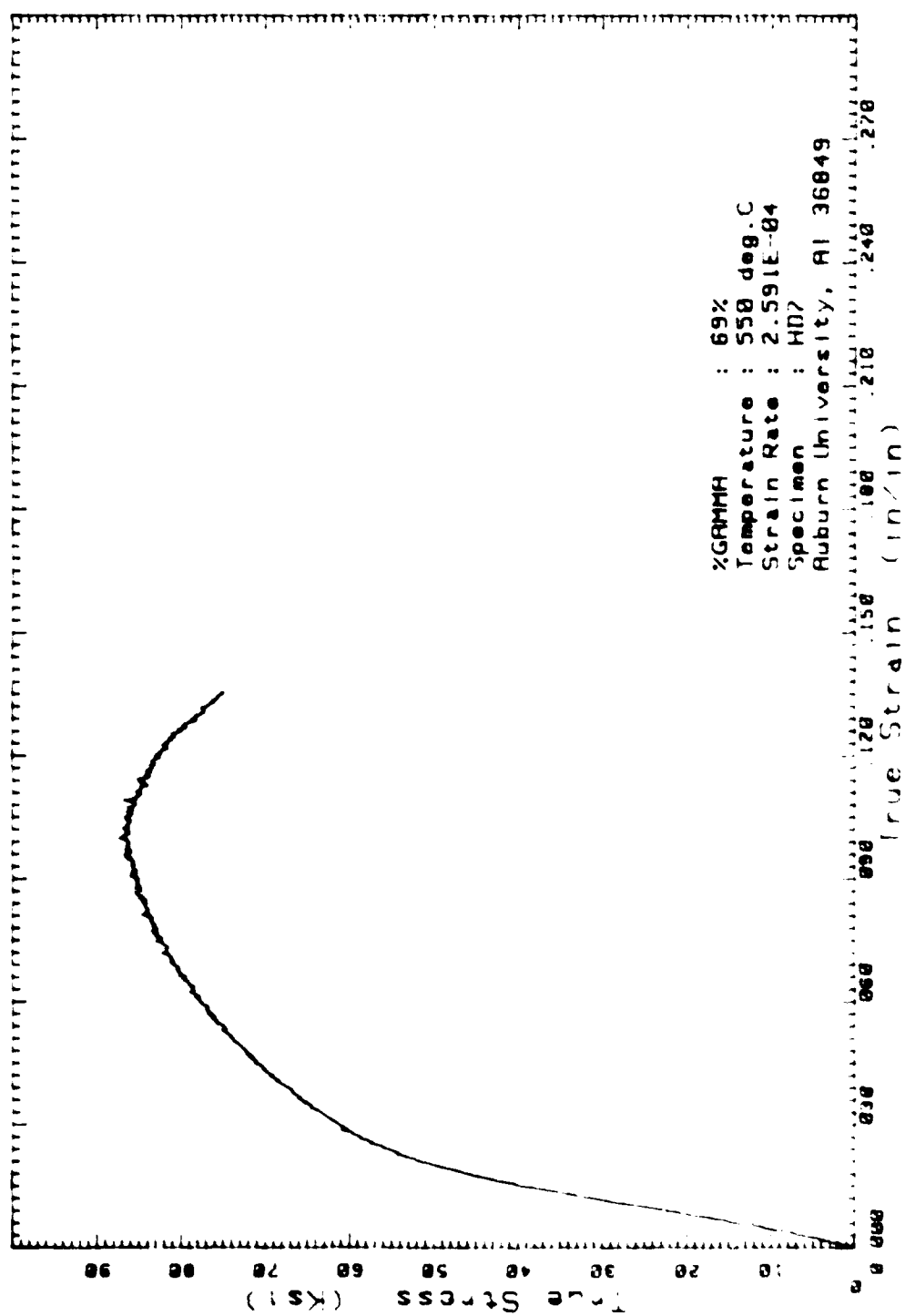


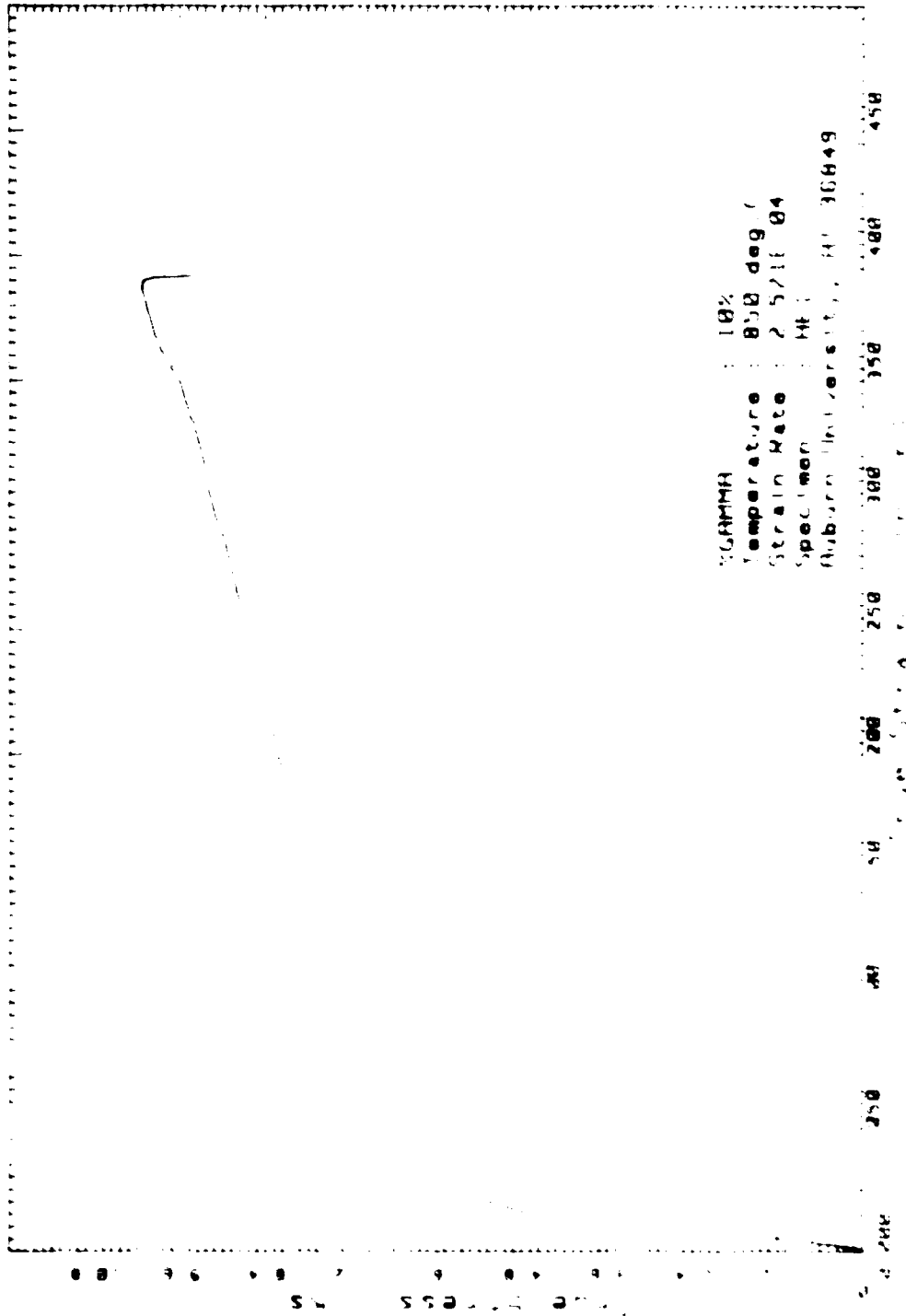


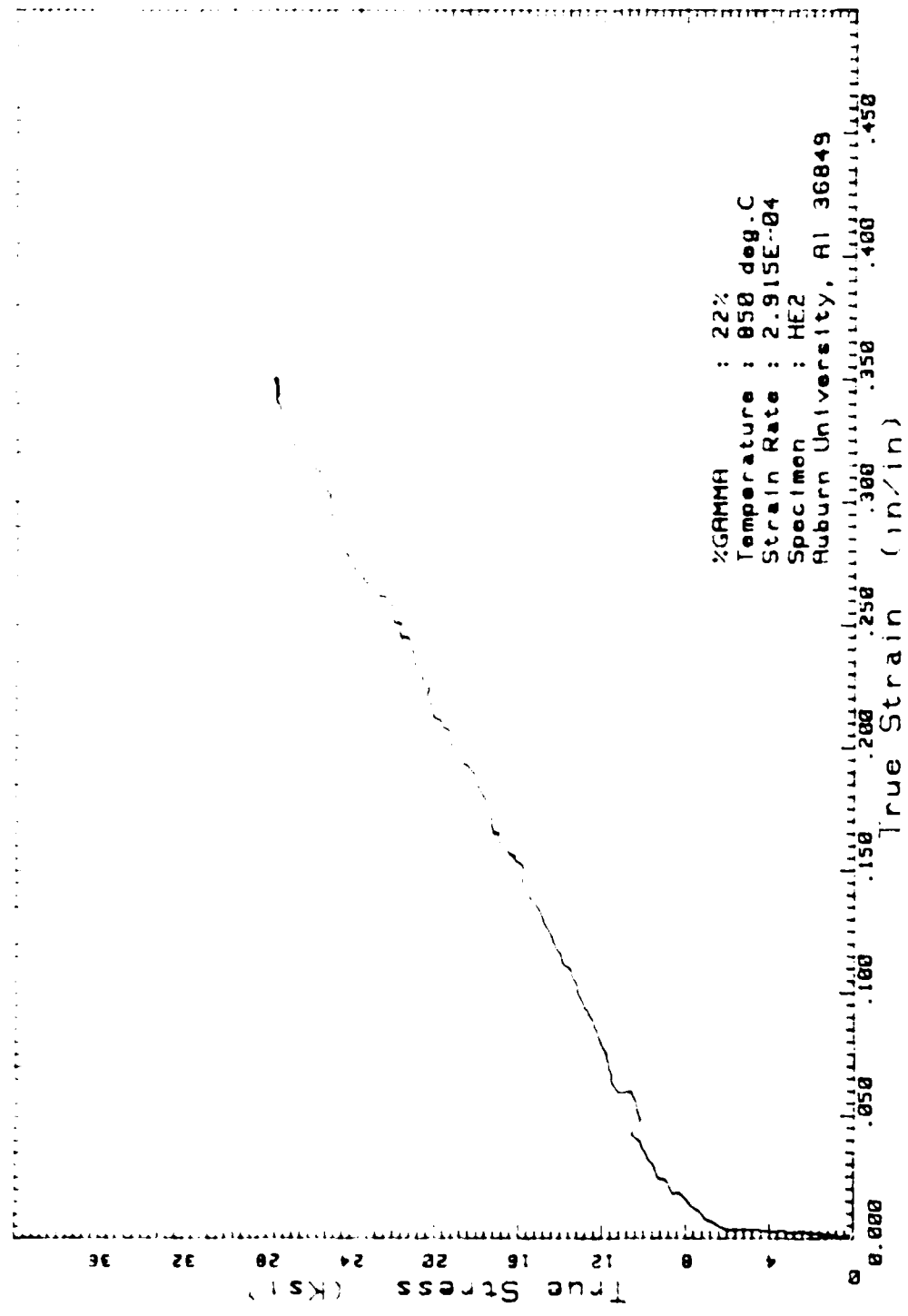




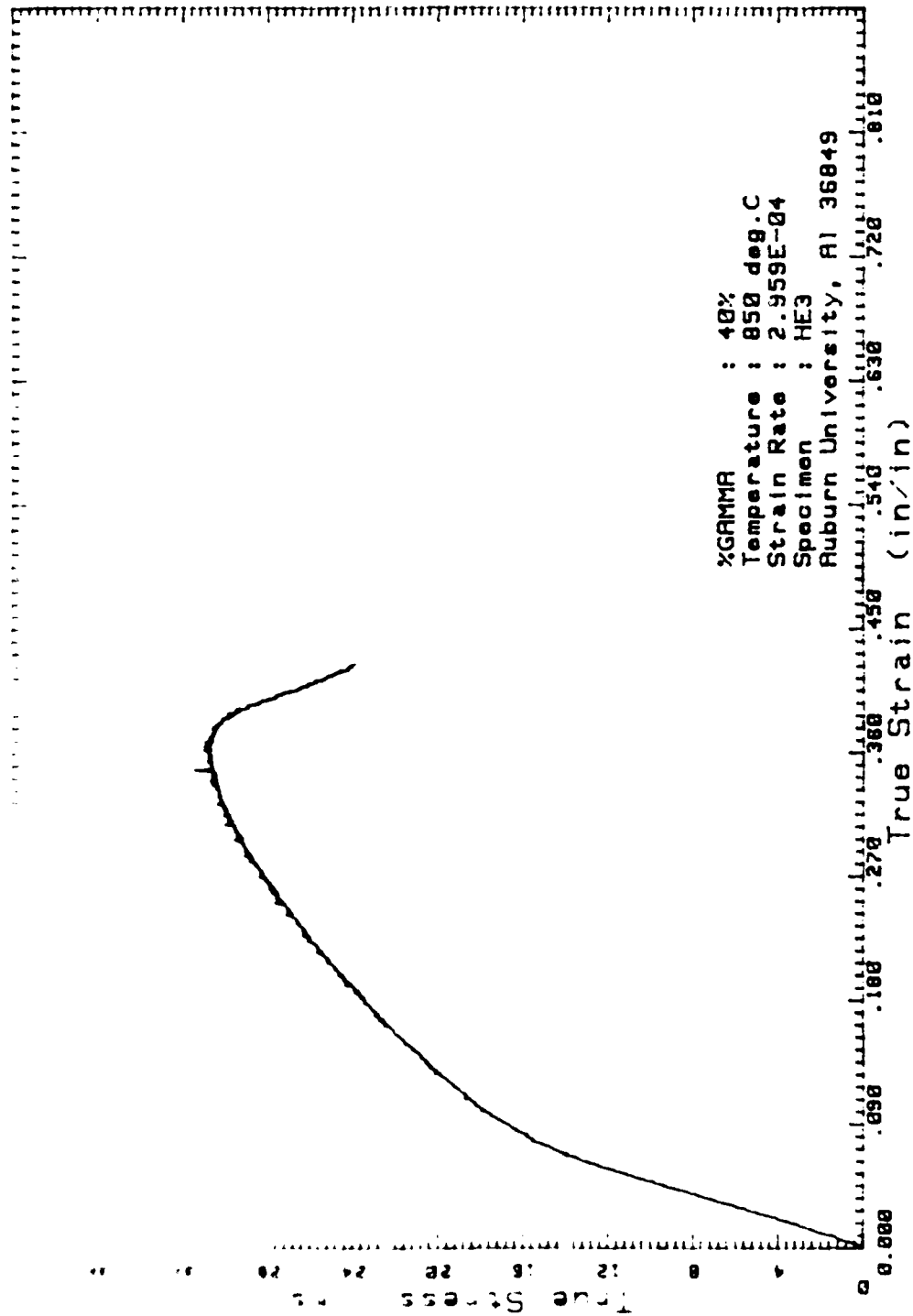


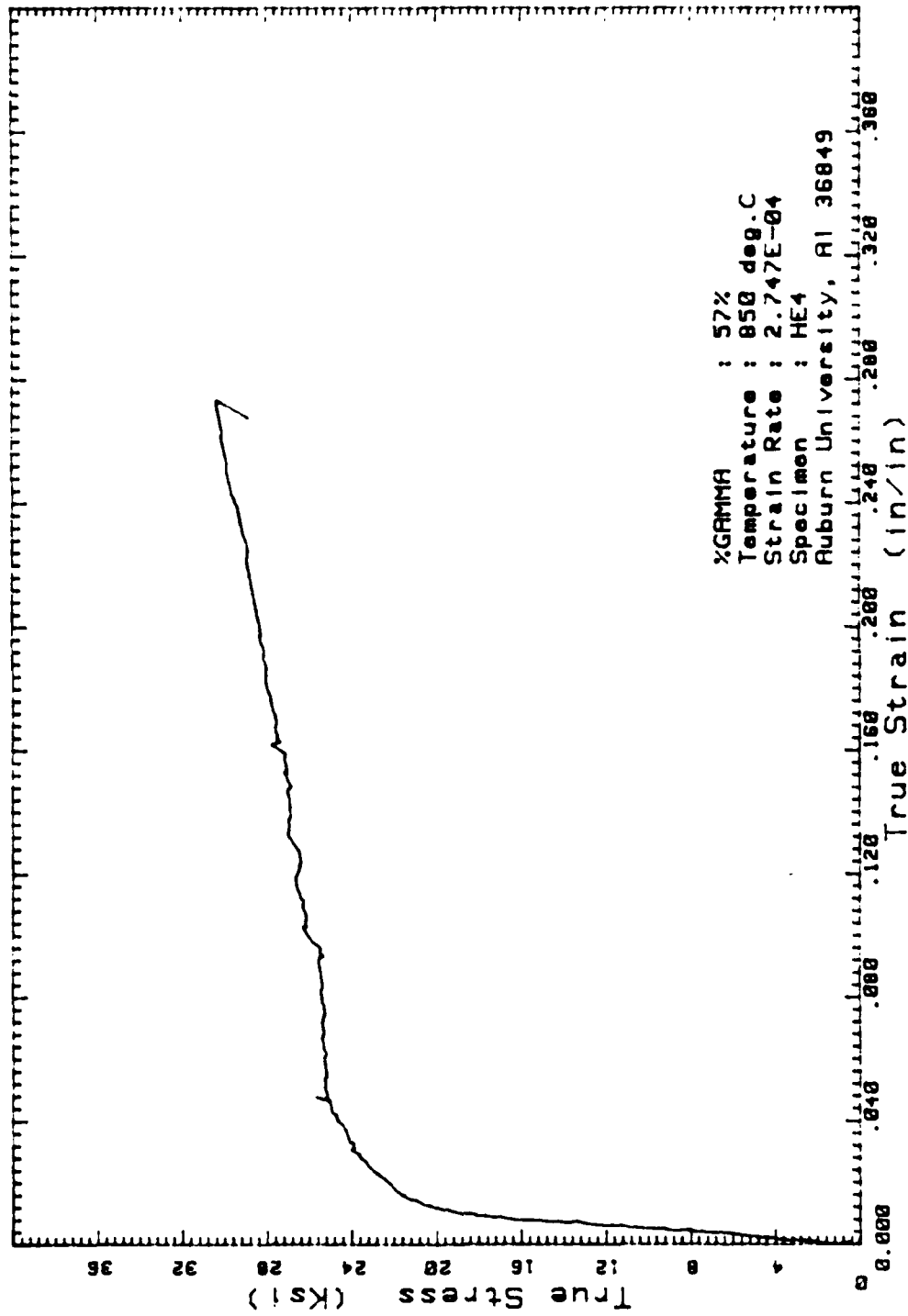


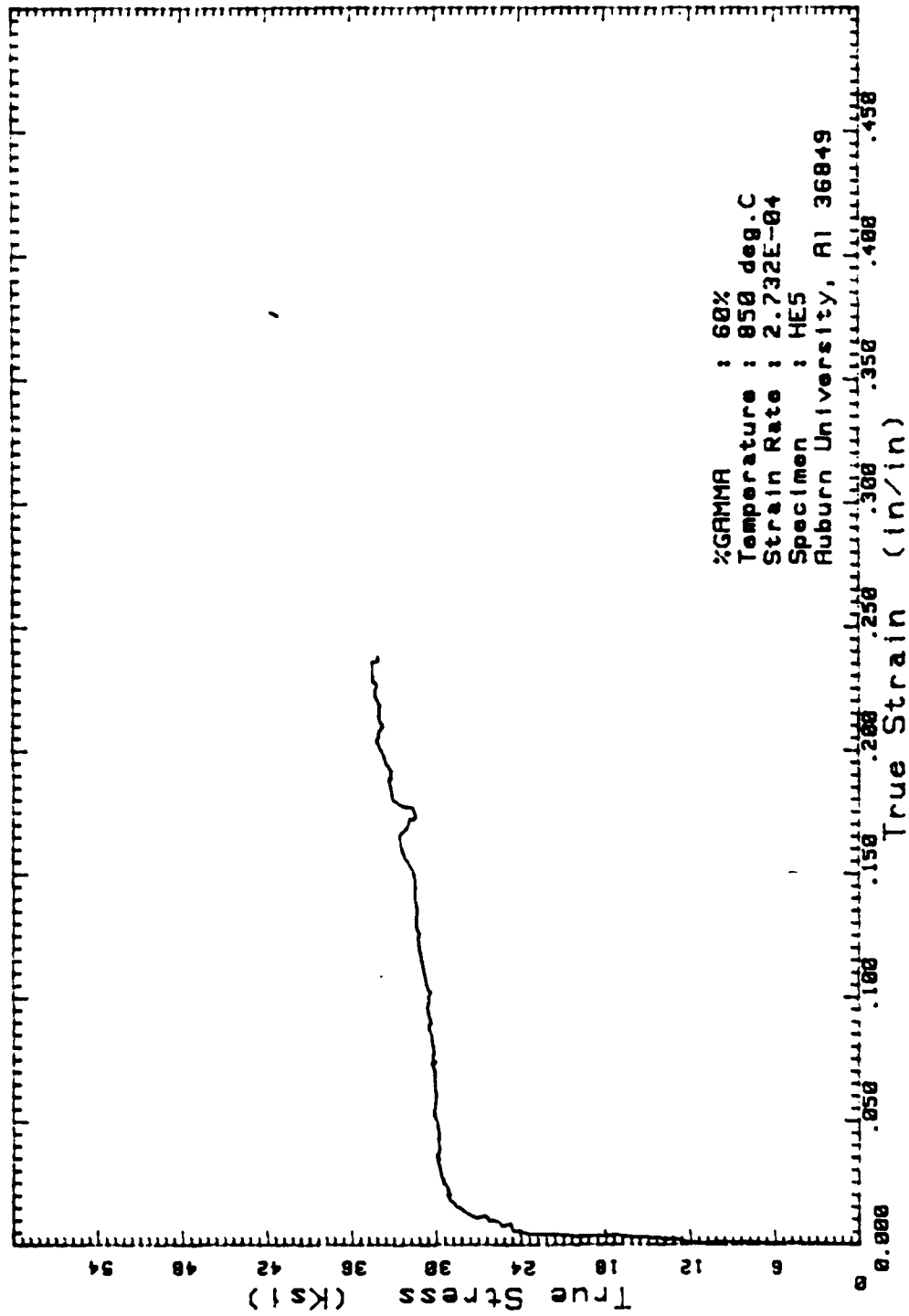












END

4-87

DTIC